ALMA MATER STUDIORUM – UNIVERSITY OF BOLOGNA

SCHOOL OF ENGINEERING AND ARCHITECTURE
SECOND CYCLE DEGREE IN CIVIL ENGINEERING
Department of Civil, Chemical, Environmental and Materials Engineering DICAM

DISSERTATION
In
Structural Safety

Design, fabrication and mechanical characterization of a structural node made using Wire-and-Arc Additive Manufacturing (WAAM) technology

CANDIDATE:
Edoardo Benvenuti

SUPERVISOR:
Prof. Ing. Tomaso Trombetti

CO-SUPERVISOR:
Dott. Ing. Vittoria Laghi
Prof. Ing. Harald Kloft
Dott. Neira Babovic

ACCADEMIC YEAR 2021/2022
Session III

TABLE OF CONTENTS

CHAPTER 1

CHAPTER 2

CHAPTER 5

CHAPTER 6

CHAPTER 9

CHAPTER 1

INTRODUCTION

1.1 Additive Manufacturing of metals

Additive Manufacturing (AM), also known as 3D printing (3DP) or rapid prototyping (RP), has been defined by ISO/ASTM 52900 as "process of joining materials to make parts from 3D model data, usually layer upon layer, as opposed to subtractive manufacturing and formative manufacturing methodologies". AM derives from stereolithography using ultraviolet (UV) lasers, which initially was used to cure photopolymers into 3D shapes. Later, AM for metal was developed in 1980s and 1990s.

AM is already widely used in various sectors, from aerospace to biomedical, however it is still little used in construction. The benefits that AM can provide over conventional methods include geometric freedom, efficiency, cost and production time (Milewski, 2017).

The development of AM technologies allows to change the mind of companies and engineers, substituting the subtractive techniques, which consist in reducing the amount of material from an initial block, or formative methods, where the material is shaped (hot-rolling or cold-forming) or casted in a mould (C. Buchanan, 2019).

Generally, AM process follows eight steps: conceptualization and CAD; conversion to STL/AMF; transfer and manipulation of STL/AMF file on AM machine; machine setup; build; part removal and clean-up; post-processing of part; application (Ian Gibson, 2015).

Nowadays, AM of metals is highly used in automotive and aerospace sectors, in which it is possible to realize lightweight components for specific application and allowing to reduce considerably the production time. The most important example is the GE Aero LEAP fuel nozzle, which combines 18 elements into one part, reduces its weight of a quarter and increases its lifetime of five times. In addition, AM can be used also for medical applications, permitting to create highly customized element and in small quantities, like sternum chest implants or dental bridges (Milewski, 2017). In construction sector, AM of metals is starting to be applied for the fabrication of connection joints (Arup lighting node), façade nodes (Nematox façade node) and pedestrian bridges (MX3D bridge). The first two demonstrated the potentials of AM in terms of geometrical freedom and production time (Salomé Galjaard S. R., 2015) (Strauß, 2013), while the third one proved that it is also possible to create large steel structures using Wire-and-Arc Additive Manufacturing (WAAM).

1.2 Topology optimization

Structural optimization consists to find out which is the best way to carry a load considering some prescribed boundary conditions. The best way can be identified in a specific property of the initial structure, like self-weight, stresses, strains or stiffness.

In order to carry out a structural optimization, the designer can choose among three possible analysis: size optimization, shape optimization and topology optimization.

Size optimization allows the designer to find the optimal design changing a design variable such as the cross-sections or the thicknesses. This is the easiest and the earliest approach to improving the structural performances (X. Huang, 2010).

Then, the goal of the shape optimization is to find the optimum shape of a given initial domain without changing parameters such as thicknesses or cross-sections (M.P. Bendsøe, 2003).

Instead, topology optimization for discrete structure is to search for the optimal spatial order and connectivity of the bars, while for continuum structures, is to find the optimal design by determining the best locations and geometries of cavities in the design domains (X. Huang, 2010).

Topology optimization is the most challenging but it is the most rewarding economically and provides more freedom and creativity to the designer (Linden, 2015).

1.3 Gridshells

Gridshells are optimized structures composed of discrete members connecting nodal points following a curved shape, however they behave like shells.

The designer of the first gridshell is Vladimir Grigoryevich Shukhov(1853-1939) with the structure in Vyksa, Russia in 1897. While another important designer was Frei Otto (1925-2015) and his most famous timber gridshell structure was the Mannheim Multihalle, Mannheim, Germany in 1975.

Nowadays, gridshells are employed to create bright and innovative public spaces, like Joe and Rika Mansueto Library in Chicago and The Queen Elizabeth II Great Court, British Museum in London.

Three possible approach are possible to design a gridshell: freeform, form-finding and mathematical.

Freeform shells are generated without considering the structural efficiency based only on aesthetic preferences.

Then, using the form-finding process the shape of the surface is optimized in order to sustain the self-weight of the shell.

Finally, mathematical gridshells are derived from analytical functions.

1.4 Objective and research methodology

1.4.1 Objective of the thesis

The purpose of this thesis is to design a topology optimized structural joint for the British Museum gridshell structure. Then, the optimized node will be studied in order to understand its structural behaviour, analysing its strength and stiffness. Finally, the node will be built using Wire-and-Arc Additive Manufacturing.

1.4.2 Research methodology

Firstly, in Chapter 02, AM will be discussed considering the most common 3D-printing technologies, advantages, disadvantages and possible applications in industrial and construction sectors.

Then, gridshell structures will be presented in Chapter 03. Initially, the history of gridshells will be treated and then their structural behaviour will be studied in details.

Furthermore, structural and topology optimization will be studied in Chapter 04, in which SIMP, ESO and BESO methods will be analysed to understand their main features.

In Chapter 05, joint classification will be discussed considering two approaches. The first approach is the one presented in Eurocode 3, while the second one will be used to assess the mechanical properties of the designed joint.

In addition, in Chapter 06, the British Museum gridshell will be modelled using Rhino 7 and Grasshopper and then it will be studied to obtain the stresses acting in the trusses at the Ultimate Limit State (ULS). Later, after choosing a node of the British Museum, the topology optimization will be performed using two different approaches, SIMP and BESO, comparing the different results.

Only one topology optimized joint will be chosen and it will be studied and classified in Chapter 07, following the procedure explained before in Chapter 05. All the moment-rotation diagrams will be presented considering two different joint thicknesses, 6 and 12 mm.

Lastly, in Chapter 08, a test fabrication using WAAM technology will be presented. The main issues in fabrication, like overhang and heat deformations, will be treated and solutions will be proposed.

CHAPTER 2

ADDITIVE MANUFACTURING IN CONSTRUCTION

2.1 Overview and generic AM process

Additive Manufacturing is defined as: “The process of joining materials to make objects from 3D model data, usually layer upon layer, as opposed to subtractive manufacturing methodologies” (Wohlers, 2010).

Generally, additive manufacturing process follows eight steps (Figure 2.1) (Ian Gibson, 2015):

- Conceptualization and CAD;
- Conversion to STL/AMF;
- Transfer and manipulation of STL/AMF file on AM machine;
- Machine setup;
- Build;
- Part removal and clean-up;
- Post-processing of the part;
- Application.

These tasks are generic and common for all the applications, however there might be additional steps in relation to the final purpose of the object generated. For example, an engineer may require more stages in the design of the final product in order to achieve some mechanical and geometrical properties.

Firstly, the tri-dimensional geometry of the product is designed using a Computer Aided Design (CAD) software.

Subsequently, the CAD model is converted to a stereolithography (STL) format, which removes all history modelling information and simplifies the CAD model using a series of triangular elements (Figure 2.2). Since STL is essentially a surface description, the corresponding triangles in the files must be pointing in the correct direction; in other words, the surface normal vector associated with the triangle must indicate which side of the triangle is outside vs. inside the part (Ian Gibson, 2015). Due to the fact that STL files have no information about units, material and colours, recently a new format has been developed and it is called AMF. Its benefits are the same of a STL file but it has less limitations.

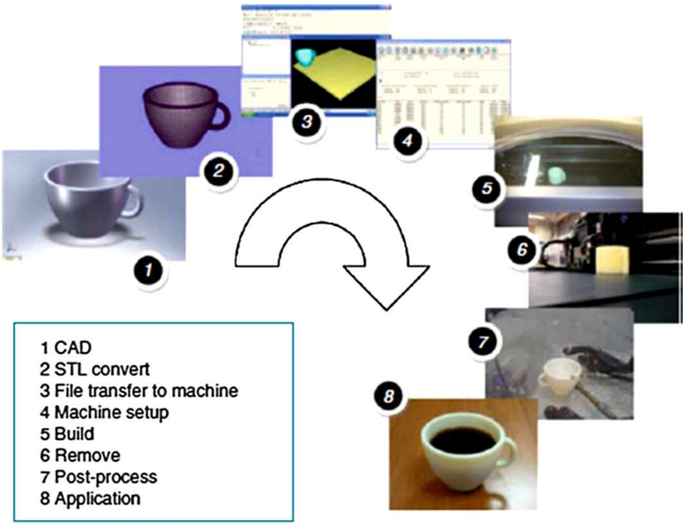

Figure 2.1 - Additive manufacturing process (Ian Gibson, 2015)

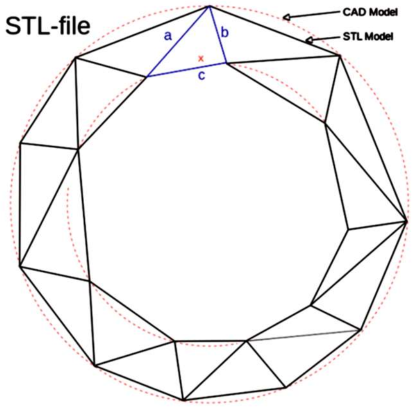

Figure 2.2 - Differences between CAD and STL files (Milewski, 2017)

At this stage, the STL can be sent to the AM machine and, if necessary, it can be modified or scaled. In some cases, it is useful to change the object orientation in order to avoid some printing problems.

Then, it is necessary to prepare the machine setting the printing parameters like speed, temperature and layer thickness. All these parameters affect the quality of the final product and the time requested for the production. Other possible adjustments can be related to the assessment of the printing path and the physical preparation of the printing area, inserting a base plate if requested (Figure 2.3).

Figure 2.3 - Base plate installation for WAAM

Once that everything has been set, it is possible to build the product. The process consists of the deposition of several successive layers until the object is completed or an error occurs.

Now, the element has to be removed from the machine and in some cases divided from the base plate. This stage is made manually.

Then, some post-processing treatments can be done on the removed element in order to improve its quality and mechanical properties. These may involve abrasive finishing, like polishing and sandpapering, or application of coatings. Even in these case, the post-processing treatments are realized manually.

Lastly, the product is finished and it is ready for the application. However, it must keep in mind that objects build using additive manufacturing technologies behave differently from products made using conventional tools. Typically, the material generated using 3D printing techniques has anisotropic properties, therefore every designer must be aware of that.

2.2 Metal additive manufacturing

Metal additive manufacturing can be classified in two ways, one related to the technology used and one to the state of the additive material. In the first case, there are four possible technologies:

- “Binder Jetting”;
- “Powder Bed Fusion”;
- “Sheet Lamination”;
- “Direct Energy Deposition”.

Indeed, in the second case, additive materials can be classified as:

- “Liquid-Based”;
- “Powder-Based”;
- “Wire-Based”.

These classifications are reported in the figures below:

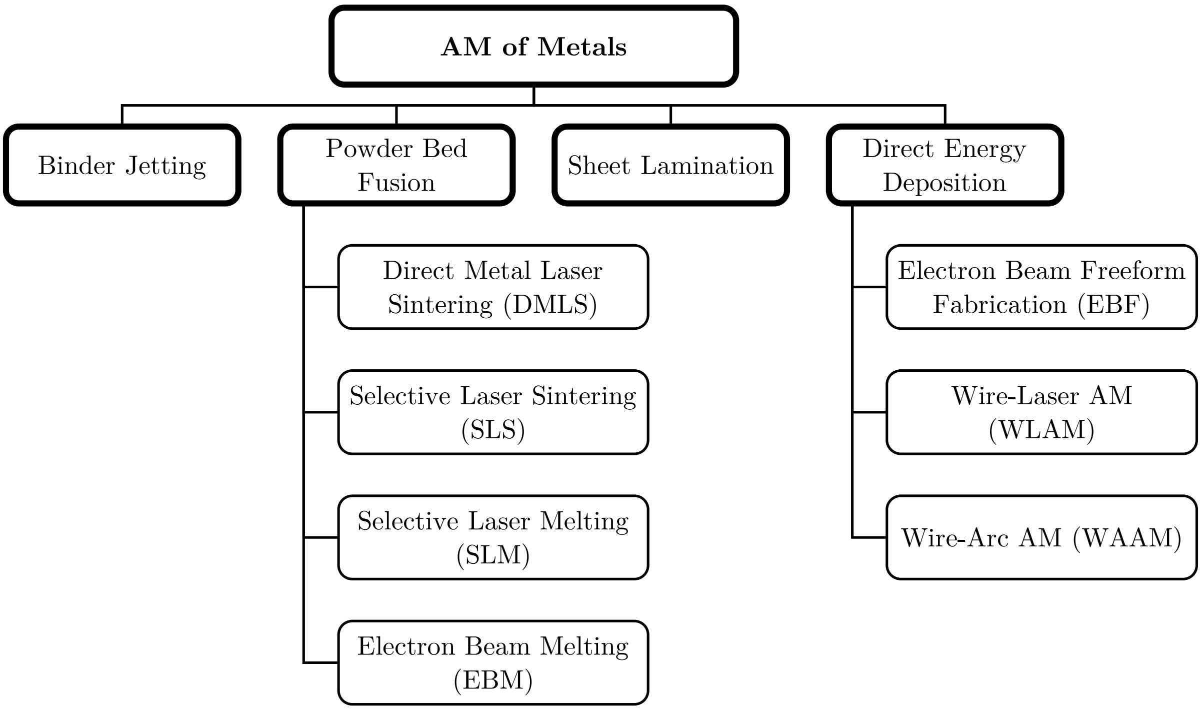

Figure 2.4 - AM classification based on technologies (Johnnie Liew Zhong Li, 2018)

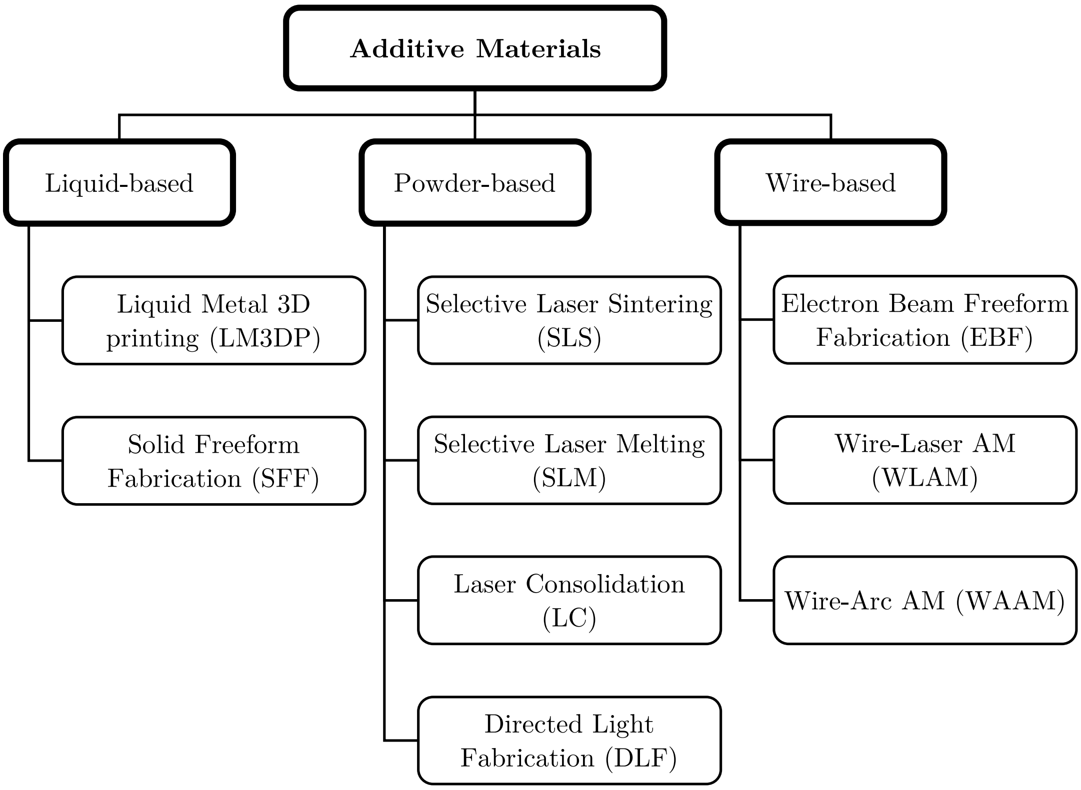

Figure 2.5 - AM of metals based on materials (Johnnie Liew Zhong Li, 2018)

In the following chapters, only the classification based on the additive manufacturing technology will be considered.

2.2.1 Binder Jetting

Binder Jetting is an AM method in which powdered material is spread into a layer and selectively joined into the desired layer shape with a binder, which is typically a polymeric liquid. As the build progresses, the layers of the print are bonded together, resulting in a box of powder with binder arranged in the 3D shape of the desired part geometry. The box may then be heated to cure or “set” the binder if needed, and then the printed parts may be removed from the powder bed in a process called “depowdering.” At this point, the printed parts are considered “green” or otherwise not suitable for end-use and are then subjected to a post-process such as sintering or infiltration to achieve desirable mechanical properties (Figure 2.7) (Amir Mostafaei, 2021).

Figure 2.6 - Binder jetting printer (Milewski, 2017)

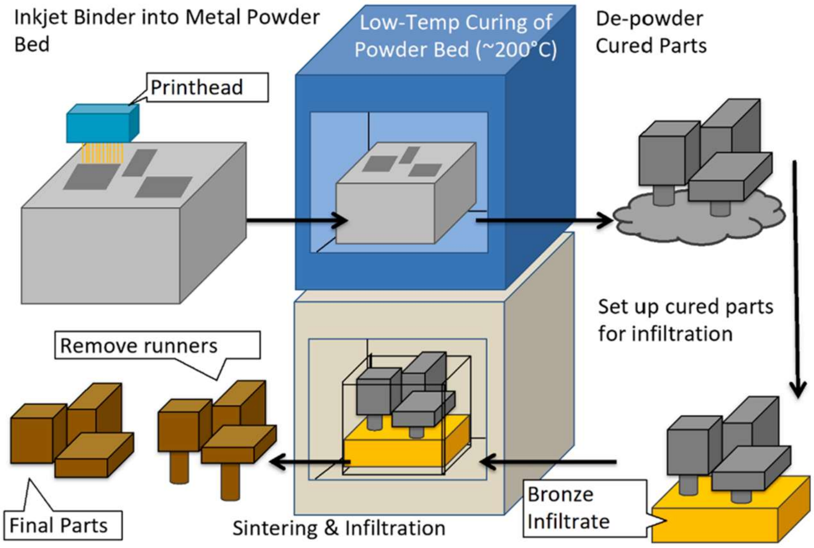

Figure 2.7 - Binder jetting process (Amir Mostafaei, 2021)

2.2.2 Powder Bed Fusion

Powder Bed Fusion (PBF) is a method of additive manufacturing in which material within a powder bed is selectively fused together using thermal energy, from either a laser or electron beam. This method is suitable for small parts with complicated geometries. The surface roughness is typically less than 20 µm and the maximum dimension of single part in general is a 250 mm cube (C. Buchanan, 2019).

2.2.2.1 Direct Metal Laser Sintering

Direct Metal Laser Sintering (DMLS) uses a laser beam in order to selectively sinter metal particles. Lower relative densities are obtained in comparison to methods that makes use of melting of the powder (Figure 2.8) (Linden, 2015). The obtained element can be reworked in order to improve its quality. The layer thickness resolution is 0.20 mm. The DMLS method is used to produce components for tools or machines as well as end use products (Strauß, 2013).

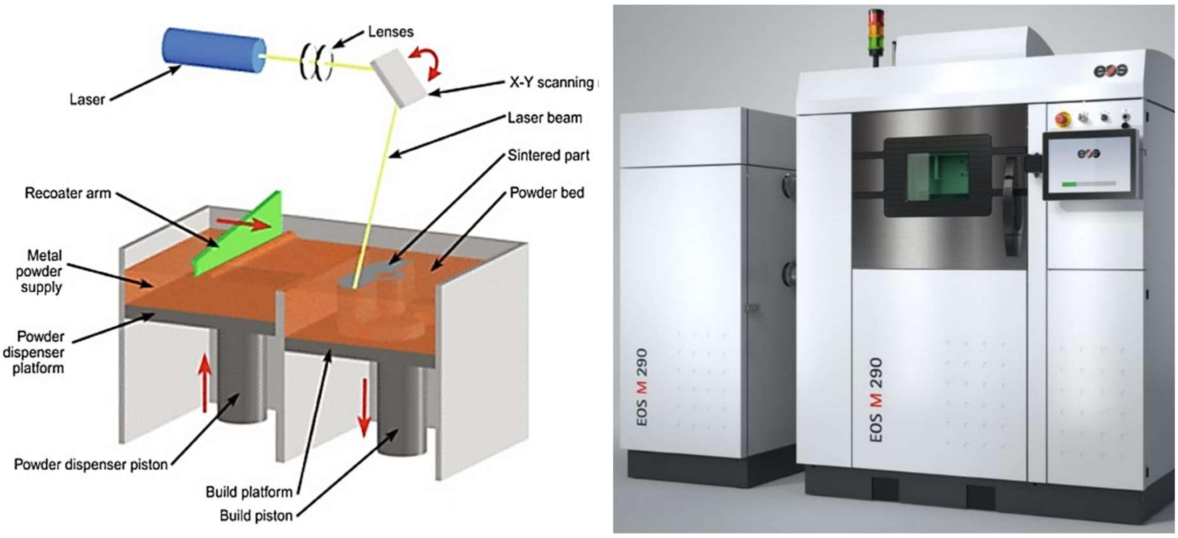

Figure 2.8 - Direct metal laser sintering process (left) and printer (right) (Linden, 2015)

2.2.2.2 Selective Laser Sintering

Selective Laser Sintering (SLS) uses a laser beam directed at a bed of powder to fuse a layer defined by the cross-sectional area of the sliced part model and a scan path of overlapping weld beads. The powder bed and part are then incrementally dropped and recoated by a roller or blade spreading a new layer of powder to allow the fusion of the next and successive layers of powder to form the part. It is important to note the powder layer thickness is greater than the fused deposit layer thickness. The depth of penetration is greater than the deposit layer thickness and can often penetrate three or more layers in depth to more fully fuse the deposit (Milewski, 2017). The following figures show the SLS process:

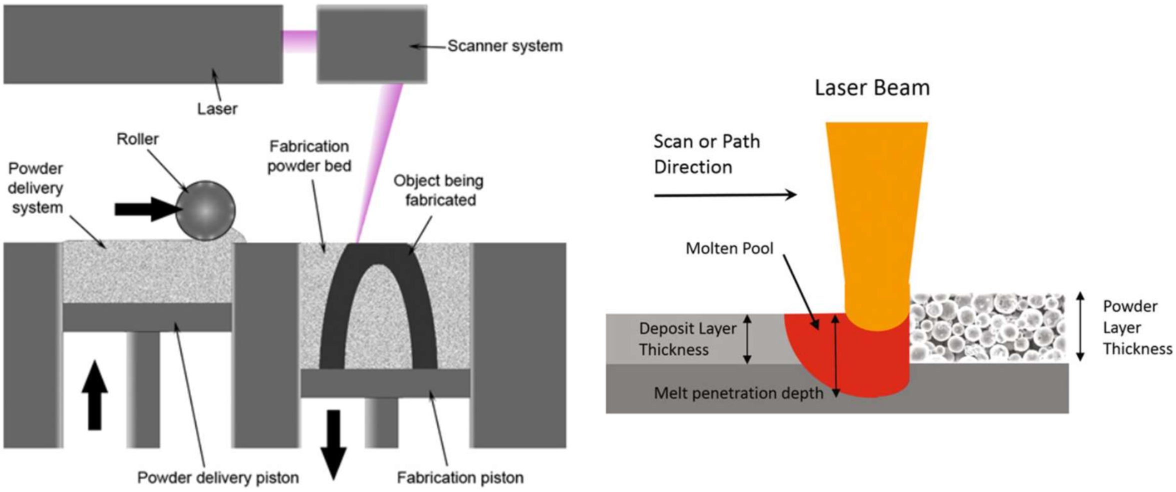

Figure 2.9 - Selective laser sintering process (Milewski, 2017)

2.2.2.3 Selective Laser Melting

Selective Laser Melting (SLM) is developed in order to generate high density parts. This is obtained by fully melting the metallic powder particles. Whereas high temperatures are required for this process, it is accompanied with residual stresses. This should be taken into account in order to prevent part failure (Linden, 2015).

Figure 2.10 - Selective laser melting printer

2.2.2.4 Electron Beam Melting

Electron Beam Melting (EBM) uses an electron beam gun which generates an electric arc to melt the metal powders. The energy generated melts the powder into the model at the powder bed surface. This is done under vacuum at an operating temperature of approximately 1000° Celsius. Metal parts produced with EBM show a higher level of melting-through than sintered parts. The cooling process is precisely controlled in order to achieve accurate cooling of the fabricated metal parts. Typically, the element produced must be reworked in order to achieve a higher surface quality (Strauß, 2013).

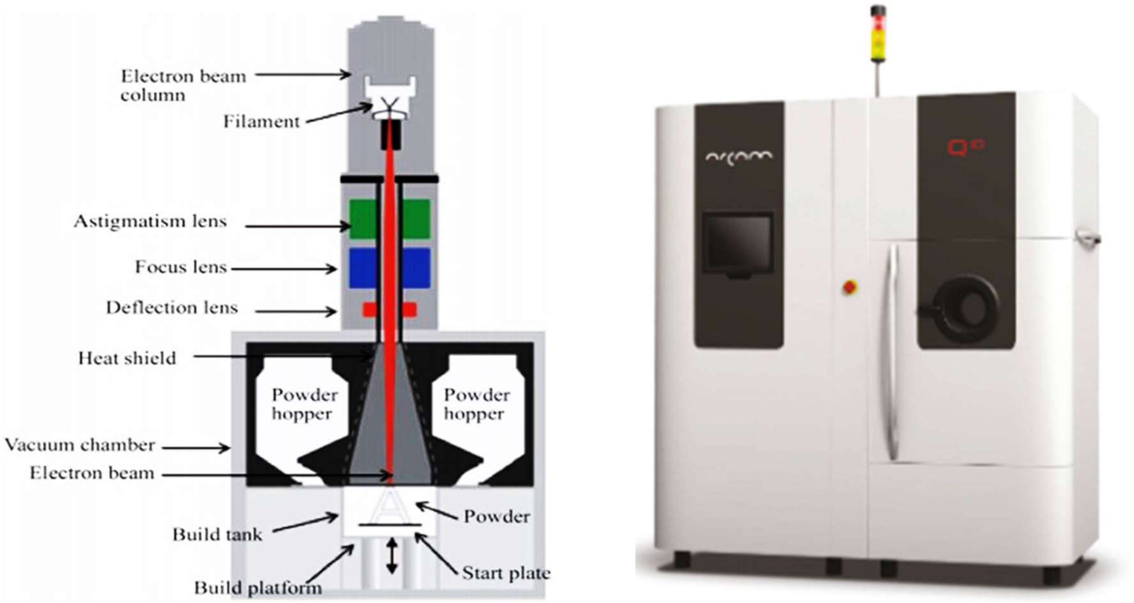

Figure 2.11 - Electron beam melting process (left) and printer (right) (Milewski, 2017)

2.2.3 Sheet Lamination

In the Sheet Lamination method, individual cross-section layers are cut out and then laminated together using diffusion binding, low melting point alloys, adhesive polymers or ultrasound (C. Buchanan, 2019). This method can be used also for different types of material and geometrical limitations of the final element depend on the machining capabilities and the layer thickness.

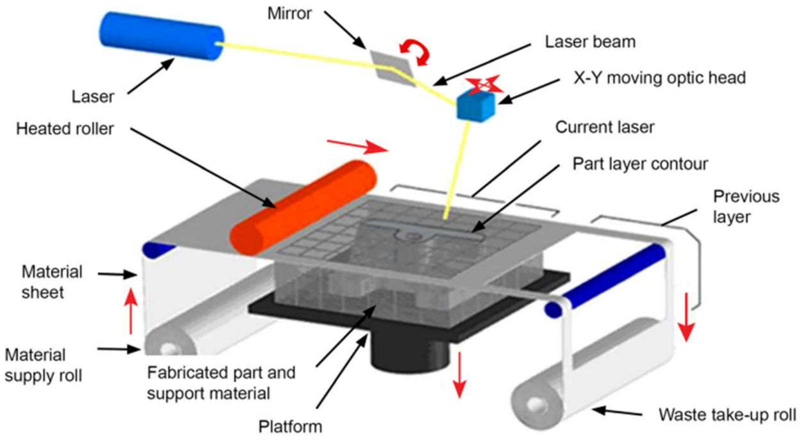

Figure 2.12 - Sheet lamination process (Francisco Mercado, 2020)

2.2.4 Directed Energy Deposition

Directed Energy Deposition (DED) is characterized by the direct melting of powder or wire using a laser or plasma arc or electron beam. The melted material is delivered to a molten pool and then is deposited following a set path.

2.2.4.1 Electron Beam Freeform Fabrication

Electron Beam Freeform Fabrication (EBF) process consists in introducing metal wire feedstock into a molten pool that is created and sustained using a focused electron beam in a high vacuum environment. The electron beam couples effectively with any electrically conductive material, including highly reflective alloys such as aluminium and copper (Donghong Ding, 2015).

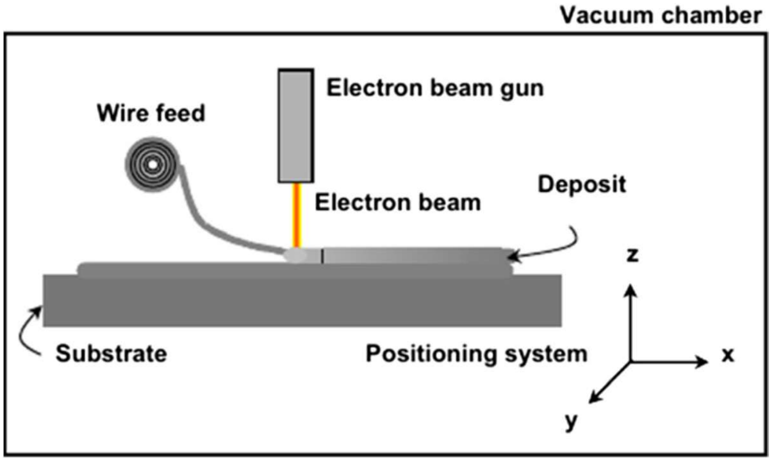

Figure 2.13 - Electron beam freeform fabrication process (Donghong Ding, 2015)

2.2.4.2 Wire-Laser Additive Manufacturing

Wire-Laser Additive Manufacturing (WLAM) uses a laser which generates a melt pool on the substrate material, into which the metal wire is fed and melted, forming a metallurgical bound with the substrate. By moving the laser processing head and wire feeder or moving the substrate, a bead is formed during solidification. The relative motion of the welding tool and the substrate could be performed by using a robot arm or a computer numerically controlled worktable (Donghong Ding, 2015). The final quality of the element generated depends on printing parameters and on the wire properties.

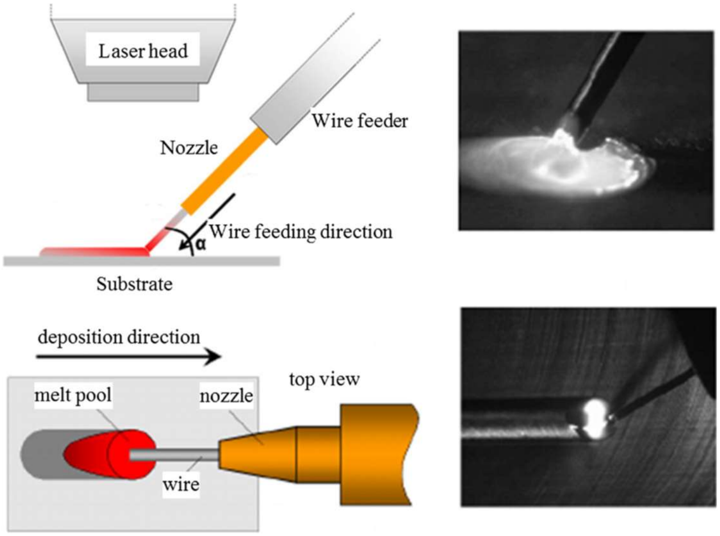

Figure 2.14 - Wire-laser additive manufacturing process (Donghong Ding, 2015)

2.2.4.3 Wire-and-Arc Additive Manufacturing

Wire-and-Arc Additive Manufacturing (WAAM) is a technique suitable to print medium and large-scale structures, it allows for high deposition rates and virtually the element produced has not geometrical limits. The placement of the wire is controlled by a robotic arm or computer gantry.
There are several research groups that are studying WAAM using some additional gases:

- Gas Metal Arc Welding (GMAW);
- Gas Tungsten Arc Welding (GTAW);
- Plasma Arc Welding (PAW).

These different processes are illustrated in the figure below:

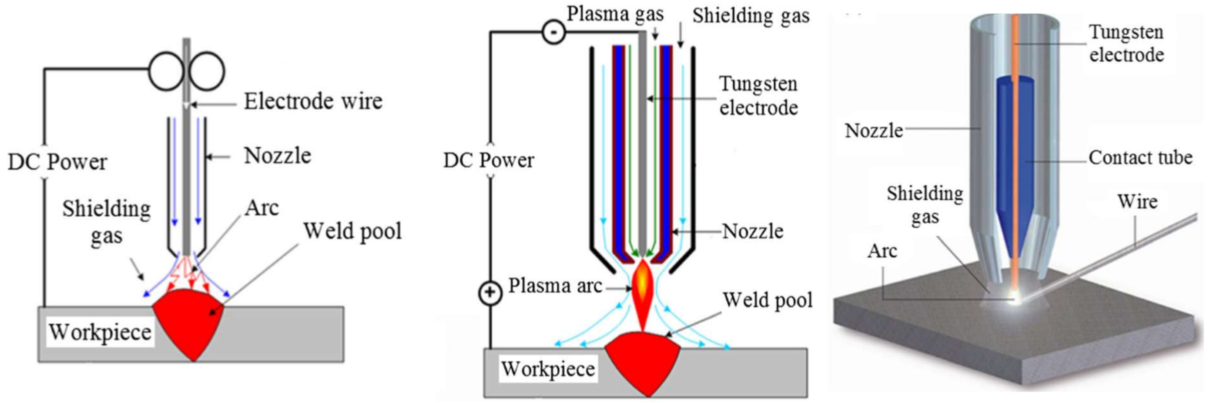

Figure 2.15 - Gas metal arc welding (left), gas tungsten arc welding (centred) and plasma arc welding (right) (Donghong Ding, 2015)

The steps that are followed in a WAAM process are:

1. The path of the robot is generated from a computer interface;
2. Using a controller cabinet, the motion of the robot and the printing parameter are set;
3. A power source is used to control the printing process;
4. All the previous data are sent to the robot;
5. The welding torch prints the material;
6. The temperature of the printed element is measured.

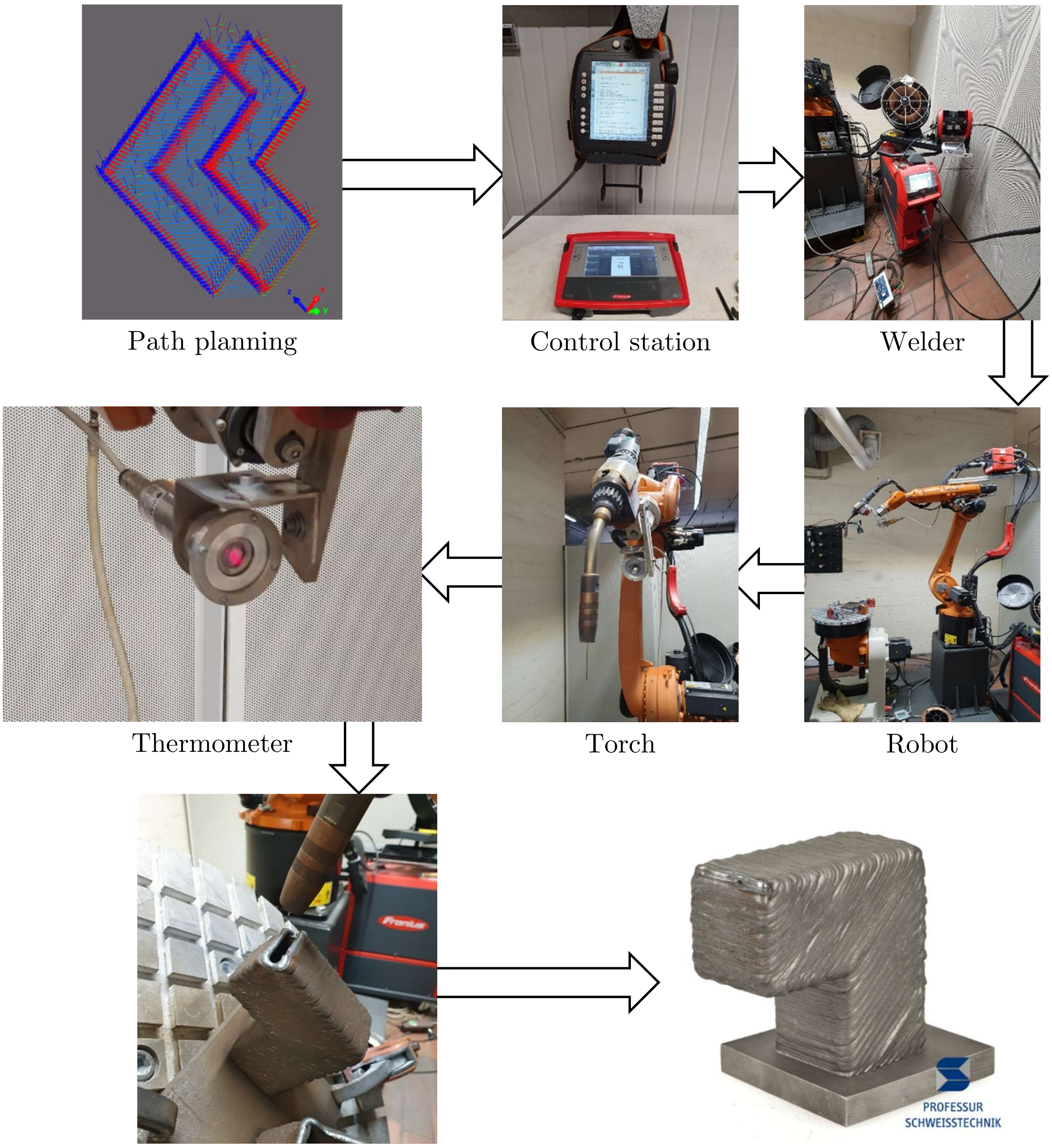

Figure 2.16 - Wire-and-arc additive manufacturing process

WAAM has two possible configurations: the so-called "continuous" printing, meaning the material is deposited in continuous, and a so-called "dot-by-dot" printing, meaning that the material is deposited by successive points (Figure 2.17). Typically, continuous printing is adopted to print planar elements, while dot-by-dot strategy is used to print line elements as parts of a continuous diagrid pattern, with no node interruptions (Vittoria Laghi, 2020).
The quality and the mechanical properties of the final outcome is influenced by the following parameters: the current and its voltage, the wire diameter, the wire-feed rate, the welding speed and the layer height. In addition, the cooling process must be taken into account because it can influence the mechanical properties. In any case, the layer-by-layer printing process causes an anisotropic behaviour of the material.

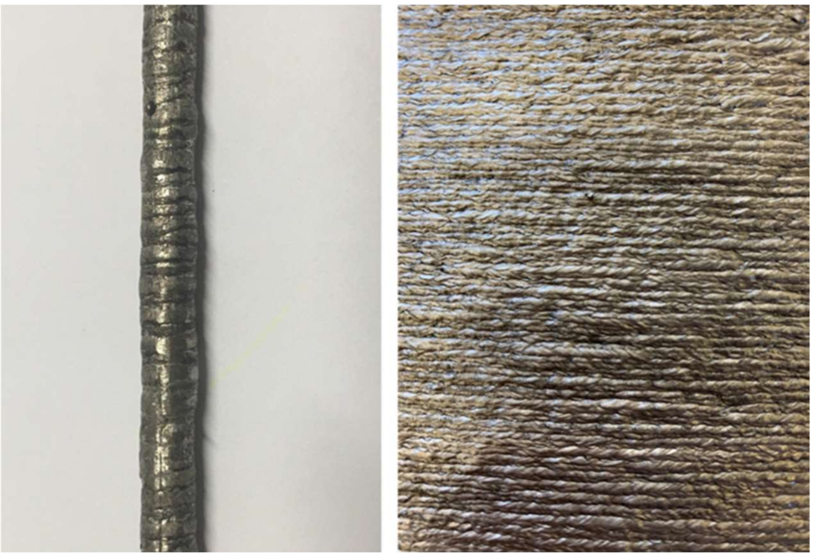

Figure 2.17 - Wire-and-arc additive manufacturing dot-by-dot (left) and layer-by-layer (right) (Vittoria Laghi, 2020)

2.3 Advantages and disadvantages for metal additive manufacturing

This new approach in construction offers many advantages, related to time, costs and sustainability, and produces also some disadvantages, connected with the manufacturing technique and the state of the technology.

2.3.1 Advantages

2.3.1.1 Geometry flexibility and optimization

The geometric flexibility of additive manufacturing at both the macro and microscale allows for highly optimized structures and engineered materials (C. Buchanan, 2019). This aspect is very important nowadays because the utilisation percentage of steel used in construction is below than 50% and the flexibility permits to the designer to work with more complex geometries. Additive manufacturing enables to discover new cross-sections and forms, allowing to vary the element thicknesses or to strengthen structural members. An example of that is shown in Figure 2.18 where it is possible to observe typical application of additive manufacturing in hollow structural members:

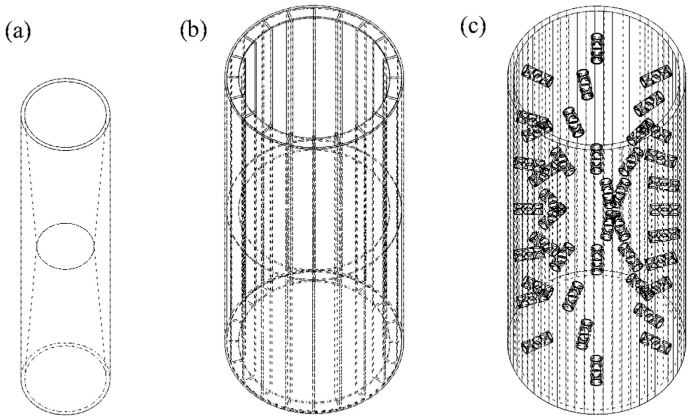

Figure 2.18 - Examples of possible AM hollow structural members featuring (a) varying wall thickness to enhance member buckling performance, (b) internal stiffening to improve local buckling resistance and (c) perforated shear keys to enhance composite action with infill material (C. Buchanan, 2019)

The possibility to place material where it is needed produces many benefits, like lower costs and better structural properties. This can be seen in Figure 2.19 where a simply supported I-type beam has been optimized putting material only where required for different load combinations:

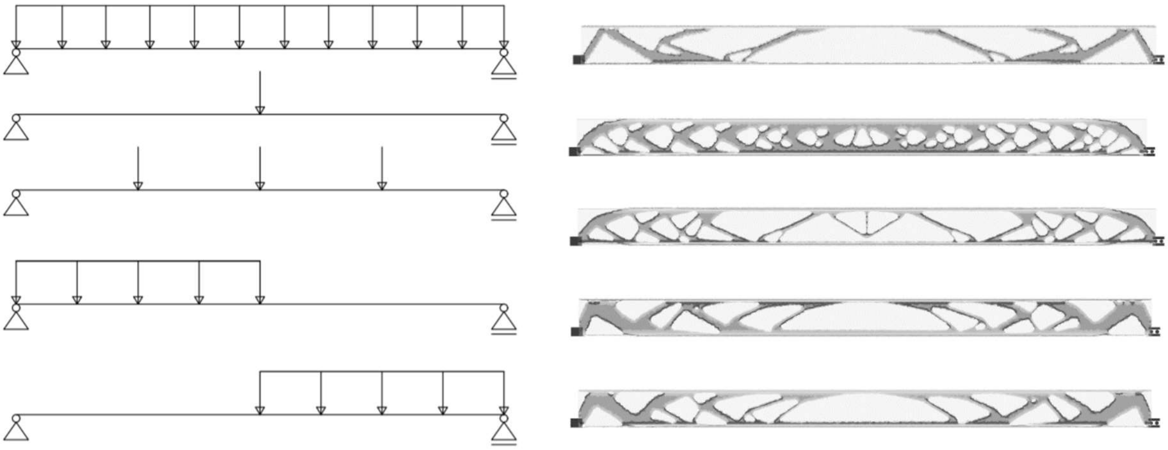

Figure 2.19 - Topology optimization of a simple supported beam under different loading conditions (Babovic, 2021)

Other possible benefits from additive manufacturing are the ones deriving from the microscale properties, in fact material porosity can be used to create dissipating systems in seismic areas or to build less stiffer members so these elements absorb less energy in certain areas (Figure 2.20). In addition, other acoustic or thermal benefits can be achieved using microscale properties of the material.

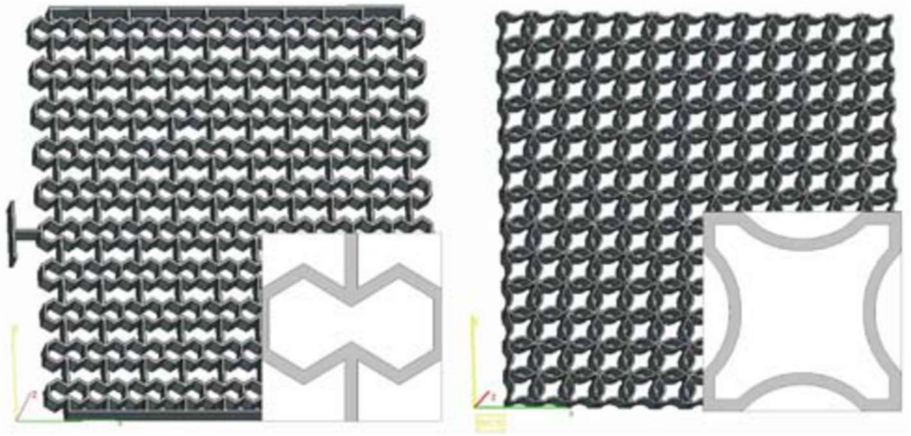

Figure 2.20 - Negative Poison's ratio honeycomb structures that could be adopted as energy absorbing elements (C. Buchanan, 2019)

2.3.1.2 Construction time

Metal additive manufacturing allows to reduce significantly the construction time, hence the costs can be decreased. The building parameters, like the layer thickness and the welding speed, strongly affect the required time and permit to realize high quality elements. For this reason, metal additive manufacturing is employed in realizing high complex elements that would require days, while it is possible to create the same objects in few hours using 3D printing.

2.3.1.3 Structural strengthening and repair

Strengthening and repair topics are really important nowadays and metal additive manufacturing can be considered as a new type of solution also for these problems. Additive manufacturing can be employed to repair damaged structural members in-situ, reducing significantly the costs and the amount of work.

2.3.1.4 Environmental impact

In general, additive manufacturing allows to reduce the environmental impact of the construction industry, decreasing the material required and optimizing structures. For example, for metallic powder bed fusion methods, up to 98% of the remaining waste powder can be recycled and reused (C. Buchanan, 2019). Generally, additive manufacturing generates a waste of material that is 40% lower than traditional techniques and moreover, it has been estimated that total environmental impact can be 70% smaller. These percentages can increase if the manufacturing process happens onsite, or closer to the final location.

2.3.1.5 Human factors

Human factors like costs, safety and manufacturing errors can be importantly reduced using additive manufacturing technologies. In fact, the labour cost is typically between 15% and 50% of the total cost of the construction. Furthermore, being the process automated, human errors can be completely avoided and the construction time decreases. Finally, additive manufacturing can be employed in countries or regions which can be dangerous or difficult for humans, like in war zones or extra-terrestrial environments.

2.3.2 Disadvantages

2.3.2.1 Costs

Nowadays, additive manufacturing costs can be a problem in construction industry. The flexibility of additive manufacturing allows to create more complex structures, however this advantage can increase significantly the costs, because structures could become unnecessarily difficult to design and more studies could be required to predict the behaviour of the optimized elements.

In addition, costs regarding additive manufacturing equipment and energy are not negligible and depend on the technique used.

Furthermore, there are also some additional costs associated with pre-processing and post-processing steps, like equipment cleaning, remove of support structures and surface treatments. All these processes are carried out by human workers.

Finally, it is possible to sum up saying that it is really complicated to estimate production costs using additive manufacturing technologies in construction industry.

2.3.2.2 Manufacturing process variability

One of the main problems in additive manufacturing is the lack of codes and standardised guidelines and practices. In fact, the same 3D CAD file can produce a wide range of results with different additive manufacturing methods (C. Buchanan, 2019). Due to this variability, verifications are required to assess strengths and stiffnesses of the built elements.

Moreover, members created with additive manufacturing technologies behave differently from components built with conventional processes. This is due to the fact that typically 3D printed material has anisotropic properties, which are affected by the printing process, temperature and layer thickness.

Finally, surfaces of the printed elements are rough compared with components made with conventional technologies and they require some post-processing treatments.

2.3.2.3 Design methodology and workflow

Additive manufacturing is completely new in construction industry, therefore it is needed to consider new workflows and methodologies in the design phase. This is due to the high variability and limitation highlighted before. The design phase in additive manufacturing is carried out by digital processes and hence it is required to integrate this approach in building information modelling (BIM) software.

2.3.2.4 Design and verifications

Additive manufacturing components have properties that are different from conventional elements, just think about anisotropic material, geometry imperfections and residual stresses. For this reason, it is needed to update the actual codes in order to take into account all the previous effects, which affect the structural behaviour, in particular the instability phenomena. Engineers and clients need to be able to fully trust the structural integrity of the built components (C. Buchanan, 2019).

2.3.2.5 Social impact

The automatization is the main aspect of additive manufacturing and it increases the safety and time in construction. However, this aspect can produce social problems in particular with construction workforce and with the entire society.

2.4 Additive manufacturing applications

Additive manufacturing can have several applications in different industrial sectors. This is possible due to the fact that additive manufacturing of metals has an amazing geometrical flexibility. 3D printing technologies can be applied to design some critical components for aerospace and medical industry, but it can also be used in completely different sectors, like in art business. In this paragraph all the possible additive manufacturing applications will be presented.

2.4.1 Artistic

Metal additive manufacturing can be used to artistic projects, allowing the realization of new freeform objects. Moreover, 3D metal printing can be widely employed in fabrication of jewellery, using special printers for precious materials. These machines are small and can create hollow sections with internal supports, so that it is possible to create larger jewellery minimizing the material (Figure 2.21).

Figure 2.21 - Artistic and jewellery applications for metal additive manufacturing (Milewski, 2017)

2.4.2 Personalized

Nowadays, 3D printing technologies can be used to realize personalized objects that meet the customer requests. These customizations are particularly common for sport items and jewellery. For example, it is possible to create customized bike frames (Figure 2.22), golf club heads (Figure 2.23) and rings (Figure 2.24).

Figure 2.22 - Customized bike frame using metal additive manufacturing (Milewski, 2017)

Figure 2.23 - Golf club head made with metal additive manufacturing (Milewski, 2017)

Figure 2.24 - Personalized rings made with metal additive manufacturing (Milewski, 2017)

2.4.3 Medical

Special elements for medical applications can be produced using 3D printing technologies. These components are typically realized using cobalt chrome and titanium alloys, due to their strength and biocompatibility. Several medical objects can be created, from dental crowns and bridges (Figure 2.25) to custom sternum chest implants (Figure 2.26).

Figure 2.25 - Dental bridge made using metal additive manufacturing (Milewski, 2017)

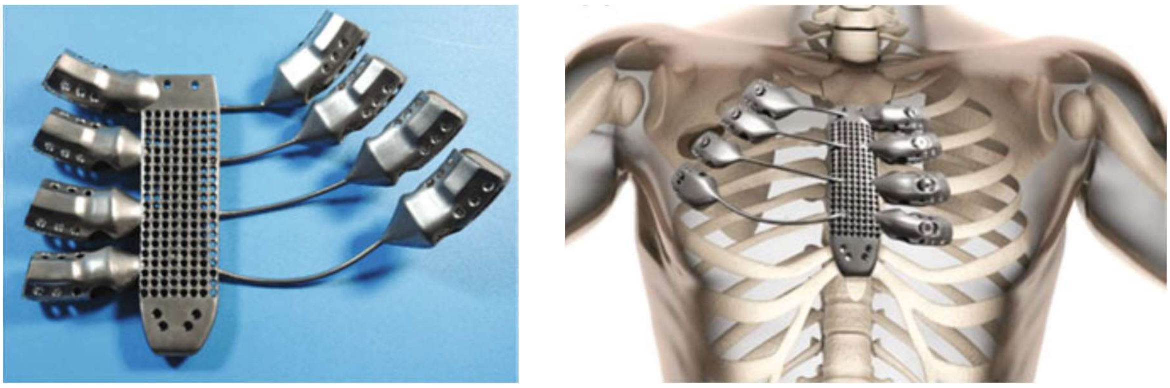

Figure 2.26 – Sternum chest implant made using metal additive manufacturing (Milewski, 2017)

2.4.4 Aerospace

Additive manufacturing is already widely used in aerospace industry because it provides several advantages, like the weight reduction, that means also a reduction of the fuel consumed, and the possibility to realize complex elements in a short time. The most famous additive manufacturing component for aerospace industry is the GE Aero LEAP fuel nozzle, which combines 18 elements into one part and it is realized using a cobalt chrome alloy (Figure 2.27). Other examples can be the copper rocket nozzle by NASA (Figure 2.28), designed to operate in extreme temperature conditions, and the nacelle hinge bracket of the Airbus A320 (Figure 2.29), planned to optimize the weight.

Figure 2.27 - GE Aero LEAP fuel nozzle (Milewski, 2017)

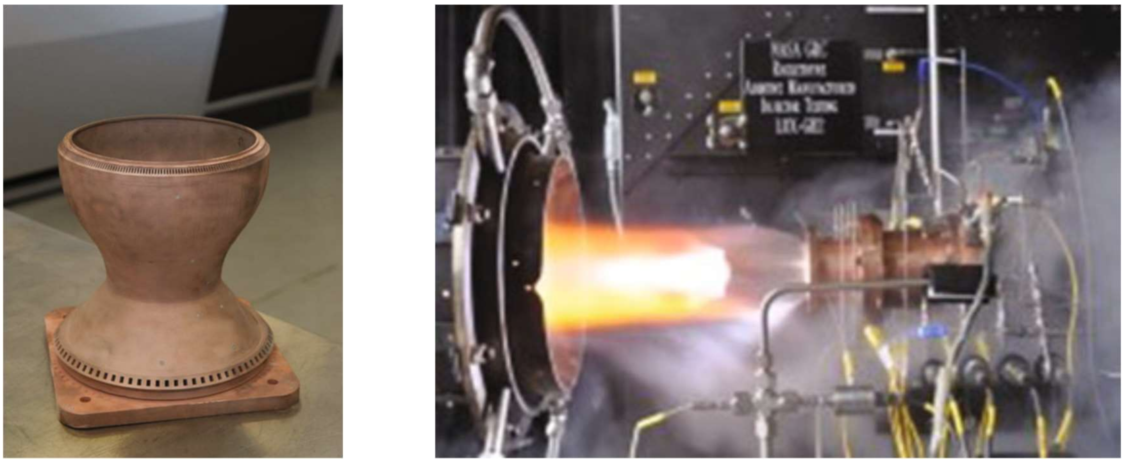

Figure 2.28 - Copper rocket nozzle by NASA (Milewski, 2017)

Figure 2.29 - Nacelle hinge bracket of the Airbus A320 (Linden, 2015)

2.4.5 Automotive

In automotive industry, additive manufacturing can produce several benefits. A clear example is given by Formula 1 cars, where 3D printed components can increase the performances reducing weights and increasing the efficiency. However, in this case, design and production costs are not a problem. With additive manufacturing technologies, it is possible to create steering knuckle (Figure 2.30), lighter brake disks (Figure 2.31) and pistons (Figure 2.32). In addition, 3D printing can also be used to build components that are no more available in car market, for example in the restoration of vintage cars.

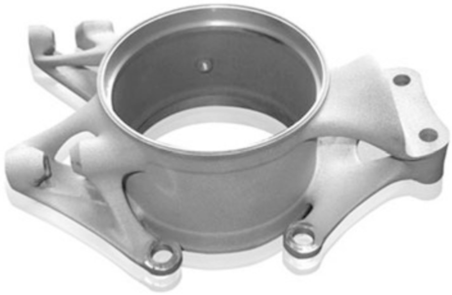

Figure 2.30 - Steering knuckle made with metal additive manufacturing (Milewski, 2017)

Figure 2.31 - Lightweight brake disk

Figure 2.32 - Optimized piston made metal additive manufacturing

2.4.6 Defence industry

Additive manufacturing can have several applications in defence industry. The main advantages can be: operational effectiveness, raw material efficiency, higher return on investment curve, rapid product deployment, growth potentials, flexibility, and anywhere-anytime production agility (Adedeji B. Badiru, 2017). Possible applications include robots for field inspection and detonation of explosive devices (Figure 2.33), but also antipersonnel mine, indeterminate mortar (Figure 2.34) and guns (Figure 2.35).

Figure 2.33 - Robot for field inspection (Adedeji B. Badiru, 2017)

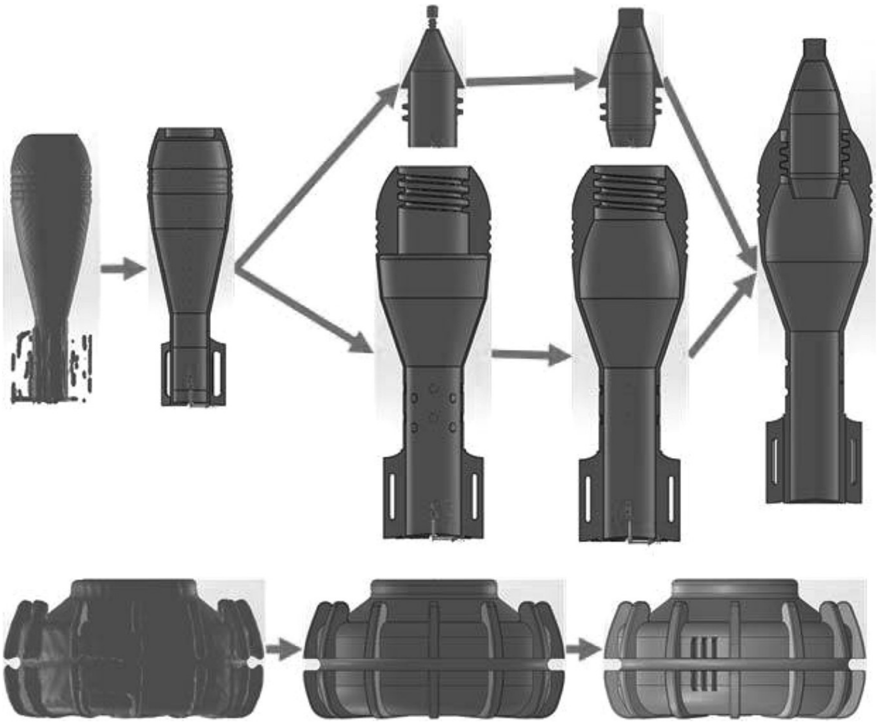

Figure 2.34 - Antipersonnel mine (bottom) and indeterminate mortar (top) (Adedeji B. Badiru, 2017)

Figure 2.35 - Commercial gun made with additive manufacturing (Milewski, 2017)

2.4.7 Construction industry

Additive manufacturing in construction is still in the experimental phase, however it can produce massive benefits with regard to reduction in working labour, construction time, material consumption, construction costs, and improving the characteristics of the building elements, like thermal or acoustic insulation.

In particular, metal additive manufacturing is used in construction to realize structural nodes, like the “Nematox façade node” (Figure 2.36) or the “Arup lighting node” (Figure 2.37). Moreover, other applications are possible as proven by the “MX3D bridge” (Figure 2.38). The two nodes have been produced using the powder bed fusion technology (PBF), while the pedestrian bridge has been made with wire-and-arc additive manufacturing (WAAM).

All these applications demonstrated that it is possible to build extremely optimized structures that would be really time and costs consuming if realized using a traditional approach. Furthermore, MX3D bridge proved that WAAM can allow us to design structural element with a scale suitable for construction applications.

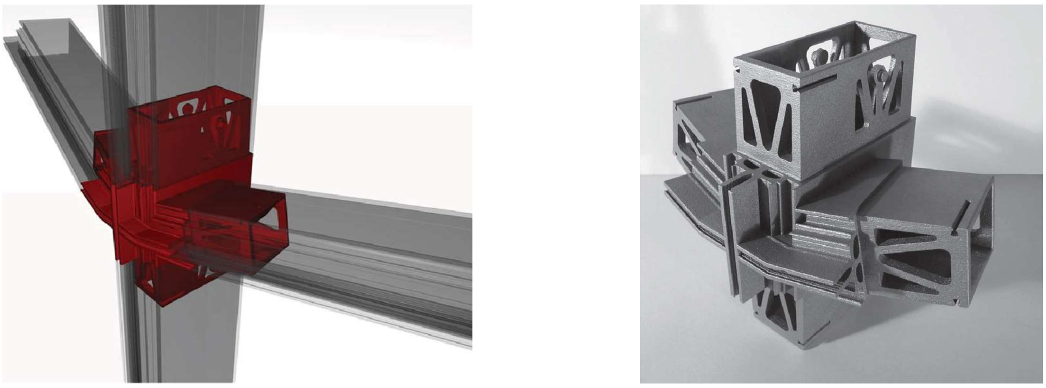

Figure 2.36 - Nematox façade node

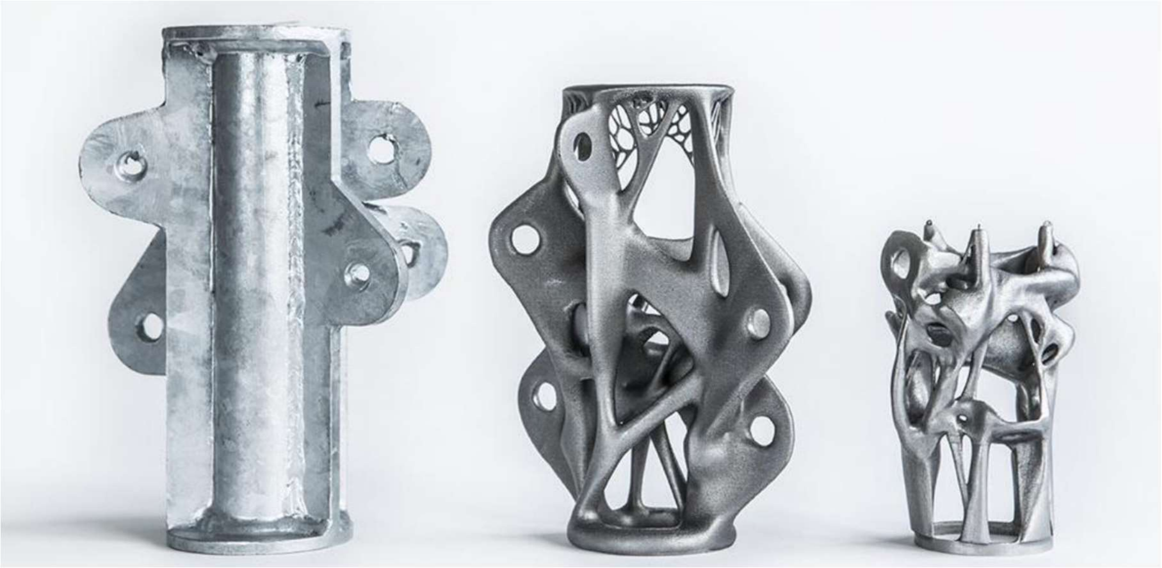

Figure 2.37 - ARUP lightweight node

Figure 2.38 - MX3D bridge

CHAPTER 3

HISTORY AND THEORY OF GRIDSHELL STRUCTURES

3.1 Overview

The word “gridshell”, also called “lattice shell structure” or “reticulated shell structure”, is the combination of “shell structures” and “space grid structures”. The following definition of gridshell can be assigned:

“A gridshell is a form- and cross-section-active, lightweight structure, composed of discrete members connecting nodal points following a curved shape” (Linden, 2015).

The main difference between a gridshell and a shell structure consists in the fact that the first are composed of several elements connected by joints, which belong to the surface of an imaginary shell.

Gridshells can be classified into two categories:

- Unstrained gridshells: they are made of short elements and then assembled into a shell. Therefore, in its initial shape, the gridshell is unstrained or does not take on strain during construction;
- Strained gridshells: they are composed of long members that take on curvature when lifted into place to span the entire surface area of a shell.

3.2 History

The development of gridshells started at the end of the 19th century with the expansion of the Russian steel industry. In this era, there was the necessity to build prefabricated structures quickly and then the designers were forced to use simple and replicable elements into their constructions to deal with the large upfront expenses needed to create joints and complex custom casting moulds.

Vladimir Grigoryevich Shukhov (1853-1939), the most important engineer in Russia, was the inventor of the first gridshell structures. His first gridshell, made from steel members with the same size, was built in 1890 for the roof of pump station in Grozny (Figure 3.1). Later, in 1897, Shukhov managed to design the first doubly curved gridshell structure in the world for a production hall in Vyksa (Figure 3.2, Figure 3.3, Figure 3.4).

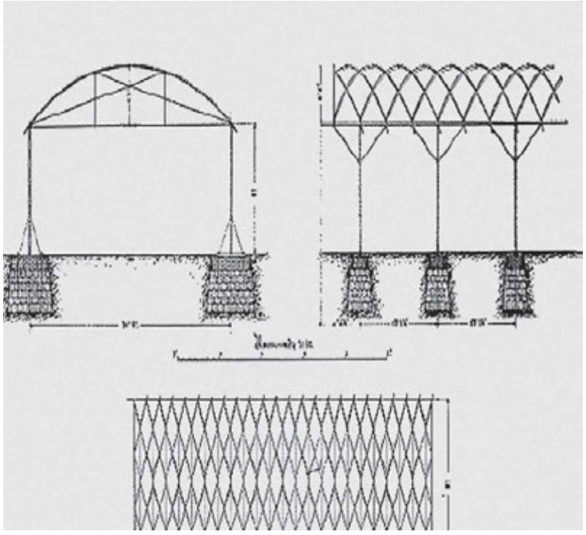

Figure 3.1 Orthographic drawings of Vladimir Shukhov's gridshell mesh roof for a pump station in Grozny, Russia (Leung)

Figure 3.2 - Vladimir Shukov's metal plate-rolling production hall, Vyska, Russia, during construction, 1897 (Leung)

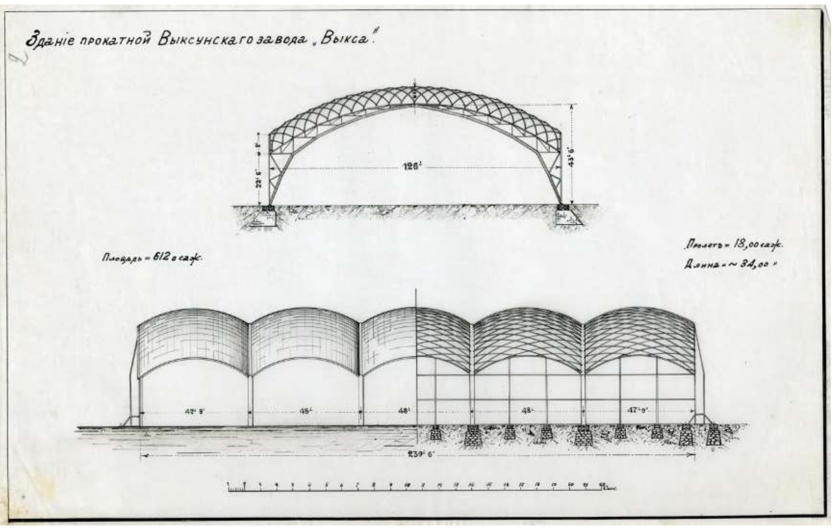

Figure 3.3 – Drawings of the first doubly curved gridshell designed by Vladimir Shukhov in Vyksa, Russia

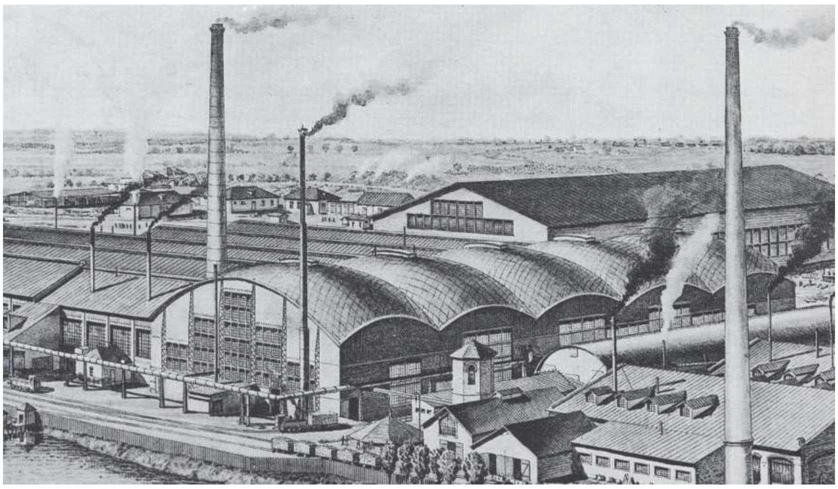

Figure 3.4 - First doubly curved gridshell designed by Vladimir Shukhov in Vyksa, Russia (Linden, 2015)

Shukhov's model was taken up by the designer Frei Otto several years later. Frei Otto (1925-2015) was a German designer who was the first to introduce the form-finding technique. Otto wanted gravity to shape the form of his structures and also proposed solutions that used less material, concrete and energy. These ideas were used into Otto's first timber gridshell for the German Exhibition Building in Essen in 1962 (Figure 3.5). However, the most important gridshell structure designed by Otto was his Multihalle (Figure 3.6) at the 1975 German Federal Garden Exhibition in Mannheim, which was the largest self-supporting timber gridshell in the world, with a span of 80 m and an area of 9500 m^2. Moreover, the Mannheim Multihalle was the first doubly layered timber gridshell to be built in the world.

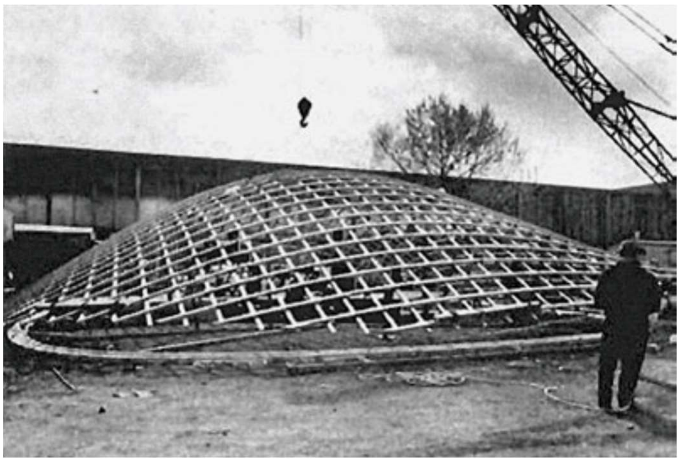

Figure 3.5 - Frei Otto's first timber gridshell in Essen, Germany, 1962 (Leung)

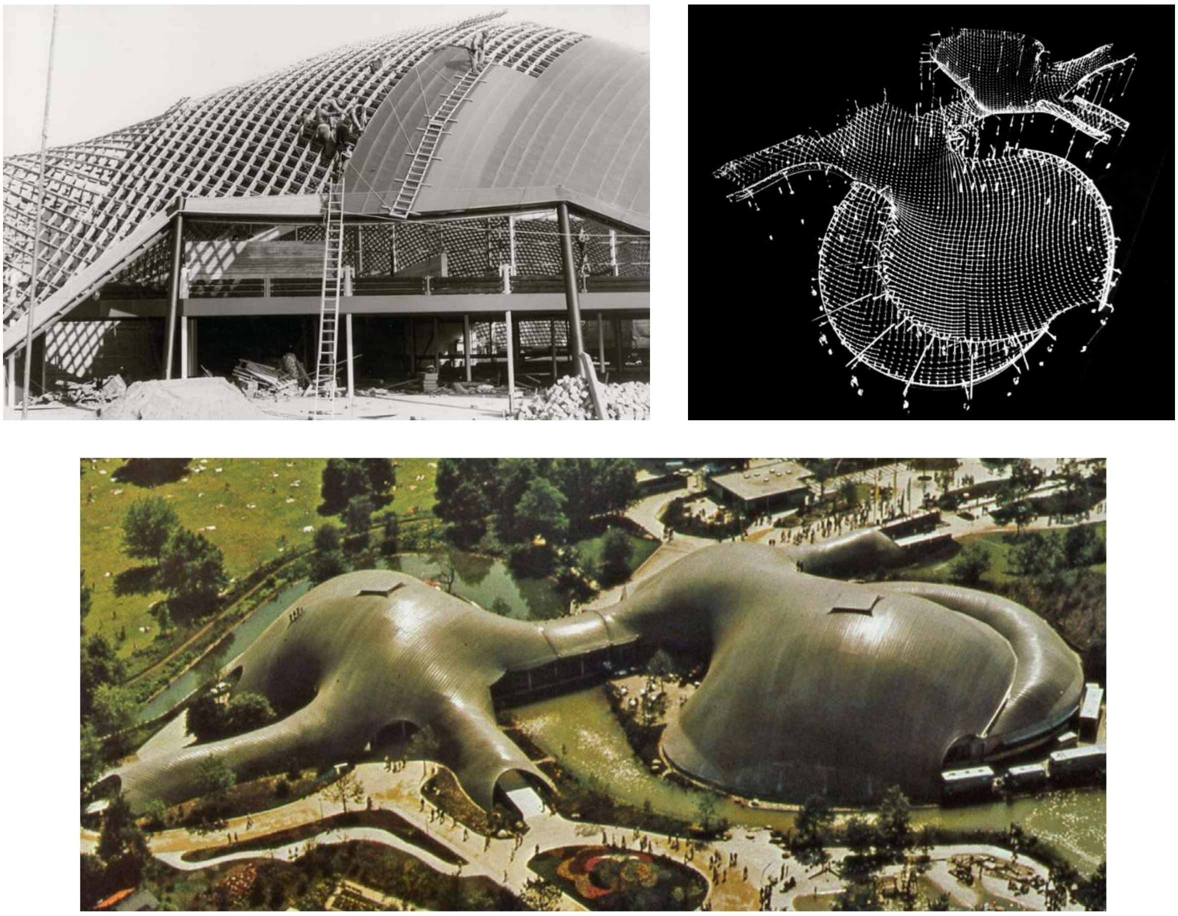

Figure 3.6 - Mannheim Multihalle timber gridshell by Otto Frei during construction (top-left) and digital model (top-right) (Liddell, 2015)

Today, gridshell structures are widely used in architecture to create attractive, bright and innovative public spaces. Some famous examples are the Queen Elizabeth II Great Court in

London, Joe and Rika Mansueto Library in Chicago, the Smithsonian's Kogod Courtyard in Washington and the Złote Tarasy in Warszawa, Poland (Figure 3.7).

Figure 3.7 - Modern gridshells applications: Queen Elizabeth II Great Court (top-left); Smithsonian's Kogod Courtyard (top-right); Joe and Rika Mansueto Library (bottom-left); Złote Tarasy (bottom-right) (Linden, 2015)

3.3 Design of gridshells

Gridshells are very particular structures and can be designed following three different approaches. Moreover, the designed approach has changed a lot over the years, especially thanks to technological evolution.

3.3.1 Freeform gridshells

Freeform shells are generated without considering the structural efficiency of the shape. The surface is modelled by the designer based only on aesthetic preferences. Example of freeform shells are the Murinsel Gridshell in Graz by Vito Acconci or the roof of the Fiera di Milano by Massimiliano and Doriana Fuksas (Figure 3.8).

Figure 3.8 - Examples of freeform gridshells: the Murinsel Gridshell and the roof of the Fiera di Milano

3.3.2 Form-finding by physical models

Form-found gridshells are derived from the process of form-finding, in which parameters are either explicitly or directly controlled to find an optimal geometry of a structure in static equilibrium with its dead load, most often being self-weight. Form-finding shells may include those derived from hanging shapes or physical models, as associated with the funicular structures of Antoni Gaudi, Frei Otto and Heinz Isler (Figure 3.9). Alternatively, digital models may be utilised to find a form, either through a numerical simulation of the physical model, or through parametrically computing imaginary properties that could not have been simulated physically (Leung).

Figure 3.9 - Example of form-finding gridshell structures: hanging chain model of Sagrada Familia by Antonio Gaudi (left) (Linden, 2015) and Highway service area in Deitingen, Switzerland, Heinz Isler, 1968, featuring a thin-shell concrete roof (right) (Leung)

3.3.3 Mathematical Gridshells

Mathematical gridshells can be derived from analytical functions. These functions are often lower-degree polynomials or trigonometric or hyperbolic functions. Example of mathematical gridshells include any of Shukhov's gridshells or more recently, the Berlin Hippo House Gridshell by J.Gribl (Figure 3.10) (Leung).

Figure 3.10 - Hippo House, Berlin Zoo, Berlin, Germany, 1996 (Linden, 2015)

3.4 Structural principles

The structural principles of a gridshell correspond to the structural principles of shells.
Plates and shells have two dimensions much larger than the third dimension, i.e. the thickness. They can be defined by their "middle plane", "thickness" and "material properties". There exists, however, a substantial difference in the behaviour of plates and shells under the action of external loading. The static equilibrium of a plate element under a lateral load is only possible by action of bending and twisting moments, usually accompanied by shearing forces, while a shell, in general, is able to transmit the surface load by "membrane" stresses which act parallel to the tangential plane at a given point of the middle surface and are distributed uniformly over the thickness of the shell. In principle the membrane forces are independent of bending and are wholly defined by the conditions of static equilibrium. The methods of determination of these forces represent the so-called "membrane theory of shells". However, the reactive forces and deformation obtained by the use of the membrane theory at the shells boundary usually become incompatible with the actually boundary conditions. To remove this discrepancy the bending of the shell in the edge zone has to be considered, which may affect slightly the magnitude of initially calculated membrane forces. Typically, bending moments in the shell are introduced in the following cases (Figure 3.11):

- At the supports where boundary conditions are not compatible with the requirements of a pure membrane field;
- Concentrated loads acting on the shell;
- Abrupt changes in the geometry.

The analysis of the behaviour by bending moments is called "bending theory".

The combination of the membrane theory with the bending theory creates the “shell theory”.

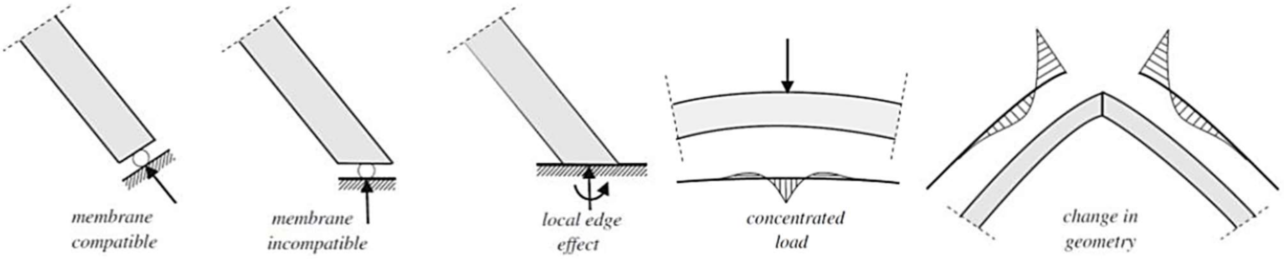

Figure 3.11 - Situations in which bending moments must be considered (Johan Blaauwendraad, 2014)

3.4.1 Membrane theory

The membrane theory is valid under the following assumptions:

- Only normal and in-plane forces are present;
- Points lying on a normal of the middle surface before the deformation will be on a straight line after the deformation has taken place;
- Lines normal to the middle surface remain perpendicular to the deformed middle surface;
- Displacements are small compared to the thickness of the shell.

Let consider a shell element with arbitrary curvatures k_x and k_y, respectively taken in the x and y direction. The shell twist is defined as k_{xy}. The external loads p_x, p_y and p_z are defined along the three main axis, where x and y are tangent to the middle surface, while z is normal to it. In the same way, the displacements are indicated as u_x, u_y and u_z. When the shell is loaded, normal stresses σ_{xx}, σ_{yy} and shear stresses σ_{xy}, σ_{yx} arise. Integrating these stresses along the thickness of the shell, it is possible to get n_{xx}, n_{yy}, n_{xy} and n_{yx}. The associated strains are $\varepsilon_{xx}, \varepsilon_{yy}$ and γ_{xy}. All these quantities are summarized in four vectors:

$$\boldsymbol{u} = [u_x \quad u_y \quad u_z]^T$$

$$\boldsymbol{p} = [p_x \quad p_y \quad p_z]^T$$

$$\boldsymbol{e} = [\varepsilon_{xx} \quad \varepsilon_{yy} \quad \gamma_{xy}]^T$$

$$\boldsymbol{s} = [n_{xx} \quad n_{yy} \quad n_{xy}]^T$$

The “equilibrium method” will be followed, hence the vector $\boldsymbol{u}$ and the vector $\boldsymbol{\varepsilon}$ will be related using the “compatibility equation”, then the “constitutive equation” will connect the stresses $\boldsymbol{s}$ with the strains $\boldsymbol{\varepsilon}$ and lastly, the “equilibrium equation” will create a relationship between the stresses $\boldsymbol{s}$ and the external loads $\boldsymbol{p}$.

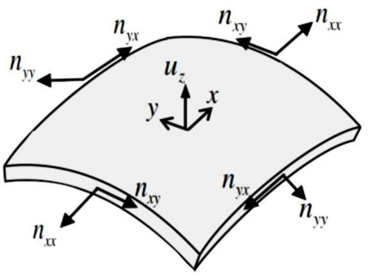

Figure 3.12 - Positive signs for an infinitesimal shell element (Johan Blaauwendraad, 2014)

3.4.1.1 Compatibility equation

The compatibility equation relates strains $\boldsymbol{e}$ with displacements $\boldsymbol{u}$:

$$\boldsymbol{e} = \boldsymbol{B}\boldsymbol{u}$$

The relationships along x and y can be easily derived:

$$\varepsilon_{xx} = \frac{\partial u_x}{\partial x}$$

$$\varepsilon_{yy} = \frac{\partial u_y}{\partial y}$$

$$\gamma_{xy} = \varepsilon_{xy} + \varepsilon_{yx} = \frac{\partial u_x}{\partial y} + \frac{\partial u_y}{\partial x}$$

In order to understand the influence of the normal deflection u_z, an infinitesimal shell element with unit width and length equal to $2dx$ is considered (Figure 3.13).

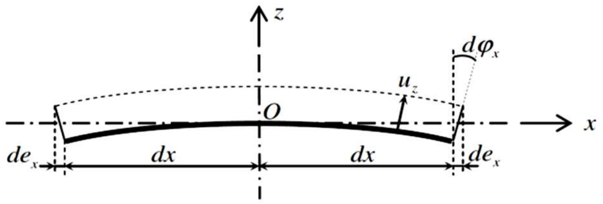

Figure 3.13 - Effect of displacement u_z in curved shell surface (Johan Blaauwendraad, 2014)

Due to the displacement u_z, the length dx increases to $dx + de_x$ and the inclination becomes $\varphi_x = -\partial z/\partial x$. For the incremental change of inclination over the distance dx, it is possible to find the following expression:

$$d\varphi_x = -\frac{\partial^2 z}{\partial x^2} dx$$

Hence, the increment of strain in the x direction can be written as:

$$de_x = u_z d\varphi_x = -\frac{\partial^2 z}{\partial x^2} dx * u_z$$

Now, knowing the relationship of the curvature k_x, the strain ε_{xx} can be derived:

$$\varepsilon_{xx} = \frac{de_x}{dx} = -\frac{\partial^2 z}{\partial x^2} u_z = -k_x u_z$$

Repeating the same passages in the yz plane, it is possible to define the strain ε_{yy} due to the displacement u_z:

$$d\varphi_y = -\frac{\partial^2 z}{\partial y^2} dy$$

$$de_y = u_z d\varphi_y = -\frac{\partial^2 z}{\partial y^2} dy * u_z$$

$$\varepsilon_{yy} = \frac{de_y}{dy} = -\frac{\partial^2 z}{\partial y^2} u_z = -k_y u_z$$

Moreover, a twisted infinitesimal shell element is considered to understand the influence of the displacement u_z on the shear strain γ_{xy} (Figure 3.14).

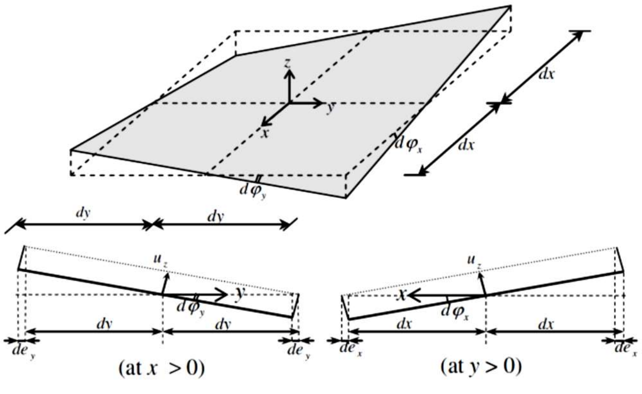

Figure 3.14 - Effect of displacement u_z in twisted shell surface (Johan Blaauwendraad, 2014)

The inclinations and the variations of inclination of the twisted shell are:

$$\varphi_x = -\frac{\partial z}{\partial x}$$

$$\varphi_y = -\frac{\partial z}{\partial y}$$

$$d\varphi_x = -\frac{\partial^2 z}{\partial y \partial x} dy$$

$$d\varphi_y = -\frac{\partial^2 z}{\partial x \partial y} dx$$

The deformations of the edges of the infinitesimal element de_x and de_y can be derived as a function of the normal displacement u_z and the variation of inclination:

$$de_x = d\varphi_x u_z$$

$$de_y = d\varphi_y u_z$$

Hence, knowing the twist relationship, it is possible to compute the shear strain:

$$\varepsilon_{xy} = \frac{de_x}{dy}$$

$$\varepsilon_{yx} = \frac{de_y}{dx}$$

$$k_{xy} = \frac{\partial^2 z}{\partial y \partial x}$$

$$\gamma_{xy} = \varepsilon_{xy} + \varepsilon_{yx} = -2k_{xy}u_z$$

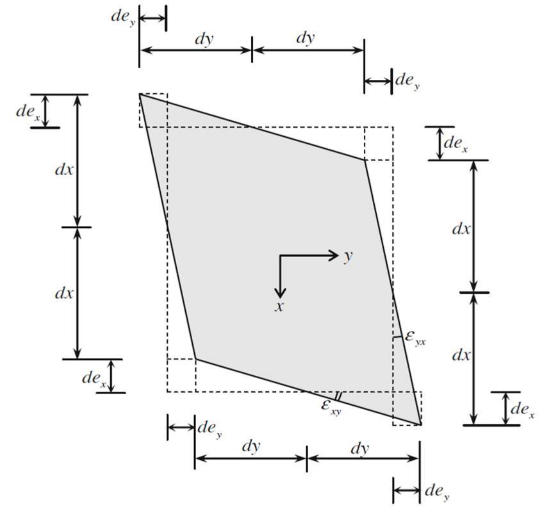

Figure 3.15 - Shear deformation of a twisted middle surface due to a normal displacement u_z (Johan Blaauwendraad, 2014)

Lastly, every component of $\boldsymbol{B}$ has been found and the compatibility equation can be rewritten as:

$$\boldsymbol{e} = \boldsymbol{B}\boldsymbol{u} = \begin{bmatrix} \varepsilon_{xx} \\ \varepsilon_{yy} \\ \gamma_{xy} \end{bmatrix} = \begin{bmatrix} \frac{\partial}{\partial x} & 0 & -k_x \\ 0 & \frac{\partial}{\partial y} & -k_y \\ \frac{\partial}{\partial y} & \frac{\partial}{\partial x} & -2k_{xy} \end{bmatrix} \begin{bmatrix} u_x \\ u_y \\ u_z \end{bmatrix}$$

Where:

$$k_x = \frac{\partial^2 z}{\partial x^2}$$

$$k_y = \frac{\partial^2 z}{\partial y^2}$$

$$k_{xy} = \frac{\partial^2 z}{\partial x \partial y}$$

3.4.1.2 Constitutive equation

The constitutive equation relates stresses $\boldsymbol{s}$ and strains $\boldsymbol{e}$:

$$\boldsymbol{s} = \boldsymbol{D}\boldsymbol{e}$$

It is assumed that the material behaves following the Hooke's law.
Multiplying the membrane stresses over the thickness:

$$\boldsymbol{s} = \boldsymbol{D}\boldsymbol{e} = \begin{bmatrix} n_{xx} \\ n_{yy} \\ n_{xy} \end{bmatrix} = \frac{Et}{1-\nu^2} \begin{bmatrix} 1 & \nu & 0 \\ \nu & 1 & 0 \\ 0 & 0 & \frac{1-\nu}{2} \end{bmatrix} \begin{bmatrix} \varepsilon_{xx} \\ \varepsilon_{yy} \\ \gamma_{xy} \end{bmatrix}$$

3.4.1.3 Equilibrium equation

The equilibrium equation relates membrane stresses $\boldsymbol{s}$ with external forces $\boldsymbol{p}$ and it can be written as:

$$\boldsymbol{B}^* \boldsymbol{s} = \boldsymbol{p}$$

For the load components in x and y directions, it is possible to write the following equilibrium equations:

$$\frac{\partial n_{xx}}{\partial x}+\frac{\partial n_{yx}}{\partial y}+p_x=0$$

$$\frac{\partial n_{xy}}{\partial x}+\frac{\partial n_{yy}}{\partial y}+p_y=0$$

Instead, to evaluate the contributions in the z direction, it is necessary to take into account the curvatures k_x and k_y, and the twist k_{xy}.
Let consider an infinitesimal shell part with unit width and length dx, the membrane stresses n_{xx} cause a downward resultant $n_{xx}d\varphi_x$ that is in equilibrium with the upward force p_z acting over dx (Figure 3.16):

$$p_z dx - n_{xx} d\varphi_x = 0$$

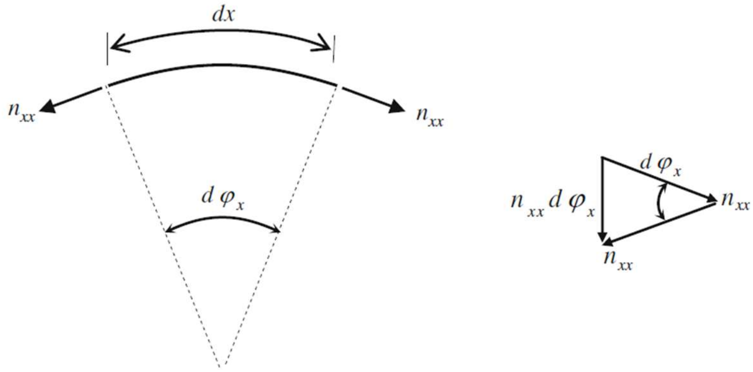

Figure 3.16 - Downward resultant of membrane force n_{xx} over length dx (Johan Blaauwendraad, 2014)

Taking into account $d\varphi_x = -\partial^2 z/\partial x^2\, dx$ and $k_x = \partial^2 z/\partial x^2$:

$$k_x n_{xx} + p_z = 0$$

Repeating this process in the y-direction:

$$k_y n_{yy} + p_z = 0$$

Doing the equilibrium, considering a shell part with dimensions dx and dy and a unit width, the following equilibrium equation is obtained:

$$p_z dxdy + n_{xx}\varphi_x dy + n_{yy}\varphi_y dx = 0$$

And using the equations of $d\varphi_x$, $d\varphi_y$, k_x and k_y:

$$k_x n_{xx} + k_y n_{yy} + p_z = 0$$

Furthermore, to investigate the influence of the shear membrane forces in a twisted shell part, an infinitesimal shell is considered (Figure 3.17). The two forces n_{xy} at $x = 0$ and at $x = dx$ have a downward resultant $n_{xy}\varphi_y$ which act over a width dx. The same is valid for the resultant $n_{yx}\varphi_x$ over a width dy. Therefore, the equilibrium equation of the twisted element is:

$$p_z dxdy + (n_{xy}\varphi_x)dx + (n_{yx}\varphi_y)dy = 0$$

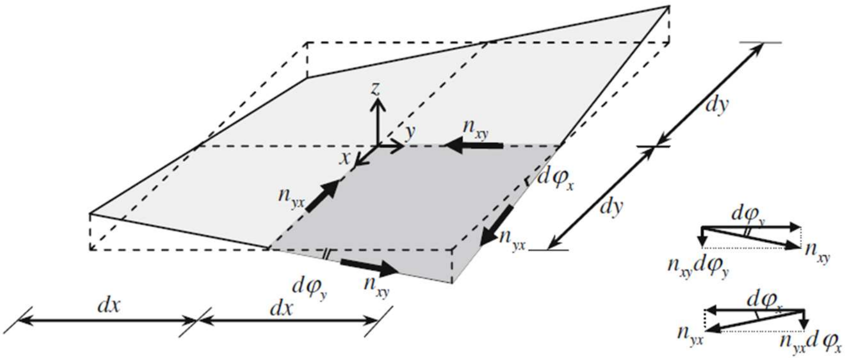

Figure 3.17 - Contribution of the shear membrane forces to equilibrium in z-direction (Johan Blaauwendraad, 2014)

Hence, considering the expressions of $d\varphi_x$, $d\varphi_y$ for the twisted element and k_{xy}, it is possible to derive:

$$2k_{xy}n_{xy} + p_z = 0$$

The equilibrium equation can be rewritten as:

$$B^* s = p = \begin{bmatrix} -\dfrac{\partial}{\partial x} & 0 & -\dfrac{\partial}{\partial y} \\ 0 & -\dfrac{\partial}{\partial y} & -\dfrac{\partial}{\partial x} \\ -k_x & -k_y & -2k_{xy} \end{bmatrix} \begin{bmatrix} n_{xx} \\ n_{yy} \\ n_{xy} \end{bmatrix} = \begin{bmatrix} p_x \\ p_y \\ p_z \end{bmatrix}$$

3.4.2 Bending theory

Bending moments do not carry the applied load, but are compensating for the shortcoming of the membrane behaviour. These disturbances of the membrane field are locally. They can be caused by deformation constraints and boundary conditions which are incompatible with the requirements of a pure membrane field. Also concentrated forces, changes in geometry and abrupt changes in curvature are leading to bending moments (Linden, 2015).

Let consider a shell element with arbitrary curvatures k_x and k_y, respectively taken in the x and y direction. The shell twist is defined as k_{xy}. The external loads p_x, p_y and p_z are defined along the three main axis, where x and y are tangent to the middle surface, while z is normal to it. In the same way, the displacements are indicated as u_x, u_y and u_z. When the shell is loaded, bending moments m_{xx}, m_{yy}, torsion moments m_{xy}, m_{yx} and lateral shear forces v_x, v_y arise. The associated strains are indicated as κ_{xx}, κ_{yy} and ρ_{xy}. The positive signs are shown in the Figure 3.18.

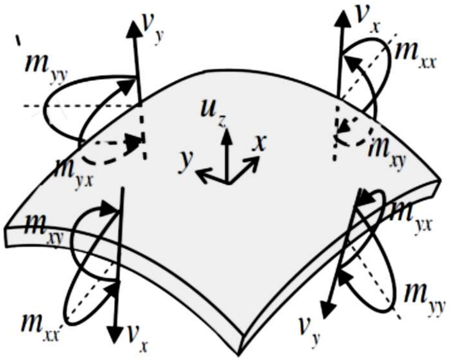

Figure 3.18 - Positive signs considering an infinitesimal shell element (Johan Blaauwendraad, 2014)

The above-mentioned quantities can be summarized in the following vectors:

$$\boldsymbol{u} = [u_x \quad u_y \quad u_z]^T$$

$$\boldsymbol{p} = [p_x \quad p_y \quad p_z]^T$$

$$\boldsymbol{e} = [\kappa_{xx} \quad \kappa_{yy} \quad \rho_{xy}]^T$$

$$\boldsymbol{s} = [m_{xx} \quad m_{yy} \quad m_{xy}]^T$$

Like for the membrane theory, also in this case, the equilibrium method will be used.

3.4.2.1 Compatibility equation

The compatibility equation relates strains $\boldsymbol{e}$ with displacements $\boldsymbol{u}$:

$$\boldsymbol{e} = \boldsymbol{B}\boldsymbol{u}$$

The bending deformations of a plate can be derived using the following expressions:

$$\varphi_x = -\frac{\partial u_z}{\partial x}$$

$$\varphi_y = -\frac{\partial u_z}{\partial y}$$

$$\kappa_{xx} = \frac{\partial \varphi_x}{\partial x} = -\frac{\partial^2 u_z}{\partial x^2}$$

$$\kappa_{yy} = \frac{\partial \varphi_y}{\partial y} = -\frac{\partial^2 u_z}{\partial y^2}$$

$$\rho_{xy} = \frac{\partial \varphi_x}{\partial y} + \frac{\partial \varphi_y}{\partial x} = -2\frac{\partial^2 u_z}{\partial x \partial y}$$

Hence, the compatibility equation can be rewritten as:

$$\boldsymbol{e} = \boldsymbol{B}\boldsymbol{u} = \begin{bmatrix} \kappa_{xx} \\ \kappa_{yy} \\ \rho_{xy} \end{bmatrix} = \begin{bmatrix} 0 & 0 & -\frac{\partial^2}{\partial x^2} \\ 0 & 0 & -\frac{\partial^2}{\partial y^2} \\ 0 & 0 & -2\frac{\partial^2}{\partial x \partial y} \end{bmatrix} \begin{bmatrix} u_x \\ u_y \\ u_z \end{bmatrix}$$

3.4.2.2 Constitutive equation

The constitutive equation is symbolically expressed as:

$$\boldsymbol{s} = \boldsymbol{D}\boldsymbol{e}$$

It is assumed that the material behaves following the Hooke's law.
Multiplying the stresses over the thickness, it is possible to find a relation that is equal to the plate bending constitutive relation:

$$\boldsymbol{s} = \boldsymbol{D}\boldsymbol{e} = \begin{bmatrix} m_{xx} \\ m_{yy} \\ m_{xy} \end{bmatrix} = \begin{bmatrix} D_b & \nu D_b & 0 \\ \nu D_b & D_b & 0 \\ 0 & 0 & D_b\left(\frac{1-\nu}{2}\right) \end{bmatrix} \begin{bmatrix} \kappa_{xx} \\ \kappa_{yy} \\ \rho_{xy} \end{bmatrix}$$

Where D_b is the flexural stiffness of the plate:

$$D_b = \frac{Et^3}{12(1-\nu^2)}$$

3.4.2.3 Equilibrium equation

The equilibrium equation relates stresses $\boldsymbol{s}$ with external forces $\boldsymbol{p}$ and it can be written as:

$$\boldsymbol{B}^{*}\boldsymbol{s} = \boldsymbol{p}$$

The equilibrium equations along x, y and z directions are respectively:

$$\frac{\partial m_{xx}}{\partial x} + \frac{\partial m_{xy}}{\partial y} - v_x = 0$$

$$\frac{\partial m_{yy}}{\partial y} + \frac{\partial m_{xy}}{\partial x} - v_y = 0$$

$$\frac{\partial v_x}{\partial x} + \frac{\partial v_y}{\partial y} + p_z = 0$$

Hence, the equilibrium equation becomes:

$$\boldsymbol{B}^{*}\boldsymbol{s} = \boldsymbol{p} = \begin{bmatrix} 0 & 0 & 0 \\ 0 & 0 & 0 \\ -\frac{\partial^2}{\partial x^2} & -\frac{\partial^2}{\partial y^2} & -2\frac{\partial^2}{\partial x \partial y} \end{bmatrix} \begin{bmatrix} m_{xx} \\ m_{yy} \\ m_{xy} \end{bmatrix} = \begin{bmatrix} p_x \\ p_y \\ p_z \end{bmatrix}$$

3.4.3 Shell theory

The shell theory is studied using the equilibrium method and it consists in combining the results got from the membrane theory and the bending theory.
The vectors of displacements, strains, stresses and external forces are reported below:

$$\boldsymbol{u} = [u_x \;\; u_y \;\; u_z]^T$$

$$\boldsymbol{p} = [p_x \;\; p_y \;\; p_z]^T$$

$$\boldsymbol{e} = [\varepsilon_{xx} \;\; \varepsilon_{yy} \;\; \gamma_{xy} \;\; \kappa_{xx} \;\; \kappa_{yy} \;\; \rho_{xy}]^T$$

$$\boldsymbol{s} = [n_{xx} \;\; n_{yy} \;\; n_{xy} \;\; m_{xx} \;\; m_{yy} \;\; m_{xy}]^T$$

Where $\boldsymbol{u}$ is the displacement vector, $\boldsymbol{e}$ the deformation vector, $\boldsymbol{s}$ the stress vector and $\boldsymbol{p}$ the load vector.

3.4.3.1 Compatibility equation

The compatibility equation relates strains $\boldsymbol{e}$ with displacements $\boldsymbol{u}$:

$$\boldsymbol{e} = \boldsymbol{B}\boldsymbol{u}$$

The membrane strains are described by:

$$\varepsilon_{xx} = \frac{\partial u_x}{\partial x} - k_x u_z$$

$$\varepsilon_{yy} = \frac{\partial u_y}{\partial y} - k_y u_z$$

$$\gamma_{xy} = \frac{\partial u_x}{\partial y} + \frac{\partial u_y}{\partial x} - 2k_{xy} u_z$$

The rotations of the bending behaviour are:

$$\varphi_x = -\frac{\partial u_z}{\partial x}$$

$$\varphi_y = -\frac{\partial u_z}{\partial y}$$

Hereby, the bending deformations become:

$$\kappa_{xx} = \frac{\partial \varphi_x}{\partial x} = -\frac{\partial^2 u_z}{\partial x^2}$$

$$\kappa_{yy} = \frac{\partial \varphi_y}{\partial y} = -\frac{\partial^2 u_z}{\partial y^2}$$

$$\rho_{xy} = \frac{\partial \varphi_x}{\partial y} + \frac{\partial \varphi_y}{\partial x} = -2\frac{\partial^2 u_z}{\partial x \partial y}$$

Consequently, the compatibility equations will be:

$$\boldsymbol{e} = \boldsymbol{B}\boldsymbol{u} = \begin{bmatrix} \varepsilon_{xx} \\ \varepsilon_{yy} \\ \gamma_{xy} \\ \kappa_{xx} \\ \kappa_{yy} \\ \rho_{xy} \end{bmatrix} = \begin{bmatrix} \frac{\partial}{\partial x} & 0 & -k_x \\ 0 & \frac{\partial}{\partial y} & -k_y \\ \frac{\partial}{\partial y} & \frac{\partial}{\partial x} & -2k_{xy} \\ 0 & 0 & -\frac{\partial^2}{\partial x^2} \\ 0 & 0 & -\frac{\partial^2}{\partial y^2} \\ 0 & 0 & -2\frac{\partial^2}{\partial x \partial y} \end{bmatrix} \begin{bmatrix} u_x \\ u_y \\ u_z \end{bmatrix}$$

3.4.3.2 Constitutive equation

The constitutive equation is symbolically expressed as:

$$\boldsymbol{s} = \boldsymbol{De}$$

It is assumed that the material behaves following the Hooke's law.
The previous relation can be written as:

$$s = De = \begin{bmatrix} n_{xx} \\ n_{yy} \\ n_{xy} \\ m_{xx} \\ m_{yy} \\ m_{xy} \end{bmatrix} = \begin{bmatrix} D_m & \nu D_m & 0 & 0 & 0 & 0 \\ \nu D_m & D_m & 0 & 0 & 0 & 0 \\ 0 & 0 & D_m\left(\frac{1-\nu}{2}\right) & 0 & 0 & 0 \\ 0 & 0 & 0 & D_b & \nu D_b & 0 \\ 0 & 0 & 0 & \nu D_b & D_b & 0 \\ 0 & 0 & 0 & 0 & 0 & D_b\left(\frac{1-\nu}{2}\right) \end{bmatrix} \begin{bmatrix} \varepsilon_{xx} \\ \varepsilon_{yy} \\ \gamma_{xy} \\ \kappa_{xx} \\ \kappa_{yy} \\ \rho_{xy} \end{bmatrix}$$

Where the membrane rigidity D_m and the flexural rigidity D_b are equal to:

$$D_m = \frac{Et}{(1-\nu^2)}$$

$$D_b = \frac{Et^3}{(1-\nu^2)}$$

3.4.3.3 Equilibrium equation

The equilibrium equation relates stresses $\boldsymbol{s}$ with external forces $\boldsymbol{p}$ and can be written as:

$$\boldsymbol{B}^* \boldsymbol{s} = \boldsymbol{p}$$

The equilibrium of forces in the tangential directions is fully governed by the membrane behaviour. In the normal direction, not only the membrane behaviour, but also the bending behaviour is taken into account. The transverse shear forces do contribute to the out-of-plane equilibrium, but the in-plane equilibrium is solely described by the membrane forces (Johan Blaauwendraad, 2014). By adding the contribution of the transverse shear forces to the normal equilibrium of the membrane relations:

$$\frac{\partial n_{xx}}{\partial x} + \frac{\partial n_{xy}}{\partial y} + p_x = 0$$

$$\frac{\partial n_{yy}}{\partial y} + \frac{\partial n_{xy}}{\partial x} + p_y = 0$$

$$\frac{\partial v_x}{\partial x} + \frac{\partial v_y}{\partial y} + k_x n_{xx} + k_y n_{yy} + 2k_{xy} n_{xy} + p_z = 0$$

For the equilibrium of moments in x and y directions:

$$v_x = \frac{\partial m_{xx}}{\partial x} + \frac{\partial m_{xy}}{\partial y}$$

$$v_y = \frac{\partial m_{yy}}{\partial y} + \frac{\partial m_{xy}}{\partial y}$$

Hence, it is now possible to write the equilibrium relation:

$$\boldsymbol{B}^* \boldsymbol{s} = \boldsymbol{p} = \begin{bmatrix} -\frac{\partial}{\partial x} & 0 & -\frac{\partial}{\partial y} & 0 & 0 & 0 \\ 0 & -\frac{\partial}{\partial y} & -\frac{\partial}{\partial x} & 0 & 0 & 0 \\ -k_x & -k_y & -2k_{xy} & -\frac{\partial^2}{\partial x^2} & -\frac{\partial^2}{\partial y^2} & -2\frac{\partial^2}{\partial x \partial y} \end{bmatrix} \begin{bmatrix} n_{xx} \\ n_{yy} \\ n_{xy} \\ m_{xx} \\ m_{yy} \\ m_{xy} \end{bmatrix} = \begin{bmatrix} p_x \\ p_y \\ p_z \end{bmatrix}$$

CHAPTER 4

OPTIMIZATION ALGORITHMS FOR CONSTRUCTION

4.1 Introduction to structural optimization

In 1978 J.E. Gordon defined a structure as "any assemblage of materials which is intended to sustain loads". Optimization is an action that wants to obtain the best result given some circumstances. Therefore, structural optimization is the subject of making an assemblage of materials sustain loads in the best way (Peter W. Christensen, 2009). To better understand the meaning of structural optimization, refer to Figure 4.1. However, it is fundamental to define the term "best" because it can be associated to different properties or mechanical responses of the considered structure. For example, quantities like the self-weight, stresses, strains or the stiffness can be considered in the optimization process.

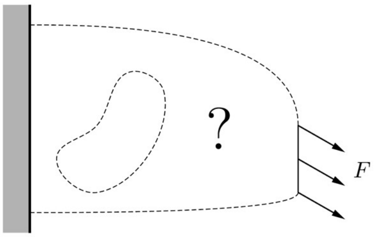

Figure 4.1 - Structural optimization problem (Peter W. Christensen, 2009)

The structural optimization problem can be defined through (Peter W. Christensen, 2009):

- Objective function f: a function that describes the objective of the structural optimization problem and return a number typically smaller than a certain value (minimization problem). f can measure weight, stresses, strains or even costs.

- Design variable x: a function or vector that describes the design, and which can be changed during the optimization. It may represent geometry or choice of material.
- State variable y: a function or a vector that represents the response of the structure for a given design variable x.

The structural optimization problem can take the form:

$$\begin{cases} \text{minimize } f(x,y) \text{ with respect to } x \text{ and } y \\ \text{subject to } \begin{cases} \text{behavioral constraints on } y \\ \text{design constraints on } x \\ \text{equilibrium constraint} \end{cases} \end{cases}$$

It is also possible to consider a problem with more than one objective function. This problem is called "multiple criteria" optimization problem:

$$\text{minimize } \left(f_1(x,y), f_2(x,y), \dots, f_l(x,y)\right)$$

where l is the number of objective functions, while the design variable x and the state variable y are kept constant. However, this problem is not like a standard optimization because typically all the objective functions are not minimized for the same x and y. In this case, it is possible to achieve the "Pareto optimality": a design is Pareto optimal if there does not exist any other design that satisfies all of the objectives better. In other words, (x^*, y^*) satistfying the constraints is Pareto optimal if there is no other (x,y) satisfying the constraints such that (Peter W. Christensen, 2009):

$$f_i(x,y) \leq f_i(x^*, y^*) \text{ for all } i = 1, \dots, l,$$

$$f_i(x,y) < f_i(x^*, y^*) \text{ for at least on } i \in \{1, \dots, l\}.$$

The easiest way to get a Pareto optimal result is to create a weighted objective function:

$$\sum_{i=1}^{l} w_i f_i(x,y)$$

Where $w_i \geq 0$ are the weight factors and their summation must be equal to one.
There are three types of constraints in structural optimization:

- Behavioural constraints: they are constraints on the state variable y. Typically, they are indicated as $g(x) \leq 0$, which g is a function which represents the constrained quantity.
- Design constraints: they are constraints which involve the design variable x. Typically, they impose to maintain a solid material or voids in the domain geometry.
- Equilibrium constraint:

$$\boldsymbol{K}(x)\boldsymbol{u} = \boldsymbol{F}(x)$$

With $\boldsymbol{K}(x)$ the stiffness matrix of the structure, $\boldsymbol{u}$ displacement vector and $\boldsymbol{F}(x)$ the force vector.
Moreover, there are some frequent situations where the equilibrium constraint can be implicit in the structural optimization formulation. These situations occur when the state variable y can be uniquely defined for the design variable x. Considering the example of a displacement state variable, the equilibrium constraint is implicit if the stiffness matrix $\boldsymbol{K}(x)$ is invertible for all x, hence the structural optimization problem becomes:

$$\begin{cases} \text{minimize } f\big(x, u(x)\big) \text{ with respect to } x \\ \text{subject to } g\big(x, u(x)\big) \leq 0 \end{cases}$$

This formulation is called "nested formulation" (Peter W. Christensen, 2009).
Translating this structural optimization process to this thesis:

- Objective function: minimization of volume $f(x, y)$;
- Design variable: topology under specified boundary conditions;
- State variable: stress distribution in the elements or stiffness of the structure.

At the same time, the following constraints are considered:

- Equilibrium constraint;
- Design constraints: boundary conditions, loads and volume target applied;
- Behavioural constraints: initially not considered, but they will be discussed in the chapter about the strength and the stiffness of the element.

4.2 Types of structural optimization problems

Structural optimization problems can be divided into three categories:

- Size optimization: the objective is to find the optimal design changing the design variable x such as the cross-sections or the thicknesses. This is the easiest and the earliest approach to improving the structural performances (X. Huang, 2010).
- Shape optimization: the goal is to find the optimum shape of the domain, that is, the shape problem is defined on a domain variable which is now the design variable x (M.P. Bendsøe, 2003).
- Topology optimization: for discrete structures, such as trusses and frames, is to search for the optimal spatial order and connectivity of the bars. For continuum structures, it is to find the optimal design by determining the best locations and geometries of cavities in the design domains (X. Huang, 2010).

The following figure represents graphically the differences of all the structural optimization problems:

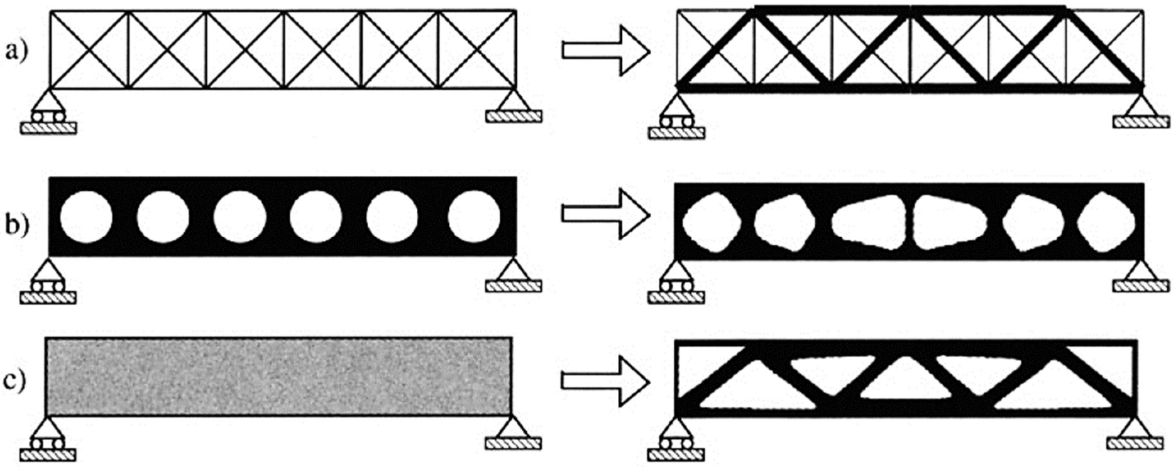

Figure 4.2 - Structural optimization problems: size optimization (a), shape optimization (b) and topology optimization (c) (M.P. Bendsøe, 2003)

In the previous figure, initial problems are shown at the left-hand side and optimal solutions are shown at the right.

Topology optimization is the type of problem that has been considered in this thesis. However, different algorithms exist and the most important ones are:

- "Solid Isotropic Material with Penalization" (SIMP);
- "Evolutionary Structural Optimization Method" (ESO);
- "Bi-directional Evolutionary Structural Optimization Method" (BESO).

The following figure sums up the different optimization types and methods:

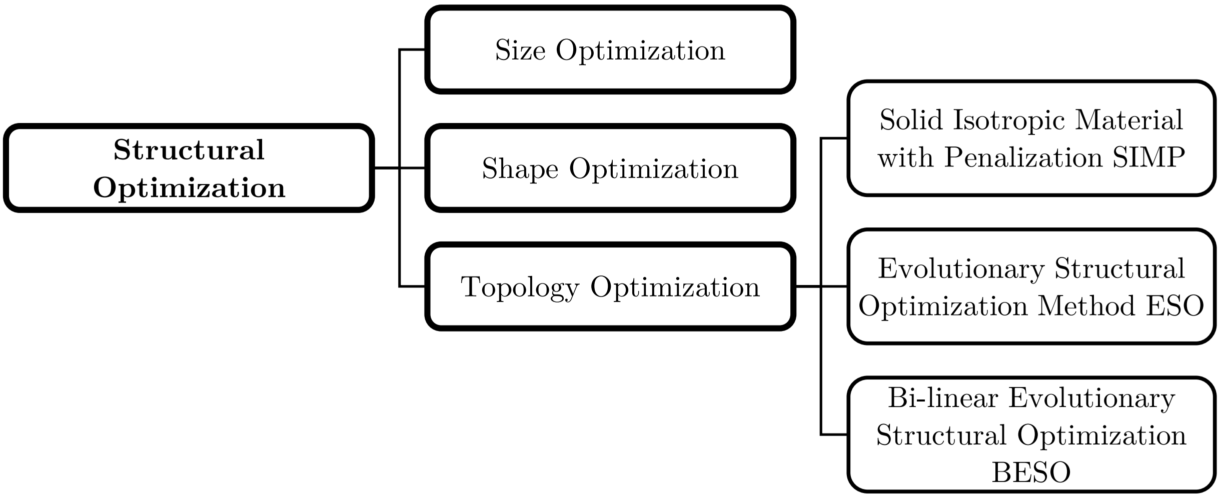

Figure 4.3 - Schematic over different optimisation types and methods

4.3 Minimum compliance design

Considering a mechanical element that occupies a domain $\Omega^{mat} \subset \Omega$, subjected to a body force f, boundary conditions on displacement Γ_u and boundary conditions on traction Γ_T (Figure 4.4), it is possible to define the problem of finding the optimal choice of stiffness tensor $E_{ijkl}(x)$.

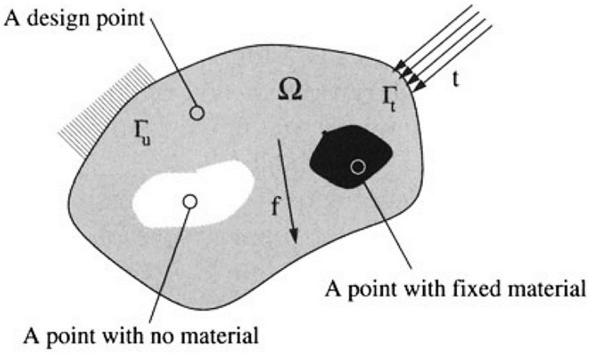

Figure 4.4 - The generalized shape design problem of finding the optimal material distribution in a two-dimensional domain (M.P. Bendsøe, 2003)

Introducing the internal virtual work of an elastic body at the equilibrium u and for an arbitrary virtual displacement v (M.P. Bendsøe, 2003):

$$a(u,v) = \int_{\Omega} E_{ijkl}(x)\varepsilon_{ij}(u)\varepsilon_{kl}(v)d\Omega$$

With linearized strains and the load linear form:

$$\varepsilon_{ij} = \frac{1}{2}\left(\frac{\partial u_i}{\partial x_j} + \frac{\partial u_j}{\partial x_i}\right)$$

$$l(u) = \int_{\Omega} fud\Omega + \int_{\Gamma_T} tuds$$

The minimum compliance (maximum global stiffness) problem becomes:

$$\begin{cases} \min\limits_{u \in U, E} l(u) \\ \text{subject to } a_E(u,v) = l(v) \text{ for all } v \in U \\ E \in E_{ad} \end{cases}$$

Here the equilibrium equation is written in its weak, variation form, with U denoting the space of kinematically admissible displacement fields, f are the body forces and t the boundary

tractions on the traction part $\varGamma_T \subset \Gamma \equiv \partial\Omega$ of the boundary. In this problem, E_{ad} is the set of admissible stiffness tensors for the design problem considered.
Taking into account that the objective is to reduce the volume of the initial domain Ω and determine the optimal subset Ω^{mat} of material points, the following limitation must be considered:

$$\int_{\Omega^{mat}} 1 d\Omega \leq V$$

Therefore, this implies that the set E_{ad} of admissible stiffness tensors consists of those tensors for which (M.P. Bendsøe, 2003):

$$E_{ijkl} = 1_{\Omega^{mat}} E^0_{ijkl}$$

$$1_{\Omega^{mat}} = \begin{cases} 1 \text{ if } x \in \Omega^{mat} \\ 0 \text{ if } x \in \Omega \backslash \Omega^{mat} \end{cases}$$

$$\int_{\Omega} 1_{\Omega^{mat}} d\Omega = Vol(\Omega^{mat}) \leq V$$

The tensor E^0_{ijkl} is the stiffness tensor for the given isotropic material. This is a 0-1 problem, therefore there is no material where the solution is zero and material is present only where the solution is equal to one.
In order to solve the previous problem, the most common approach is to discretize the problem using the finite element method. In this way, keeping constant the stiffness tensor of an element E_e for each element and manipulating displacement u as the main variable, the problem can be rewritten as:

$$\begin{cases} \min\limits_{u \in u, E_e} \mathbf{f}^T \mathbf{u} \\ \text{subject to } \boldsymbol{K}(E_e)\mathbf{u} = \mathbf{f} \\ E_e \in E_{ad} \end{cases}$$

Where the stiffness matrix $\boldsymbol{K}$ depends on the stiffness E_e of the element e. The global stiffness matrix is:

$$\boldsymbol{K} = \sum_{e=1}^{N} \boldsymbol{K}_e(E_e)$$

4.4 Solid Isotropic Material with Penalization

Starting from the 0-1 problem explained before, it is possible to solve the same problem replacing the integer variable with a continuous variable and introducing a penalization factor

that drives the solution to values between 0 and 1. This type of problem can be formulated considering a density function of the material that modifies the stiffness matrix. This new density function will be the new design variable of the problem.
This method is called “Solid Isotropic Material with Penalization” (SIMP) and it has the following form (M.P. Bendsøe, 2003):

$$E_{ijkl}(x) = \rho(x)^p E^0_{ijkl} \quad \text{with} \quad p > 1$$

$$\int_\Omega \rho(x) d\Omega \leq V \quad \text{with} \quad 0 \leq \rho(x) \leq 1 \ \text{ and } x \in \Omega$$

With the density function $\rho(x)$, the penalization factor p and the material properties of a given isotropic material E^0_{ijkl}.
It can be seen that:

$$E_{ijkl}(\rho = 0) = 0$$

$$E_{ijkl}(\rho = 1) = E^0_{ijkl}$$

While for intermediate values of $\rho(x)$, $E_{ijkl}(x)$ is penalized using different penalization factors p.
For this purpose, typically values of p are chosen larger than one, in order to distinguish between favourable and unfavourable densities. Hence, for problem where volume constraint is present, it is suggested to choose $p \geq 3$ (M.P. Bendsøe, 2003). The effect of the penalization factor p is shown in the figure below:

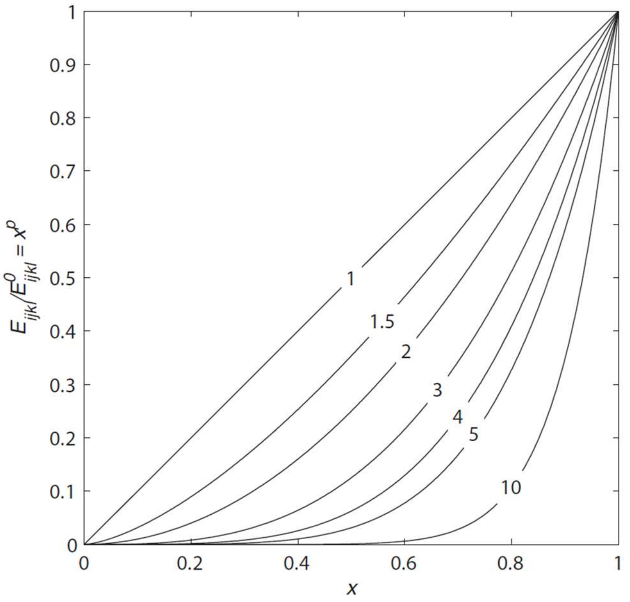

Figure 4.5 - Intermediate densities decrease in efficiency for increased penalisations (Johannes Lundgren, 2012)

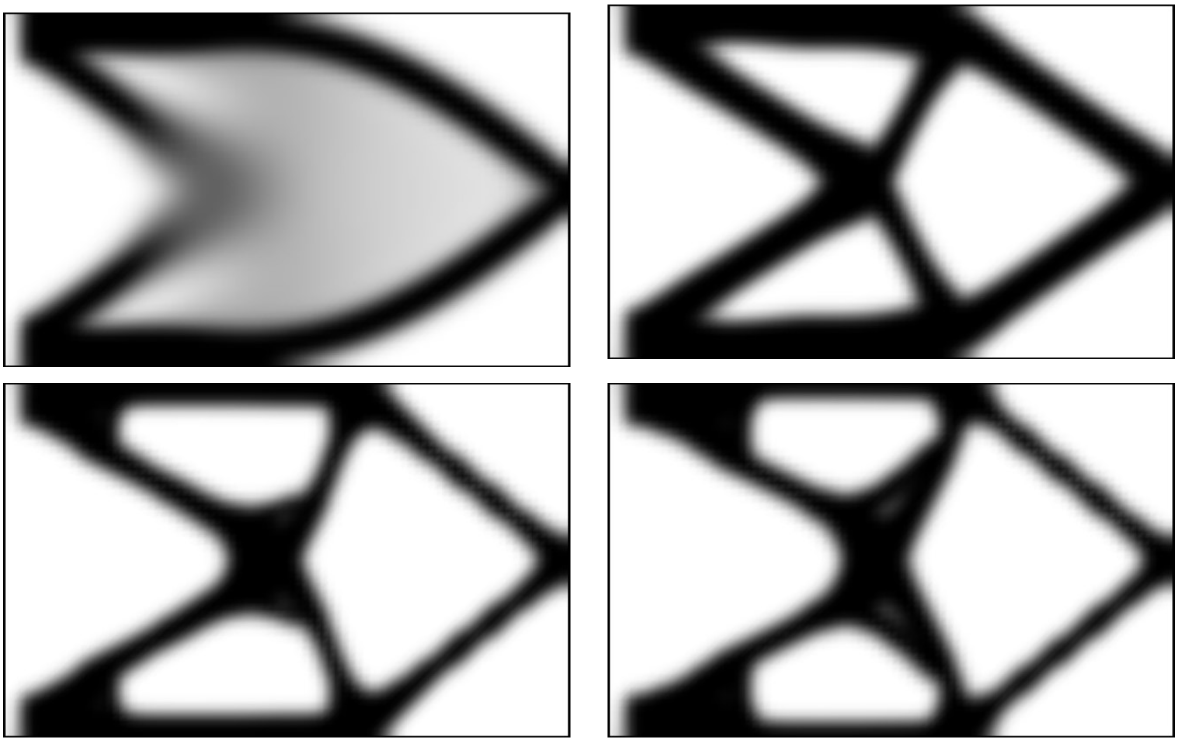

Figure 4.6 - Effects of penalization factor p considering a clamped beam: $p = 1$ (top-left); $p = 3$ (top-right); $p = 8$ (bottom-left); $p = 10$ (bottom-right)

The standard procedure to solve problems using mathematical programming algorithms is to consider the design problem as an optimization problem in the design variable only, and with the displacement fields regarded as a function of these design variables. The displacement fields are given implicitly in terms of the design variables through the equilibrium equation and finding the derivatives of the displacements with respect to the design variables is termed "sensibility analysis" (M.P. Bendsøe, 2003).

Hence, translating the previous result to the discrete minimum compliance formulation:

$$\begin{cases} \min\limits_{\mathbf{u},\rho_e} \mathbf{f}^T \mathbf{u} \\ \textit{subject to } \left(\sum\limits_{e=1}^{N} \rho_e^p \boldsymbol{K}_e \right) \mathbf{u} = \mathbf{f} \\ \sum\limits_{e=1}^{N} v_e \rho_e \le V\,, \quad 0 < \rho_{min} \le \rho_e \le 1, \quad e = 1, \dots, N \end{cases}$$

In this case, the volume is expressed in a discrete form and v_e is the volume of the single element. In addition, ρ_{min} is introduced to avoid any singularity of the problem and typically it is equal to 10^{-3}.

Then, rewriting the previous problem as a function of the design variable only (nested formulation):

$$\begin{cases} \min_{\rho_e} c(\rho_e) \\ \text{subject to } \sum_{e=1}^{N} v_e \rho_e \leq V\,, \quad 0 < \rho_{min} \leq \rho_e \leq 1, \quad e = 1, \ldots, N \end{cases}$$

Now, the equilibrium constraint is implicit:

$$c(\rho_e) = \mathbf{f}^T \mathbf{u}, \quad \text{where } \mathbf{u} \text{ solves:} \quad \sum_{e=1}^{N} \rho_e^p \boldsymbol{K}_e \boldsymbol{u} = \mathbf{f}$$

And the sensitivity analysis can be simply expressed as:

$$\frac{\partial c}{\partial \rho_e}$$

Typically, there are few constraints in topology optimization problems, therefore it is more convenient to compute the derivatives using the "adjoint method" rather than determine them explicitly. Hence, the function $c(\rho)$ is rewritten as:

$$c(\rho) = \mathbf{f}^T \mathbf{u} - \tilde{\mathbf{u}}^T (\boldsymbol{K}\mathbf{u} - \mathbf{f})$$

Where $\tilde{\mathbf{u}}$ is any arbitrary, but fixed real vector.
From this, the derivative of $c(\rho)$ can be expressed as:

$$\frac{\partial c}{\partial \rho_e} = (\mathbf{f}^T - \tilde{\mathbf{u}}^T \boldsymbol{K}) \frac{\partial \mathbf{u}}{\partial \rho_e} - \tilde{\mathbf{u}}^T \frac{\partial \boldsymbol{K}}{\partial \rho_e} \mathbf{u}$$

Satisfying the adjoint equation with the vector $\tilde{\mathbf{u}}$:

$$\mathbf{f}^T - \tilde{\mathbf{u}}^T \boldsymbol{K} = 0$$

It is possible to obtain the following result:

$$\frac{\partial c}{\partial \rho_e} = -\tilde{\mathbf{u}}^T \frac{\partial \boldsymbol{K}}{\partial \rho_e} \mathbf{u} = -p \rho_e^{p-1} \mathbf{u}^T \boldsymbol{K}_e \mathbf{u}$$

This is the final form of the sensitivity analysis. It can be seen that the sensitivity is negative for all the elements, so the compliance decreases in any element and the stiffness increases. Lastly, the optimization process ends when the derivative of the compliance becomes zero or, in other words, when the strain energy of the structure is constant.

4.5 Evolutionary Structural Optimization Method

The "Evolutionary Structural Optimization" method is based on the simple concept of gradually removing inefficient material from a structure. Through this process, the resulting structure will evolve towards its optimal shape and topology (X. Huang, 2010).
This method can be based on the stress level or it can optimize the stiffness or the displacement of the initial structure.

4.5.1 ESO based on stress level

Using finite element methods, it is possible to determine the stress level in each element of a structure. Ideally, the stresses should be uniformly distributed inside in the structure, therefore zones with low stress (or strain) levels are characterized by an inefficient use of material. Hence, the elements under-utilized can be removed from the finite element model.
The stress level is determined computing the ratio between the von Mises stress of the element σ_e^{vm} and the maximum von Mises stress obtained from the analysis σ_{max}^{vm}. Then, if the ratio is lower than a certain rejection ratio RR, the element is deleted:

$$\frac{\sigma_e^{vm}}{\sigma_{max}^{vm}} < RR_i$$

This process is repeated using the same RR_i until it is not more possible to delete elements using the current rejection ratio. Now, an evolutionary ratio ER is introduced and it is added to the previous rejection ratio RR_i, obtaining an increased rejection ratio RR_{i+1}:

$$RR_{i+1} = RR_i + ER$$

This process continues until a new steady-state condition is reached.
The Evolutionary Structural Optimization method can be summarized in five steps (X. Huang, 2010):

1. Discretize the structure using a fine mesh of finite elements;
2. Carry out finite element analysis for the structure;
3. Remove elements with a rejection ratio lower than an imposed value;
4. Increase the rejection ratio using an evolutionary ratio if the steady state is reached;
5. Repeat steps 2 to 4 until a desired optimum is obtained.

4.5.2 ESO for stiffness or displacement optimization

Stiffness is an important structural parameter that can be considered in optimization problems. However, from a computational point of view, it is more convenient to use the compliance C, which is the inverse of the overall structural stiffness. The compliance C can be computed as the total strain energy of the structure or the external work done by applied loads (X. Huang, 2010):

$$C = \frac{1}{2}\mathbf{f}^T\mathbf{u}$$

With $\mathbf{f}$ and $\mathbf{u}$ the force and displacement vectors, respectively.
Removing the ith element, the stiffness matrix changes:

$$\Delta\boldsymbol{K} = \boldsymbol{K}^* - \boldsymbol{K} = -\boldsymbol{K}_i$$

Where $\boldsymbol{K}$ is the initial stiffness matrix, $\boldsymbol{K}^*$ is the new stiffness matrix removing the ith element and $\boldsymbol{K}_i$ is the stiffness of the ith element.
Starting from the equilibrium equation:

$$\boldsymbol{K}\mathbf{u} = \mathbf{f}$$

It is possible to compute the variation of the displacement vector:

$$\Delta\mathbf{u} = -\boldsymbol{K}^{-1}\Delta\boldsymbol{K}\mathbf{u}$$

The change of compliance is:

$$\Delta C = \frac{1}{2}\mathbf{f}^T\Delta\mathbf{u} = -\frac{1}{2}\mathbf{f}^T\boldsymbol{K}^{-1}\Delta\boldsymbol{K}\mathbf{u} = \frac{1}{2}\mathbf{u}_i^T\boldsymbol{K}_i\mathbf{u}_i$$

With $\mathbf{u}_i$ the displacement of the ith element.
Hence, the sensitivity number can be defined as:

$$\alpha_i^e = \frac{1}{2}\mathbf{u}_i^T\boldsymbol{K}_i\mathbf{u}_i$$

The previous expression means that the increase in the mean compliance removing the ith element is equal to its elemental strain energy. Therefore, deleting the elements with the lowest values of α_i, it is possible to minimize the compliance increment.
A new parameter is introduced and it is called “element removal ratio” *ERR*, which is the ratio between the number of elements removed at each iteration and the total number of elements in the initial finite element model. This parameter indicates the number of elements that has to be removed.
Instead, it is possible to get a different sensitivity number if a displacement constraint is assumed. Consider a displacement constraint on the jth displacement component $\mathbf{u}_j$, in the form $\left|\mathbf{u}_j\right| \leq \mathbf{u}_j^*$, where $\mathbf{u}_j^*$ is the limit displacement. In order to compute the variation of displacement due to an element removal, a unit load vector is introduced $\mathbf{F}_j$, in which only the corresponding jth component is equal to unity. The change of displacement is:

$$\Delta \mathbf{u}_j = \mathbf{F}_j^T \Delta \mathbf{u} = -\mathbf{F}_j^T \boldsymbol{K}^{-1} \Delta \boldsymbol{K} \mathbf{u} = -\mathbf{u}_j^T \Delta \boldsymbol{K} \mathbf{u} = \mathbf{u}_{ij}^T \boldsymbol{K}_i \mathbf{u}_i$$

Where $\mathbf{u}_j$ is the solution of the equilibrium equation for the unit load vector $\mathbf{F}_j$, $\mathbf{u}_i$ and $\mathbf{u}_{ij}$ are the element displacement vectors containing the entries of $\mathbf{u}$ and $\mathbf{u}_j$, respectively, which are related to ith element (D. Nha Chu, 1996). This final result indicates the increase of displacement $\mathbf{u}_j$ due to the removal of the ith element, therefore it is better to delete the elements that generate the smallest increments. Hence, the sensitivity number is:

$$\alpha_i = |\alpha_{ij}| = |\mathbf{u}_{ij}^T \boldsymbol{K}_i \mathbf{u}_i|$$

The absolute value is considered because the displacement can have different directions.
Moreover, it should be noted that considering an optimization for stiffness or displacement, there is no steady state condition.
Lastly, the optimization process considering stiffness or displacement constraints can be summarized in the following steps (X. Huang, 2010):

1. Discretize the structure using a fine mesh of finite elements;
2. Carry out finite element analysis for the structure;
3. Calculate the sensitivity number for each element;
4. Remove a number of elements with the lowest sensitivity numbers according to a predefined element removal ratio *ERR*;
5. Repeat steps 2 to 4 until the mean compliance or the maximum displacement of the resulting structure reaches a prescribed limit.

4.6 Bi-directional evolutionary structural optimization method

Sometimes ESO method can find solutions that are not optimum and this is due to the application of large element removal ratio or inappropriate constraint. For this reason, the "Bi-directional Evolutionary Structural Optimization" method has been introduced and it is an implementation of the ESO method. Differently from ESO, the BESO method is able to optimize an initial structure, in terms of stiffness, adding and removing elements.
It is possible to distinguish between two types of BESO problems: "Hard-Kill BESO" and "Soft-Kill BESO".

4.6.1 Hard-Kill BESO

The optimization problem with the volume constraint is stated as (X. Huang, 2010):

$$\begin{cases} \text{minimize } C = \dfrac{1}{2}\mathbf{f}^T\mathbf{u} \\ \text{subject to } V^* - \displaystyle\sum_{i=1}^{N} V_i x_i = 0 \\ \text{where } x_i = 0 \quad \text{or} \quad 1 \end{cases}$$

Where:

- C is the mean compliance;
- $\mathbf{f}$ is the applied load vector;
- $\mathbf{u}$ is the displacement vector;
- V^* is the prescribed total structural volume;
- V_i is the element volume;
- N is the total number of elements;
- x_i is a design variable that is equal to 0 when there is absence of material and 1 when there is presence of material.

The elemental sensibility number is:

$$\alpha_i^e = \Delta C_i = \frac{1}{2}\mathbf{u}_i^T \boldsymbol{K}_i \mathbf{u}_i$$

However, if the mesh is not uniform, the elemental sensibility number has to take into account the volume of the element:

$$\alpha_i^e = e_i = \left(\frac{1}{2}\mathbf{u}_i^T \boldsymbol{K}_i \mathbf{u}_i\right) / V_i$$

Moreover, in the ESO method the discretization of a structure using low order bilinear (2D) or trilinear (3D) finite elements leads to checkerboard patterns (Figure 4.7) and different optimizations related to the mesh size (mesh-dependency). To avoid these problems, in the BESO method the nodal sensitivity number, which has any physical meaning, is computed as follows:

$$\alpha_j^n = \sum_{i=1}^{M} w_i \alpha_i^e$$

Where M is the total number of elements connected to the jth node, w_i is the weight factor of the ith element and the sum of all the weight factors is equal to 1. w_i is defined as:

$$w_i = \frac{1}{M-1}\left(1 - \frac{r_{ij}}{\sum_{i=1}^{M} r_{ij}}\right)$$

Where r_{ij} is the distance between the centre of the ith element and the jth node. It can be noted that α_j^n is larger if the distance r_{ij} is small.

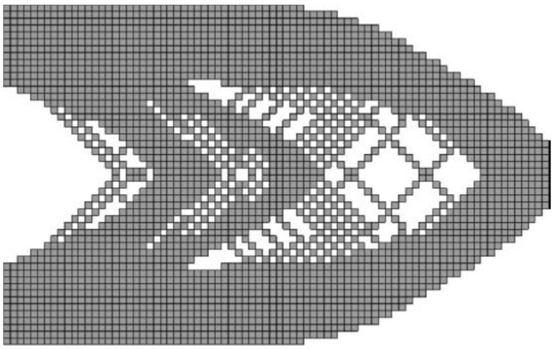

Figure 4.7 - A typical checkerboard pattern in the ESO method (X. Huang, 2010)

From the previous nodal sensitivity number α_j^n, it is possible to get the elemental sensitivity number α_i using a filter scheme. This filter scheme requires a scale parameter r_{min}, independent from the mesh size, which is used to identify the node that will influence the sensitivity of the ith element. r_{min} generates a sub-domain Ω_i (**Figure 4.8**) and it should be big enough to contain more than one element.

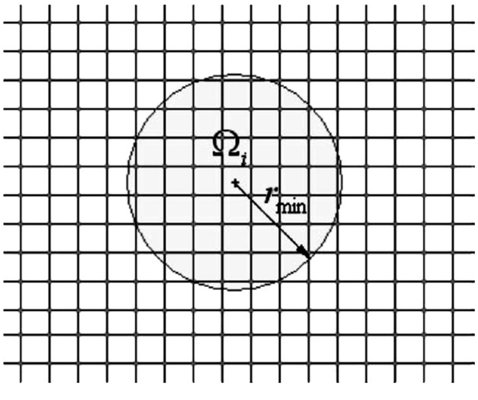

Figure 4.8 - Nodes located inside the circular sub-domain $\Omega_\mathrm{i}$are used in the filter scheme for the ith element (X. Huang, 2010)

Nodes located inside Ω_i contribute to the computation of the improved sensitivity number of the ith element as (X. Huang, 2010):

$$\alpha_i = \frac{\sum_{j=1}^{K} w(r_{ij})\alpha_j^n}{\sum_{j=1}^{K} w(r_{ij})}$$

Where K is the total number of nodes in the sub-domain Ω_i and $w(r_{ij})$ is the linear weight factor defined as:

$$w(r_{ij}) = r_{min} - r_{ij} \quad (j = 1,2, \dots , K)$$

Another common problem in the BESO method is the stability of the process. This can be easily solved considering the historical evolution of the sensitivity number:

$$\alpha_i = \frac{\alpha_i^k + \alpha_i^{k-1}}{2}$$

Where k is the number of the iteration.
It can be noted that this computation of the sensitivity number affects the search path of the BESO algorithm, but the effects on the final solution are really small and they can be neglected. The figure below highlights the differences with and without a stabilization scheme:

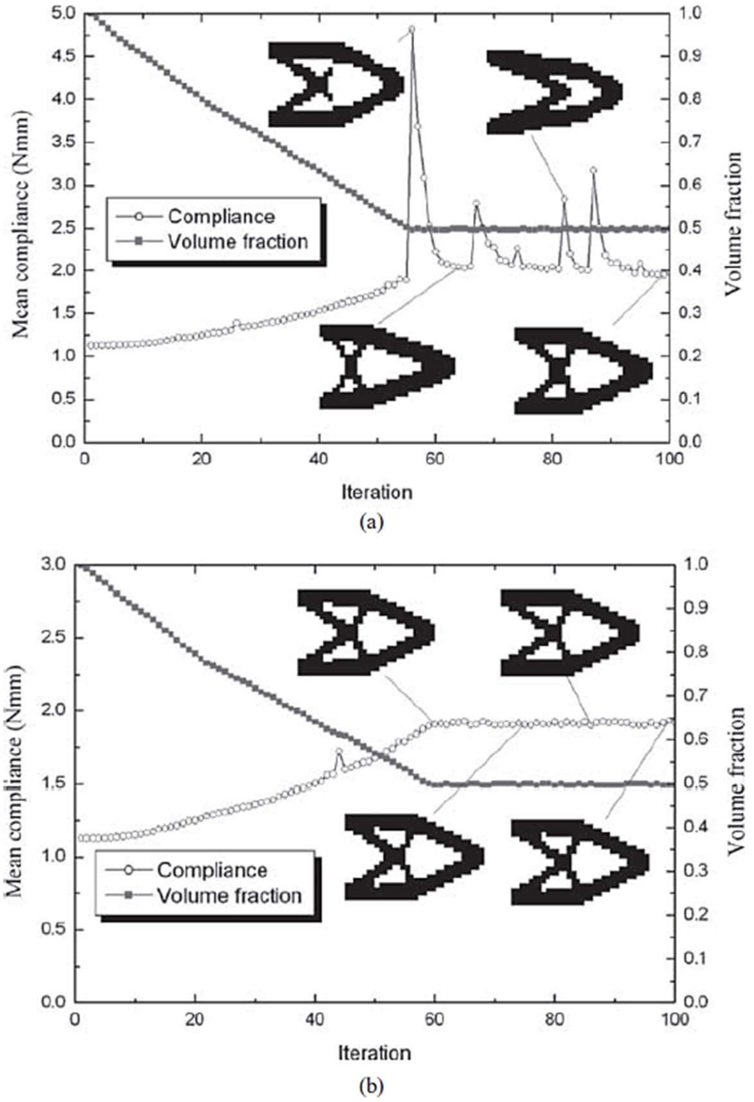

Figure 4.9 - Comparison of evolution histories: (a) without the stabilization scheme; (b) with the stabilization scheme (X. Huang, 2010)

The final objective of the optimization process is to reduce the volume of the initial structure. Hence, the evolution of the volume can be expressed by:

$$V_{k+1} = V_k(1 \pm ER) \quad (k = 1{,}2{,}3, \dots)$$

Where ER is the evolutionary volume ratio. Then, when the volume target V^* is reached, it is maintained constant for the remaining iterations. Then, the sensitivity number of the elements are computed as explained before. At this point, solid element with a sensitivity number lower than a certain threshold α_{del}^{th} are deleted:

$$\alpha_i \leq \alpha_{del}^{th}$$

and void elements with a sensitivity number higher than a certain threshold α_{add}^{th} are added:

$$\alpha_i > \alpha_{add}^{th}$$

The thresholds α_{del}^{th} and α_{add}^{th} are computed following these steps (X. Huang, 2010):

1. Let $\alpha_{add}^{th} = \alpha_{del}^{th} = \alpha_{th}$, thus α_{th} can be easily determined by V_{k+1}. For example, there are 1000 elements in the design domain $\alpha_1 > \alpha_2 > \cdots > \alpha_{1000}$ and if V_{k+1} corresponds to a design with 725 solid elements than $\alpha_{th} = \alpha_{725}$.
2. Calculate the volume addition ratio AR, which is defined as the number of added elements divided by the total number of elements. If $AR \leq AR_{max}$ where AR_{max} is a prescribed volume addition ratio, skip step 3.
3. Calculate α_{add}^{th} by sorting the sensitivity number of void elements. The number of elements to be switched from void to solid can be computed using the inverse formula of the volume addition ratio AR. As a consequence, α_{del}^{th} is determined so that the removed volume is equal to:

$$V_k - V_{k+1} + \text{the volume of the added elements}$$

AR_{max} must be chosen to ensure that only few elements are added in a single iteration.
The BESO optimization continues until the volume target is reached and the converge criterion is satisfied:

$$error = \frac{\left|\sum_{i=1}^{N} C_{k-i+1} - \sum_{i=1}^{N} C_{k-N-i+1}\right|}{\sum_{i=1}^{N} C_{k-i+1}} \leq \tau$$

Where τ is the tolerance, k is the iteration number and N is an integer number, typically chosen equal to 5.
Lastly, the Hard-Kill BESO can be summarized in these steps:

1. Discretization of the design domain and assignment of the initial property values;

2. Perform finite element analysis and calculate the elemental sensitivity number α_i;
3. Compute the average sensitivity number and save the result for next iteration;
4. Determine the volume target for the next iteration;
5. Add and delete elements according to α_{del}^{th} and α_{add}^{th};
6. Repeat steps 2 to 5 until the volume target V^* is achieved and the convergence is reached.

The Hard-Kill BESO flowchart is reported below:

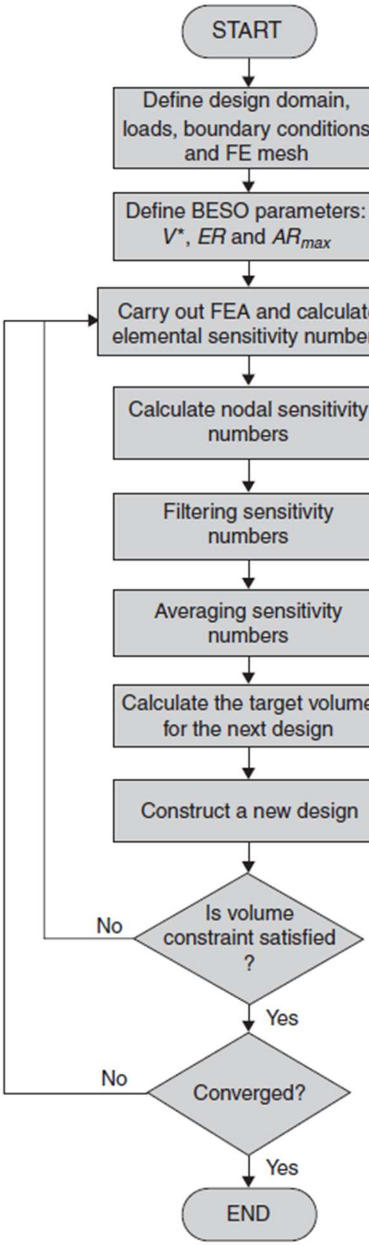

Figure 4.10 - Flowchart of the BESO method (X. Huang, 2010)

4.6.2 Soft-Kill BESO

Differently from the Hard-Kill BESO, the Soft-Kill BESO problem can be stated as:

$$\begin{cases} \text{minimize } C = \dfrac{1}{2}\mathbf{f}^T\mathbf{u} \\ \text{subject to } V^* - \displaystyle\sum_{i=1}^{N} V_i x_i = 0 \\ \text{where } x_i = x_{min} \quad \text{or} \quad 1 \end{cases}$$

Where V^* is the volume target of the optimization and V_i is the volume of an individual element. The only difference is that the design variable x_i can not be equal to zero, but it can have a very small value (e.g., 0.001). This means that no element is allowed to be completely removed from the design volume.

In order to get a nearly solid-void design, the material interpolation scheme is used. This scheme indicates that the Young's modulus of the intermediate material is interpolated as a function of the element density (X. Huang, 2010):

$$E(x_i) = E_1 x_i^p$$

Where E_1 is the Young's modulus of the solid material and p is a penalty exponent. The Poisson's ratio is kept constant and the global stiffness matrix is computed as a function of the elemental design variables and stiffness matrix:

$$\boldsymbol{K} = \sum_i x_i^p \boldsymbol{K}_i^0$$

Where $\boldsymbol{K}_i^0$ is the elemental stiffness matrix of the solid element.

Now it is possible to determine the sensitivity analysis and the sensitivity number. Considering the mean compliance as objective function, the sensitivity can be written as:

$$\frac{dC}{dx_i} = \frac{1}{2}\frac{d\mathbf{f}^T}{dx_i}\mathbf{u} + \frac{1}{2}\mathbf{f}^T\frac{d\mathbf{u}}{dx_i}$$

To determine the sensitivity of the displacement vector, the adjoint method is used. Hence, a Lagrangian multiplier λ is introduced and an extra term $\lambda^T(\mathbf{f} - \boldsymbol{K}\mathbf{u})$ can be added to the mean compliance function without changing the equilibrium equation $\boldsymbol{K}\mathbf{u} = \mathbf{f}$:

$$C = \frac{1}{2}\mathbf{f}^T\mathbf{u} + \lambda^T(\mathbf{f} - \boldsymbol{K}\mathbf{u})$$

Therefore, the sensitivity equation becomes:

$$\frac{dC}{dx_i} = \frac{1}{2}\frac{d\mathbf{f}^T}{dx_i}\mathbf{u} + \frac{1}{2}\mathbf{f}^T\frac{d\mathbf{u}}{dx_i} + \frac{d\lambda^T}{dx_i}(\mathbf{f} - \boldsymbol{K}\mathbf{u}) + \lambda^T\left(\frac{d\mathbf{f}}{dx_i} - \frac{d\boldsymbol{K}}{dx_i}\mathbf{u} - \boldsymbol{K}\frac{d\mathbf{u}}{dx_i}\right)$$

Assuming that the load vector is not influenced and taking into account the equilibrium equation, the sensitivity of the objective function becomes:

$$\frac{dC}{dx_i} = \left(\frac{1}{2}\mathbf{f}^T - \lambda^T \boldsymbol{K}\right)\frac{d\mathbf{u}}{dx_i} - \lambda^T \frac{d\boldsymbol{K}}{dx_i}\mathbf{u}$$

At this point, the Lagrangian multiplier λ can be chosen freely because $(\mathbf{f} - \boldsymbol{K}\mathbf{u})$ is equal to zero. Hence, λ is chosen to delete the derivative of the displacement vector that is unknown:

$$\frac{1}{2}\mathbf{f}^T - \lambda^T \boldsymbol{K} = 0$$

Therefore, considering the equilibrium equation, the solution for λ is:

$$\lambda = \frac{1}{2}\mathbf{u}$$

Rewriting the sensitivity of the objective function:

$$\frac{dC}{dx_i} = -\frac{1}{2}\mathbf{u}^T \frac{d\boldsymbol{K}}{dx_i}\mathbf{u}$$

Finally, substituting the material interpolation scheme:

$$\frac{\partial C}{\partial x_i} = -\frac{1}{2} p x_i^{p-1} \mathbf{u}_i^T \boldsymbol{K}_i^0 \mathbf{u}_i$$

The sensitivity number of an element is:

$$\alpha_i = -\frac{1}{p}\frac{\partial C}{\partial x_i} = \begin{cases} \dfrac{1}{2}\mathbf{u}_i^T \boldsymbol{K}_i^0 \mathbf{u}_i & \text{when } x_i = 1 \\ \dfrac{x_{min}^{p-1}}{2}\mathbf{u}_i^T \boldsymbol{K}_i^0 \mathbf{u}_i & \text{when } x_i = x_{min} \end{cases}$$

Considering an infinite penalty exponent p, the sensitivity number is:

$$\alpha_i = -\frac{1}{p}\frac{\partial C}{\partial x_i} = \begin{cases} \dfrac{1}{2}\mathbf{u}_i^T \boldsymbol{K}_i^0 \mathbf{u}_i & \text{when } x_i = 1 \\ 0 \quad \text{when } x_i = x_{min} \end{cases}$$

This is the sensitivity number in the Hard-Kill BESO. Hence, it is concluded that the Hard-Kill BESO method is a special case of the Soft-Kill BESO method where the penalty exponent p approaches infinity (X. Huang, 2010).

4.7 Algorithm implementation software

In this thesis, SIMP and BESO methods have been employed. The first one has been implemented in the software called “nTopology” and the second one has been developed using the Grasshopper plug-in called “Ameba”.

4.7.1 nTopology

nTopology is a software that is able to perform topology optimization analysis using the SIMP method. Before using the topology optimization block (Figure 4.11), it is needed to set the FE model, the objective of the optimization analysis and the constraint of the process (“Empty” spaces in the figure):

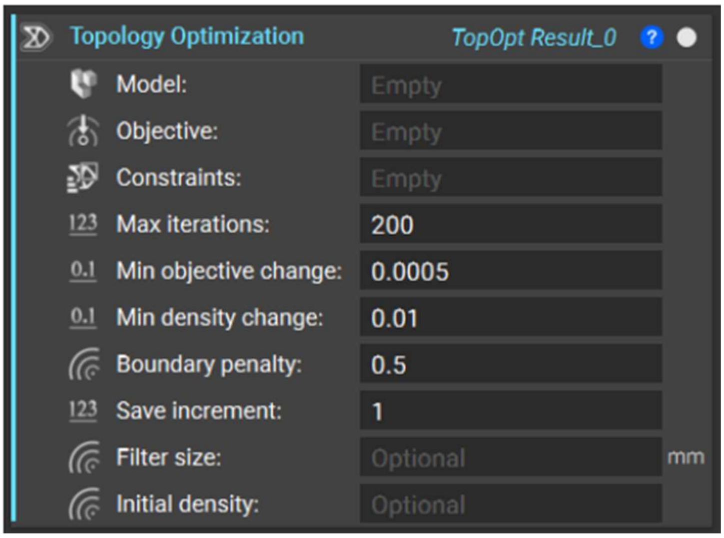

Topology Optimization TopOpt Result_0

Model: Empty
Objective: Empty
Constraints: Empty
Max iterations: 200
Min objective change: 0.0005
Min density change: 0.01
Boundary penalty: 0.5
Save increment: 1
Filter size: Optional mm
Initial density: Optional

Figure 4.11 - Topology Optimization block in nTopology

Firstly, the FE Model needs to be generated using the FE Model block (Figure 4.12), which contains all the information like the FE Mesh, the FE Attributes and the material properties. In this thesis, the following blocks have been employed respectively:

- “FE Model”;
- “FE Component”;
- “FE Volume Mesh”;
- “FE Solid Attribute”.

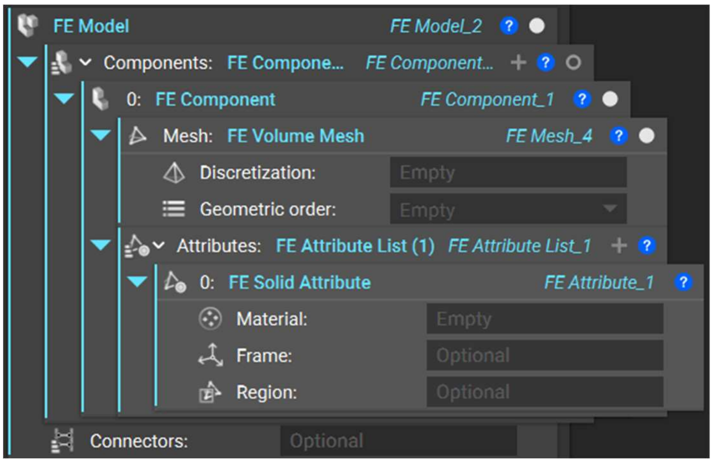

FE Model FE Model_2
Components: FE Compone... FE Component...
0: FE Component FE Component_1
Mesh: FE Volume Mesh FE Mesh_4
Discretization: Empty
Geometric order: Empty
Attributes: FE Attribute List (1) FE Attribute List_1
0: FE Solid Attribute FE Attribute_1
Material: Empty
Frame: Optional
Region: Optional
Connectors: Optional

Figure 4.12 - FE Model block in nTopology

Then, the material can be considered isotropic, using the blocks "Isotropic Material" and "Isotropic Linear Elastic Material", or orthotropic, employing the blocks "Orthotropic Material" and "Orthotropic Linear Elastic Material":

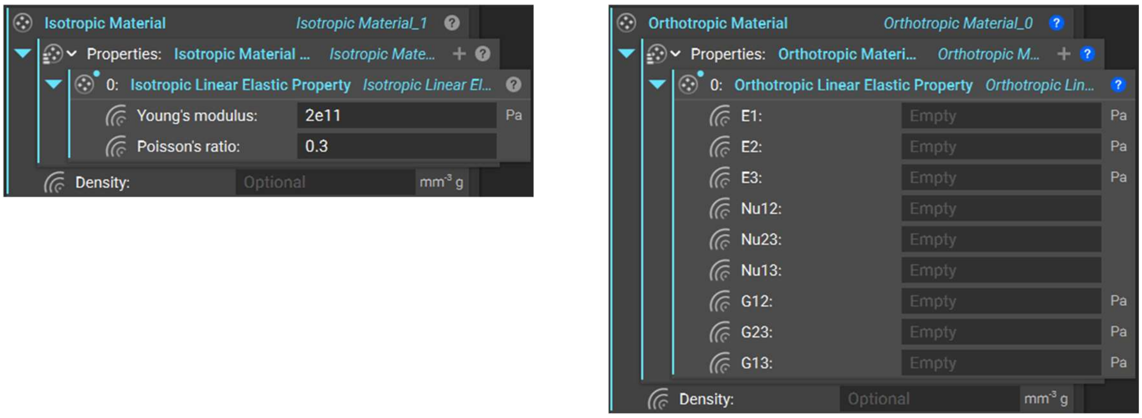

Isotropic Material Isotropic Material_1
Properties: Isotropic Material ... Isotropic Mate...
0: Isotropic Linear Elastic Property Isotropic Linear El...
Young's modulus: 2e11 Pa
Poisson's ratio: 0.3
Density: Optional mm³ g

Orthotropic Material Orthotropic Material_0
Properties: Orthotropic Materi... Orthotropic M...
0: Orthotropic Linear Elastic Property Orthotropic Lin...
E1: Empty Pa
E2: Empty Pa
E3: Empty Pa
Nu12: Empty
Nu23: Empty
Nu13: Empty
G12: Empty Pa
G23: Empty Pa
G13: Empty Pa
Density: Optional mm³ g

Figure 4.13 - Isotropic Material block (left) and Orthotropic Material block (right) in nTopology

Once that the FE Model has been created successfully, it is needed to impose the boundary conditions. In this thesis, "Surface Load" and "Displacement Restraint" blocks have been used:

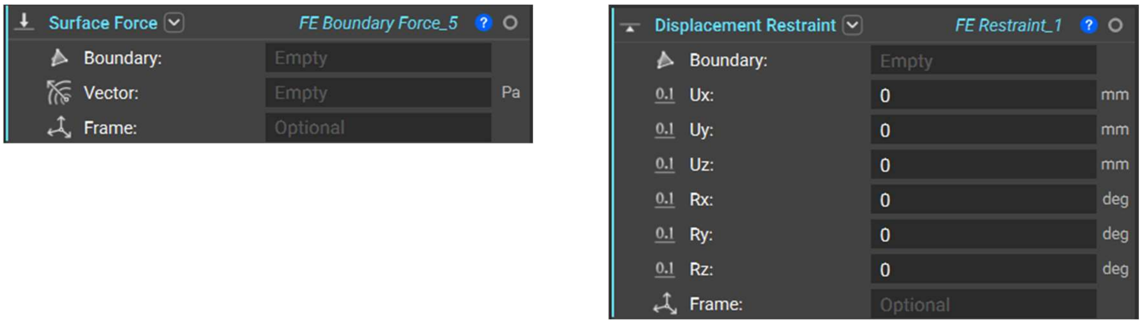

Surface Force FE Boundary Force_5
Boundary: Empty
Vector: Empty Pa
Frame: Optional

Displacement Restraint FE Restraint_1
Boundary: Empty
Ux: 0 mm
Uy: 0 mm
Uz: 0 mm
Rx: 0 deg
Ry: 0 deg
Rz: 0 deg
Frame: Optional

Figure 4.14 - Surface Load block (left) and Displacement Restraint block (right) in nTopology

At this stage, it is necessary to define the optimization objective and it is possible to maximize or minimize different structural quantities. In order to do that, the block “Optimization Objective” is used with some other blocks that specify which quantity minimize or maximize:

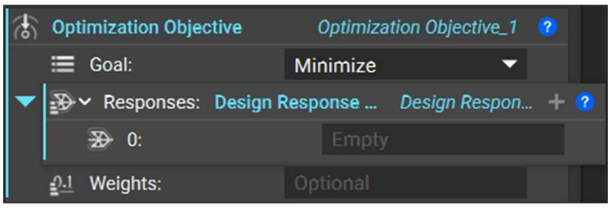

Optimization Objective — Optimization Objective_1
Goal: Minimize
Responses: Design Response ... — Design Respon...
0: Empty
Weights: Optional

Figure 4.15 - Optimization Objective block in nTopology

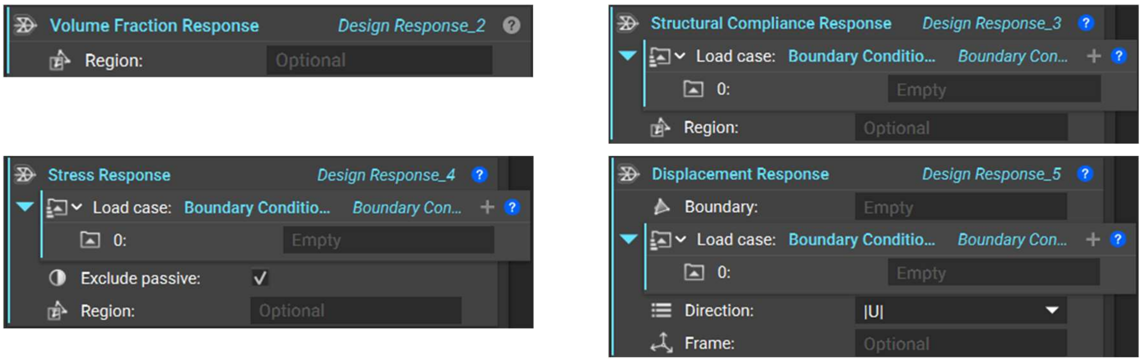

Volume Fraction Response — Design Response_2
Region: Optional

Structural Compliance Response — Design Response_3
Load case: Boundary Conditio... — Boundary Con...
0: Empty
Region: Optional

Stress Response — Design Response_4
Load case: Boundary Conditio... — Boundary Con...
0: Empty
Exclude passive: ✓
Region: Optional

Displacement Response — Design Response_5
Boundary: Empty
Load case: Boundary Conditio... — Boundary Con...
0: Empty
Direction: |U|
Frame: Optional

Figure 4.16 - Response blocks in nTopology

The last blocks to be inserted are the topology constraints, which may concern design and manufacturing aspects:

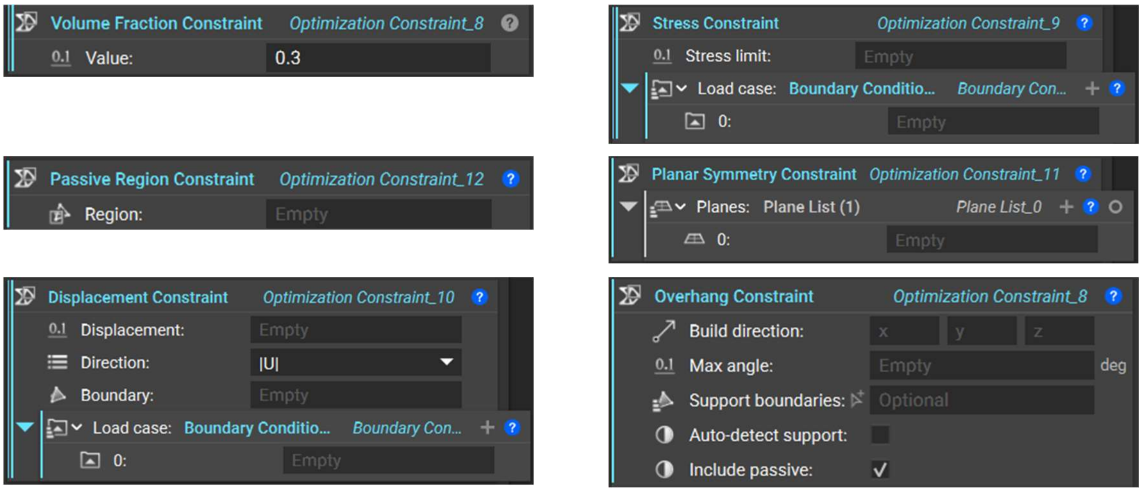

Volume Fraction Constraint — Optimization Constraint_8
Value: 0.3

Stress Constraint — Optimization Constraint_9
Stress limit: Empty
Load case: Boundary Conditio... — Boundary Con...
0: Empty

Passive Region Constraint — Optimization Constraint_12
Region: Empty

Planar Symmetry Constraint — Optimization Constraint_11
Planes: Plane List (1) — Plane List_0
0: Empty

Displacement Constraint — Optimization Constraint_10
Displacement: Empty
Direction: |U|
Boundary: Empty
Load case: Boundary Conditio... — Boundary Con...
0: Empty

Overhang Constraint — Optimization Constraint_8
Build direction: x y z
Max angle: Empty deg
Support boundaries: Optional
Auto-detect support: ☐
Include passive: ✓

Figure 4.17 - Topology Constraint blocks in nTopology

Finally, the analysis is run inserting all these objects inside the “Topology Optimization” block.

4.7.2 Ameba

Ameba is a plug-in for Grasshopper and it is able to perform topology optimization analysis using the Soft-Kill BESO method with $x_{min} = 0.001$ and $p = 3$.
Initially, the pre-processing in Ameba requires the mesh generation of the initial domain using the component “Mesh Parting”:

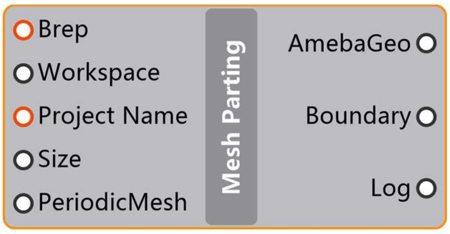

Figure 4.18 - Mesh Parting component in Ameba

At this stage, all the loads, boundary conditions and constraints must be applied using the components “Load3dSurface”, “Load3dSurfaceNormal”, “Support3dSurface” and “NonDomain”, respectively:

Figure 4.19 - Load, boundary condition and non-domain element components in Ameba

All these components are connected to the “PreProcessing” component, which enables to set the parameters discussed in the previous chapter:

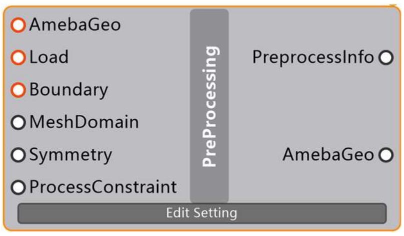

Figure 4.20 - Preprocessing component in Ameba

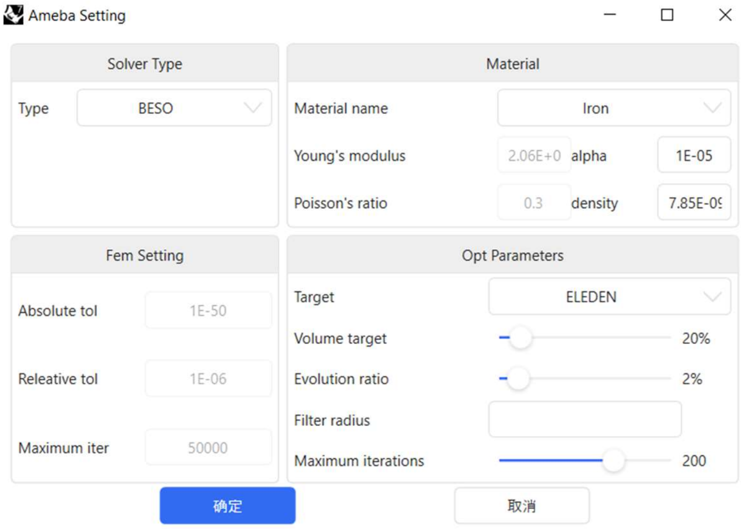

Ameba Setting

Solver Type

Type: BESO

Material

Material name: Iron

Young's modulus: 2.06E+0

alpha: 1E-05

Poisson's ratio: 0.3

density: 7.85E-0

Fem Setting

Absolute tol: 1E-50

Releative tol: 1E-06

Maximum iter: 50000

Opt Parameters

Target: ELEDEN

Volume target: 20%

Evolution ratio: 2%

Filter radius:

Maximum iterations: 200

Figure 4.21 - Setting parameter for the topology optimization analysis in Ameba

Finally, using the "Solver" component, it is possible to run the topology optimization analysis. The optimization is terminated once both the volume target and the tolerance are satisfied. The solver component provides also a graph during the optimization, which shows the volume reduction and the total strain energy of the structure:

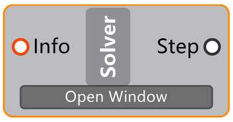

Figure 4.22 - Solver component in Ameba

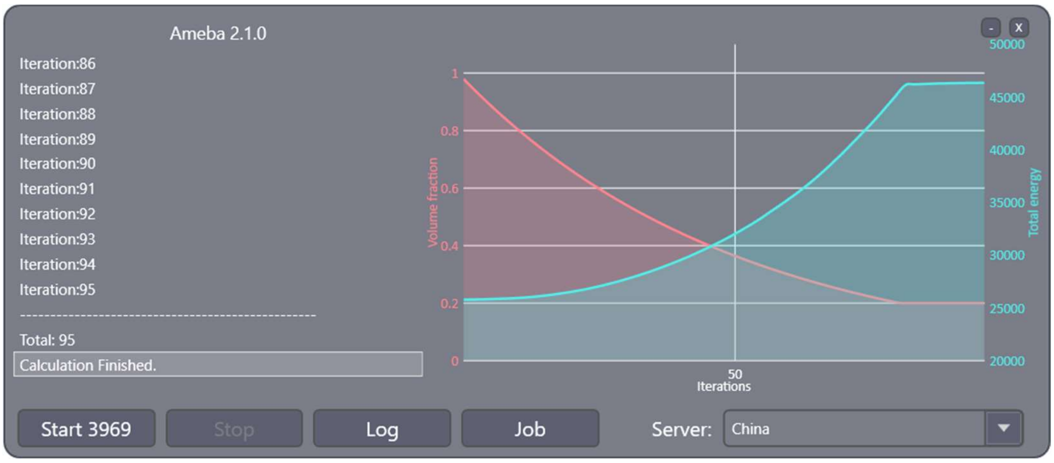

Ameba 2.1.0

```
Iteration:86
Iteration:87
Iteration:88
Iteration:89
Iteration:90
Iteration:91
Iteration:92
Iteration:93
Iteration:94
Iteration:95
------------------------------------------------
Total: 95
Calculation Finished.
```

Figure 4.23 - Solver graph in which is possible to watch the volume reduction and the strain energy evolution during the topology optimization process

CHAPTER 5

JOINT CLASSIFICATION

5.1 Overview

Joints affect significantly the behaviour of gridshell structures, therefore is fundamental to design and classify them properly. Typically, failure of gridshell structures is due to instability problems, hence it is important to take into account the following phenomena:

- Member buckling: in this case only a single element buckles without affecting the global structural behaviour;
- Local instability: snap-through of one or more joints;
- Global instability: the whole structure buckles;
- It is also possible a combination of the above-mentioned modes.

It is important to observe that the stiffnesses and strengths of joints influence the failure mode of the structure.

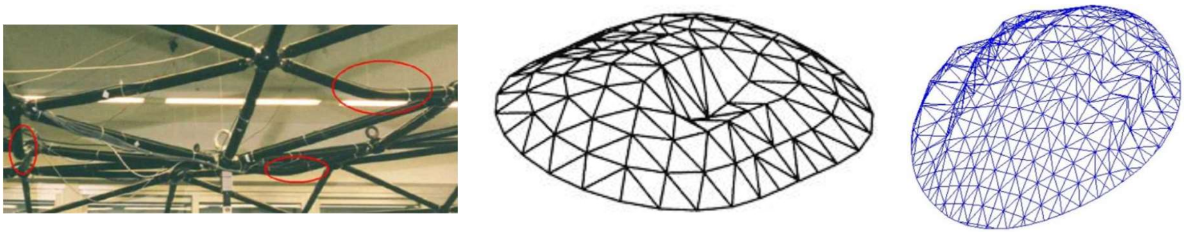

Figure 5.1 - Member buckling (left), local instability (centred) and global instability (right) (Linden, 2015)

5.2 Joint classification according to Eurocode 8 part 1-8

The Eurocode 3 Part 1-8 classifies joints in three different categories according to their stiffness capacity and their strength.

For stiffness classification there are three categories (Eurocode 3: Design of steel structures - Part 1-8: Design of joints, 1993):

- Nominally pinned joints: they should be capable of transmitting the internal forces, without developing significant moments which might adversely affect the members or the structure as a whole, and should be able of accepting the resulting rotation under the design loads;
- Rigid joints: they may be assumed to have sufficient rotational stiffness to justify analysis based on full continuity;
- Semi-rigid joints: they do not meet the criteria for rigid joints or a nominally pinned joints and they should be capable of transmitting the internal forces and moments.

Moreover, Eurocode 3 provides a moment-rotation graph that represents the stiffness classification:

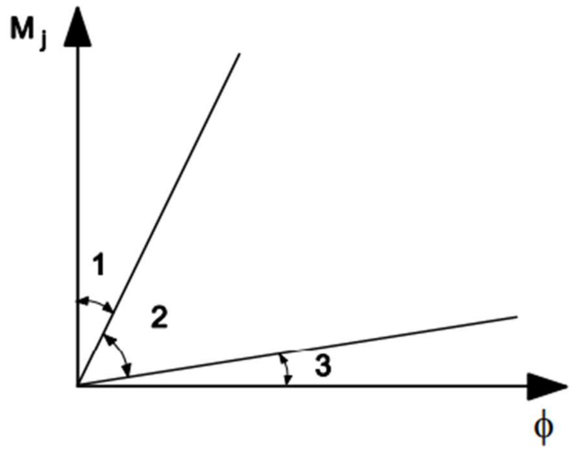

Figure 5.2 - Moment-rotation graph for joint classification based on stiffness (Eurocode 3: Design of steel structures - Part 1-8: Design of joints, 1993)

Then, considering strength classification, joints are classified as:

- Nominally pinned joints: they should be capable of transmitting the internal forces, without developing significant moments which might adversely affect the members or the structure as a whole;
- Full strength joints: the design resistance should be not less than that of the connected members;
- Partial-strength joints: they do not meet the criteria for full-strength joints or nominally pinned joints.

5.3 Joint classification according with Fan, Ma, Cao and Shen

There are also researches describing simplified ways to analyse the joint behaviour. One of them has been carried out by Fan, Ma, Cao and Shen in the paper called "A new classification system for the joints used in lattice shells". The authors consider a joint classification that takes into account stiffness and strength simultaneously and they identify three categories:

- Rigid joints: they have a high rotational strength and a high rotational stiffness;
- Pinned joints: they have a low rotational strength and a low rotational stiffness;
- Semi-rigid joints: they have a moderate rotational strength and a moderate rotational stiffness.

5.3.1 Joint classification based on the stiffness *k*

Starting from the stiffness classification, the authors have considered a simple structure made of two beams and they have taken into account different rotational stiffnesses as shown in the figures:

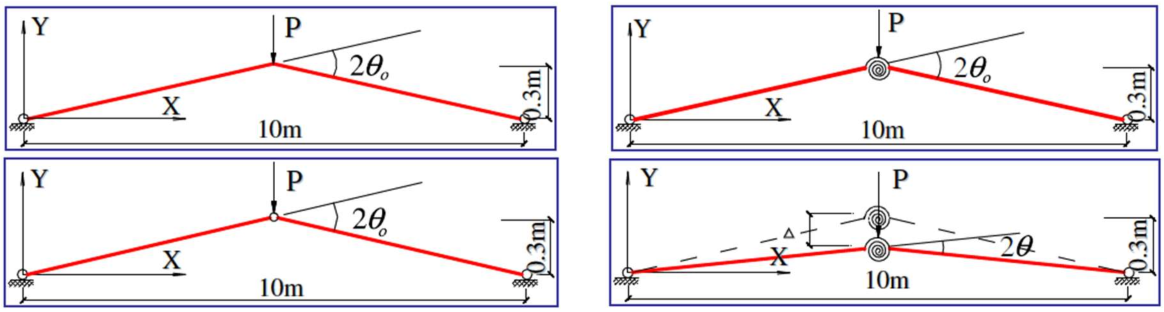

Figure 5.3 - Two-member structure: Structure with rigid joint (top-left), structure with flexible joint (top-right), structure with pinned joint (bottom-left) and deformation equilibrium state (bottom-right) (Feng Fan H. M., 2011)

The relationships between moment and the angle are written below:

$$M_{zr} = \frac{4EI}{L_0}(\theta_0 - \theta) + \frac{6EI}{L_0} cos\theta(sin\theta_0 - sin\theta)$$

$$M_{zs} = k * 2(\theta_0 - \theta)$$

Where:

- M_{zr} is the bending moment in the rigid joint;
- M_{zs} is the bending moment in the flexible joint;
- θ is the angle variable between the members and the horizontal plane;

- θ_0 is the initial angle between the members and the horizontal plane;
- L_0 is the length of the elements;
- E is the Young's modulus;
- I is the moment of inertia of the members.

Imposing $M_{zs} = M_{zr}$, it is possible to compute the stiffness k for which the node behaves like a rigid connection:

$$\frac{4EI}{L_0}(\theta_0 - \theta) + \frac{6EI}{L_0} cos\theta(sin\theta_0 - sin\theta) = k * 2(\theta_0 - \theta)$$

$$k = \frac{2EI}{L_0} + \frac{3EI(sin\theta_0 - sin\theta)}{L_0(\theta_0 - \theta)} cos\theta$$

Taking into account the hypothesis of small deformations:

$$k = \frac{2EI}{L_0} + \frac{3EI}{L_0} cos\theta$$

For this structure $cos\theta_0 \approx 0.998$ and $0.998 \leq \theta \leq \theta_0$, therefore $0.998 \leq cos\theta \leq 1$ and $cos\theta \approx 1$. Hence, the smallest stiffness that guarantees a rigid behaviour of the joint is:

$$k = \frac{5EI}{L_0}$$

It is possible to introduce a coefficient α that is the ratio between the stiffness k of the joint and the stiffness EI/L_0 of the members connected to the node.
The influence of the coefficient α with respect to the critical load of the structure can be represented in the following graphs:

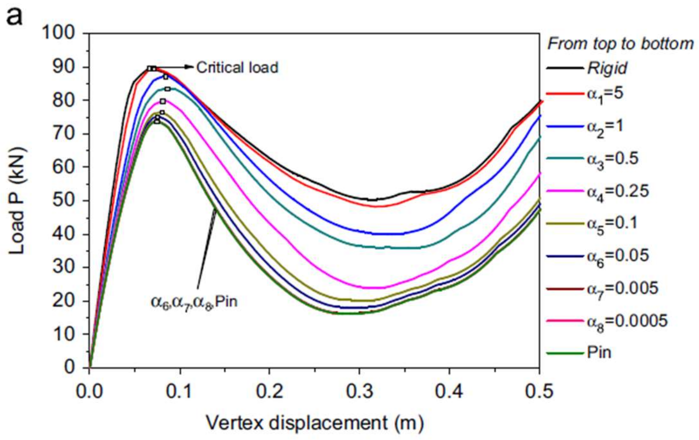

Figure 5.4 - Influence of the coefficient α with respect to the critical load P_{cr} (Feng Fan H. M., 2011)

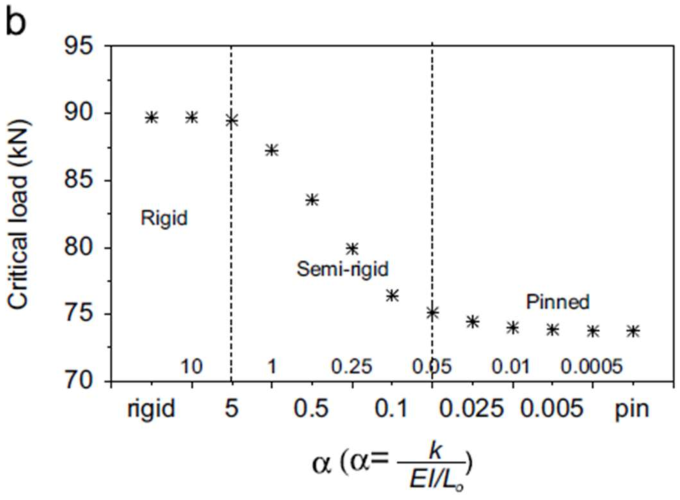

Figure 5.5– Critical load P_{cr} of structures with different determination coefficients α (Feng Fan H. M., 2011)

The results are summarized in the table below:

Categories	**Determination coefficient α**
Rigid	$\alpha \geq 5$
Semi-rigid	$5 > \alpha > 0.05$
Pinned	$\alpha \leq 0.05$

Table 5.1 - Joint classification based on stiffness

5.3.2 Joint classification based on stiffness k and moment capacity $M_{j,u}$

For what concerns the strength classification of the joints, knowing that nodes with same stiffness can have different bending moment resistances, as shown in the figure, it is important to introduce a new factor called β. This coefficient β is used to investigate the effect of the moment capacity of joints on the mechanical behaviour of spatial structures:

$$\beta = \frac{M_{j,u}}{M_{e,u}}$$

Where $M_{j,u}$ is the moment capacity of the joint and $M_{e,u}$ is the moment capacity of the member connected to the joint.

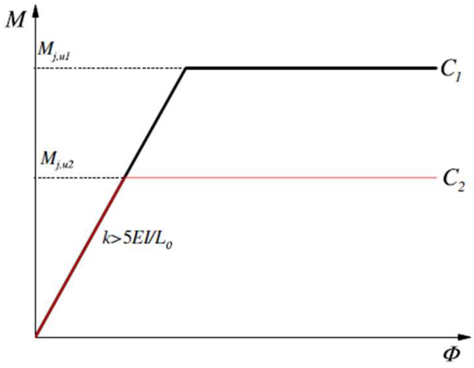

Figure 5.6 – Moment-rotation curves with different moment capacities (Feng Fan H. M., 2011)

Studying the effects of β on the critical load of the structure, it is possible to get the following results.

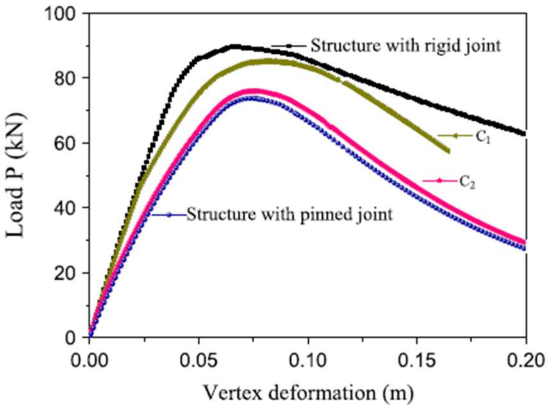

Figure 5.7 - Load–displacement curves for structures with different bending-rotation curves (Feng Fan H. M., 2011)

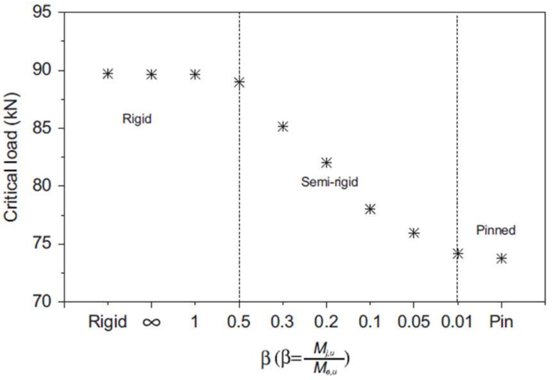

Figure 5.8 - Critical load of structures with different determination coefficients β (Feng Fan H. M., 2011)

Hence, for the initial simple structure, considering an initial stiffness of the node, it is possible to notice that the joint behaves like rigid for values of β larger than 0.5.
Combining the results obtained in terms of stiffness and strength, a joint is classified as rigid, semi-rigid and pinned if α and β are inside the range of the table below:

Categories	**Determination coefficient α**
Rigid	$\alpha \geq 5$ and $\beta \geq 0.5$
Semi-rigid	$\beta \geq 0.5$ and $5 > \alpha > 0.05$
	$\alpha \geq 5$ and $0.01 < \beta < 0.5$
Pinned	$\alpha \leq 0.05$ or $\beta \leq 0.01$

Table 5.2 - Joint classification based on stiffness and strength

CHAPTER 6

OPTIMIZATION STUDY OF A GRIDSHELL NODE

6.1 History of the British Museum

The British Museum was constructed in the eighteenth century and it is arranged as a quadrangle surrounding the Great Court (Figure 6.1), the centre piece of which is the historic Reading Room. Initially, the Great Court was occupied by the British Library while now it has been transformed in an elegant public space covered by a glazed roof the size of a football field. This new space permitted to design new galleries and a destination restaurant.
The erection of the glazed roof began in 1999, it has been completed and opened to the public in November 2000.
Today it has a worldwide reputation for the scope, quality and rarity of its collections and for its role as a centre of education and scholarship. Every year the museum attracts 5.4 million visitors compared to the Louvre's 5.7 million and the New York Metropolitan Museum's 5.2 million (Michael Barnes, 2000).

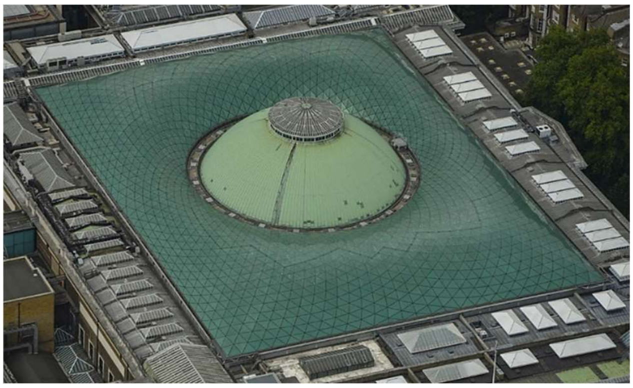

Figure 6.1 - British Museum roof

6.2 Real geometry

The roof covers the whole area of the Great Court with a length of 95 m and a width of 74 m and spans from the edge of the surrounding buildings to the Reading Room in the middle. The whole structure is formed by a net of triangular cells in a shell shape. The final geometry for the roof net and the structural design was developed by Buro Happold using a form-finding process. An essential factor to determine the net geometry was the maximum possible size for the glass panels from the fabrication point of view considering the required glass performance. The final net includes 4878 members and 1566 nodes within the net, all of them different from each other. The span in the north is 28.8 m, the arch height 5.48 m, the span in the east and west is 14.4 m, the arch height 5.1 m and the span in the south 23.8 m with an arch height of 6.4 m (Michael Barnes, 2000).

The shape of the roof is defined by a surface on which the nodes of the steel grid lie. The height of the surface, z, is a function of x in the easterly direction and y in the northerly direction. The origin lies on a vertical line through the centre of the Reading Room. The function is:

$$z = z_1 + z_2 + z_3$$

Where:

$$z_1 = (h_{centre} - h_{edge})\eta + h_{edge}$$

$$\begin{aligned}
\frac{z_2}{\alpha} = (1-\lambda)\Bigg(&\left(\frac{35+10\psi}{2}\right)(1+\cos 2\theta) + \frac{24}{2}\left(\frac{1}{2}(1-\cos 2\theta) + \sin\theta\right) \\
&+ (7.5+12\psi)\left(\frac{1}{2}(1-\cos 2\theta) - \sin\theta\right) - 1.6\Bigg) + \frac{10}{2}(1+\cos 2\theta) \\
&+ 10\left[\frac{1}{2}\left(\frac{1}{2}(1-\cos 2\theta) + \sin\theta\right)\right]^2 (1-3\alpha) \\
&+ 2.5\left[\frac{1}{2}\left(\frac{1}{2}(1-\cos 2\theta) - \sin\theta\right)\right]^2 \left(\frac{r}{a} - 1\right)^2
\end{aligned}$$

$$\begin{aligned}
\frac{z_3}{\beta} = \lambda&\left(\frac{3.5}{2}(1+\cos 2\theta) + \frac{3}{2}(1-\cos 2\theta) + 0.3\sin\theta\right) \\
&+ 1.05\left(e^{-\mu\left(1-\frac{x}{b}\right)} + e^{-\mu\left(1+\frac{x}{b}\right)}\right)\left(e^{-\mu\left(1-\frac{y}{c}\right)} + e^{-\mu\left(1+\frac{y}{c}\right)}\right)
\end{aligned}$$

In these expressions the polar coordinates are:

$$r = \sqrt{x^2 + y^2}$$

$$\theta = \cos^{-1}\frac{x}{r} = \sin^{-1}\frac{y}{r}$$

$$\eta = \frac{\left(1-\frac{x}{b}\right)\left(1+\frac{x}{b}\right)\left(1-\frac{y}{c}\right)\left(1+\frac{y}{d}\right)}{\left(1-\frac{ax}{rb}\right)\left(1+\frac{ax}{rb}\right)\left(1-\frac{ay}{rc}\right)\left(1+\frac{ay}{rd}\right)}$$

$$\psi = \left(1-\frac{x}{b}\right)\left(1+\frac{x}{b}\right)\left(1-\frac{y}{c}\right)\left(1+\frac{y}{d}\right)$$

$$\alpha = \left(\frac{r}{a}-1\right)\psi$$

$$\frac{1-\frac{a}{r}}{\beta} = \frac{\sqrt{(b-x)^2+(c-y)^2}}{(b-x)(c-y)} + \frac{\sqrt{(b-x)^2+(d+y)^2}}{(b-x)(d+y)} + \frac{\sqrt{(b+x)^2+(c-y)^2}}{(b+x)(c-y)} + \frac{\sqrt{(b+x)^2+(d+y)^2}}{(b+x)(d+y)}$$

And the constants are:

- $a = 22.245$;
- $b = 36.625$;
- $c = 46.025$;
- $d = 51.125$;
- $\lambda = 0.5$;
- $\mu = 14.0$;
- $h_{centre} = 20.955$;
- $h_{edge} = 19.71$.

The crucial functions to determine z_1, z_2 and z_3 are respectively η, α and β:

$$\eta = \frac{\left(1-\frac{x}{b}\right)\left(1+\frac{x}{b}\right)\left(1-\frac{y}{c}\right)\left(1+\frac{y}{d}\right)}{\left(1-\frac{ax}{rb}\right)\left(1+\frac{ax}{rb}\right)\left(1-\frac{ay}{rc}\right)\left(1+\frac{ay}{rd}\right)}$$

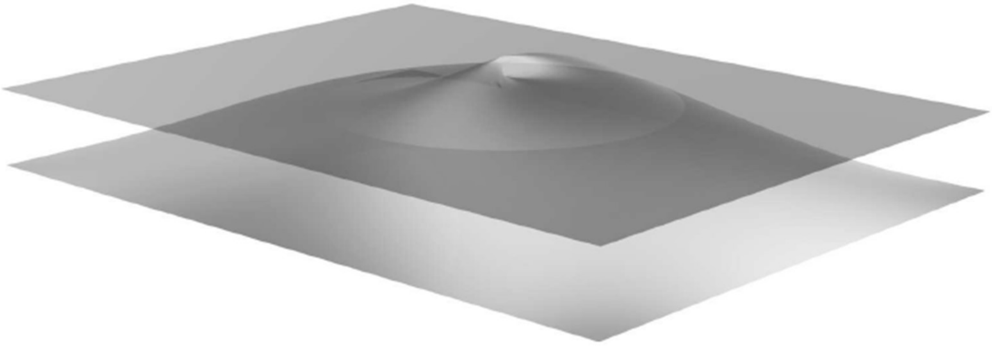

Figure 6.2 - Level change function (Williams, 2001)

$$\alpha = \left(\frac{r}{a}-1\right)\left(1-\frac{x}{b}\right)\left(1+\frac{x}{b}\right)\left(1-\frac{y}{c}\right)\left(1+\frac{y}{d}\right)$$

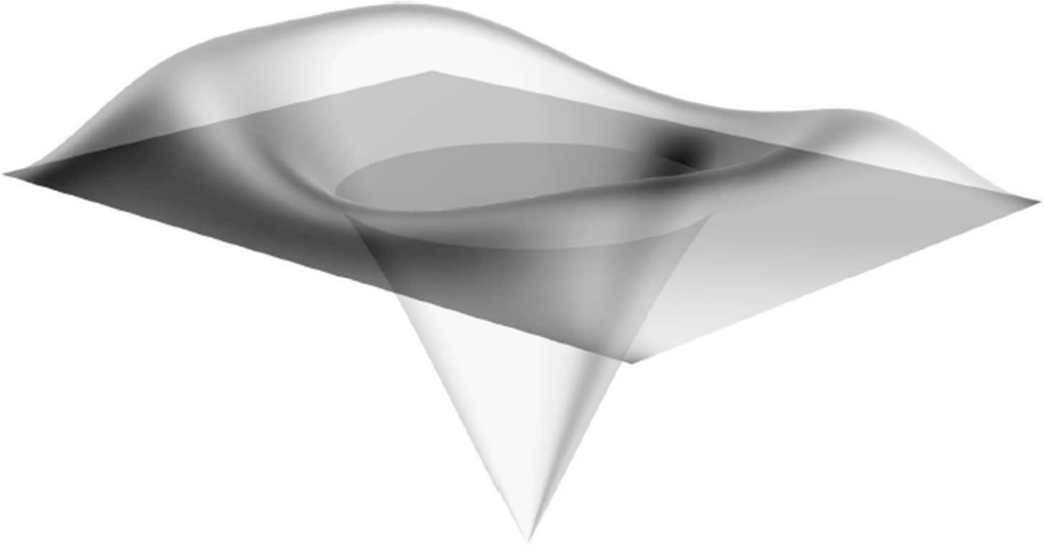

Figure 6.3 - Function with finite curvature at corners (Williams, 2001)

$$\beta = \frac{1-\frac{a}{r}}{\frac{\sqrt{(b-x)^2+(c-y)^2}}{(b-x)(c-y)}+\frac{\sqrt{(b-x)^2+(d+y)^2}}{(b-x)(d+y)}+\frac{\sqrt{(b+x)^2+(c-y)^2}}{(b+x)(c-y)}+\frac{\sqrt{(b+x)^2+(d+y)^2}}{(b+x)(d+y)}}$$

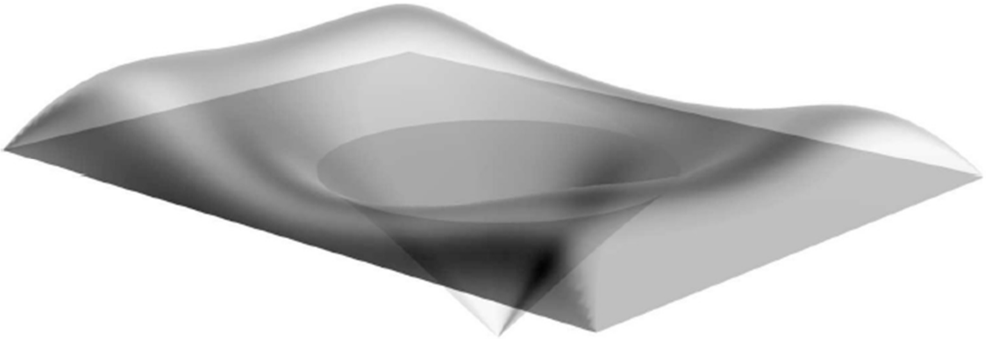

Figure 6.4 - Function with conical corners (Williams, 2001)

The first function, shown in Figure 6.2, supplies the correct change in level between the rectangular boundary and the circular Reading Room. The second fundamental function is shown in Figure 6.3. Both this function and the first produce a horizontal surface at the corners. This is inevitable unless the curvature tends to infinity at the corners, like approaching the tip of a cone and this is what happens with the third fundamental function shown in Figure 6.4 (Williams, 2001).

Summing up the different surfaces:

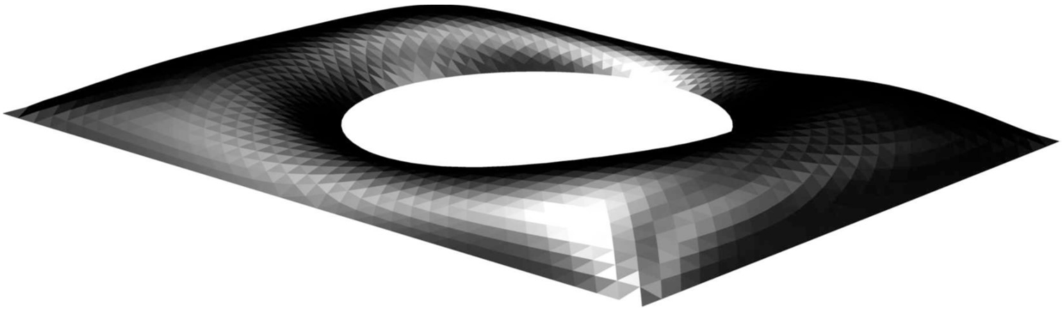

Figure 6.5 - Final surface (Williams, 2001)

Successively, the structural grid is designed following multiple steps. Initially, points equally spaced around the Reading Room have been connected to points equally spaced around the rectangular boundary. Then, these radial lines have been divided equally and joined to create the structural grid (Figure 6.6).

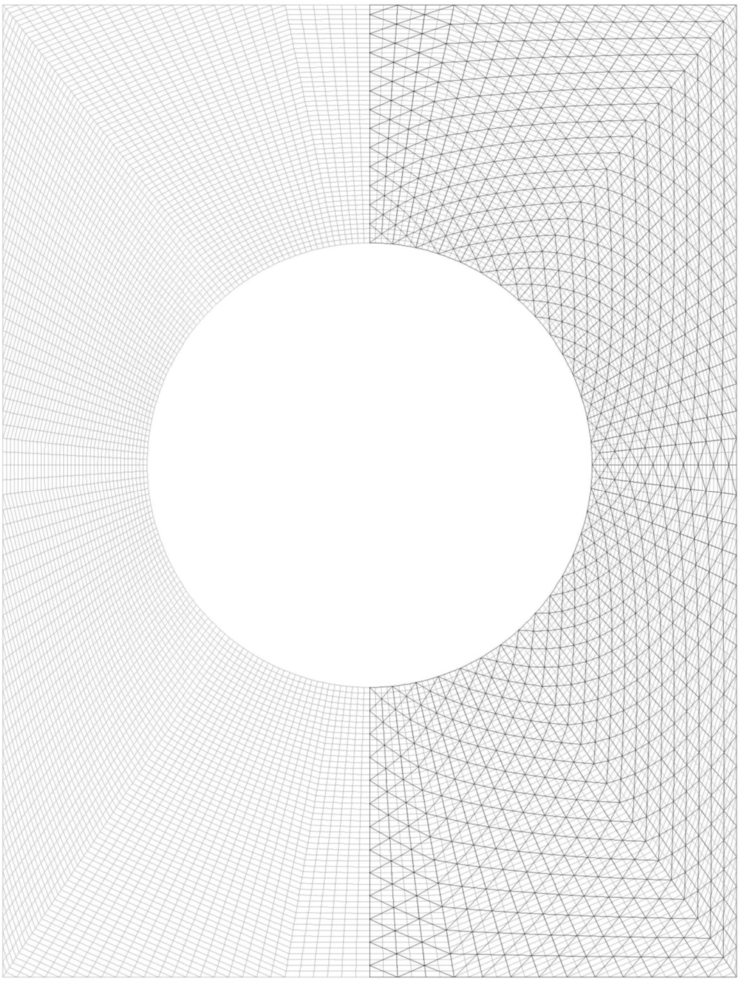

Figure 6.6 - Starting grid (Williams, 2001)

However, this procedure creates some discontinuities, in particular on the diagonal direction. In order to solve this problem, the “dynamic relaxation”, invented by Alister Day, has been used.

Let consider a typical node i, j of the mathematical grid and its four neighbours (Figure 6.7). It is possible to say that the fictitious force applied on the node by the attached strings is:

$$\boldsymbol{f}_{i,j} = (\boldsymbol{p}_{i-1,j} - \boldsymbol{p}_{i,j}) + (\boldsymbol{p}_{i+1,j} - \boldsymbol{p}_{i,j}) - (2-\zeta)(\boldsymbol{p}_{i-1,j} - \boldsymbol{p}_{i,j}) - \zeta(\boldsymbol{p}_{i-1,j} - \boldsymbol{p}_{i,j})$$

Where $\boldsymbol{p}_{i,j}$ is the position vector of the typical node, the tension coefficients are 1, 1, $(2-\zeta)$ and ζ. The tension coefficient is the tension in a member divided by its length.

If the node can slide on the previously defined surface, they will move until the force $\boldsymbol{q}_{i,j}$ tangential to the surface is equal to zero. The force on the node can be expressed by the following formula:

$$\boldsymbol{q}_{i,j} = \boldsymbol{f}_{i,j} - (\boldsymbol{f}_{i,j} * \boldsymbol{n}_{i,j})\boldsymbol{n}_{i,j}$$

And $\boldsymbol{n}_{i,j}$ is the unit normal vector to the surface.

Lastly, the variable ζ has been defined using the following expression:

$$\zeta = 1 - 0.004(1.5m - j)(1 - \cos 2\theta)$$

With $m = 70$ is the value of j on the Reading Room boundary and θ is the polar coordinate. This variable takes into account the maximum size of the glass triangles which occur near the centre of the southern boundary.

In order to solve the non-linear problem $\boldsymbol{q}_{i,j} = 0$, the following algorithm has been used:

$$(\delta\boldsymbol{p}_{i,j})_{\text{this cycle}} = c_1\boldsymbol{q}_{i,j} + c_2(\delta\boldsymbol{p}_{i,j})_{\text{this previous cycle}}$$

With $\delta\boldsymbol{p}_{i,j}$ the movement of the node and the constants c_1 and c_2 used to optimize the speed of convergence.

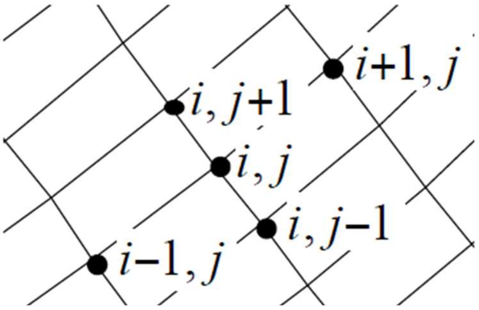

Figure 6.7 - Typical grid nodes (Williams, 2001)

The relaxed grid is shown below:

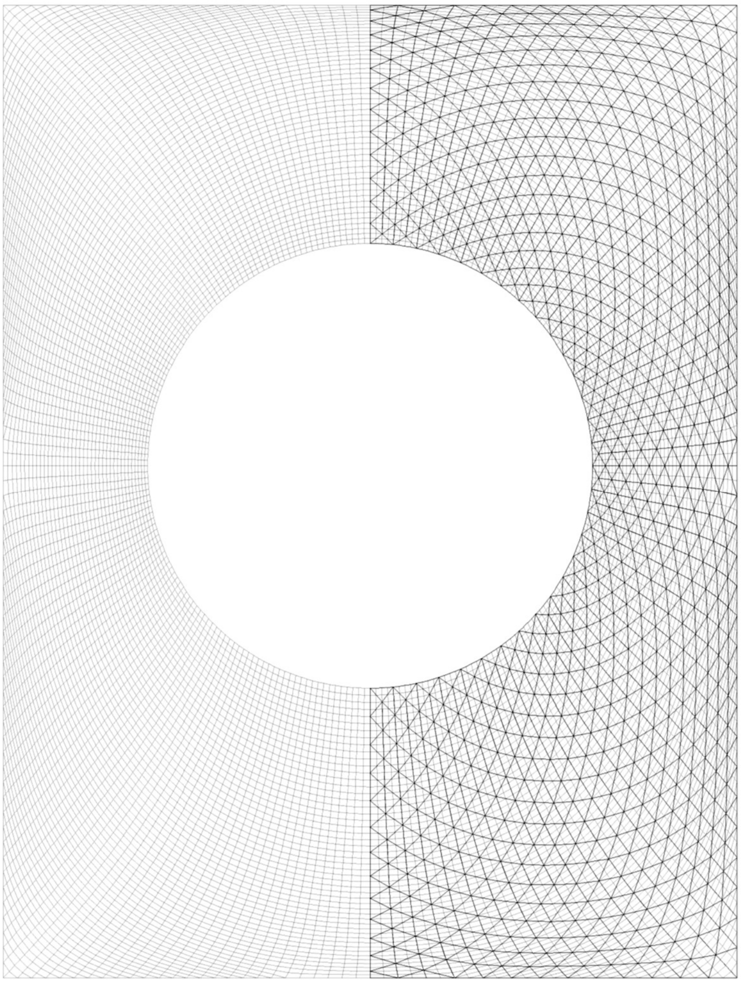

Figure 6.8 - Relaxed grid (Williams, 2001)

The final grid geometry is shown in the following figures:

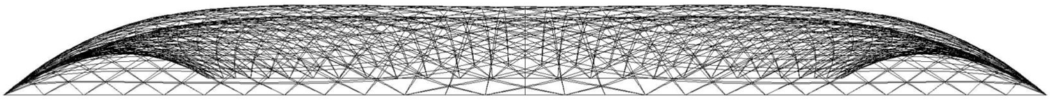

Figure 6.9 - Elevation of structural grid looking north (Williams, 2001)

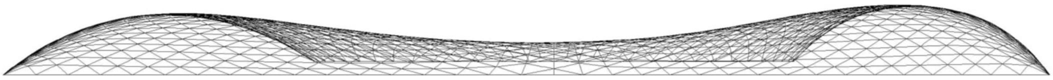

Figure 6.10 - Elevation of structural grid looking west (Williams, 2001)

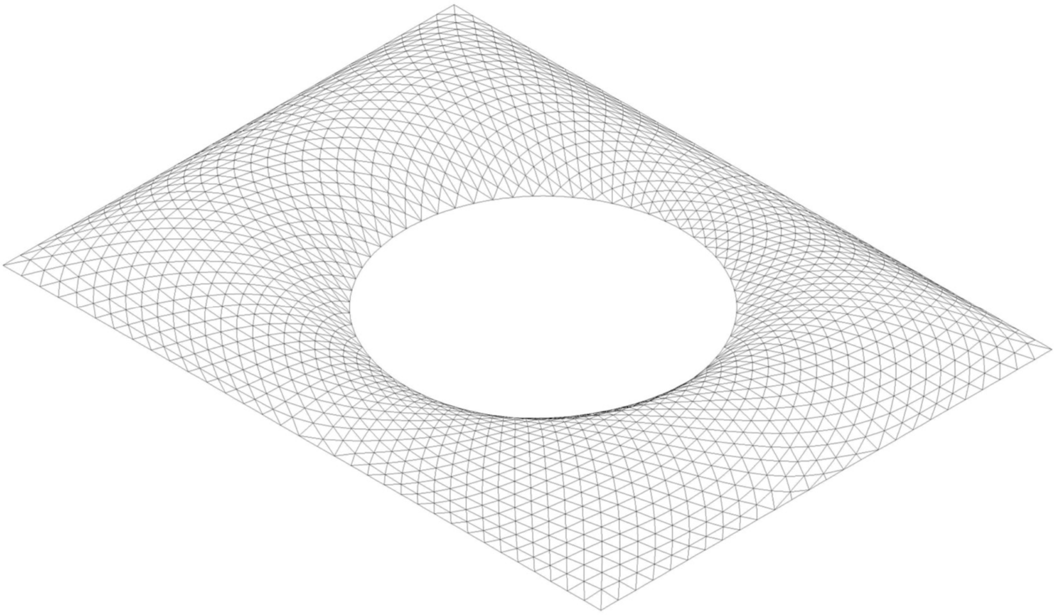

Figure 6.11 - Isometric of structural grid (Williams, 2001)

6.3 Modelling the roof of the British Museum

This section will illustrate the several steps that have been followed to model the roof of the British Museum. Modelling has been carried out with Rhino7 and Grasshopper software.
Starting from the initial boundaries of the roof, previously drawn in Rhino7, it is requested to create the initial plane surface, which is done using the component “Loft” (Figure 6.12 and Figure 6.13).

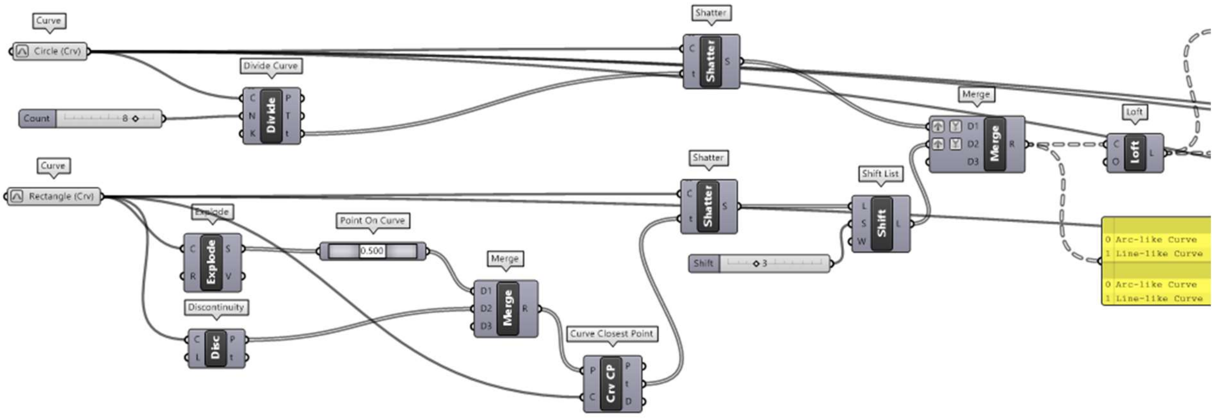

```
0 Arc-like Curve
1 Line-like Curve

0 Arc-like Curve
1 Line-like Curve
```

Figure 6.12 - Creation of the initial plane surface with the component "Loft"

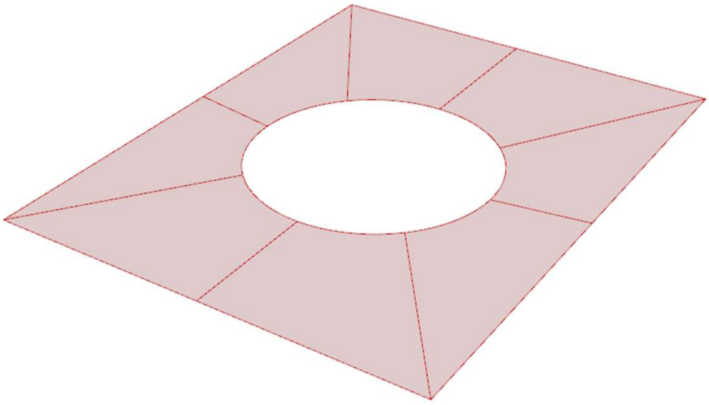

Figure 6.13 - Initial surface obtained using the component "Loft"

Once the initial plane surface has been created, it is desired to generate the mesh, whose nodes and edges will be used to obtain the curved surface of the British Museum. To do this, the “Mesh Surface” component has been used.
Then, to extract nodes and edges from the previous mesh, the component called “Join Meshes and Weld” from the Grasshopper plug-in “Weaverbird” is employed (Figure 6.14 and Figure 6.15).

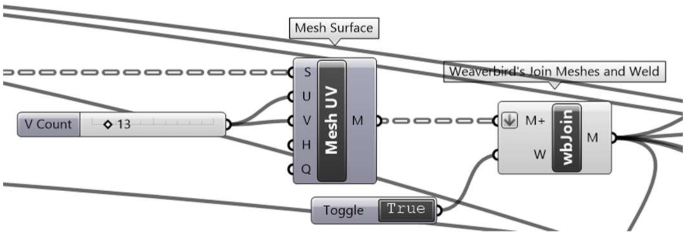

Figure 6.14 – Mesh generation with the components “Mesh Surface” and “Join Meshes and Weld”

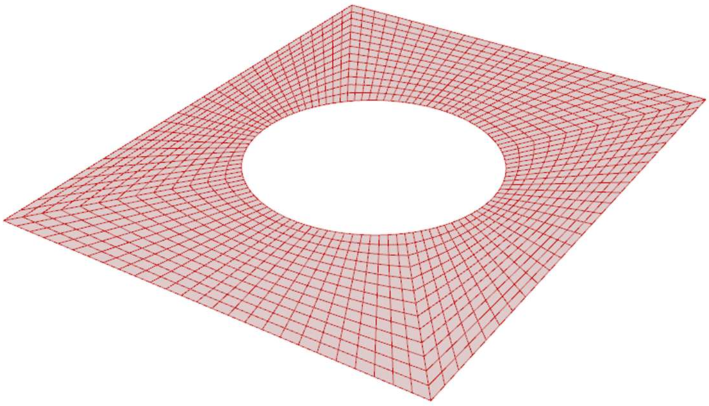

Figure 6.15 - Initial mesh generated using Grasshopper

At this point, the “Kangaroo” component for Grasshopper is used to find the surface of the roof. Kangaroo is a form-finding component and it requires essentially three things:

- The loads applied on the nodes;
- The stiffnesses of the members;
- The nodes restrained.

These inputs for the Kangaroo solver are generated using the components “Load”, “Length” and “Anchor” respectively (Figure 6.16). The values for the loads and the stiffnesses have been taken to reproduce the real geometry.

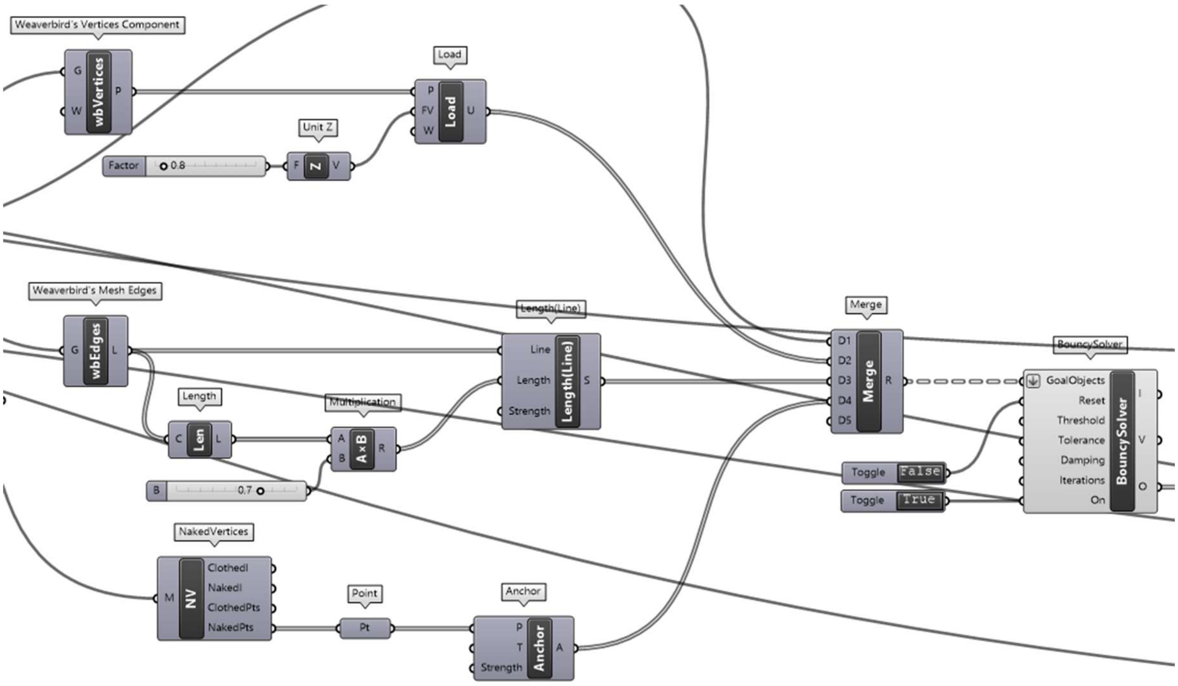

Figure 6.16 - Curved surface through form-finding process using “Kangaroo”

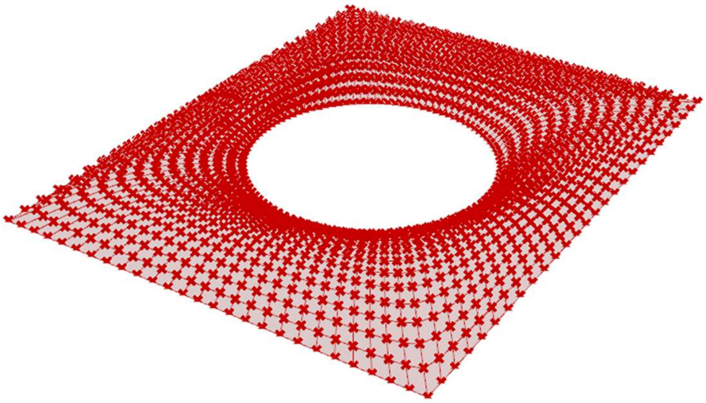

Figure 6.17 - Obtained surface using "Kangaroo"

At this stage, it has been needed to generate the grid. To do that, the component “WarpWeft” has been used to divide the members into two groups according with their directions (Figure 6.18, Figure 6.19 and Figure 6.20).

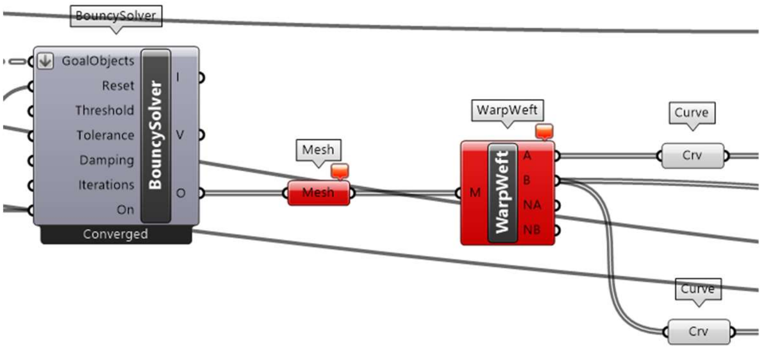

Figure 6.18 - "WrapWelf" component

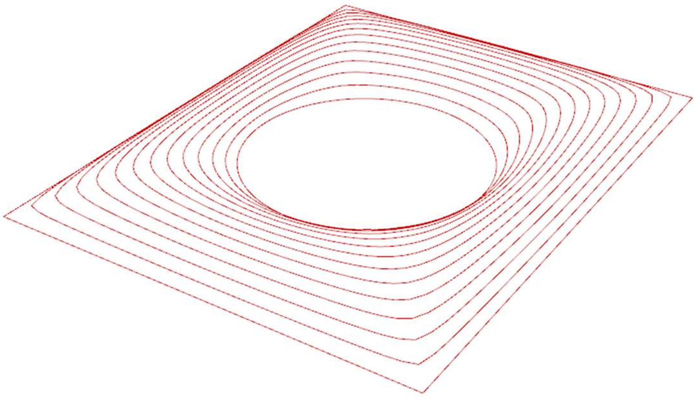

Figure 6.19 - First group of curves generated by "WrapWelf"

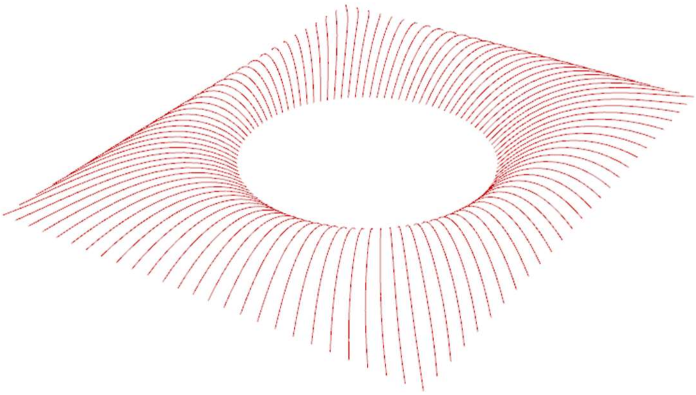

Figure 6.20 - Second group of curves generated by "WrapWelf"

Then, using the Grasshopper plug-in called “PanelingTools”, the previous quad mesh is converted to a mesh made of diamond elements. The components of “PanelingTools” have been used in this order: “Intersect Curves”; “Wrap Grids”; “Convert to Diamond”; and “Generate Borders” (Figure 6.21 and Figure 6.22).

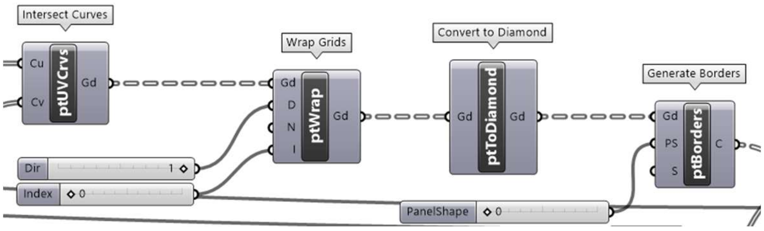

Dir 1

Index 0

PanelShape 0

Figure 6.21 - "Intersect Curves", "Wrap Grids", "Convert to Diamond" and "Generate Borders" from left to right

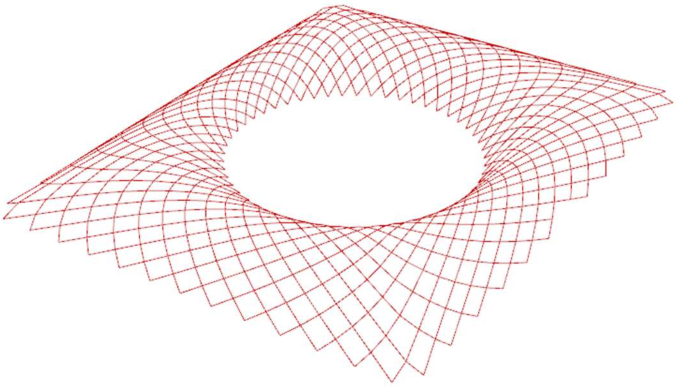

Figure 6.22 - Grid generated

Finally, the diamond elements have been joined with the radial elements to generate the final grid (Figure 6.23, Figure 6.24, Figure 6.25 and Figure 6.26).

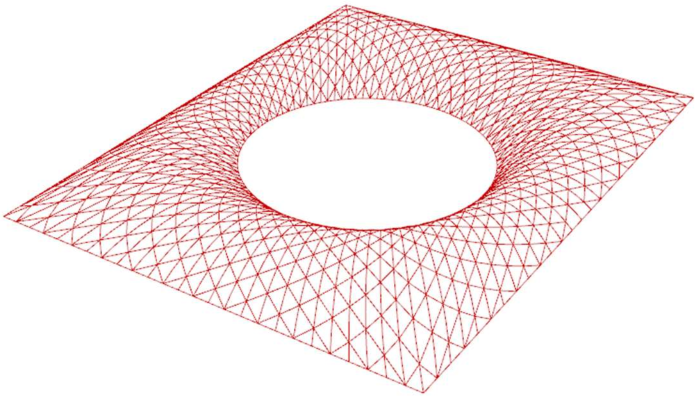

Figure 6.23 - Final grid from a prospective point of view

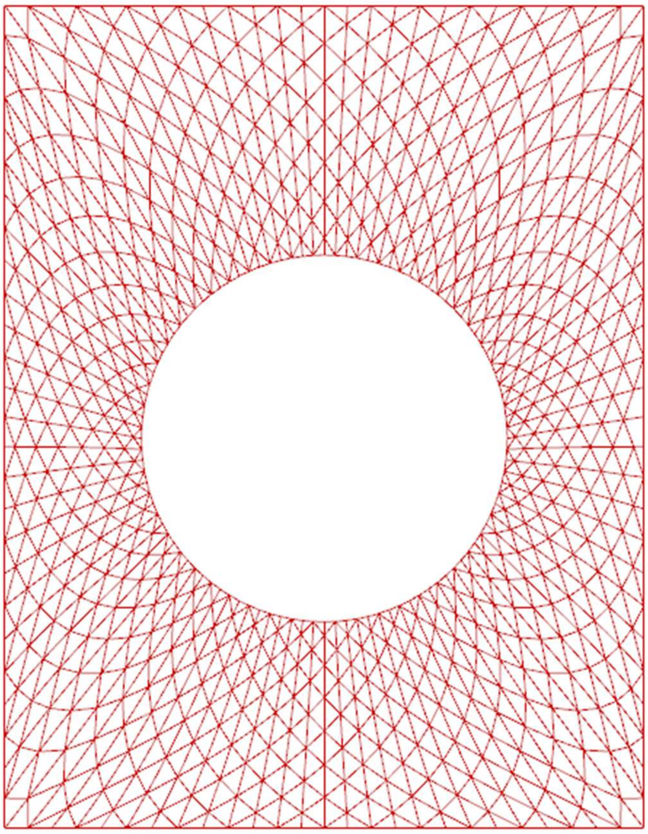

Figure 6.24 - Plan view of the final grid

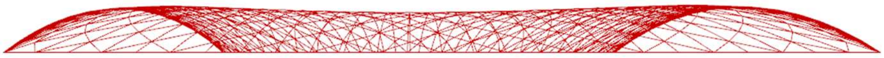

Figure 6.25 - Elevation of final grid looking west

Figure 6.26 - Elevation of final grid looking north

6.4 Structural analysis

At this stage, the gridshell structure has been analysed using Straus7 software to extract the stresses and the strains acting on each member. Afterwards, these stresses will be useful to perform the topology optimization of one node and to study its strength and stiffness.

Once that the structure has been imported in Straus7, all the properties must be set. Initially, all the members are considered like trusses with the following mechanical and geometrical properties:

- Young's Modulus $E = 200$ GPa;
- Steel Density $\rho = 7850$ kg/m^3;
- $B = 80$ mm;
- $D = 180$ mm;
- $t_1 = 10$ mm;
- $t_2 = 20$ mm.

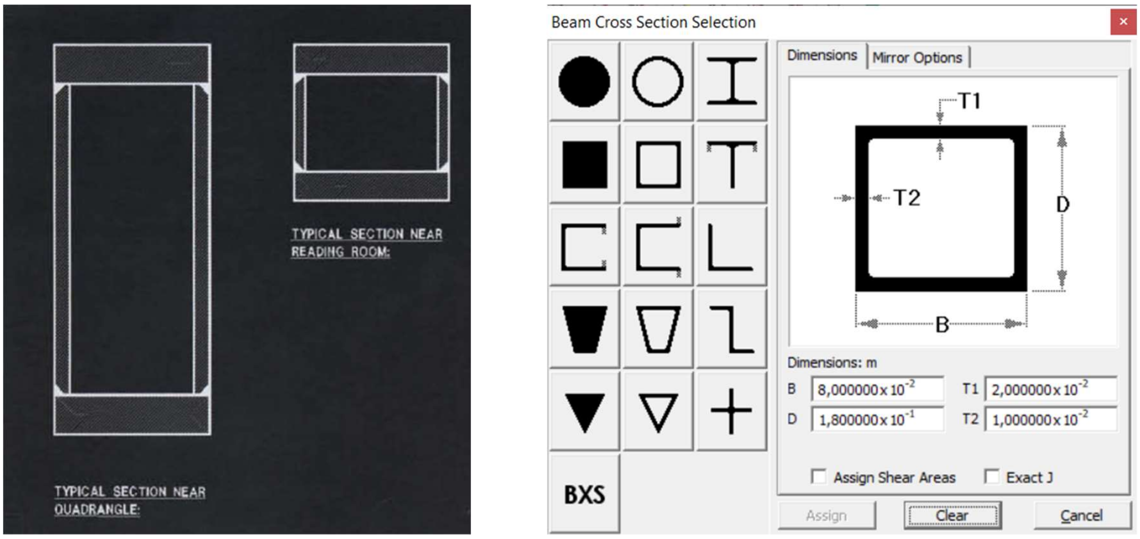

Dimensions: m

B $8{,}000000 \times 10^{-2}$

D $1{,}800000 \times 10^{-1}$

T1 $2{,}000000 \times 10^{-2}$

T2 $1{,}000000 \times 10^{-2}$

☐ Assign Shear Areas ☐ Exact J

Figure 6.27 - Cross-section of the members

To simplify, the cross-section has been held the same for all the truss elements.
In addition, every glass plate has been added manually in order to consider their self-weight (Figure 6.28). The panels have been considered with a thickness $t = 10$ cm and a density $\rho = 2500$ kg/m^3. They will not give any structural contribution.

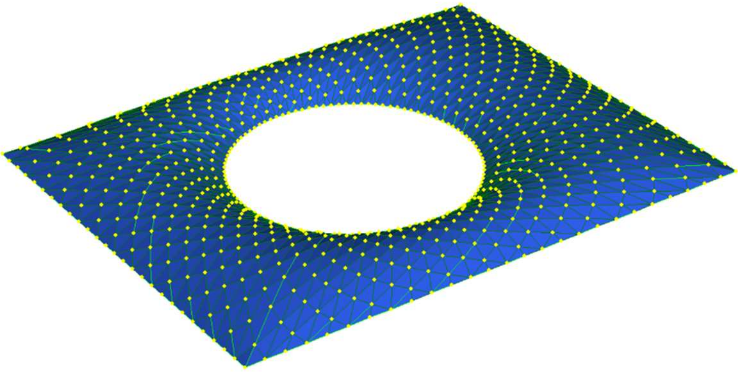

Figure 6.28 - Grid with glazed panels

After that, all the boundary conditions have been applied to all perimeter nodes (Figure 6.29). Each restraint has been considered like a fixed hinge.

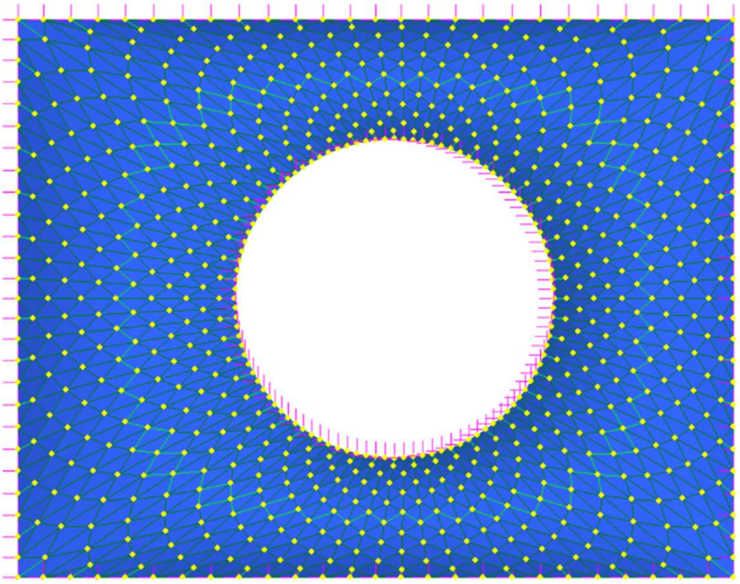

Figure 6.29 - Applied boundary conditions

Then, snow and variable loads have been applied on the structure. In accordance with EC1 Annex C, they are equal to 0.294 kN/m^2 and 0.4 kN/m^2 respectively.

The loads have been combined according with the Ultimate Limit State combination proposed in EC0:

$$\sum_{j\geq 1}\gamma_{G,j}G_{k,j}"+"\gamma_{Q,1}Q_{k,1}"+"\sum_{j>1}\gamma_{Q,i}\psi_{0,1}Q_{k,i}$$

Where:

- $G_{k,j}$ are the permanent loads;
- $Q_{k,1}$ is the principal variable load;
- $Q_{k,i}$ are the secondary variable loads;
- $\gamma_{G,j}$ is the partial factor for permanent loads, in this case taken equal to 1.35;
- $\gamma_{Q,i}$ is the partial factor for variable loads, in this case taken equal to 1.50;
- $\psi_{0,1}$ is the partial factor that takes into account the interaction of different variable loads, for roofs equal to 0.

Finally, a “Static Linear Analysis” has been performed to obtain the internal actions of the gridshell structure, the results are shown below:

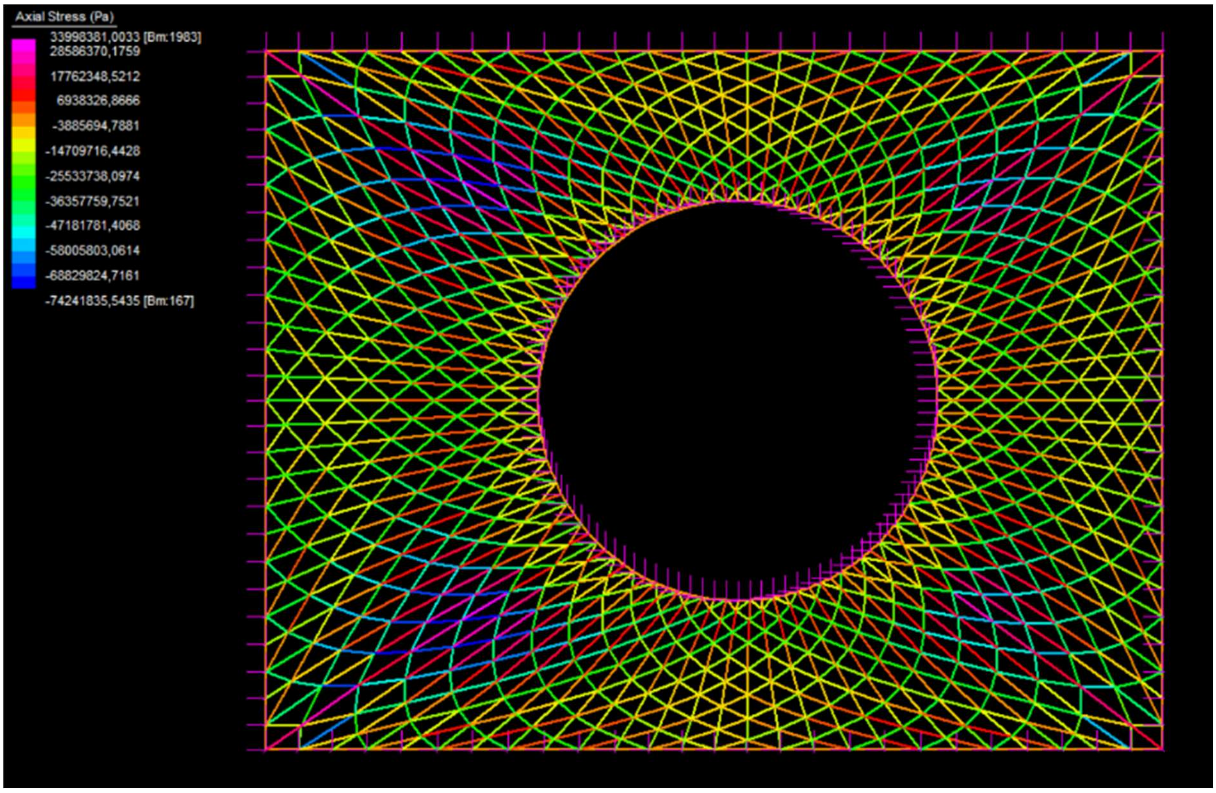

Figure 6.30 - Stresses in each member

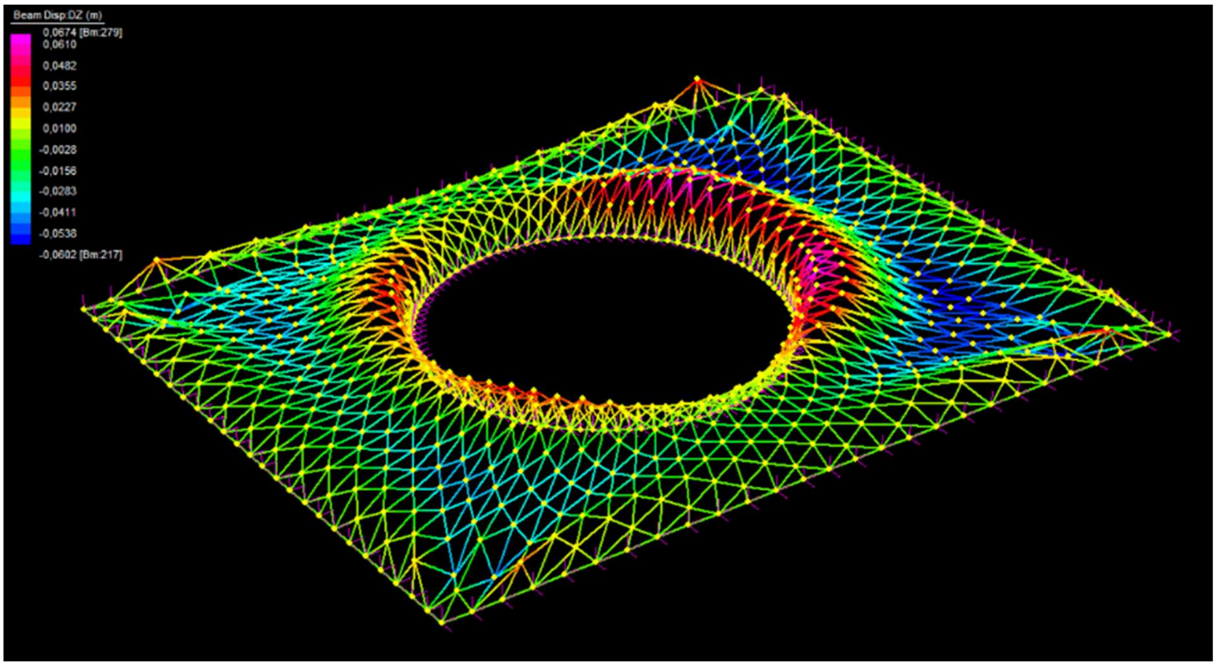

Figure 6.31 - Deformation of the gridshell

The plates have been hidden to allow better visualization.

6.5 Node chosen for Topology Optimization

The objective of this thesis is to realize a topology optimization of a gridshell joint. Therefore, the chosen node is highlighted below:

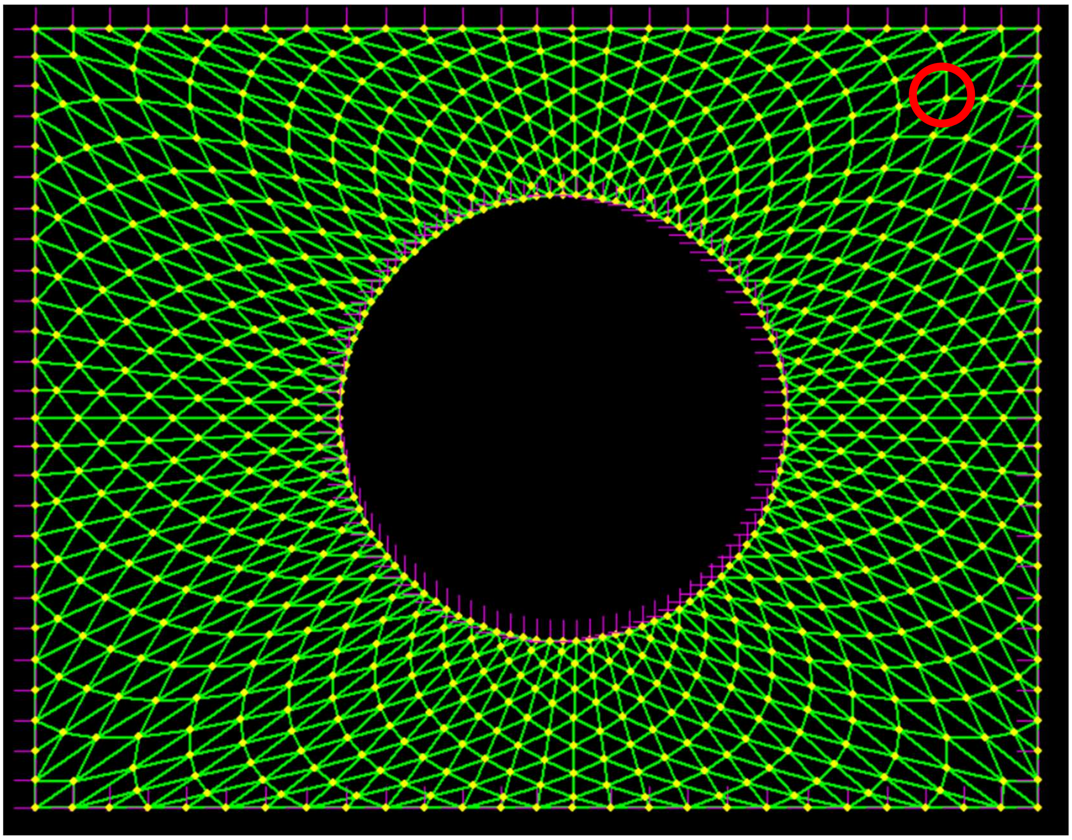

Figure 6.32 - Position of the chosen joint in the gridshell

This node has been chosen because it is placed in a critical zone of the gridshell, where the maximum stresses and strains are present.

Therefore, from Straus7 it is possible to get the actions of the trusses connected to this joint, as shown in the table below:

Truss Element	Stress (MPa)
01	33.15
02	−64.44
03	−58.42
04	22.34
05	−54.58
06	−81.82

Table 6.1 - Stresses acting on the joint

The number of the truss is indicated in the figure below:

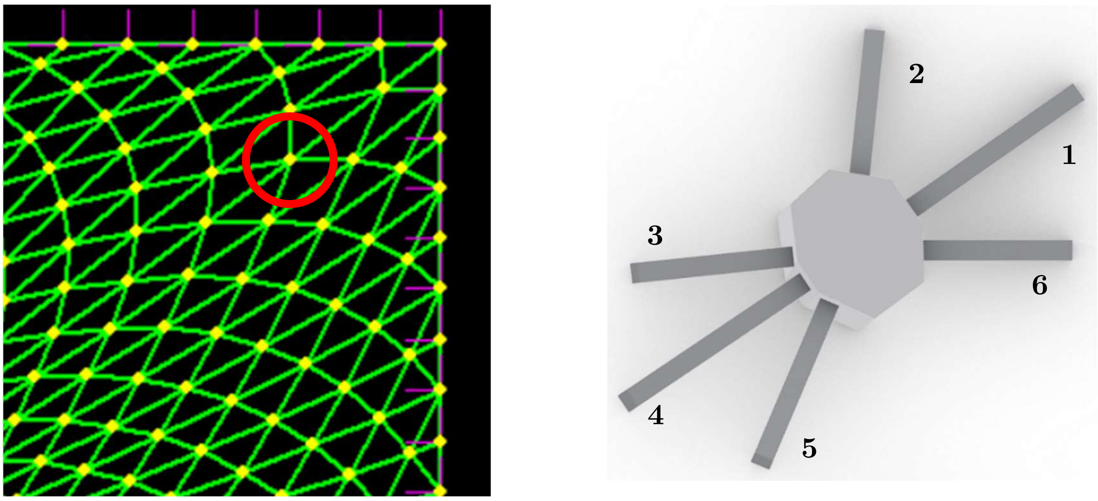

Figure 6.33 - Position of the joint (left) and numeration of the truss elements (right)

6.6 Topology optimization of the case study

Once that the joint of the British Museum has been chosen to be optimized, the initial domain, loads, boundary conditions and constraints of this structural node have to be defined to perform the topology optimization using the methods described in Chapter 4.

6.6.1 Definition of the initial domain

The joint initial domain for the optimization analysis has been created considering two main aspects:

- The distance between the faces and the centre of the connection is equal to 25 cm;
- The faces of the initial domain are orthogonal to the truss elements.

Following these initial aspects, the domain has been created using Rhino7 and the result is shown below:

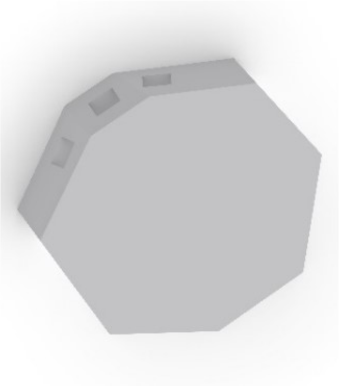

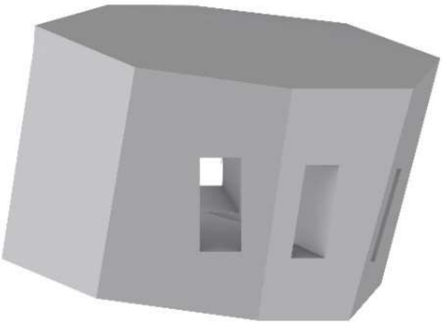

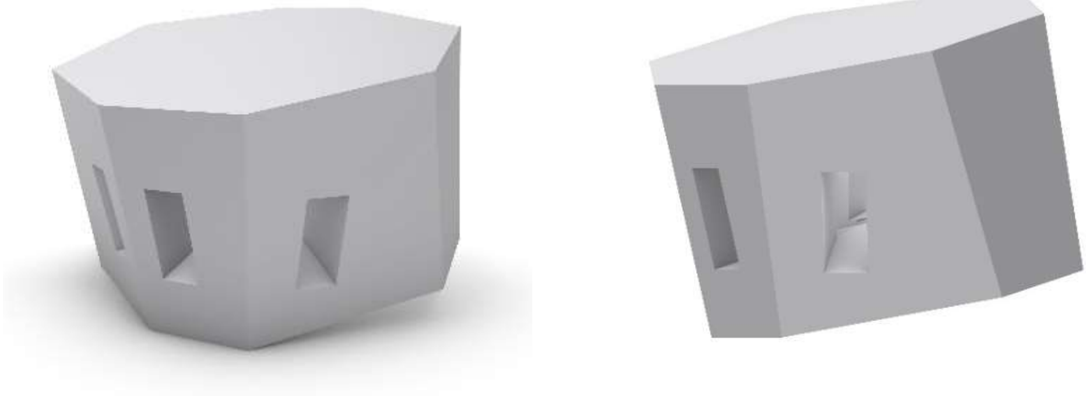

Figure 6.34 - Initial domain for the topology optimization

Considering also the presence of the beams:

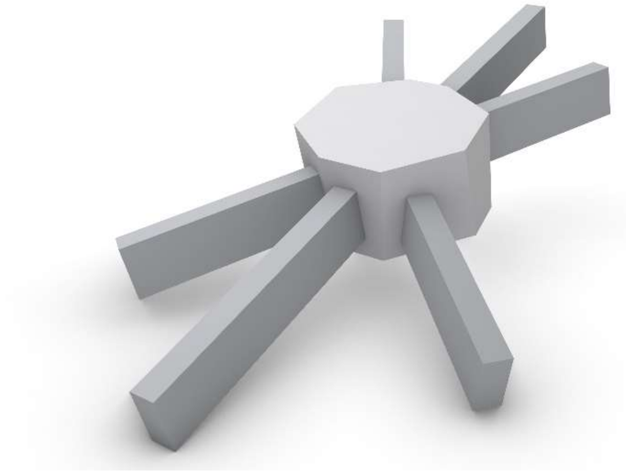

Figure 6.35 - Initial domain including the truss elements

6.6.2 Definition of loads and boundary conditions

Once that the initial domain has been created, it is needed to set loads and boundary conditions. Boundary conditions have been applied on only one profile, which is considered clamped. As a consequence, the load of the profile restrained must be redistributed on the other trusses. Loads have been applied considering the stresses obtained from Straus7, as shown in the previous paragraph.
Three different profiles have been restrained in three different situations and loads have been redistributed as shown in the following figures:

- Beam 01 restrained: the load of the beam 01 has been redistributed to the beam 04;

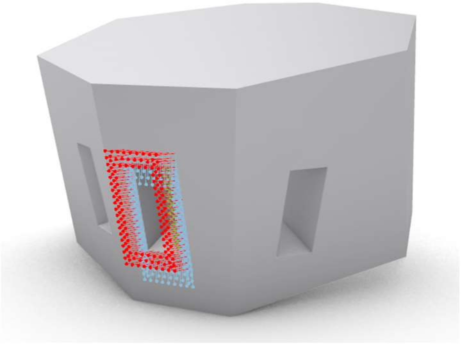

Figure 6.36 - Initial domain considering Beam01 restrained

- Beam 02 restrained: the load of the beam 02 has been redistributed among the other profiles;

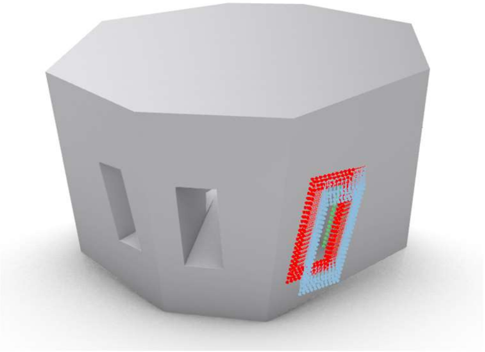

Figure 6.37 - Initial domain withe Beam02 restrained

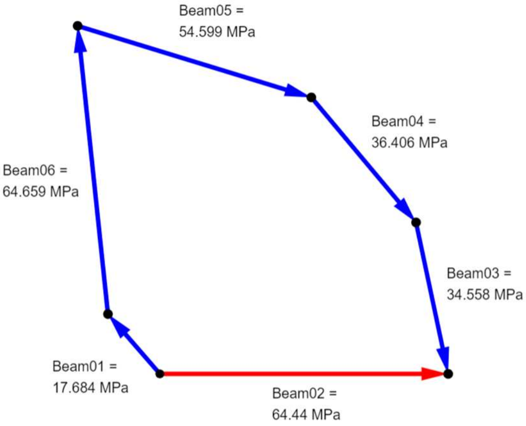

Figure 6.38 - Stress redistribution

- Beam 06 restrained: the load of the beam 06 has been redistributed among the other profiles.

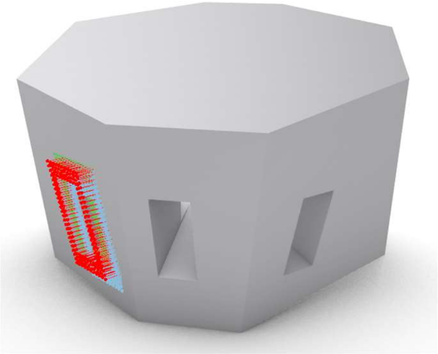

Figure 6.39 - Initial domain with Beam06 restrained

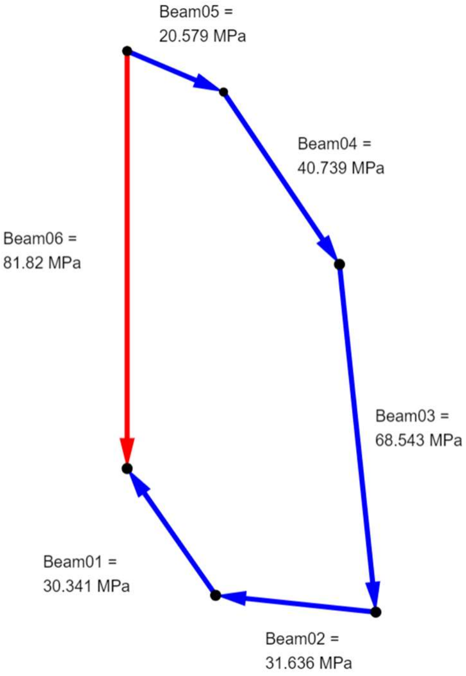

Figure 6.40 - Stress redistribution

6.6.3 Definition of the non-domain elements

In order to connect properly the beams to the joint, it is mandatory to select some regions that will not be optimized. Therefore, in correspondence of the six profiles and internally to the initial domain, some additional elements with a length of 5 and 10 cm have been created and excluded from the topology optimization analysis.

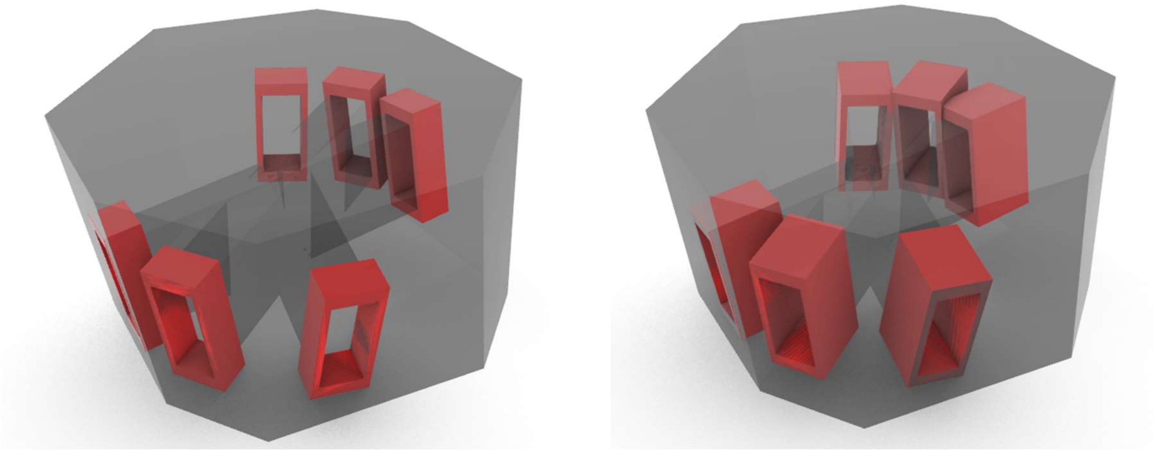

Figure 6.41 - Non-domain regions: 5 cm (left) and 10 cm (right) long

6.7 Resulting topologies

6.7.1 First attempt

In this first attempt the topology optimization analysis has been performed using the following general parameters:

Beam restrained	01
Volume Target	25 %
Evolutionary Ratio *ER* (only with BESO)	1 %
Maximum number of iterations	200

Table 6.2 - Features of the first topology optimization analysis

6.7.1.1 First attempt with BESO method

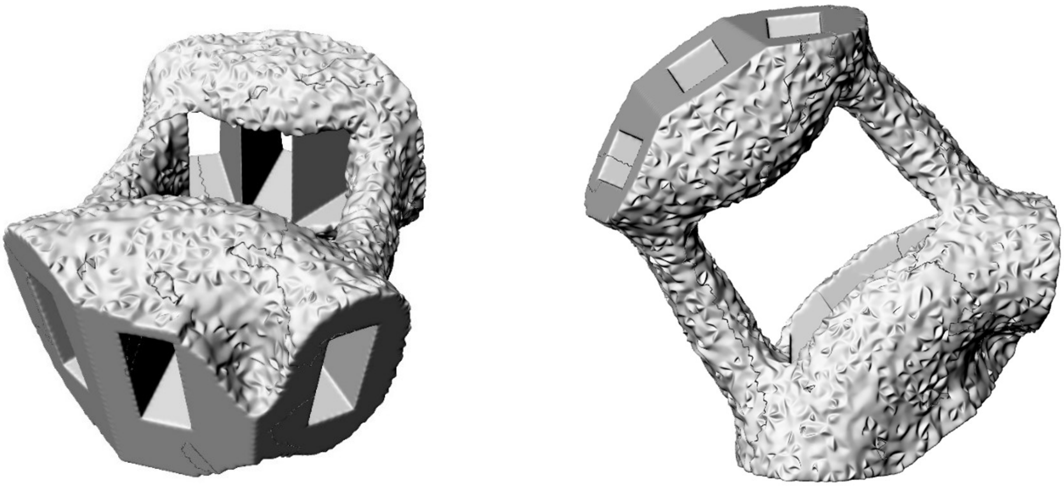

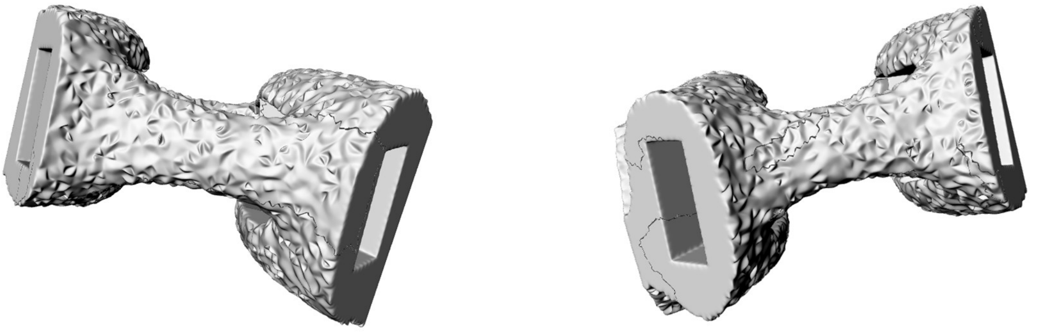

Figure 6.42 - First attempt: topology optimization of the joint using Ameba

6.7.1.2 First attempt with SIMP method

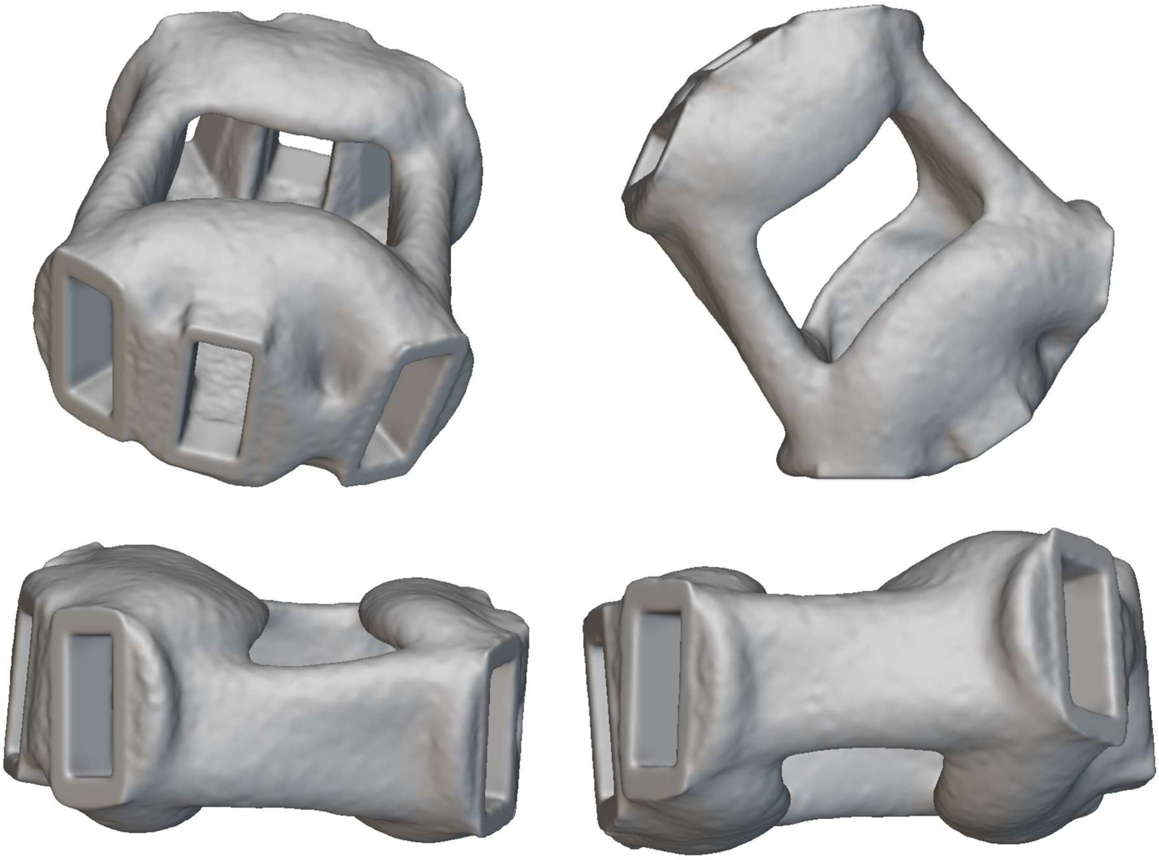

Figure 6.43 - First attempt: topology optimization of the joint using nTopology

6.7.2 Second attempt

In this second attempt the topology optimization analysis has been performed using the following general parameters:

Beam restrained	01
Volume Target	20 %
Evolutionary Ratio *ER* (only with BESO)	2 %
Maximum number of iterations	200

Table 6.3 - Features of the second topology optimization analysis

6.7.2.1 Second attempt with BESO method

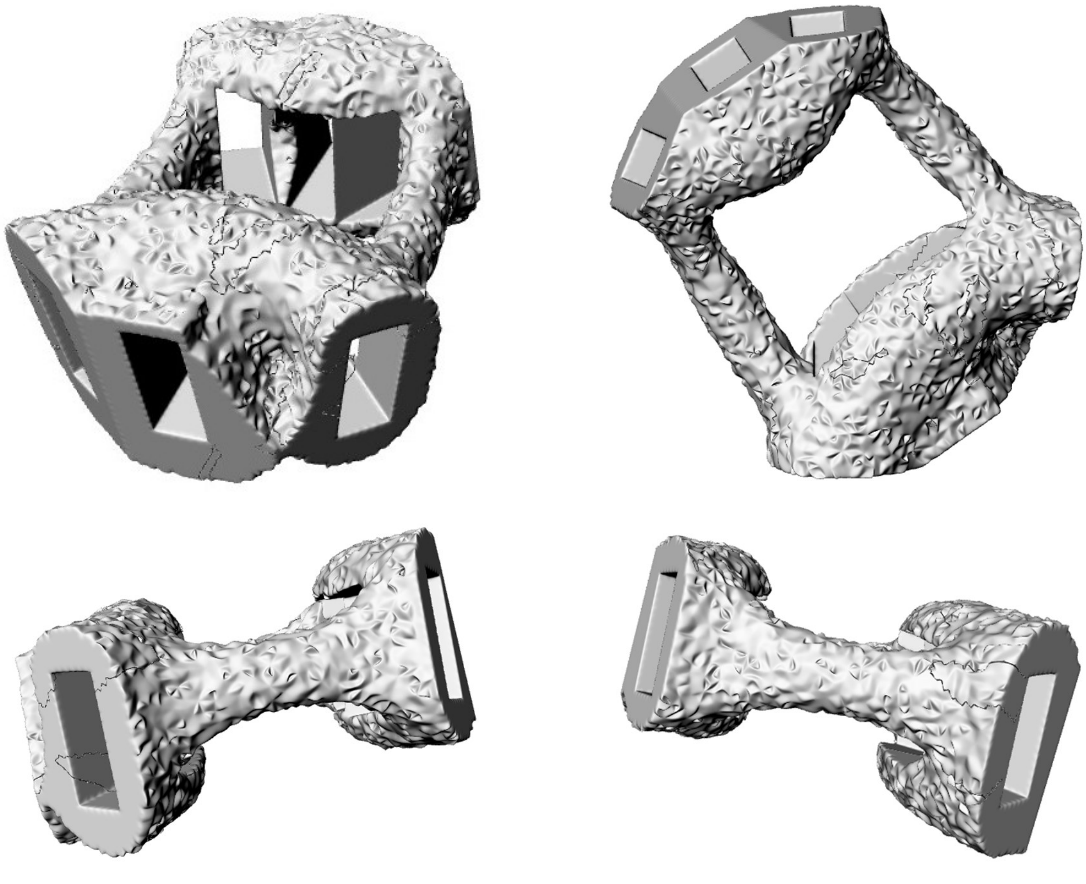

Figure 6.44 - Second attempt: topology optimization of the joint using Ameba

6.7.2.2 Second attempt with SIMP method

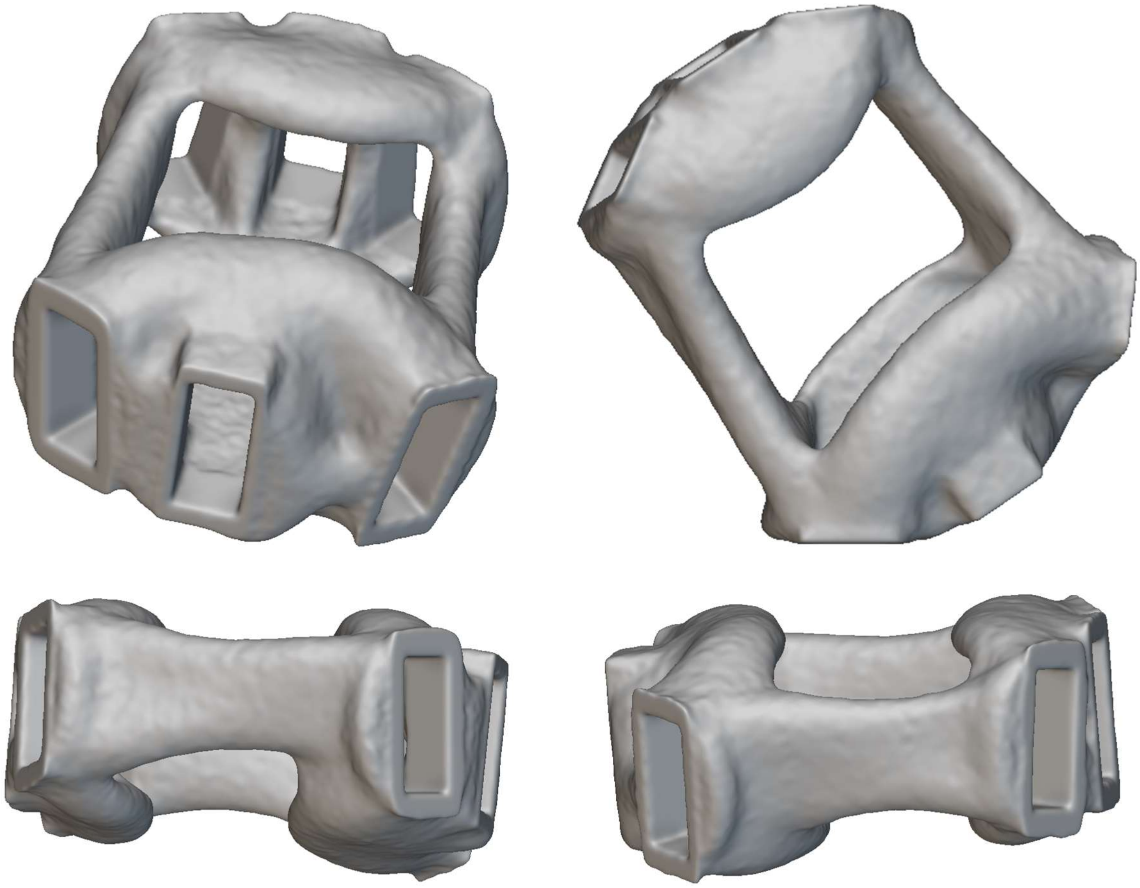

Figure 6.45 - Second attempt: topology optimization of the joint using nTopology

6.7.3 Third attempt

In this third attempt the topology optimization analysis has been performed using the following general parameters:

Beam restrained	01
Volume Target	30 %
Evolutionary Ratio *ER* (only with BESO)	2 %
Maximum number of iterations	200

Table 6.4 - Features of the third topology optimization analysis

6.7.3.1 Third attempt with BESO method

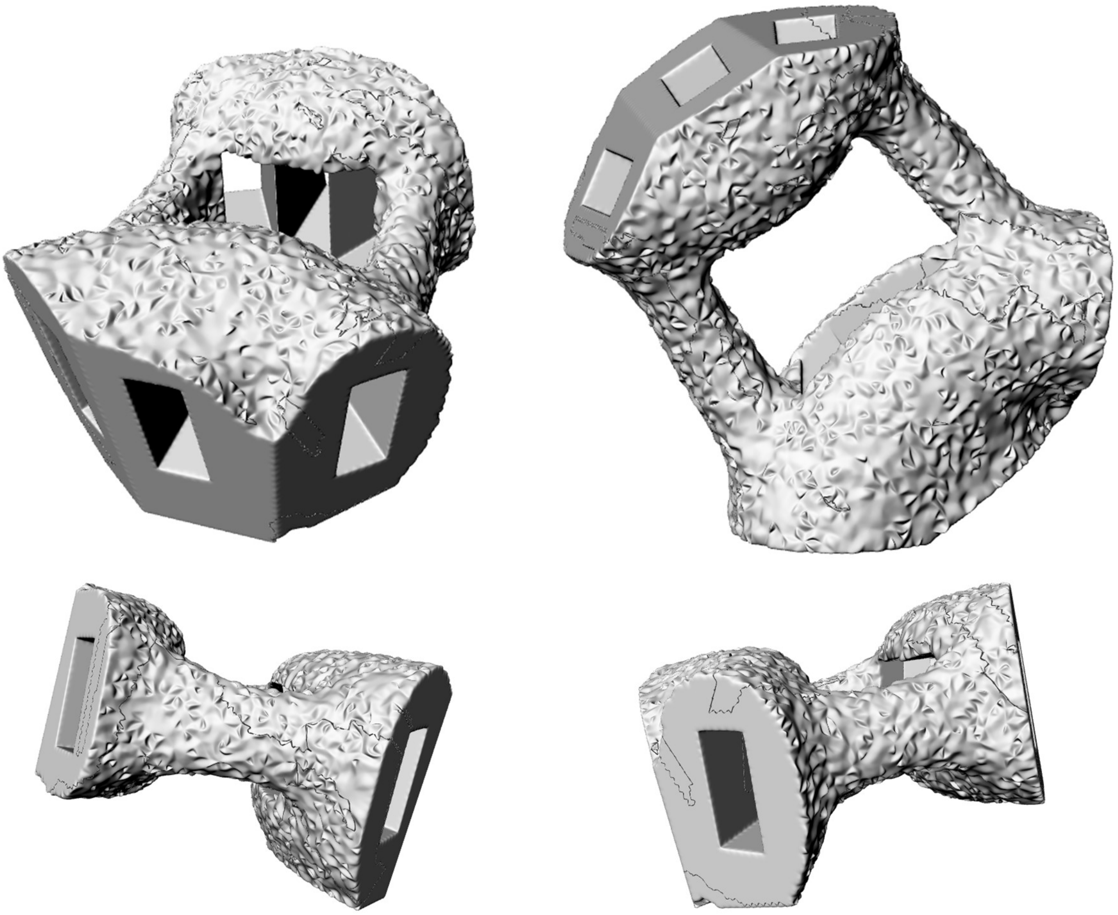

Figure 6.46 - Third attempt: topology optimization of the joint using Ameba

6.7.3.2 Third attempt with SIMP method

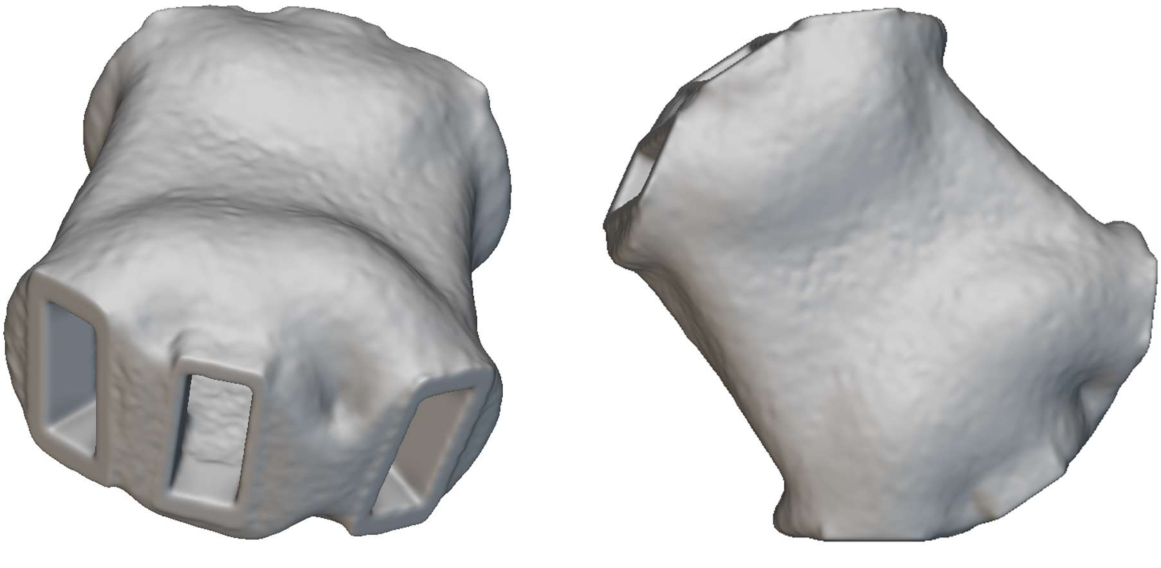

Figure 6.47 - Third attempt: topology optimization of the joint using nTopology

6.7.4 Fourth attempt

In this fourth attempt the topology optimization analysis has been performed using the following general parameters:

Beam restrained	06
Volume Target	20 %
Evolutionary Ratio ER(only with BESO)	2 %
Maximum number of iterations	200

Table 6.5 - Features of the fourth topology optimization analysis

6.7.4.1 Fourth attempt with BESO method

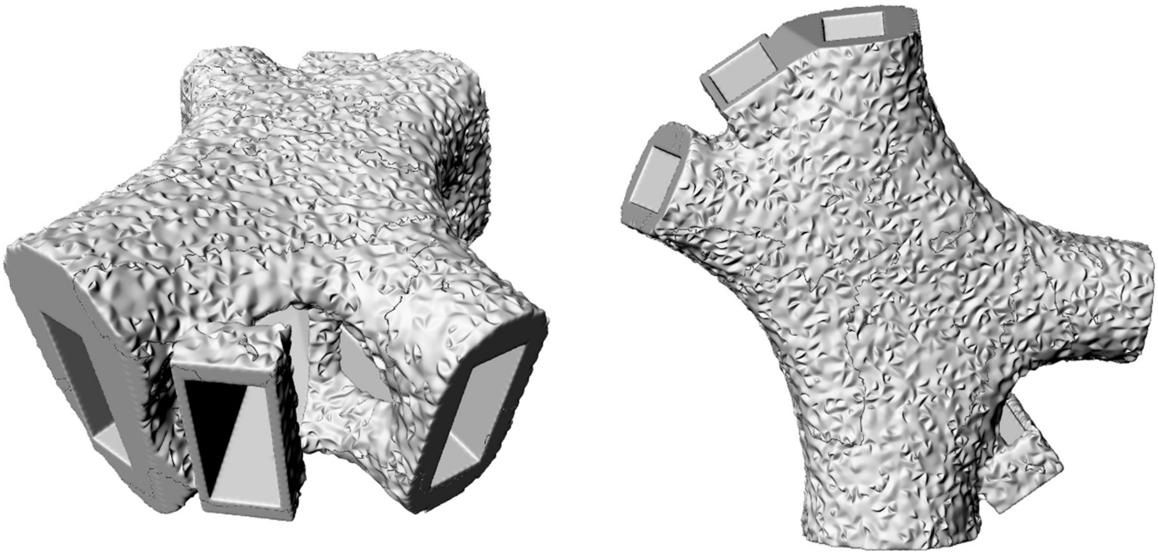

Figure 6.48 - Fourth attempt: topology optimization of the joint using Ameba

6.7.4.2 Fourth attempt with SIMP method

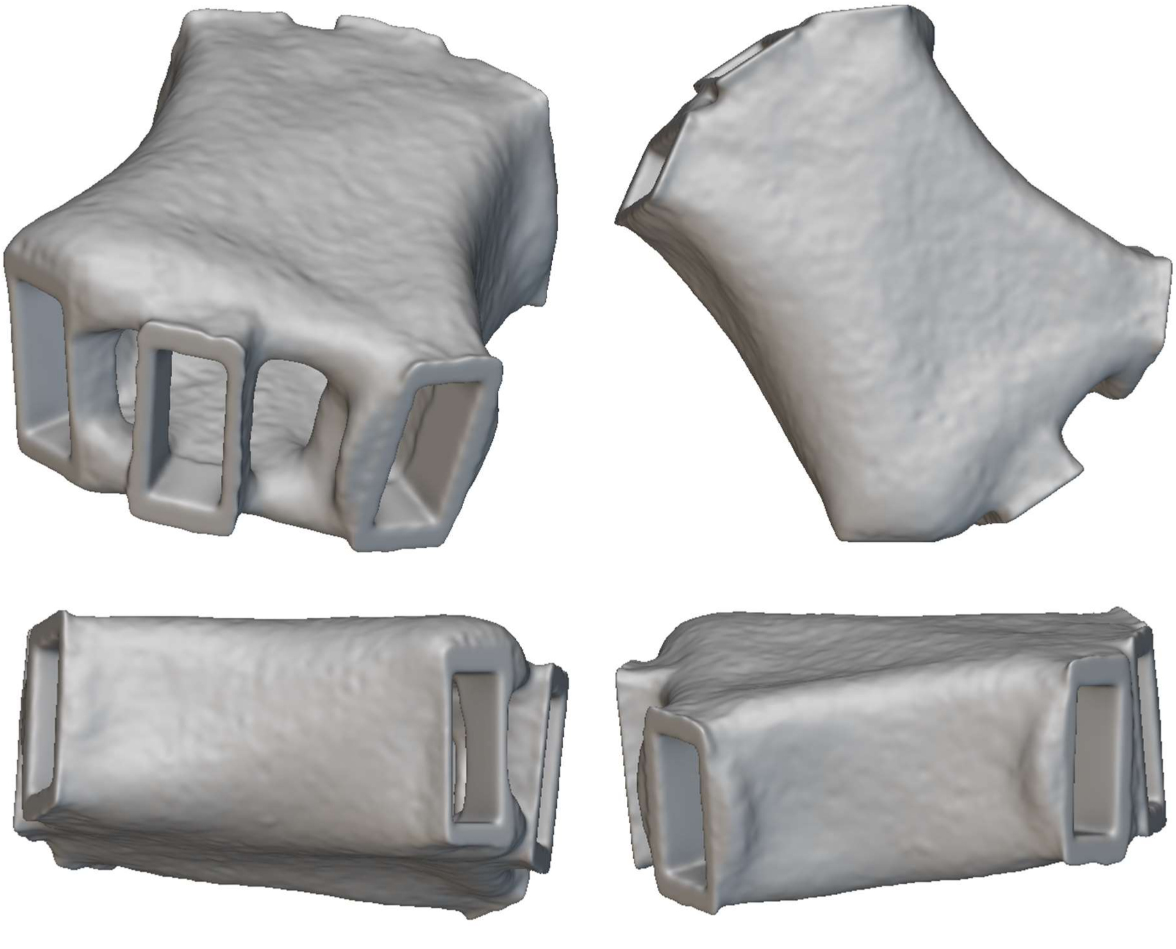

Figure 6.49 - Fourth attempt: topology optimization of the joint using nTopology

6.7.5 Fifth attempt

In this fifth attempt the topology optimization analysis has been performed using the following general parameters:

Beam restrained	06
Volume Target	15 %
Evolutionary Ratio ER(only with BESO)	2 %
Maximum number of iterations	200

Table 6.6 - Features of the fifth topology optimization analysis

6.7.5.1 Fifth attempt with BESO method

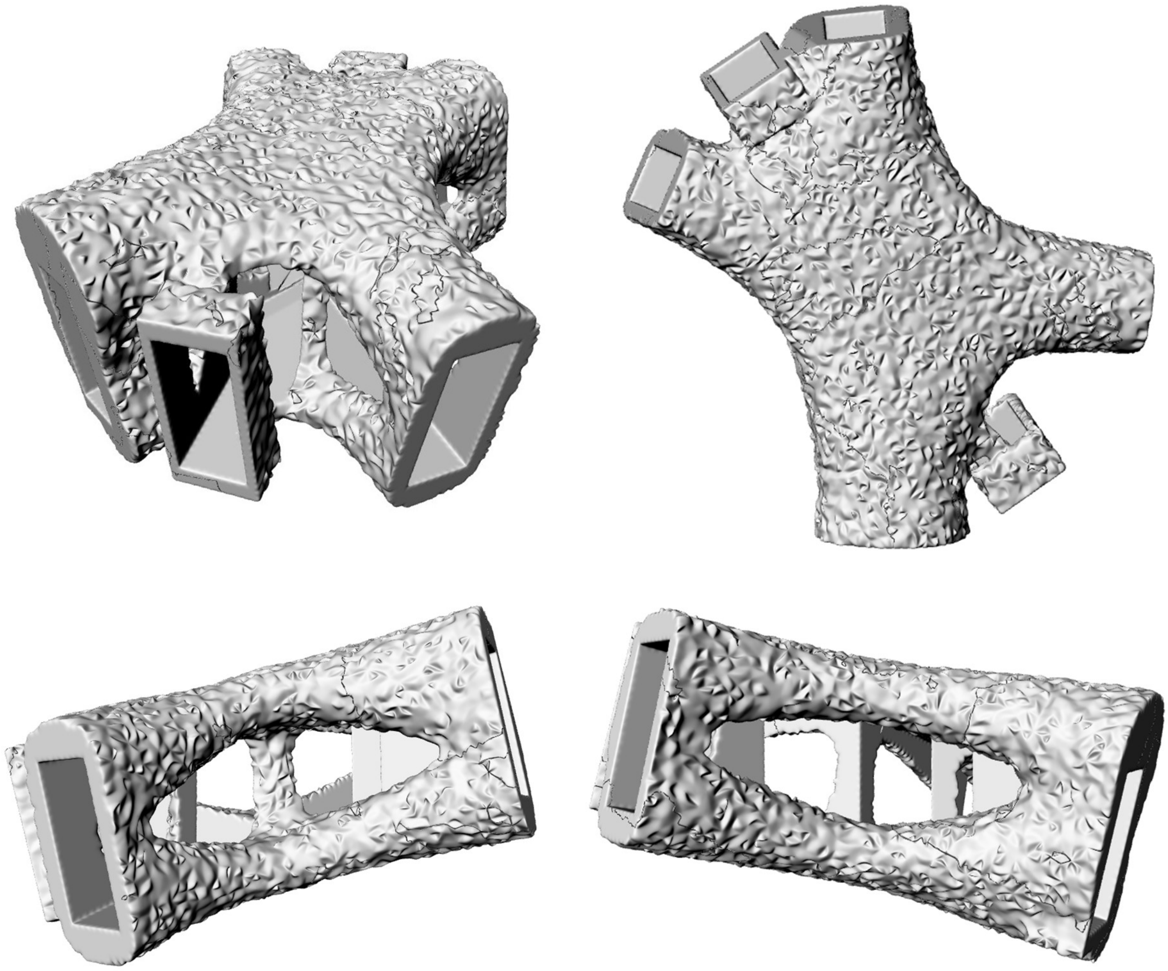

Figure 6.50 - Fifth attempt: topology optimization of the joint using Ameba

6.7.5.2 Fifth attempt with SIMP method

Figure 6.51 - Fifth attempt: topology optimization of the joint using nTopology

6.7.6 Sixth attempt

In this sixth attempt the topology optimization analysis has been performed using the following general parameters:

Beam restrained	02
Volume Target	20 %
Evolutionary Ratio ER (only with BESO)	2 %
Maximum number of iterations	200

Table 6.7 - Features of the sixth topology optimization analysis

6.7.6.1 Sixth attempt with BESO method

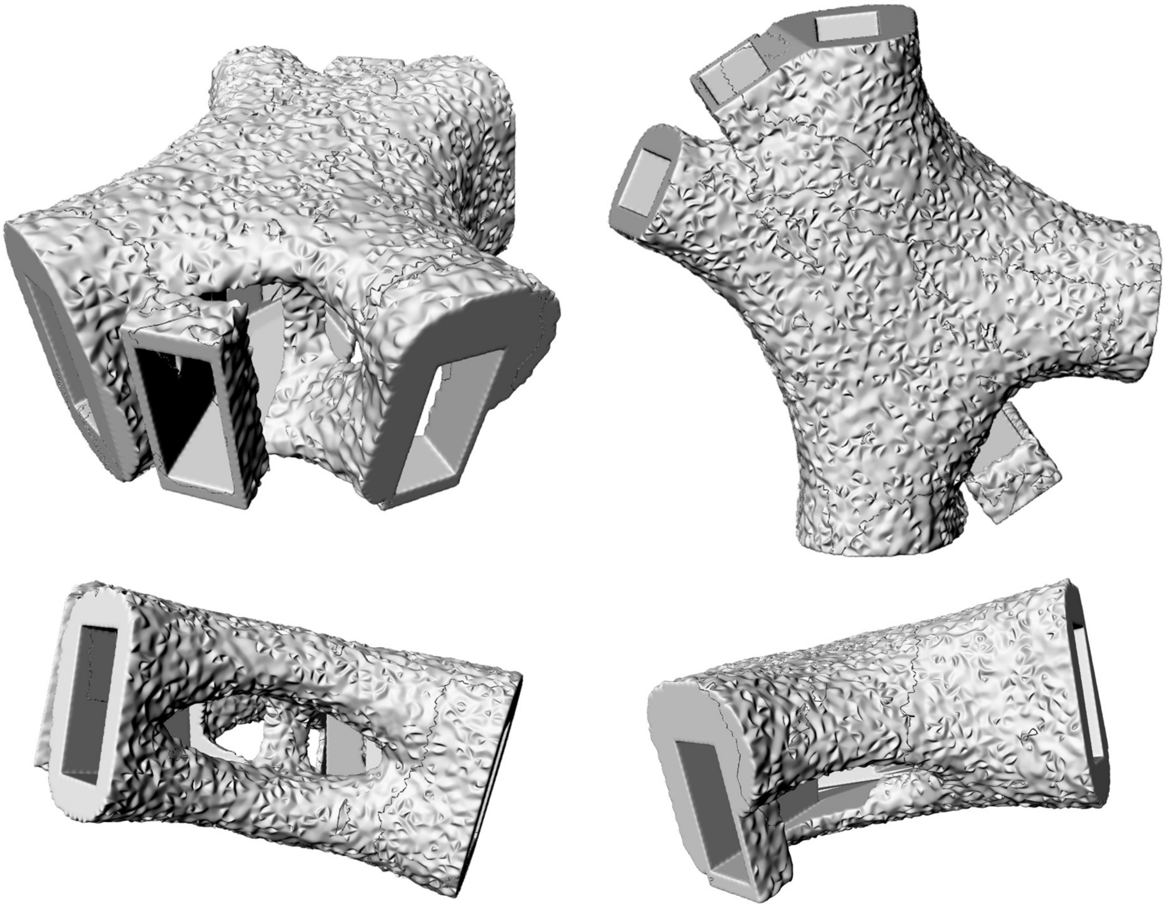

Figure 6.52 - Sixth attempt: topology optimization of the joint using Ameba

6.7.6.2 Sixth attempt with SIMP method

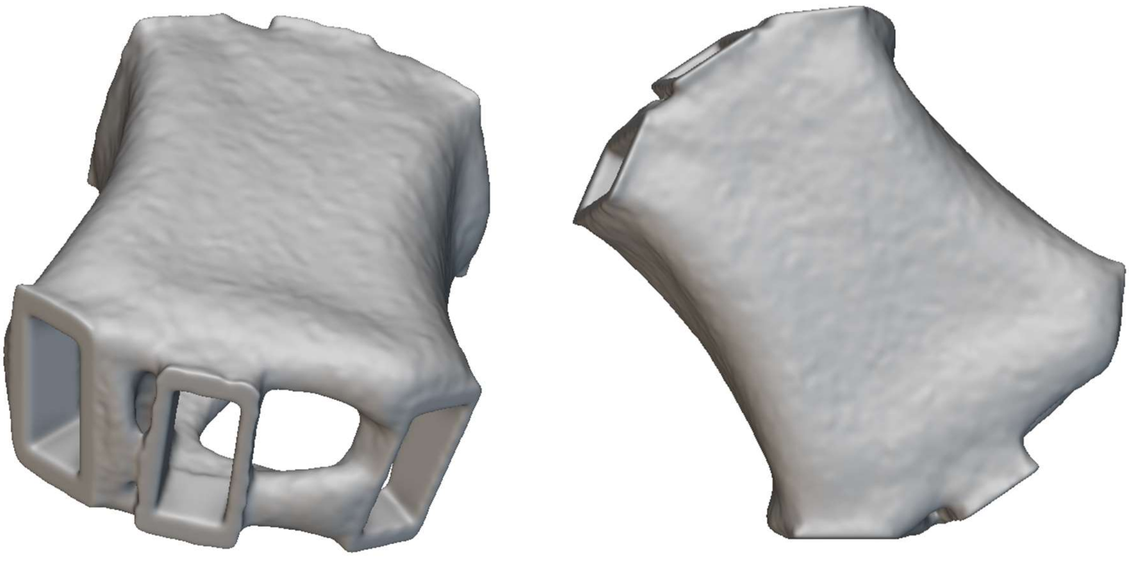

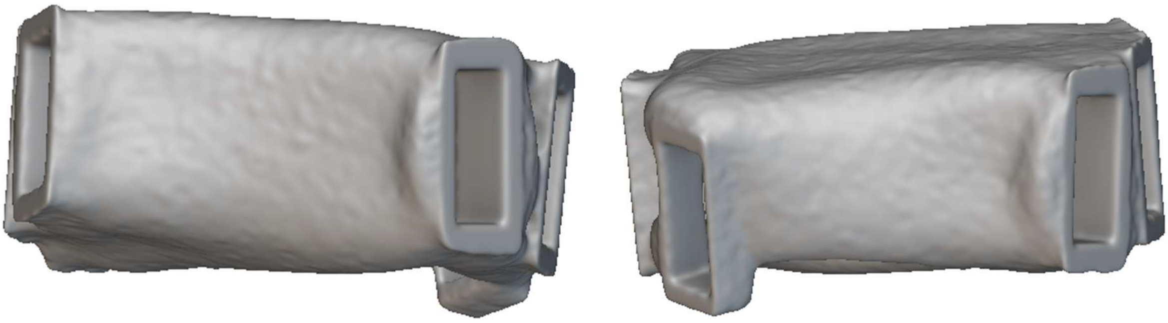

Figure 6.53 - Sixth attempt: topology optimization of the joint using nTopology

6.7.7 Seventh attempt

In this seventh attempt the topology optimization analysis has been performed using the following general parameters, but differently from the fifth attempt, the length of the non-domain zones has been imposed to be equal to 10 cm:

Beam restrained	06
Volume Target	15 %
Evolutionary Ratio *ER* (only with BESO)	2 %
Maximum number of iterations	200

Table 6.8 - Features of the seventh topology optimization analysis

6.7.7.1 Seventh attempt with BESO method

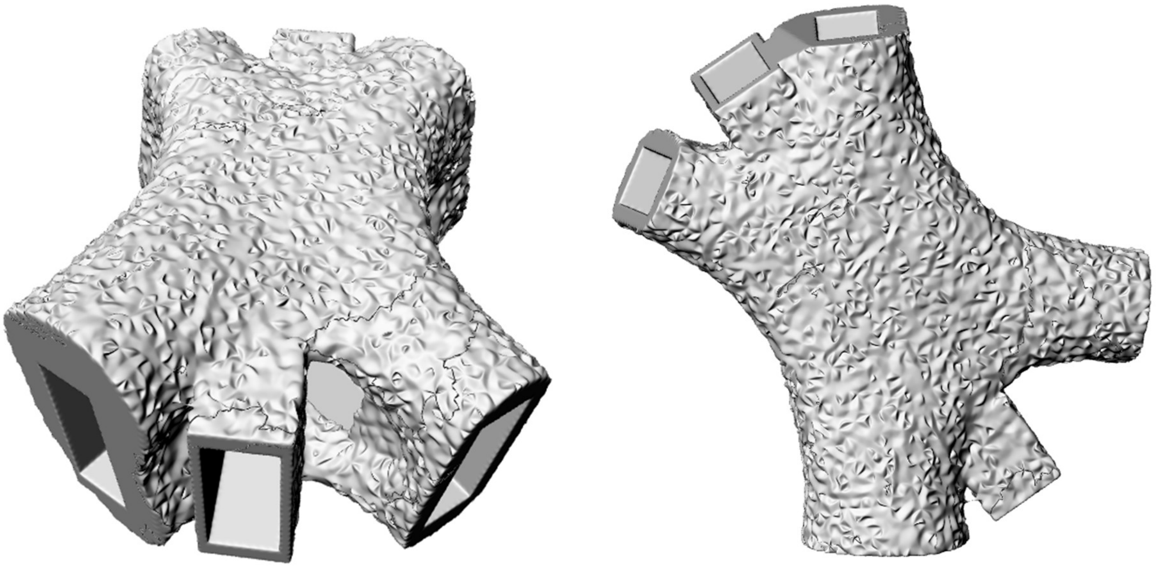

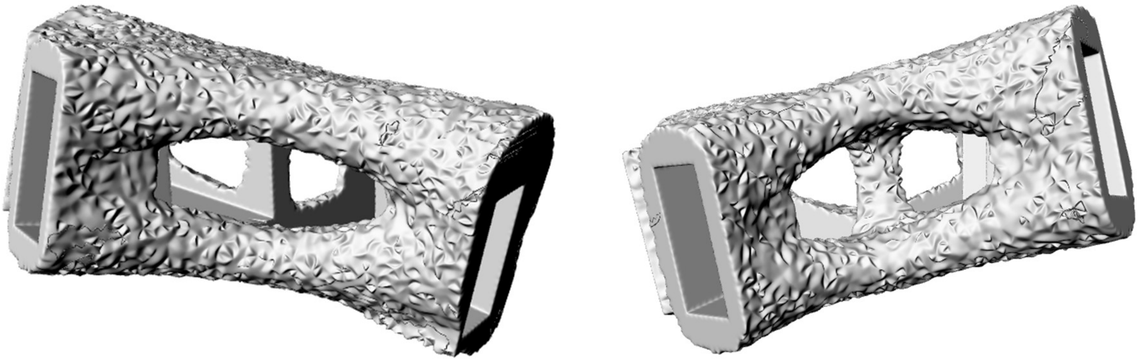

Figure 6.54 - Seventh attempt: topology optimization of the joint using Ameba

6.7.7.2 Seventh attempt with SIMP method

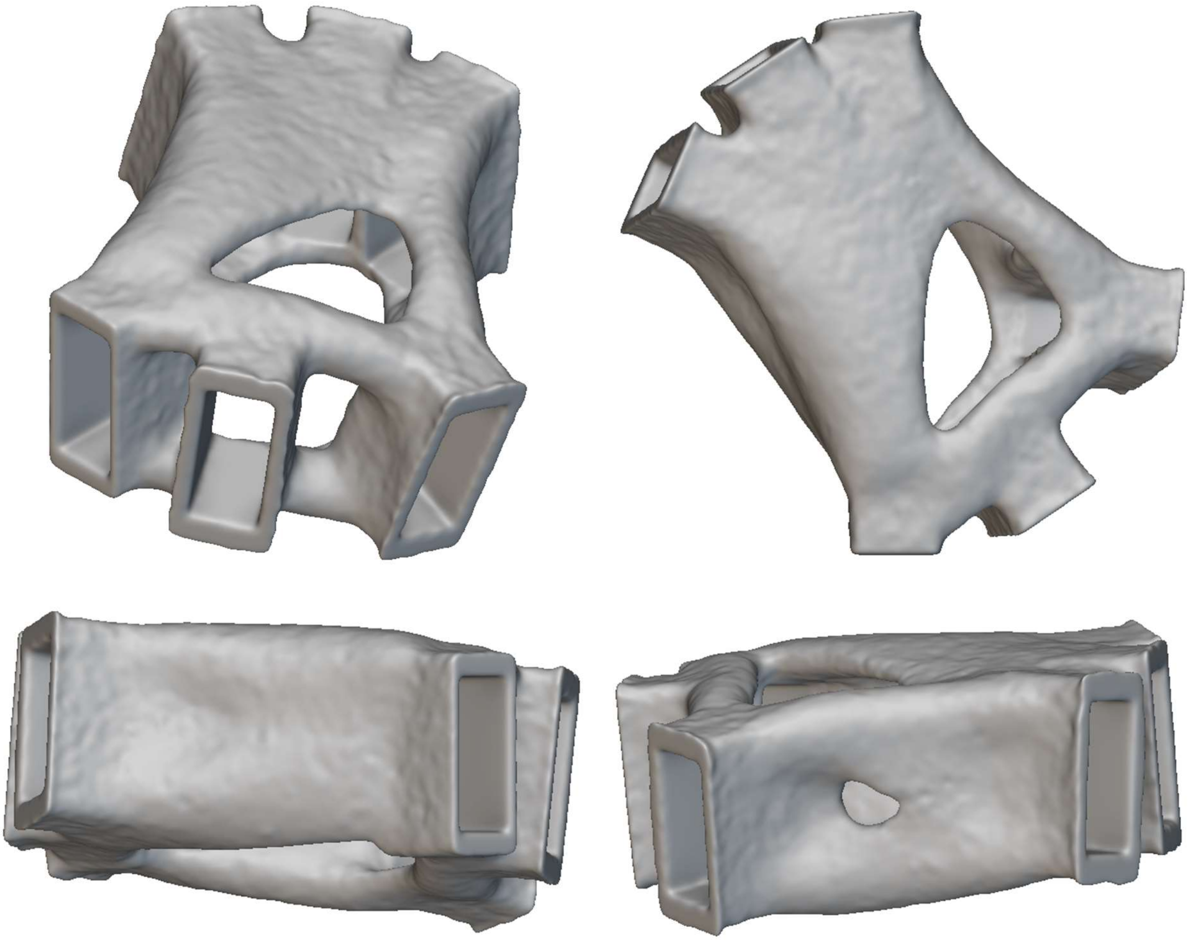

Figure 6.55 - Seventh attempt: topology optimization of the joint using nTopology

6.8 Discussion of the results

From the previous computations, it is possible to observe that the two topology optimization methods work really differently, as demonstrated by the obtained geometries. These differences are particularly relevant in attempts 4, 5, 6 and 7, and are due to the chosen optimization paramters.

Only one topology optimization must be chosen among the results previously obtained. The chosen solution must satisfy the following geometrical requirements:

- The holes must be distributed inside the final geometry of the joint;
- The holes in correspondence of the beams do not have to present any type of additional opening;
- The remaining material must be distributed almost uniformly.

Based on these requirements the best solution to be manufactured using Wire and Arc Additive Manufacturing is the seventh attempt obtained through Ameba. However, this solution is initially too rough to be studied and printed, therefore some modifications are required and they have been performed in Rhino7.

The changes have been done using “Smooth” and “QuadRemesh” tools:

Figure 6.56 - Initial joint geometry (top-left), smooth joint (top-right) and final joint geometry (bottom)

Hence, the joint geometry shown in Figure 6.56 is the one that will be studied in the following chapters.

In addition, the joint will not be printed like a solid element, in order to save material and hence save also time and costs. Therefore, it is necessary to assign a certain thickness to this element. This has been done using a plug-in for Grasshopper called “Weaverbird” and its component “Weaverbird’s Mesh Thicken”:

Figure 6.57 - Weaverbird's Mesh Thicken component

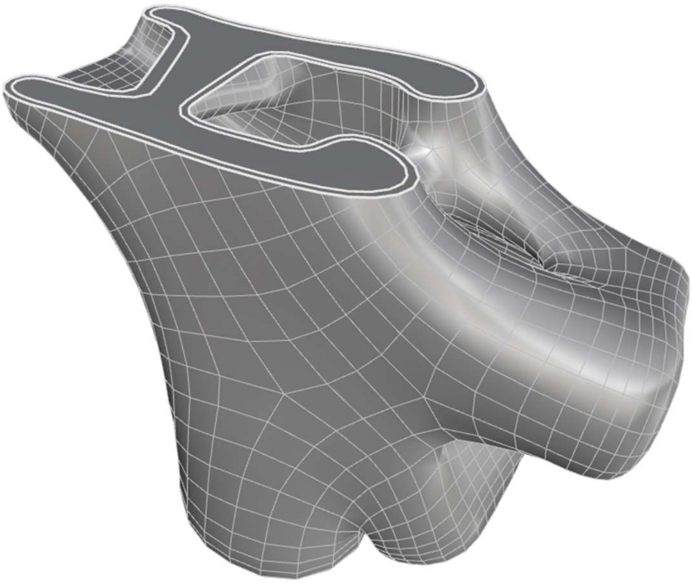

Figure 6.58 - Joint thickness

CHAPTER 7

MECHANICAL CHARACTERIZATION OF THE OPTIMIZED JOINT

7.1 Joint classification for the real case study

The computation mentioned in Chapter 5 is valid only for the initial simple structure but, the case study of this thesis is the gridshell structure of the British Museum in London.
In order to study the behaviour of the considered node, it is necessary to follow these steps:

- Evaluation of the limits of α to classify the node stiffness;
- Evaluation of the limits of β to classify the node strength;
- FEA of the node to obtain the moment-rotation graph in each direction.

It is necessary to introduce a new coefficient λ that is the ratio of the critical load of the lattice shell with flexible joints $P_{cr,}$ to that of the rigidly jointed shell $P_{cr,rigid}$:

$$\lambda = \frac{P_{cr,\alpha}}{P_{cr,rigid}}$$

The criteria to choose the boundaries for α and β are:

- If the ratio λ is greater than or equal to 90%, the joint will be considered rigid;
- If the ratio λ is smaller than or equal to 30%, the joint will be considered pinned;
- If the ratio λ is between 30% and 90%, the joint will be considered semi-rigid.

7.1.1 Boundaries computation of the stiffness coefficient $\boldsymbol{\alpha}$

The software Strand7 is employed to compute rapidly the critical load of the structure. The critical load for the stiffness classification is computed considering the following values of α: Rigid, 100, 20, 15, 10, 5, 2, 1.5, 1, 0.5, 0.2, 0.1, 0.05, 0.01, Pinned.

The profiles used in this structure are rectangular hollow cross-sections with the following properties:

- $B = 80$ mm;
- $H = 180$ mm;
- $t_1 = 20$ mm;
- $t_2 = 10$ mm;
- $A = 6000$ mm^2;
- $I_{11} = 25160000$ mm^4;
- $I_{22} = 5160000$ mm^4;
- $J_T = 1290000$ mm^4;
- $S_{11} = 279556$ mm^3;
- $S_{22} = 129000$ mm^3;

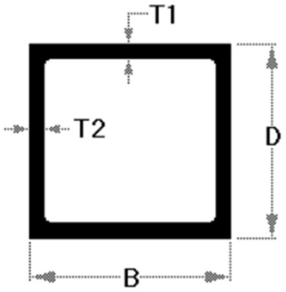

Figure 7.1 - Cross-section dimensions

Therefore, the stiffnesses of the beams in their principal directions are:

$$R_{11} = \frac{EI_{11}}{L} = \frac{2 * 10^{11} * 2.516 * 10^{-5}}{3.42} = 1471345.029 \text{ N/m}$$

$$R_{22} = \frac{EI_{22}}{L} = \frac{2 * 10^{11} * 5.16 * 10^{-6}}{3.42} = 301754.386 \text{ N/m}$$

$$R_{33} = \frac{GJ_T}{L} = \frac{\frac{2 * 10^{11}}{2 * (1 + 0.3)} * 1.29 * 10^{-6}}{3.42} = 29014.845 \text{ N/m}$$

Where:

- E is the Young's Modulus;
- G is the Shear Modulus;

- I_{11} is the moment of inertia in the direction 1-1;
- I_{22} is the moment of inertia in the direction 2-2;
- J_T is the torsional rigidity of the cross-section;
- L is the average length of the beam in the structure.

Furthermore, the stiffness in the node is applied using the command “End Release” in “Beam Attributes” and the values used in the three directions are simply the product of the stiffnesses of the beam for the coefficient α considered. For example, for $\alpha = 0.5$:

$$k_{11} = R_{11} * 0.5 = 735672.51\ N/m$$

$$k_{22} = R_{22} * 0.5 = 150877.19\ N/m$$

$$k_{33} = R_{33} * 0.5 = 14507.42\ N/m$$

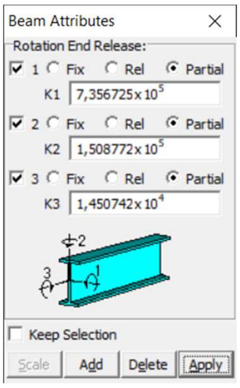

Beam Attributes

Rotation End Release:

☑ 1 ○ Fix ○ Rel ● Partial

K1 7,356725x10^5

☑ 2 ○ Fix ○ Rel ● Partial

K2 1,508772x10^5

☑ 3 ○ Fix ○ Rel ● Partial

K3 1,450742x10^4

☐ Keep Selection

Figure 7.2 - "Beam attribute" command

Before starting the analysis, it is needed to define the nonlinearity of material and section, therefore the stress-strain diagram and the moment-curvature diagram are set in Strand7. The material and cross-section behaviours are considered perfectly elasto-plastic. Then, the limit moment and curvature are computed with the following formulas:

$$M_{pl,plane_1} = f_{yk} * W_{pl} = f_{yk} * \frac{I}{z} = 355 * 10^6 * \frac{5.16 * 10^{-6}}{0.04} = 45795 \text{ Nm}$$

$$\chi_{pl,plane_1} = \frac{M_{pl}}{EI} = \frac{45795}{2 * 10^{11} * 5.16 * 10^{-6}} = 0.044375\ \frac{1}{\text{m}}$$

$$M_{pl,plane_2} = f_{yk} * W_{pl} = f_{yk} * \frac{I}{z} = 355 * 10^6 * \frac{2.516 * 10^{-5}}{0.09} = 99242 \text{ Nm}$$

$$\chi_{pl,plane_2} = \frac{M_{pl}}{EI} = \frac{99242}{2 * 10^{11} * 2.516 * 10^{-5}} = 0.01972\ \frac{1}{\text{m}}$$

The diagrams are reported below:

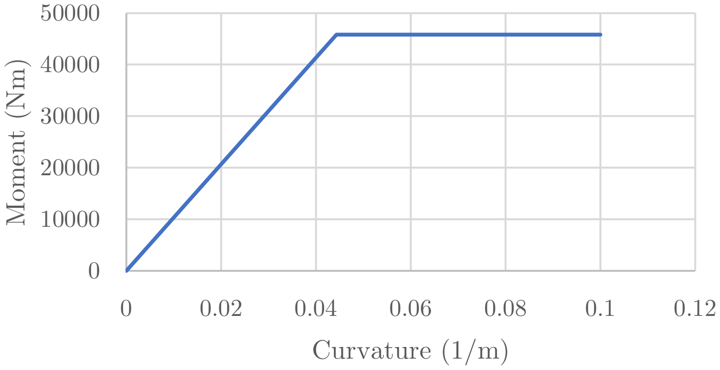

Figure 7.3 - Moment-curvature graph in plane 1

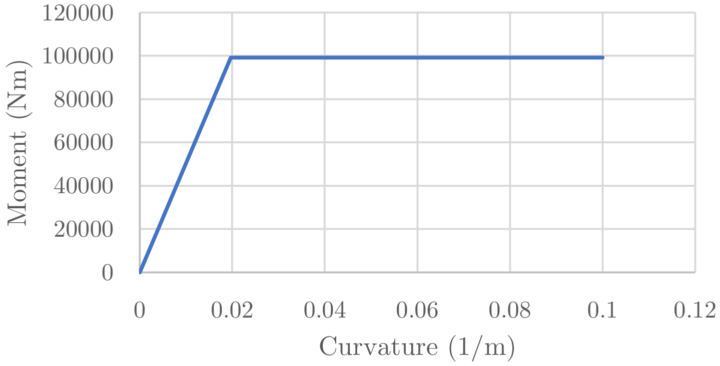

Figure 7.4 - Moment-curvature graph in plane 2

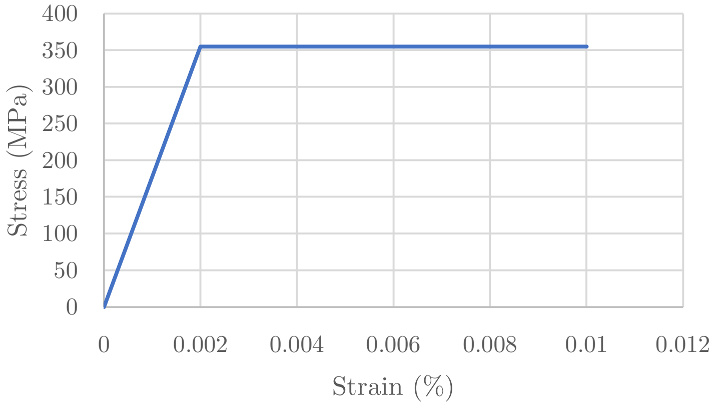

Figure 7.5 - Stress-strain graph

After that these diagrams have been assigned to the beams, it is possible to run a nonlinear analysis. From this analysis, the last increment factor that multiplies the load is extracted and this step is the critical load of the structure. This procedure is repeated for different values of α.

Lastly, the formula of λ has been applied and the results are shown in the table and the graph below:

Computation of λ for different values of α

α	K_{11} (Nm)	K_{22} (Nm)	K_{33} (Nm)	Load Increment	λ
Pinned	0,00	0,00	0,00	0,18	0,06
0, 01	14713,45	3017,54	2687,07	0,18	0,06
0, 05	73567,25	15087,72	13435,34	0,18	0,06
0, 1	147134,50	30175,44	26870,67	0,19	0,06
0, 2	294269,01	60350,88	53741,34	0,35	0,11
0, 5	735672,51	150877,19	134353,35	0,53	0,17
1	1471345,03	301754,39	268706,70	0,60	0,20
1, 5	2207017,54	452631,58	403060,05	1,05	0,34
2	2942690,06	603508,77	537413,41	1,23	0,40
5	7356725,15	1508771,93	1343533,51	2,08	0,67
10	14713450,29	3017543,86	2687067,03	2,55	0,83
15	22070175,44	4526315,79	4030600,54	2,75	0,90
20	29426900,58	6035087,72	5374134,05	2,86	0,93
100	147134502,92	30175438,60	26870670,27	3,03	0,98
Rigid	∞	∞	∞	3,08	1,00

Table 7.1 - Computation of λ for different values of α

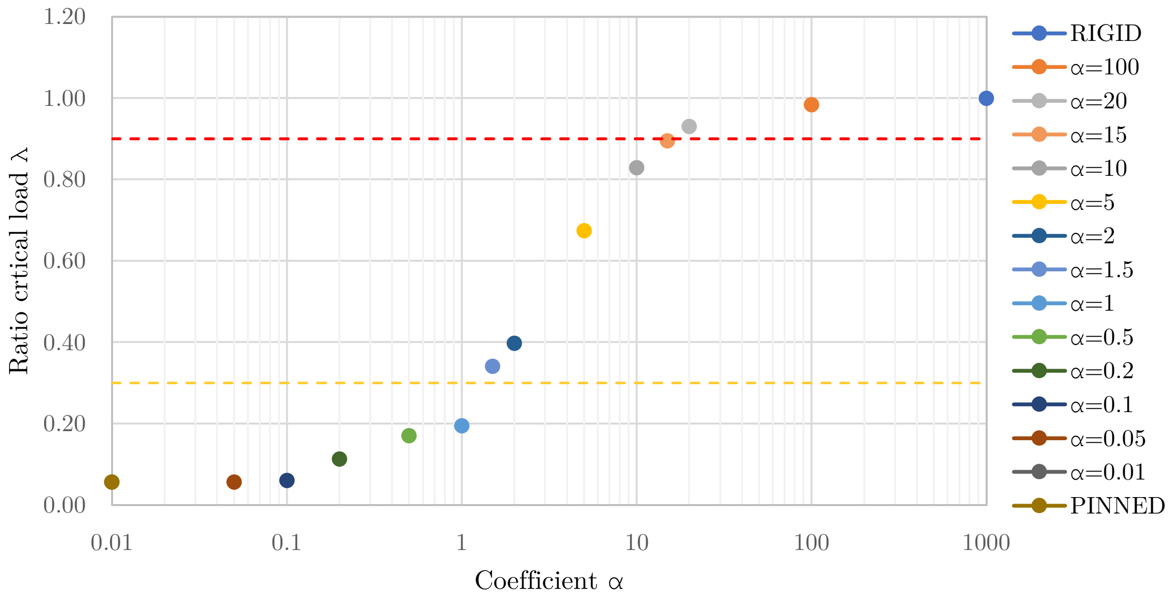

Figure 7.6 - Critical load ratio λ of lattice shells with different coefficients α

Hence, it is possible to find the following boundaries for α:

- Rigid joints: $\alpha \geq 15$;
- Semi-rigid joints: $1.5 < \alpha < 15$;
- Pinned joints: $\alpha \leq 1.5$.

7.1.2 Boundaries computation of the strength coefficient β

To evaluate the coefficient β the procedure is slightly different because it is necessary to consider the nonlinearity of the material. Moreover, an initial value of α is used to compute the critical load with different values of β. In this specific case α is taken equal to 20, in order to ensure the joints rigidity.

Then, in order to consider different values of β, it is necessary to scale down the values of the above moment-curvature diagram with these formulas:

$$M_{pl,\beta} = \beta * M_{pl}$$
$$\chi_{pl,\beta} = \beta * \chi_{pl}$$

Lastly, applying the formula of λ, it is possible to define a graph for different values of β. λ has been computed for these values of β: Rigid, 1, 0.8, 0.5, 0.4, 0.3, 0.2, 0.1, 0.08, 0.05, 0.02, 0.01.

The results are reported in the following table and graph:

Computation of λ for different values of β with an initial α

β	α	$M_{pl,plane_1}$(Nm)	$\chi_{pl,plane_1}$(1/m)	$M_{pl,plane_2}$(Nm)	$\chi_{pl,plane_2}$(1/m)	*Load Increment*	λ
0,01	20	457,95	0,000444	992,42	0,000197	0,15	0,05
0,02	20	915,90	0,000888	1984,84	0,000394	0,30	0,11
0,05	20	2289,75	0,002219	4962,11	0,000986	0,65	0,23
0,08	20	3663,60	0,003550	7939,38	0,001578	1,01	0,36
0,1	20	4579,50	0,004438	9924,22	0,001972	1,19	0,42
0,2	20	9159,00	0,008875	19848,45	0,003944	1,84	0,64
0,3	20	13738,50	0,013313	29772,67	0,005917	2,24	0,79
0,4	20	18318,00	0,017750	39696,90	0,007889	2,53	0,89
0,5	20	22897,50	0,022188	49621,12	0,009861	2,68	0,94
0,8	20	36636,00	0,035500	79393,79	0,015778	2,84	1,00
1	20	45795,00	0,044375	99242,24	0,019722	2,85	1,00
Rigid	20	∞	∞	∞	∞	2,85	1,00

Table 7.2 - Computation of λ for different values of β

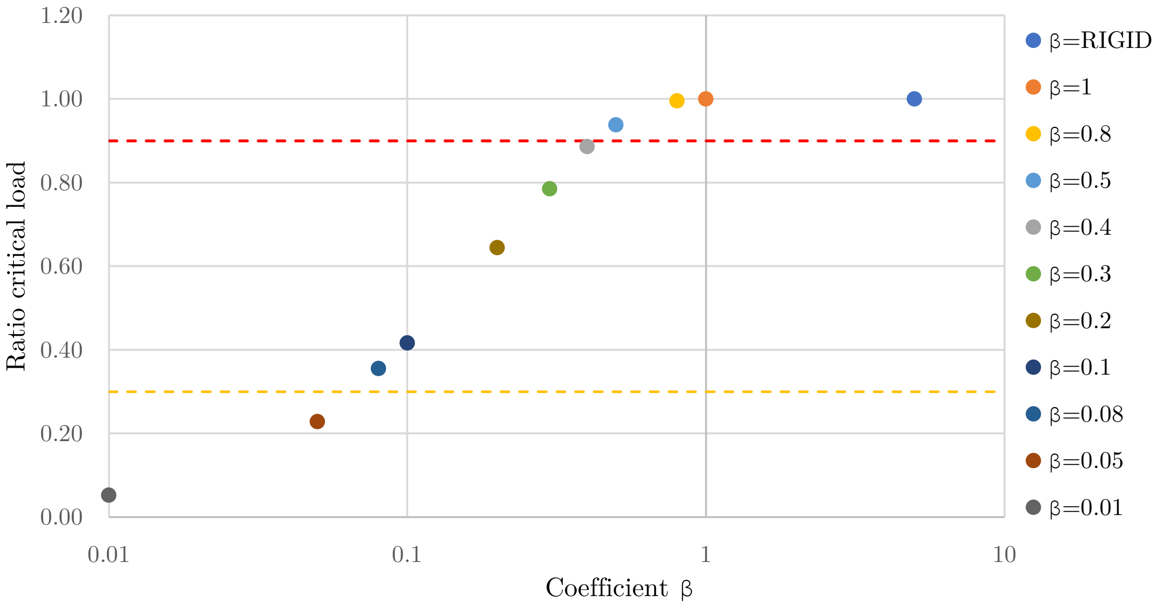

Figure 7.7 - Critical load ratio λ of lattice shells with different coefficients β

Hence, it is possible to find the following boundaries for β:

- Rigid joints: $\beta \geq 0.5$;
- Semi-rigid joints: $0.08 < \beta < 0.5$;
- Pinned joints: $\beta \leq 0.08$.

7.1.3 Combined classification of joints

Combining the results obtained for the coefficients α and β respectively for the stiffness and the moment capacity of the joints, the classification of the joint types is determined by:

- Rigid joints: $\alpha \geq 15$ and $\beta \geq 0.5$;
- Semi-rigid joints: $\alpha \geq 15$ and $0.08 < \beta < 0.5$ or $\beta \geq 0.5$ and $1.5 < \alpha < 15$;
- Pinned joints: $\alpha \leq 1.5$ or $\beta \leq 0.08$.

It is important to notice that joints with $\alpha \gg 15$ and $\beta \gg 0.5$ behave like joints with $\alpha = 15$ and $\beta = 0.5$, therefore this can be advantageous in a design phase. In fact, using $\alpha = 15$ and $\beta = 0.5$ as design parameters, it is possible to design lighter joints with a reduced quantity of material.

7.1.4 FEA and determination of the coefficients α and β for the joint considered

Now, it is possible to evaluate the behaviour of the joints with the classification defined previously. At this point a Finite Element Analysis must be performed in six different directions

(in the directions of the profiles connected) for the joint considered to obtain the moment-rotation diagrams. Abaqus software is employed to draw them.
To analyse the node an increasing moment is applied on only one rectangular hollow cross-section while all the others are restrained liked shown in the figure below:

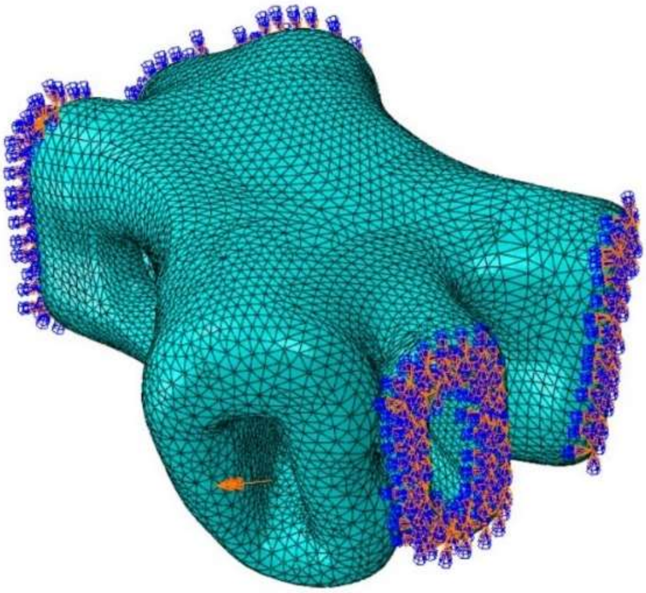

Figure 7.8 – Example of loads and boundary conditions

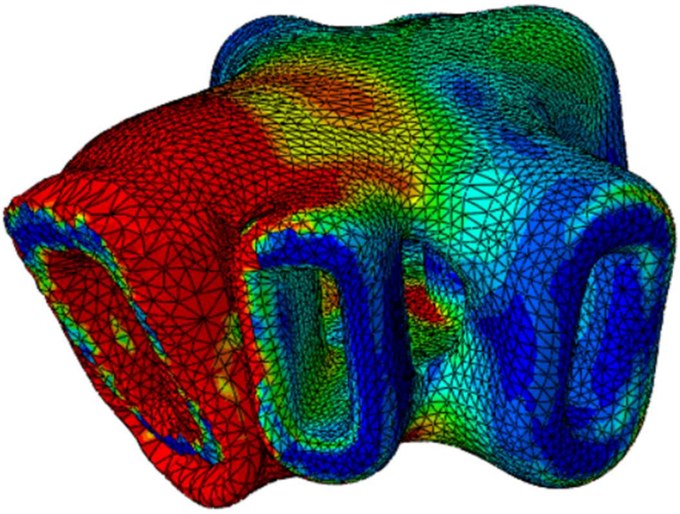

Figure 7.9 – Example of stress distribution and deformed joint

The moment-rotation diagrams for each direction are obtained from the analysis, an example is reported below:

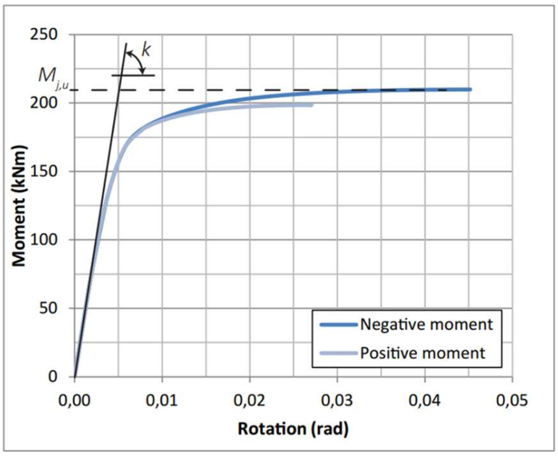

Figure 7.10 - Example of moment-rotation diagram

The node is studied as a shell with a certain thickness due to the manufacturing constraint. Moreover, the thickness of the shell element can be varied in order to ensure the requirements for a rigid joint.
From this graph, α and β are computed easily following these steps:

- The initial stiffness k of the joint along a chosen direction is calculated with this formula:

$$k = \frac{M}{\theta}$$

- The coefficient α is simply the ratio between the initial stiffness k of joint and the stiffness of the adjacent beam EI/L:

$$\alpha = \frac{k}{\frac{EI}{L}}$$

- The resisting bending moment of the joint $M_{pl,j,u}$ is obtained from the FEA and the resisting bending moment of the beam $M_{pl,e,u}$ is calculated with this expression:

$$M_{pl,e,u} = W_{pl} * f_{yk}$$

- The coefficient β is simply the ratio between the strength of the joint $M_{pl,j,}$ and the strength of the beam $M_{pl,e,}$:

$$\beta = \frac{M_{pl,j,u}}{M_{pl,e,u}}$$

Obviously, these steps must be repeated for all the profiles in each direction and considering positive and negative bending moments.

7.1.5 Joint classification

Given α and β, it is possible to classify the joint as rigid, semi-rigid or pinned and hence understand its real structural behaviour.
At the beginning the joint is studied taking into consideration a thickness of 6 mm, which will be used in printing, and the moment-rotation diagrams for moments in X-X and Y-Y directions are reported in Figure 7.11 and Figure 7.12.

Directions		k_j**(kNm/rad)**	k_b**(kNm/rad)**	$M_j(kNm)$	$M_b(kNm)$	α	β	**Verification**
01	M +	10554.57	1471.35	62.55	99.24	7.17	0.63	**Semi-Rigid**
	M −	10563.41		62.31		7.18	0.63	**Semi-Rigid**
02	M +	9529.80	1471.35	69.75	99.24	6.48	0.70	**Semi-Rigid**
	M −	9525.59		70.35		6.47	0.71	**Semi-Rigid**
03	M +	18260.29	1471.35	72.33	99.24	12.41	0.73	**Semi-Rigid**
	M −	18231.62		74.55		12.39	0.75	**Semi-Rigid**
04	M +	13520.36	1471.35	64.40	99.24	9.19	0.65	**Semi-Rigid**
	M −	13501.58		65.16		9.18	0.66	**Semi-Rigid**
05	M +	11948.27	1471.35	72.03	99.24	8.12	0.73	**Semi-Rigid**
	M −	11945.78		72.86		8.12	0.73	**Semi-Rigid**
06	M +	15453.97	1471.35	71.75	99.24	10.50	0.72	**Semi-Rigid**
	M −	15458.95		77.22		10.51	0.78	**Semi-Rigid**

Table 7.3 - Joint classification for 6 mm thickness joint and moments in X-X direction

Directions		k_j**(kNm/rad)**	k_b**(kNm/rad)**	$M_j(kNm)$	$M_b(kNm)$	α	β	**Verification**
01	M +	3138.75	301.75	29.35	45.80	10.40	0.64	**Semi-Rigid**
	M −	3125.43		28.89		10.36	0.63	**Semi-Rigid**
02	M +	4663.03	301.75	42.16	45.80	15.45	0.92	**Rigid**
	M −	4670.55		42.26		15.48	0.92	**Rigid**
03	M +	8042.21	301.75	36.66	45.80	26.65	0.80	**Rigid**
	M −	8030.16		37.15		26.61	0.81	**Rigid**
04	M +	4420.63	301.75	31.01	45.80	14.65	0.68	**Semi-Rigid**
	M −	4402.19		29.24		14.59	0.64	**Semi-Rigid**
05	M +	4136.54	301.75	37.55	45.80	13.71	0.82	**Semi-Rigid**
	M −	4127.92		37.08		13.68	0.81	**Semi-Rigid**
06	M +	6063.69	301.75	35.90	45.80	20.09	0.78	**Rigid**
	M −	6069.53		37.96		20.11	0.83	**Rigid**

Table 7.4 - Joint classification for 6 mm thickness joint and moments in Y-Y direction

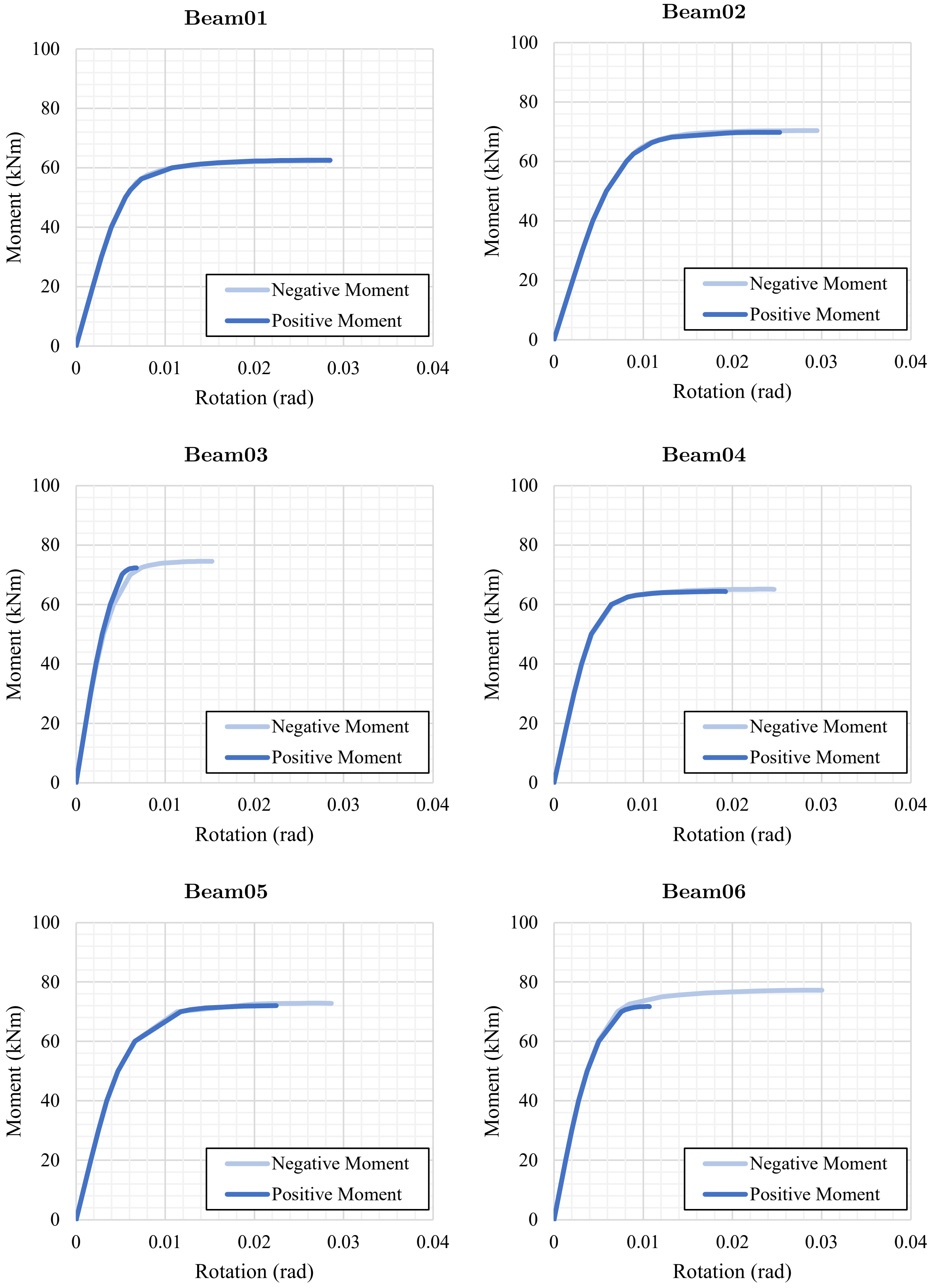

Figure 7.11 - Moment-rotation graphs considering a 6 mm thickness joint and moments in X-X direction

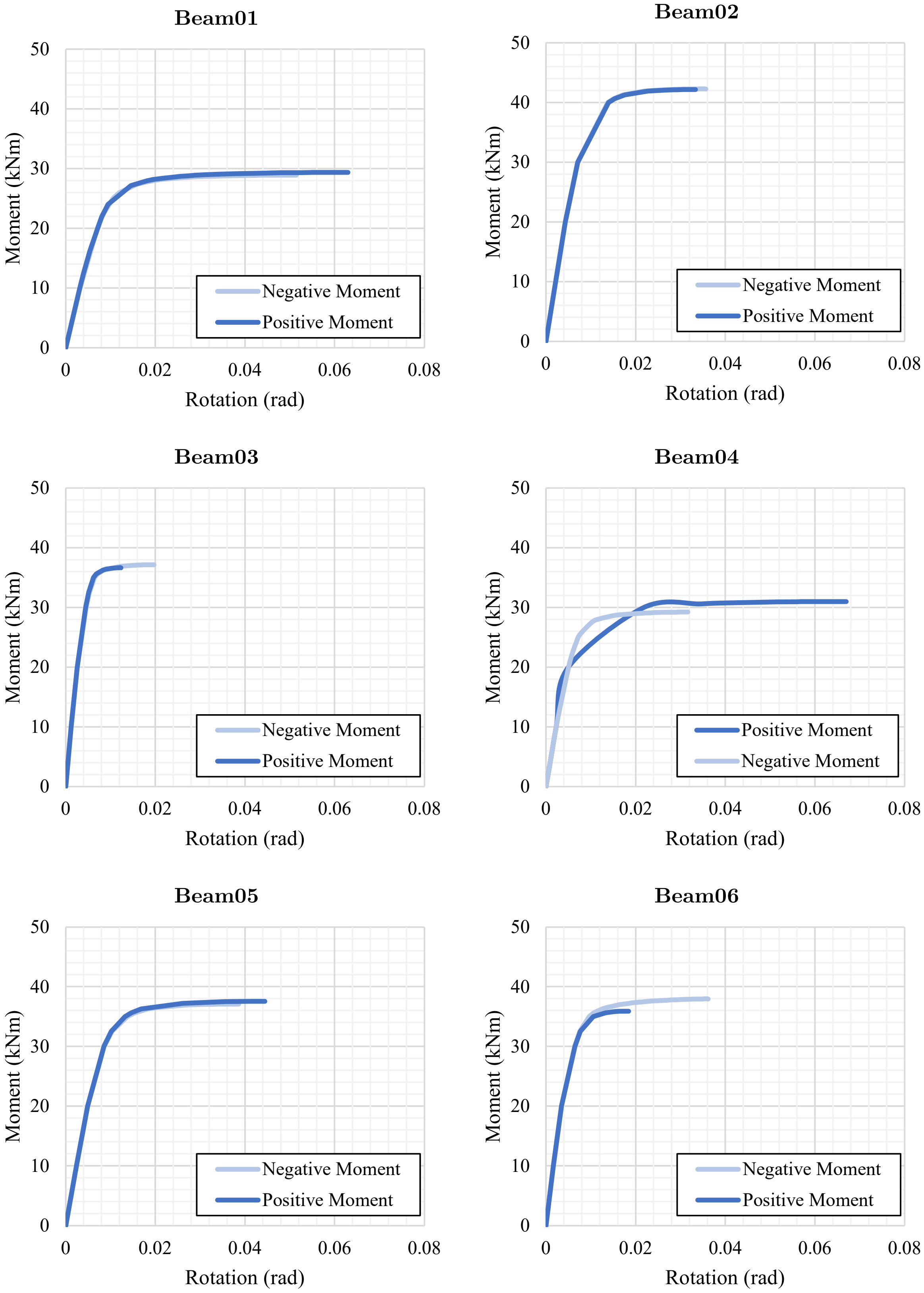

Figure 7.12 - Moment-rotation graphs considering a 6 mm thickness joint and moments in Y-Y direction

From the previous results, the optimized joint must be considered like semi-rigid, as indicated in Table 7.3 and Table 7.4.

In order to evaluate the joint as rigid, the thickness can be increased to 12 mm. Analysing the joint in the direction of the profiles, the following moment-rotation diagrams for moments in X-X and Y-Y directions are obtained.

Directions		k_j**(kNm/rad)**	k_b**(kNm/rad)**	$M_j(kNm)$	$M_b(kNm)$	α	β	**Verification**
01	M+	25750.09	1471.35	141.94	99.24	17.50	1.43	**Rigid**
	M−	25771.71		142.70		17.52	1.44	**Rigid**
02	M+	24618.97	1471.35	164.63	99.24	16.73	1.66	**Rigid**
	M−	24627.15		163.93		16.74	1.65	**Rigid**
03	M+	42097.93	1471.35	172.27	99.24	28.61	1.74	**Rigid**
	M−	42109.94		172.63		28.62	1.74	**Rigid**
04	M+	32439.71	1471.35	132.64	99.24	22.05	1.34	**Rigid**
	M−	32411.85		133.84		22.03	1.35	**Rigid**
05	M+	29617.85	1471.35	161.56	99.24	20.13	1.63	**Rigid**
	M−	29603.17		159.01		20.12	1.60	**Rigid**
06	M+	41019.30	1471.35	188.14	99.24	27.88	1.90	**Rigid**
	M−	31482.55		194.51		21.40	1.96	**Rigid**

Table 7.5 - Joint classification for 12 mm thickness joint and moments in X-X direction

Directions		k_j**(kNm/rad)**	k_b**(kNm/rad)**	$M_j(kNm)$	$M_b(kNm)$	α	β	**Verification**
01	M+	8910.17	301.75	68.20	45.80	29.53	1.49	**Rigid**
	M-	8923.74		65.22		29.57	1.42	**Rigid**
02	M+	11194.66	301.75	88.40	45.80	37.10	1.93	**Rigid**
	M-	11553.53		88.44		38.29	1.93	**Rigid**
03	M+	19051.30	301.75	96.81	45.80	63.14	2.11	**Rigid**
	M-	18986.98		94.42		62.92	2.06	**Rigid**
04	M+	11183.49	301.75	65.60	45.80	37.06	1.43	**Rigid**
	M-	11200.88		66.92		37.12	1.46	**Rigid**
05	M+	10044.72	301.75	79.69	45.80	33.29	1.74	**Rigid**
	M-	10052.39		80.89		33.31	1.77	**Rigid**
06	M+	22168.99	301.75	96.07	45.80	73.47	2.10	**Rigid**
	M-	22162.36		108.71		73.45	2.37	**Rigid**

Table 7.6 - Joint classification for 12 mm thickness joint and moments in Y-Y direction

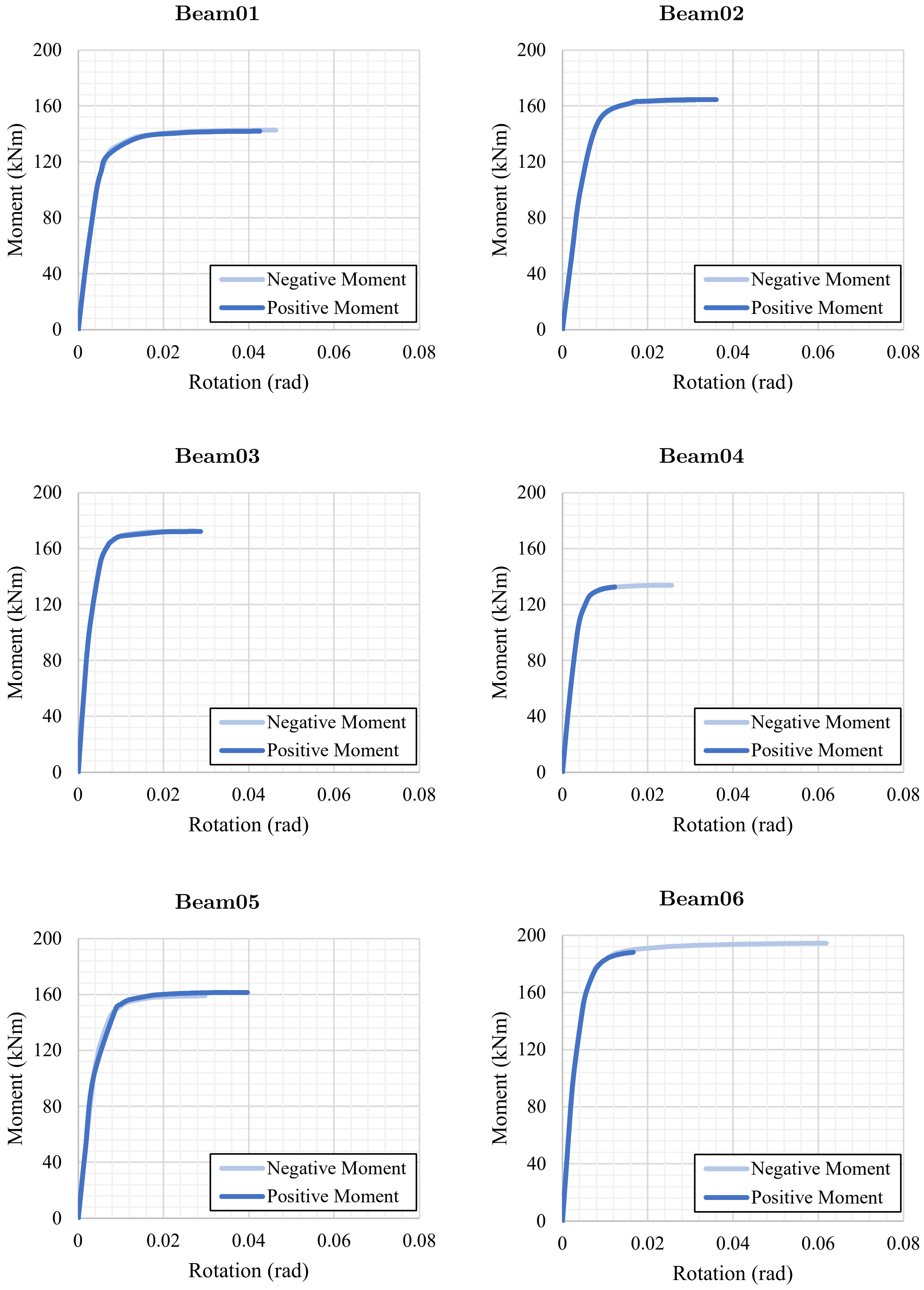

Figure 7.13 - Moment-rotation graphs considering a 12 mm thickness joint and moments in X-X direction

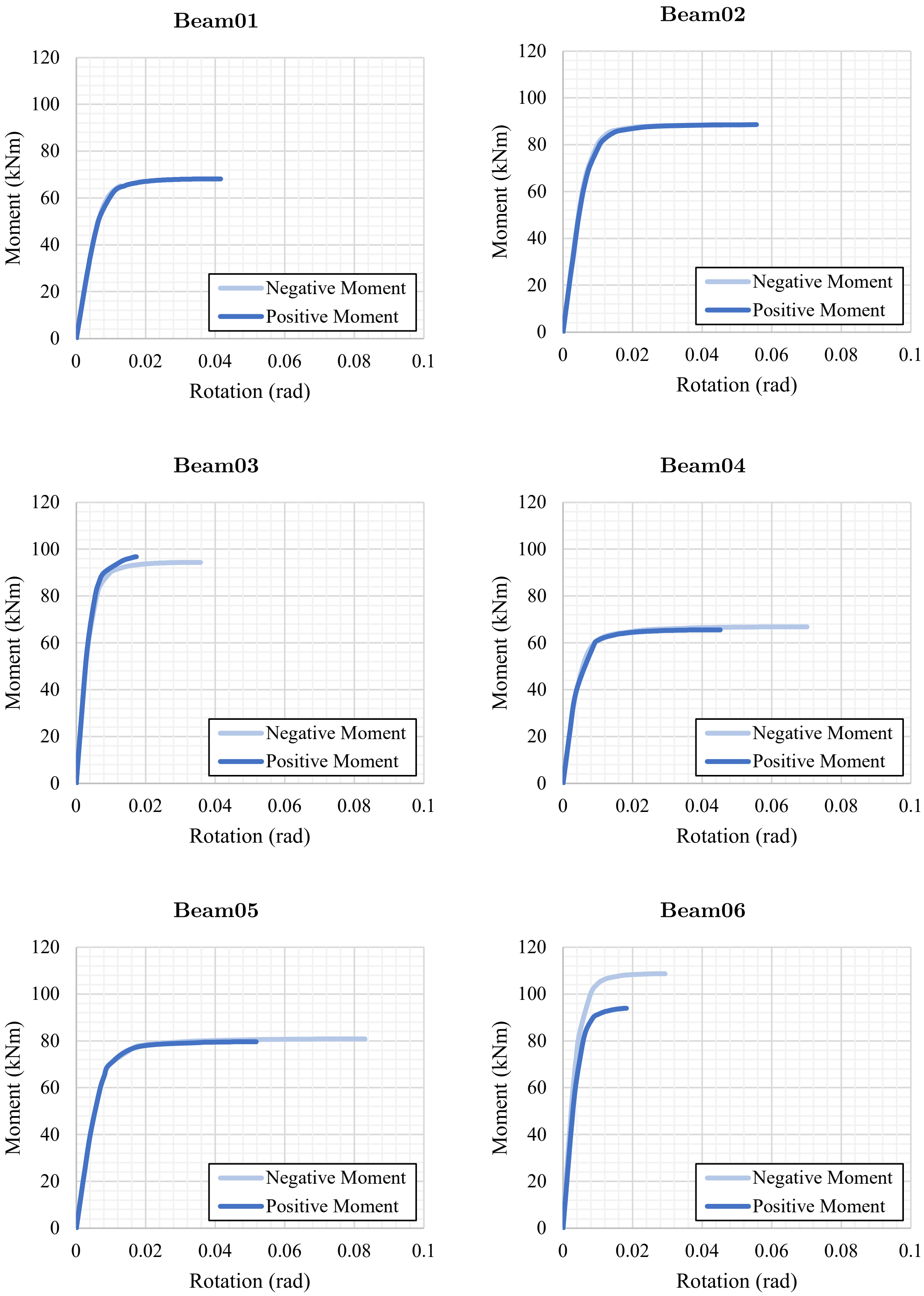

Figure 7.14 - Moment-rotation graphs considering a 12 mm thickness joint and moments in Y-Y direction

As indicated in Table 7.5 and Table 7.6, considering a thickness of 12 mm, the joint can be studied as rigid.

7.2 Buckling verification

The optimized joint is subjected to some compression loads, therefore it can be interesting to study the ultimate load before instability phenomena occur. In order to evaluate the ultimate buckling load, the joint has been examined using the "Buckling Analysis" block in nTopology (Figure 7.15) and studying one profile direction at a time. Then, the buckling analysis will determine a "buckling coefficient", which multiplied for the initial load applied will allow to compute the ultimate buckling load.

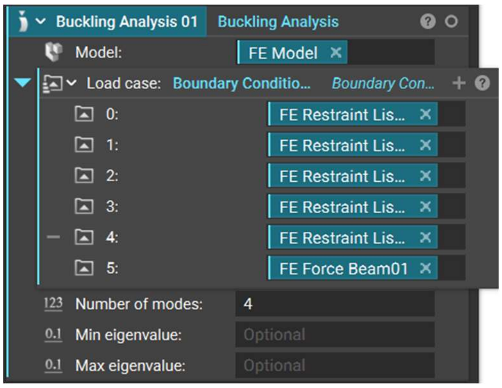

Buckling Analysis 01 Buckling Analysis
Model: FE Model
Load case: Boundary Conditio... Boundary Con...
0: FE Restraint Lis...
1: FE Restraint Lis...
2: FE Restraint Lis...
3: FE Restraint Lis...
4: FE Restraint Lis...
5: FE Force Beam01
Number of modes: 4
Min eigenvalue: Optional
Max eigenvalue: Optional

Figure 7.15 - "Buckling Analysis" block

The buckling analysis has been performed on the joint taking into account the two thicknesses of 6 mm and 12 mm considered in the previous paragraphs and the initial compression load applied correspond to 1000 kN. The results are summarized in Table 7.7 and Table 7.8.

	Beam01	Beam02	Beam03	Beam04	Beam05	Beam06
			Buckling factors			
Mode 1	19.1431	20.6393	29.533	22.8698	28.1665	23.5258
Mode 2	22.1683	21.4959	34.9671	24.3694	31.3702	26.9124
Mode 3	23.4929	29.2497	38.014	33.9301	33.0674	27.686
Mode 4	27.1755	31.0123	38.1241	37.9618	33.9804	28.548
			Buckling loads (kN)			
Mode 1	19143.1	20639.3	29533	22869.8	28166.5	23525.8
Mode 2	22168.3	21495.9	34967.1	24369.4	31370.2	26912.4
Mode 3	23492.9	29249.7	38014	33930.1	33067.4	27686
Mode 4	27175.5	31012.3	38124.1	37961.8	33980.4	28548

Table 7.7 - Buckling factors and loads for 6 mm thickness joint

The deformed shapes for mode 1, the ones with the lowest eigenvalues, are reported below, for 6 and 12 mm thicknesses respectively, in Figure 7.16 and Figure 7.17:

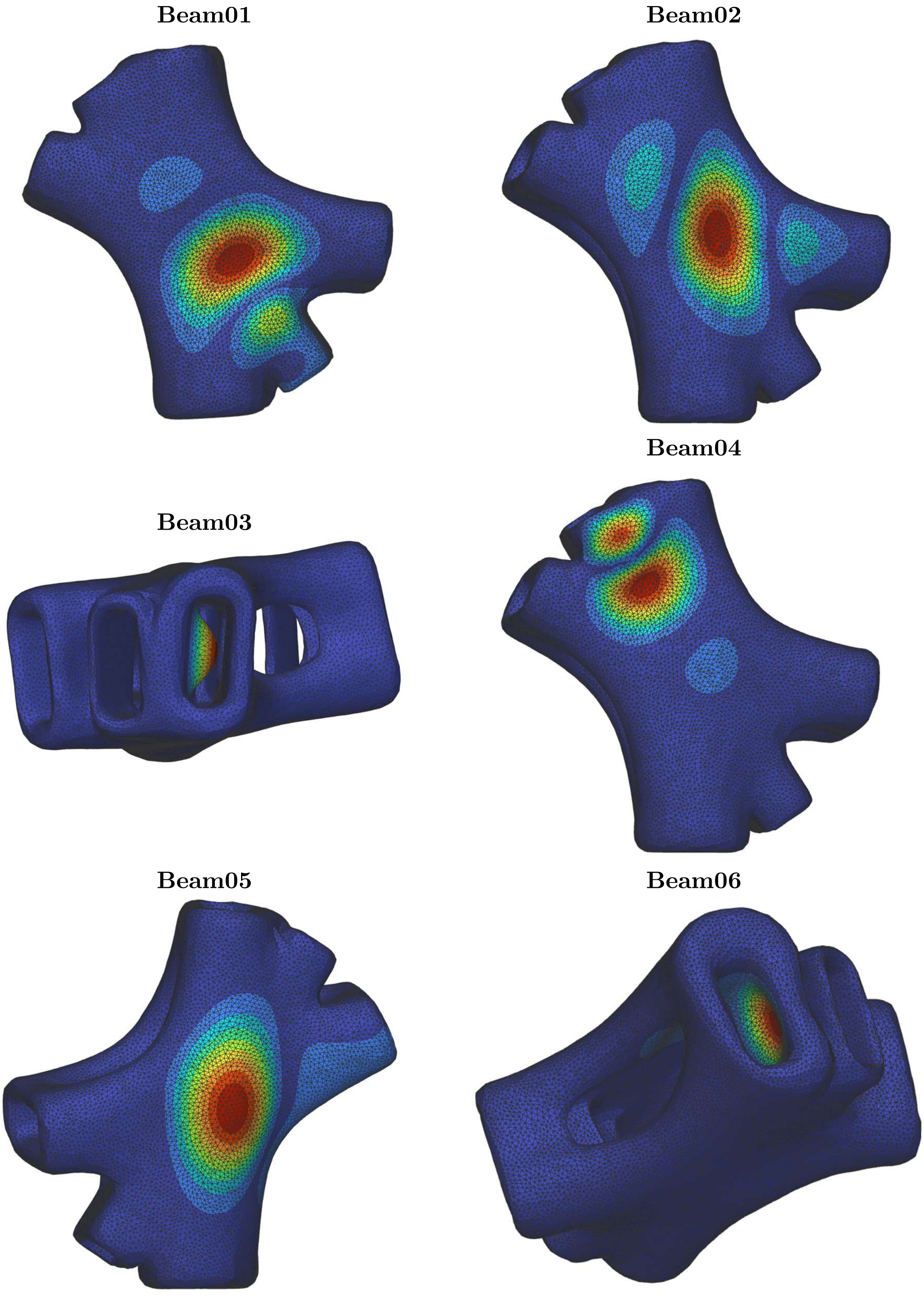

Beam01

Beam02

Beam03

Beam04

Beam05

Beam06

Figure 7.16 - Deformed shapes for mode 1 considering the joint with a thickness of 6 mm

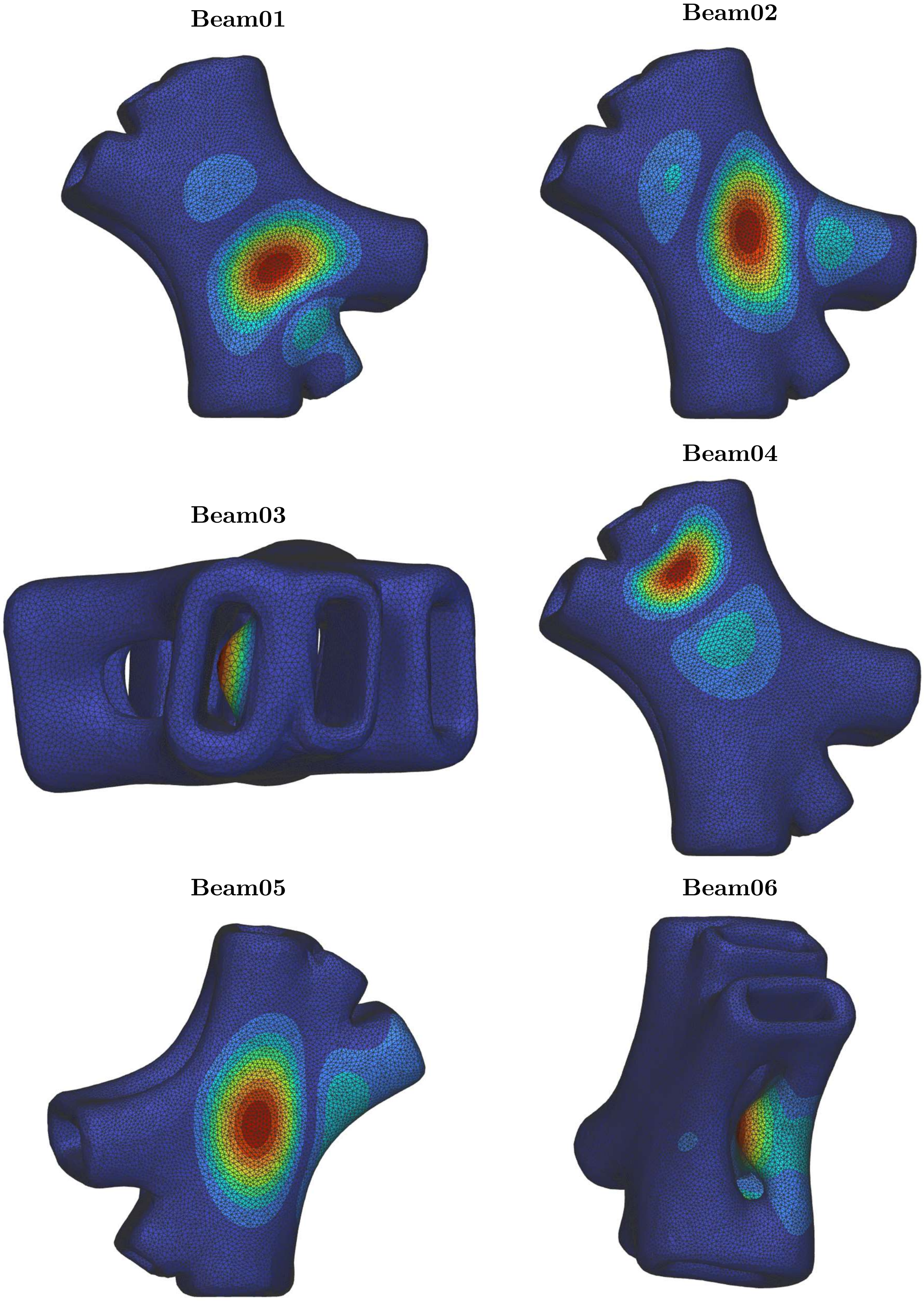
Beam01

Beam02

Beam03

Beam04

Beam05

Beam06

Figure 7.17 - Deformed shapes for mode 1 considering the joint with a thickness of 12 mm

	Beam01	**Beam02**	**Beam03**	**Beam04**	**Beam05**	**Beam06**
			Buckling factors			
Mode 1	78.9186	75.3877	118.901	116.002	96.894	93.8826
Mode 2	86.6612	78.5858	133.247	128.138	105.973	96.3217
Mode 3	107.477	103.783	141.183	144.604	108.613	100.758
Mode 4	112.63	107.829	145.988	159.374	112.1	108.136
			Buckling loads (kN)			
Mode 1	78918.6	75387.7	118901	116002	96894	93882.6
Mode 2	86661.2	78585.8	133247	128138	105973	96321.7
Mode 3	107477	103783	141183	144604	108613	100758
Mode 4	112630	107829	145988	159374	112100	108136

Table 7.8 - Buckling factors and loads for 12 mm thickness joint

Comparing the buckling loads with the maximum compression load at the ultimate limit state condition obtained from Straus7, equal to 447.029 kN (Figure 7.18), it can be noticed that we are really far from these limit values.

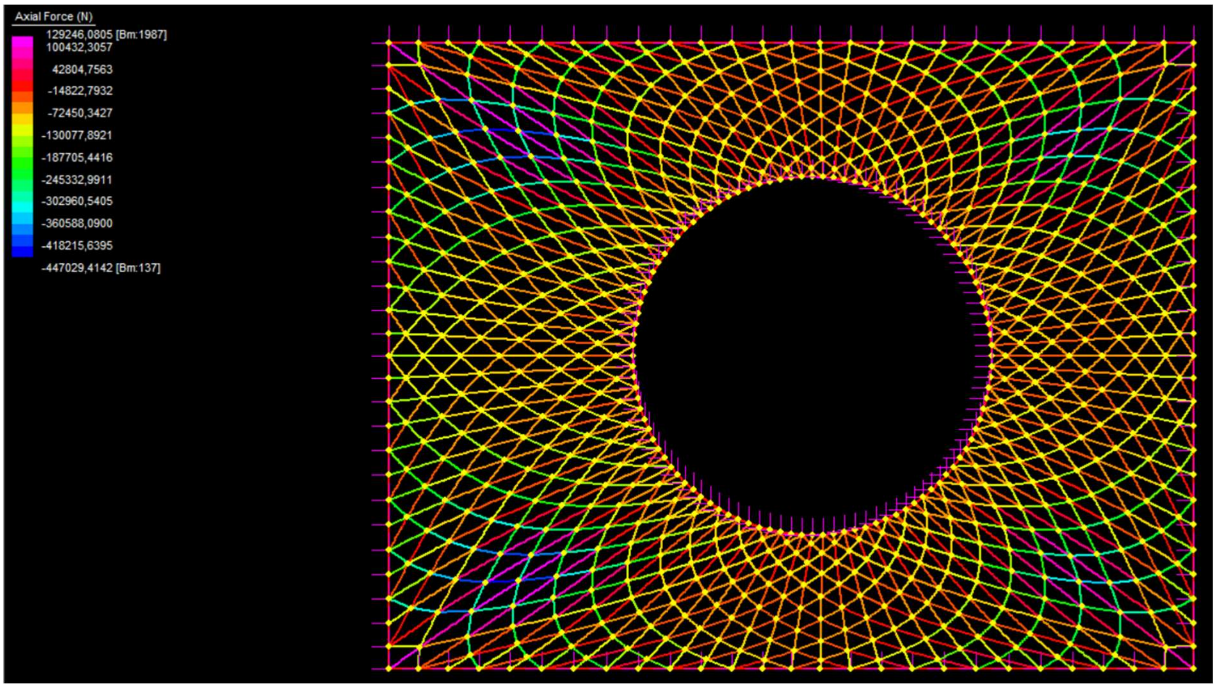

Figure 7.18 - Axial force distribution in the gridshell

7.3 Stress verification

The last verification performed consists to assess the maximum stress in the joint at the ultimate limit state. This check wants to verify that the maximum stress in the joint is lower than the yielding stress, equal to 355 MPa.

The verification has been carried out using nTopology and considering two thicknesses, 6 mm and 12 mm (Figure 7.19 and Figure 7.20).

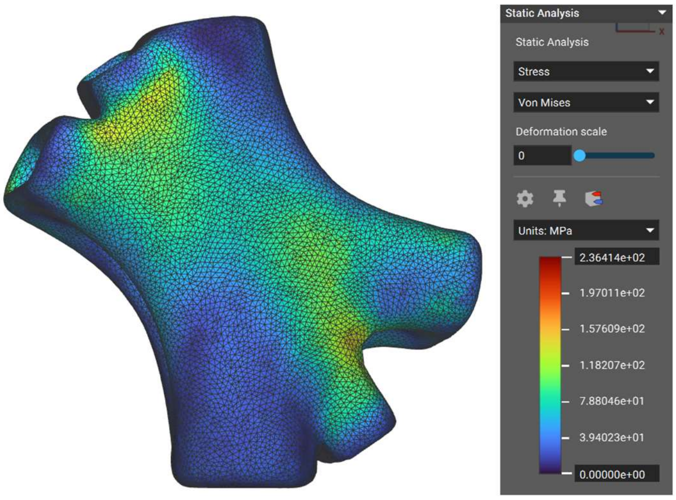

Static Analysis

Static Analysis

Stress

Von Mises

Deformation scale

0

Units: MPa

Figure 7.19 - Stress distribution considering the joint with a thickness of 6 mm

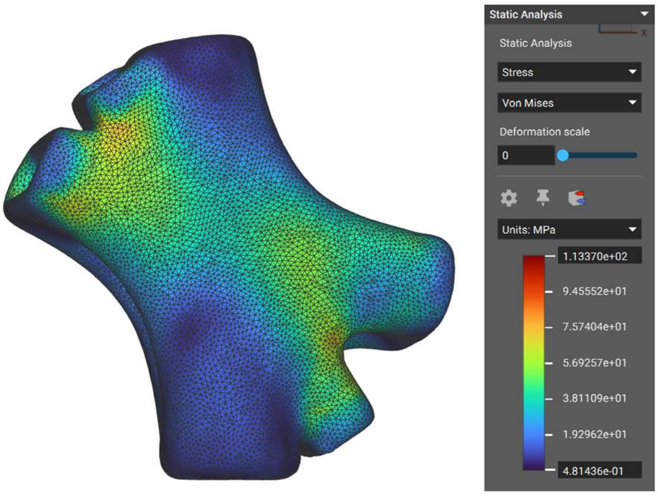

Static Analysis

Static Analysis

Stress

Von Mises

Deformation scale

0

Units: MPa

Figure 7.20 - Stress distribution considering the joint with a thickness of 12 mm

So, the maximum stresses are 236.4 MPa and 113.4 MPa, for the 6 mm and 12 mm thickness joints respectively. These values are lower than the yielding stress, therefore the stress verification is satisfied.

7.4 WAAM material properties

Until now, the printed material has been considered isotropic, however this assumption could not be completely true, due to layer-by-layer deposition. This type of anisotropic behaviour is mainly influenced by the layer height.

In the paper called "Simultaneous design of the topology and the build orientation of Wire-and-Arc Additively Manufactured structural elements" by Matteo Bruggi, Vittoria Laghi and Tomaso Trombetti, the anisotropic behaviour of WAAM has been modelled taking into account an orthotropic material model and considering different mechanical properties between the longitudinal and transversal direction. In such way, it is possible to obtain a 3D model with one longitudinal axis and two equal transversals. This type of model is called "transversal isotropic".

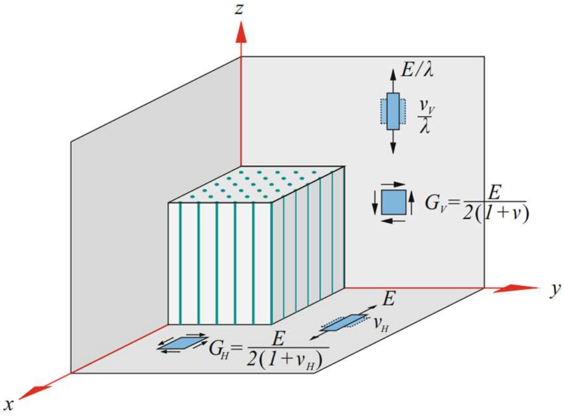

Figure 7.21 - Transversely isotropic material (Valentin L. Popov, 2019)

A transversely isotropic medium is a medium which has a favored direction and is isotropic in the plane perpendicular to this direction (Valentin L. Popov, 2019). The model is described by the following relationship:

$$\begin{bmatrix} \varepsilon_{xx} \\ \varepsilon_{yy} \\ \varepsilon_{zz} \\ 2\varepsilon_{xz} \\ 2\varepsilon_{yz} \\ 2\varepsilon_{xy} \end{bmatrix} = \frac{1}{E} \begin{bmatrix} 1 & -\nu_H & -\nu_V & 0 & 0 & 0 \\ -\nu_H & 1 & -\nu_V & 0 & 0 & 0 \\ -\nu_V & -\nu_H & \lambda & 0 & 0 & 0 \\ 0 & 0 & 0 & 2(1+\nu) & 0 & 0 \\ 0 & 0 & 0 & 0 & 2(1+\nu) & 0 \\ 0 & 0 & 0 & 0 & 0 & 2(1+\nu_H) \end{bmatrix} \begin{bmatrix} \sigma_{xx} \\ \sigma_{yy} \\ \sigma_{zz} \\ \sigma_{xz} \\ \sigma_{yz} \\ \sigma_{xy} \end{bmatrix}$$

Where:

- E is the Young's modulus in the XY-plane;
- E/λ is the Young's modulus in the z-direction;
- ν_H is the Poisson's ratio in the XY-plane;
- ν_V is the Poisson's ratio when stress is applied along the symmetry axis;
- G_V is the shear modulus for shear parallel to the axis of symmetry;

- G_H is the shear modulus in the plane of symmetry.

It must be noted that ν has not a physical interpretation.
Inverting the system of equations:

$$\begin{bmatrix}\sigma_{xx}\\ \sigma_{yy}\\ \sigma_{zz}\\ \sigma_{xz}\\ \sigma_{yz}\\ \sigma_{xy}\end{bmatrix}=\begin{bmatrix}C_{11} & C_{12} & C_{13} & 0 & 0 & 0\\ C_{12} & C_{11} & C_{13} & 0 & 0 & 0\\ C_{13} & C_{13} & C_{33} & 0 & 0 & 0\\ 0 & 0 & 0 & C_{44} & 0 & 0\\ 0 & 0 & 0 & 0 & C_{44} & 0\\ 0 & 0 & 0 & 0 & 0 & \frac{1}{2}(C_{11}-C_{12})\end{bmatrix}\begin{bmatrix}\varepsilon_{xx}\\ \varepsilon_{yy}\\ \varepsilon_{zz}\\ 2\varepsilon_{xz}\\ 2\varepsilon_{yz}\\ 2\varepsilon_{xy}\end{bmatrix}$$

The constants of the compliance matrix can be written as:

$$C_{11}=\frac{E(\lambda-\nu_V^2)}{(\lambda-\lambda\nu_H-\nu_V^2)(1+\nu_H)}$$

$$C_{12}=\frac{E(\lambda\nu_H+\nu_V^2)}{(\lambda-\lambda\nu_H-\nu_V^2)(1+\nu_H)}$$

$$C_{13}=\frac{E\nu_V}{(\lambda-\lambda\nu_H-\nu_V^2)}$$

$$C_{33}=\frac{E(1-\nu_H)}{(\lambda-\lambda\nu_H-\nu_V^2)}$$

$$C_{44}=\frac{E}{2(1+\nu)}$$

$$\frac{1}{2}(C_{11}-C_{12})=\frac{E}{2(1+\nu_H)}$$

From experimental results reported in (Matteo Bruggi, 2021), dog-bone specimens made with 304L stainless steel have been printed along the longitudinal direction (L), transversal direction (T) and 45°-diagonal direction (D). The specimens have been tested to assess their Young's modulus, yielding stress $R_{p(0.2)}$, ultimate tensile stress UTS and elongation at failure A:

Material	$\boldsymbol{E}(\boldsymbol{GPa})$	$\boldsymbol{R_{p(0.2)}}(\boldsymbol{MPa})$	$\boldsymbol{UTS}(\boldsymbol{MPa})$	$\boldsymbol{A}(\%)$
WAAM-L	135.84 ± 15.42	340.67 ± 20.21	567.39 ± 17.12	0.46 ± 0.07
WAAM-T	106.09 ± 2.98	352.54 ± 18.36	552.53 ± 48.30	0.38 ± 0.04
WAAM-D	243.09 ± 32.79	412.90 ± 39.33	604.81 ± 61.68	–
Grade 304L	200	$190 \div 230$	$500 \div 540$	0.3

Table 7.9 - Key material properties for different directions (Matteo Bruggi, 2021)

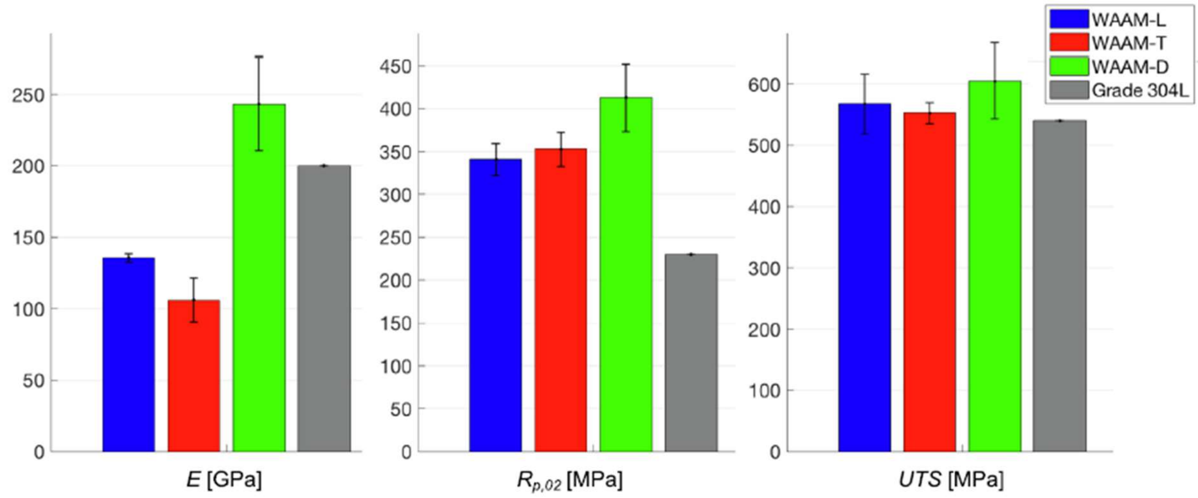

Figure 7.22 - Key material properties for different directions (Matteo Bruggi, 2021)

Hence, it is possible to find out all the values of the compliance matrix. Following (Matteo Bruggi, 2021) and (Babovic, 2021):

$$E = 106.09\ GPa$$

$$\frac{E}{\lambda} = 135.84 \rightarrow \lambda = 0.78$$

$$\nu_H = 0.38$$

$$\frac{\nu_V}{\lambda} = 0.46 \rightarrow \nu_V = 0.3588$$

$$G_V = 151.25\ GPa = \frac{E}{2(1+\nu)} \rightarrow 2(1+\nu) = 0.7$$

$$G_H = \frac{E}{2(1+\nu_H)} = 38.438\ GPa \rightarrow 2(1+\nu_H) = 2.76$$

So, the compliance matrix for steel 304L becomes (Babovic, 2021):

$$\boldsymbol{C} = \begin{bmatrix} 0.00943 & -0.00358 & -0.00338 & 0 & 0 & 0 \\ -0.00358 & 0.00943 & -0.00338 & 0 & 0 & 0 \\ -0.00338 & -0.00338 & 0.00736 & 0 & 0 & 0 \\ 0 & 0 & 0 & 0.00660 & 0 & 0 \\ 0 & 0 & 0 & 0 & 0.00660 & 0 \\ 0 & 0 & 0 & 0 & 0 & 0.02602 \end{bmatrix} GPa^{-1}$$

CHAPTER 8

FABRICATION OF THE OPTIMIZED JOINT

8.1 Overview

The last chapter of this thesis wants to explain how to fabricate the joint described before and what is the procedure that has been followed to print the node.
The process consists of the following steps:

- Creation of the slicing of the designed joint;
- Assigning the slicing to the path of the robot;
- Setting the fabrication parameters;
- Printing the joint layer-by-layer.

However, several problems must be taken into account. The three main ones are: overhang, deformations due to heat propagation and accumulation of material at the start and stop points.
In the following paragraphs, these issues will be explained and some solutions will be proposed to overcome the problems.

8.2 Overhang

Overhang can be defined as the maximum inclination angle that can be printed without the use of additional supports (Figure 8.1 and Figure 8.2). In this case, the maximum overhang angle allowed for wire-and-arc additive manufacturing is 72 degrees. However, the designed joint is full of bridges and regions where the overhang angle is larger than 72 degrees. In order to overcome these issues, there are four possible solutions:

- Printing of supports;

- Printing the joint in parts and join them later;
- Changing the topology optimization design considering the maximum overhang angle;
- Using a difference inclination of the building plane, to not exceed the maximum overhang.

The first two solutions have been neglected because the objective of the thesis is to create a unique element without supports, that should be removed in the post-processing phase.

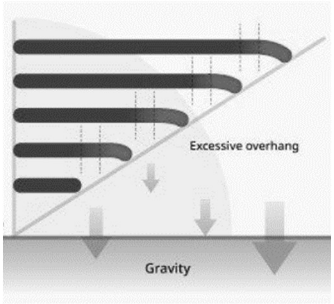

Figure 8.1 – Overhang angle

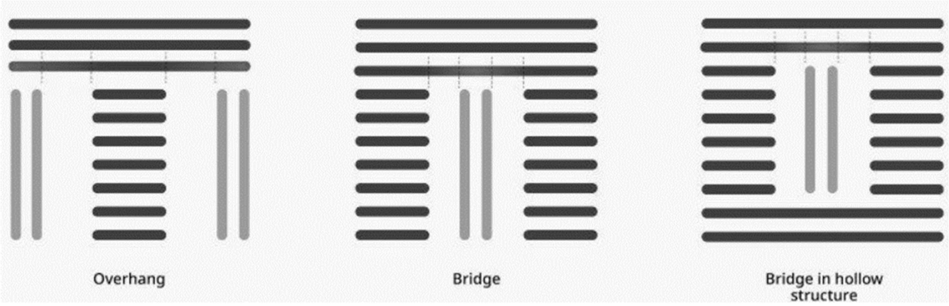

Figure 8.2 - Different types of overhang angles

8.2.1 Changing the topology optimization design

Using the software nTopology, it is possible to change the topology optimization of the joint including the block called "Overhang Constraint" (Figure 8.3). Using this block and imposing the maximum angle, the topology optimization of the joint change completely, as shown in Figure 8.4.

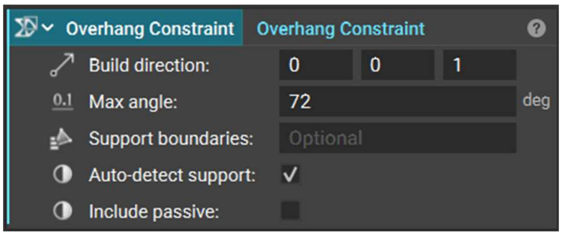

Overhang Constraint — Overhang Constraint

Build direction: 0 0 1

Max angle: 72 deg

Support boundaries: Optional

Auto-detect support: ✓

Include passive: ☐

Figure 8.3 - "Overhang Constraint" block in nTopology

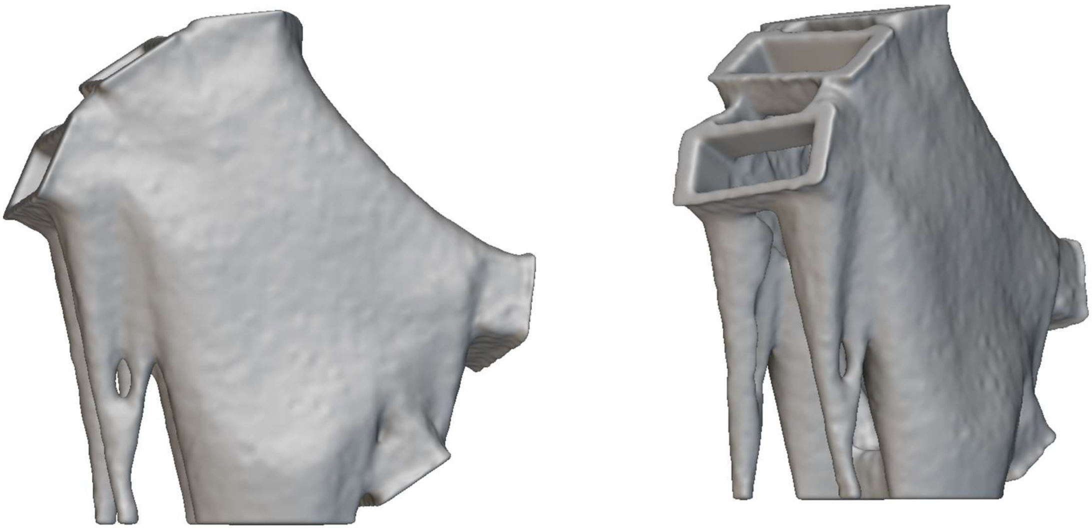

Figure 8.4 - Topology optimization design using the "Overhang Constraint" block in nTopology

However, the obtained solution is not useful for the real application considered, therefore this joint has not been considered.

8.2.2 Changing the building direction angle

The second possible solution considered was to changing the inclination of the base plate of 45 degrees and hence also the building direction. In this case, it was possible to print the whole node without exceeding the maximum allowed angle. The inclined slicing is reported below:

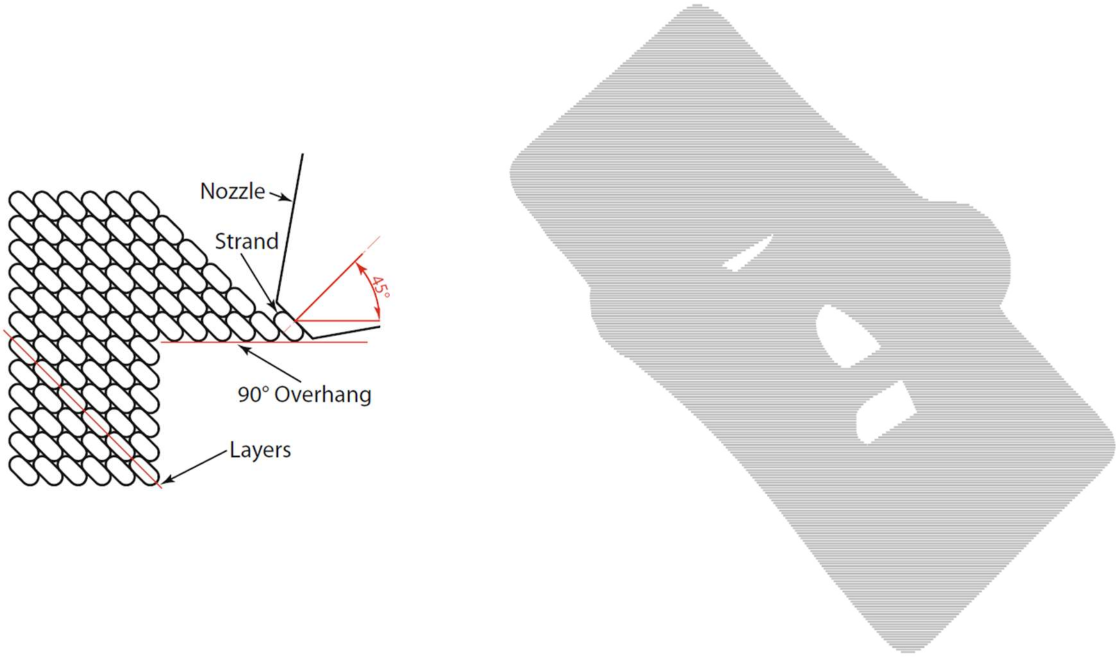

Figure 8.5 - Schematic view and inclined slicing of the joint (Mirko Meboldt, 2021)

This is the solution that we have considered because it allows us to print directly the joint, saving material, time, costs and avoiding the use of additional supports.

8.3 Test fabrication

Before proceeding with the realization of the real joint, it has been decided to print a smaller L-shape element in order to understand if it was feasible printing with an inclined building direction. This decision has been taken because there are not enough scientific papers about this topic.

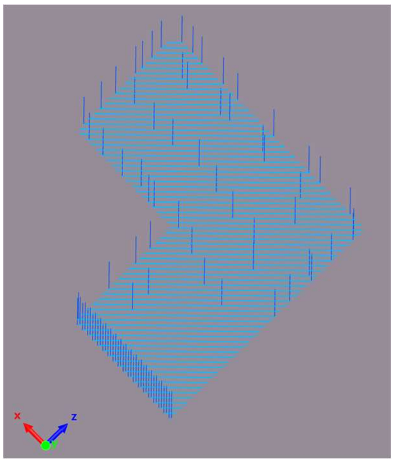

Figure 8.6 – Slicing of the L-element

8.3.1 Steel properties

The steel employed in printing is called "3Dprint AM80" and its properties and composition are reported in the table below:

Steel	C	Si	Mn	P	S	Cr	Mo	Ni	Ni
3Dprint AM80	0.107	0.359	1.69	0.0111	0.0033	0.384	0.594	2.18	0.0092
	Al	**Co**	**Cu**	**Nb**	**Ti**	**V**	**W**		
	0.0092	0.0063	0.0551	0.0021	0.0015	0.0079	0.006		

Table 8.1 – 3Dprint AM80 steel composition

Steel	$R_{p(0.2)}$(MPa)	R_m(MPa)	A(%)
3Dprint AM80	820	920	20

Table 8.2 - 3Dprint AM80 mechanical properties

Where:

- $R_{p(0.2)}$ is the stress that causes the stress-strain curve to deviate from proportionality by 0.2% of the initial length. In other words, it is the stress that provokes a plastic strain equal to 0.2%.
- R_m is the maximum stress before failure.
- A is the elongation to failure.

The base plate has a thickness of 15 mm and is made of S355J2+N.

8.3.2 Printing parameters

The printing process has been performed using the parameters in the following table:

$\boldsymbol{v_{wire}}$**(m/min)**	$\boldsymbol{v_{weld}}$**(cm/min)**	***IPT*(°C)**	**Cooling**	***I*(A)**	***U*(V)**	***E*(kJ/cm)**
6	45	200	Compressed Air	192.8 ± 4.1	18 ± 0.3	4.6

Table 8.3 - Printing parameters

8.3.3 Printing process

Initially, the steel substrate is set up on the tilting table and the parameters are assigned to the robot and the welder (Figure 8.7).

Then, the robot has started printing following the path assigned. After each layer, the printing process has been stopped, the printed layer has been cooled using compressed air until the temperature was lower than 200°C. At this point the printing process has been restarted. This type of procedure has been followed because the heat generated has a great influence on the mechanical properties of the steel, as reported by Johanna Mueller in “Mechanical properties of wire and arc additively manufactured high-strength steel structures”. In Figure 8.8, it is possible to notice that with 400°C the yielding stress and the elongation at failure decrease significantly. Moreover, from Figure 8.8, it is evident that yielding and failure stresses are greater when an active cooling is used.

Figure 8.7 - Substrate installation and setting parameters

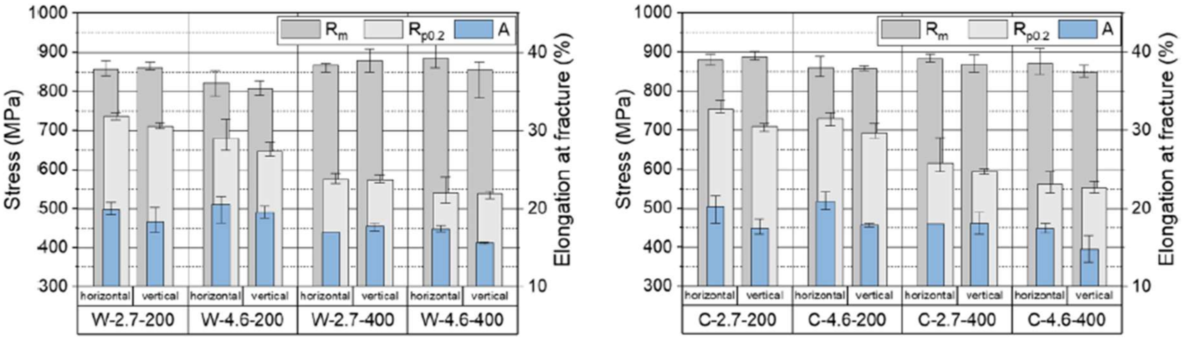

Figure 8.8 - Mechanical properties of 3Dprint AM80 without active cooling (left) and with active cooling (right) (Johanna Müller, 2021)

Furthermore, in order to avoid material accumulation at the start and stop points, these points have been uniformly distributed in the path and after each layer the movement of the torch in reversed.

Lastly, some additional straight printed elements have been added every three layers in order to compensate heat deformations (Figure 8.9) that have been arisen during the building process. The construction time was almost 4 hours, considering the cooling time and some technical issues arose during the process.

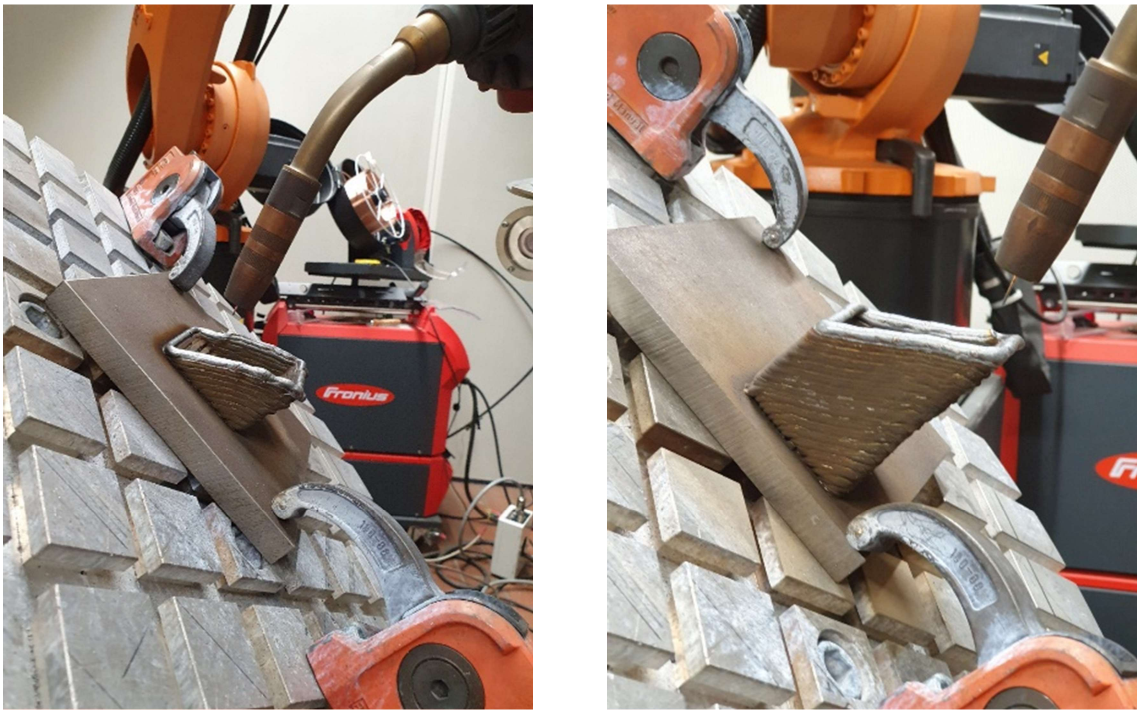

Figure 8.9 - Heat deformations (left) and deformations compensated by straight layers (right)

The printing process and the final element are shown below:

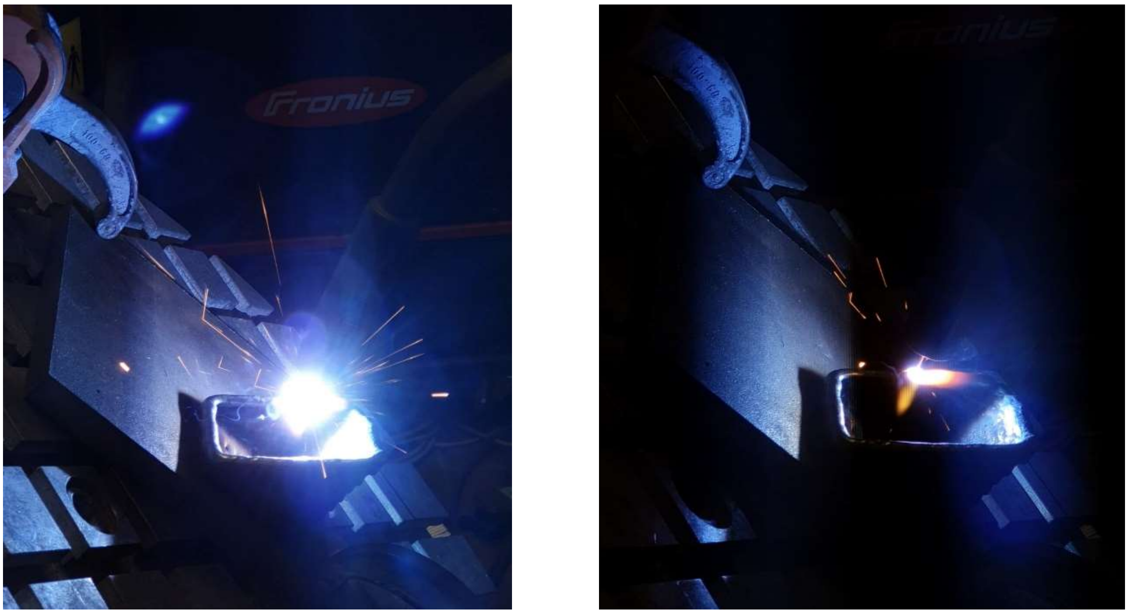

Figure 8.10 - WAAM printing process

Finally, the printed element is reported in the next figure:

Figure 8.11 - Final printed element

This test highlighted the following things:

- It is possible to overcome the overhang problem, changing the slicing inclination;
- Heat distortions must be taken into account before and during the printing process because they affect significantly the resultant geometry.

CHAPTER 9

CONCLUSION

Several interesting results have been achieved designing a topology optimized structural joint. First of all, it has been observed that topology optimization is a really powerful tool, regardless of the method used. Obviously, SIMP, ESO and BESO have several theoretical differences that can affect the final optimization. However, these features are really useful for the designer, who can manipulate parameters, like the penalization p or the evolutionary ratio ER, to obtain the best possible solution for each specific case. The main possible problem is the fact that these methods assume an isotropic material and this assumption is not completely true if the object is made using WAAM, hence the engineer must be able to study carefully the effects in terms of strength and stiffness.

Another important aspect of this thesis concerns the structural classification of the joint. The approach presented in this thesis wants to classify complex joints taking into account their application in the structure and introduce a general procedure, which can be valid in different situations. Therefore, the introduction of α and β parameters allows the engineer to apply a general approach and simplify a verification which otherwise would not be easy using Eurocodes. Moreover, Eurocodes does not deal with complex elements like the one presented in this dissertation, hence this different approach could be employed for 3D-printed elements.

Furthermore, the joint fabrication highlighted different difficulties, the most important ones are overhang and heat deformations. Overhang can be overcome setting correctly the printing parameters and modifying the inclination of the building direction respect to the base plate in order to have at least 45° degrees of layer inclination. While for heat deformations, printing parameters strongly affect the quality of the final printed element. Therefore, it would be better to create a FE model able to predict correctly the heat dissipation during the printing process and then modify the parameters to achieve the best possible result. Despite these fabrication issues, it is feasible to build structural joints made with WAAM.

To conclude, in this thesis it has been demonstrated that WAAM has a really big potential in construction sector, in particular considering freedom of shape and production times. However, fabrication issues must be studied deeply in order to further reduce the construction time. Instead, in the designing part, the engineer must be open-minded because several aspects are not treated in codes, and be aware of the mechanical properties of a 3D-printed element, considering the transversely isotropic behaviour of the material.

ACKNOWLEDGEMENTS

I would like to thank all the people who helped me in the writing of this thesis. I am grateful to them for their advice, suggestions, criticisms and comments during these months.
First of all, I would like to acknowledge the supervisor Prof. Ing. Tomaso Trombetti and co-superivors Dr. Ing. Vittoria Laghi, Prof. Ing. Harald Kloft and Dr. Neira Babovic. Without their guidance, this thesis would not exist.
Finally, I would like to acknowledge Dr. Johanna Müller for all the help and time she gave me for the laboratory experiments.

BIBLIOGRAPHY

Adedeji B. Badiru, V. V. (2017). *Additive Manufacturing Handbook Product Development for the Defence Industry.* CRC Press Taylor & Francis Group.

Aitziber López, I. P. (2006). Direct evaluation of the buckling loads of semi-rigidly jointed single-layer latticed domes under symmetric loading. *Engineering Structures.*

Aitziber López, I. P. (2007). Numerical model and experimental tests on single-layer latticed domes with semi-rigid joints. *Computers & Structures.*

Aitziber López, I. P. (2011). Experimental and analytical studies on the rotational stiffness of joints for single-layer structures. *Engineering Structures.*

Amir Mostafaei, A. M. (2021). Binder jet 3D printing—Process parameters, materials, properties, modeling, and challenges. *Progress in Material Science.*

Anastasia Puzatova, P. S. (2022). Large-Scale 3D Printing for Construction Application by Means of Robotic Arm and Gantry 3D Printer: A Review.

Arrè, L. (2021). *Design, Fabrication and Mechanical Characterization studies on Wire-and-Arc Additively Manufactured (WAAM) diagrid elements.*

Babovic, N. (2021). *Optimized studies for European I-type beams produced with Wire-and-Arc technologies.*

Bernuzzi, C. (2018). *Progetto e verifica delle strutture in acciaio.* HOEPLI.

Białkowski, S. (s.d.). Structural Optimisation Methods as a New Toolset for Architecture. *Design Tools.*

C. Buchanan, L. G. (2019). Metal 3D printing in construction: A review of methods, research, applications, opportunities and challenges. *Engineering Structures.*

D. Nha Chu, Y. X. (1996). Evolutionary structural optimization for problems with stiffness constraints. *Finite Elements in Analysis and Design.*

David Ian Wimpenny, P. M. (2017). *Advances in 3D Printing & Additive Manufacturing Technologies.* Springer.

Donghong Ding, Z. P. (2015). Wire-feed Additive Manufacturing of Metal Components: technologies, developments and future interests. *International Journal of Advanced Manufacturing Technology.*

Eurocode 3: Design of steel structures - Part 1-8: Design of joints. (1993).

Feng Fan, H. M. (2011). A new classification system for the joints used in lattice shells. *Thin-Walled Structures.*

Feng Fan, J. Y. (2012). Stability of reticulated shells considering member buckling . *Journal of Constructional Steel Research.*

Feng Fan, Z. C. (2010). Elasto-plastic stability of single-layer reticulated shells. *Thin-Walled Structures.*

Fengcheng Liu, R. F. (2021). Form finding of assembled lattice structure considering the effect of joint stiffness. *Structures.*

Francisco Mercado, A. J. (2020). Additive manufacturing methods: techniques, materials, and closed-loop control applications. *The International Journal of Advanced Manufacturing Technology.*

Gioncu, V. (1994). Buckling of Reticulated Shells: State-of-the-Art. *International Journal ofSpace Structures.*

Gomes, F. C. (2002). The EC3 classification of joints and alternative proposals.

Guoying Dong, Y. F. (2018). Numerical and experimental investigation of the joint stiffness in lattice structures fabricated by additive manufacturing. *International Journal of Mechanical Sciences.*

Hamed Seifi, A. R. (2018). Design optimization and additive manufacturing of nodes in gridshell structures. *Engineering Structures.*

Ian Gibson, D. R. (2015). *Additive Manufacturing Technologies.* Springer.

ISO/ASTM 52900 Additive manufacturing — General principles — Terminology. (2015).

J.P. Kruth, L. F. (2004). Selective laser melting of iron-based powder. *Journal of Materials Processing Technology.*

Jan Knippers, T. H. (2009). Recent Developments in the Design of Glazed Grid Shells. *International Journal of Space Structures.*

Jianguo Cai, Y. X. (2012). Nonlinear Stability of a Single-Layer Hybrid Gridshell. *Journal of Civil Engineering and Management.*

Johan Blaauwendraad, J. H. (2014). *Structural Shell Analysis.* Springer.

Johanna Müller, J. H. (2021). Mechanical properties of wire and arc additively manufactured high-strength steel structures. *Welding in the World.*

Johannes Lundgren, C. P. (2012). *Structural Form Optimisation.* Chalmers University of Technology.

Johnnie Liew Zhong Li, M. R. (2018). *Review of Wire Arc Additive Manufacturing for 3D Metal Printing.* Universiti Teknikal Malaysia Melaka.

Leung, R. K. (s.d.). History and Theory of Gridshell Architecture.

Liddell, I. (2015). Frei Otto and the development of gridshells. *Case Studies in Structural Engineering.*

Linden, L. v. (2015). *Innovative Joints for Gridshells.*

M.P. Bendsøe, O. S. (2003). *Topology Optimization.* Springer.

Matteo Bruggi, V. L. (2021). Simultaneous design of the topology and the build orientation of Wire-and-Arc Additively Manufactured structural elements. *Computers and Structures.*

Michael Barnes, M. D. (2000). *Widespan Roof Structures.* Thomas Telford.

Milewski, J. O. (2017). *Additive Manufacturing of Metals.* Springer.

Mirko Meboldt, C. K. (2017). *Industrializing Additive Manufacturing - Proceedings of Additive Manufacturing in Products and Applications - AMPA2017.* Springer.

Mirko Meboldt, C. K. (2021). *Industrilizing Additive Manufacturing Proceedings of AMPA2020.* Springer.

Muniyasamy Kalanchiam, B. M. (2013). Topology Optimization of Aircraft Fuselage Structure. *International Journal of Aerospace and Mechanical Engineering.*

Peter W. Christensen, A. K. (2009). *An Introduction to Structural Optimization.* Springer.

Qinghua Han, Y. L. (2016). Stiffness characteristics of joints and influence on the stability of single-layer latticed domes . *Thin-Walled Structures.*

Rozvany, G. (1992). *Shape and Layout Optimization of Structural Systems and Optimality Crteria Methods.* Springer-Verlag Wien GMBH.

Rozvany, G. I. (2009). *A critical review of established methods of structural topology optimization.* Springer.

Salomé Galjaard, S. H. (2015). Optimizing Structural Building Elements in Metal by using Additive Manufacturing. *Proceedings of the International Association for Shell and Spatial Structures.*

Salomé Galjaard, S. R. (2015). New opportunities to optimize structural designs in metal by using additive manufacturing.

Shiro Kato, T. Y. (2001). Evaluation of Elasto-plastic Buckling Strength of Two-way Grid Shells using Continuum Analogy. *International Journal of Space Structures.*

Sigrid Adriaenssens, P. B. (2014). *Shell Structures for Architecture Form Finding and Optimization.* Routledge Taylor & Francis Group.

Strauß, H. (2013). *AM Envelope.* Delft University of Technology.

Tedeschi, A. (2014). *AAD_Algorithmd-Aided Design Parametric Strategies using Grasshopper.* Le Penseur.

Thomas See, R. E. (1986). Large Displacement Elastic Buckling of Space Structures . *Journal of Structural Engineering.*

Toshiro Suzuki, T. O. (1992). Elasto-Plastic Buckling Analysis of Rigidly Jointed Single Layer Reticulated Domes. *International Journal oj Space Structures.*

Valentin L. Popov, M. H. (2019). *Handbook of Contact Mechanics.* Springer.

Vittoria Laghi, M. P. (2020). Computational design and manufacturing of a half-scaled 3D-printed stainless steel diagrid column. *Additive Manufacturing.*

Williams, C. J. (2001). The analytic and numerical definition of the geometry of the British Museum Great Court Roof. *Mathematics & design.*

Wohlers, T. (2010). *Wohlers Report 2010.* Wohlers Associates.

X. Huang, Y. X. (2010). *Evolutionary Topology Optimization of Continuum Structures.* Wiley.

Yang Guo, H. S. (2017). Inkjet and inkjet-based 3D printing: Connecting fluid properties and printing performance. *Rapid Prototyping Journal.*

APPENDIX A

A.1 British Museum Grasshopper file

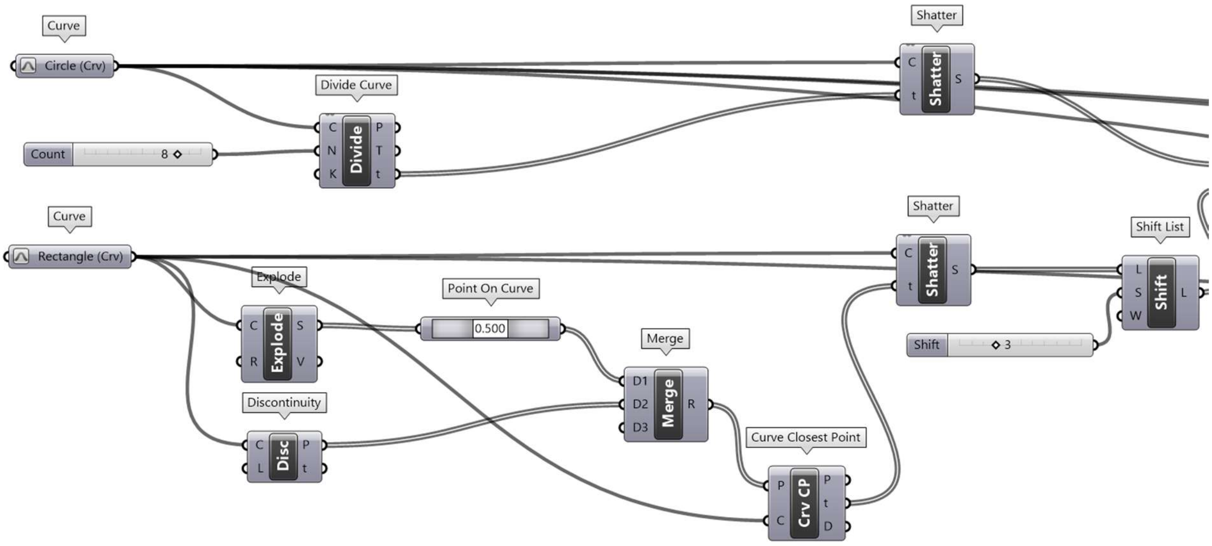

Figure A.1 - British Museum Grasshopper file Part 1

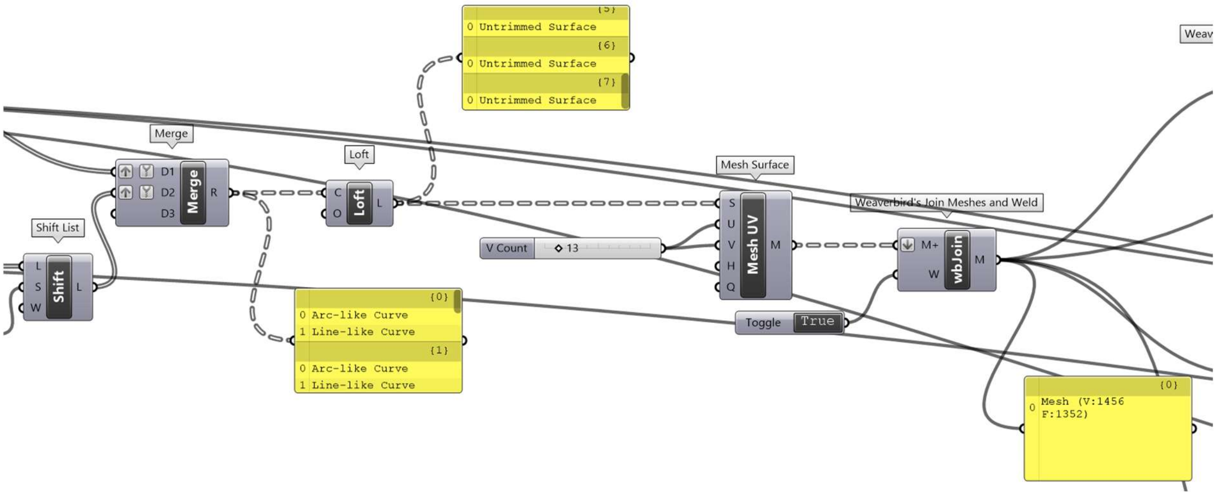

```
{5}
0 Untrimmed Surface
{6}
0 Untrimmed Surface
{7}
0 Untrimmed Surface
```

```
{0}
0 Arc-like Curve
1 Line-like Curve
{1}
0 Arc-like Curve
1 Line-like Curve
```

```
{0}
0 Mesh (V:1456
  F:1352)
```

Figure A.2 - British Museum Grasshopper file Part 2

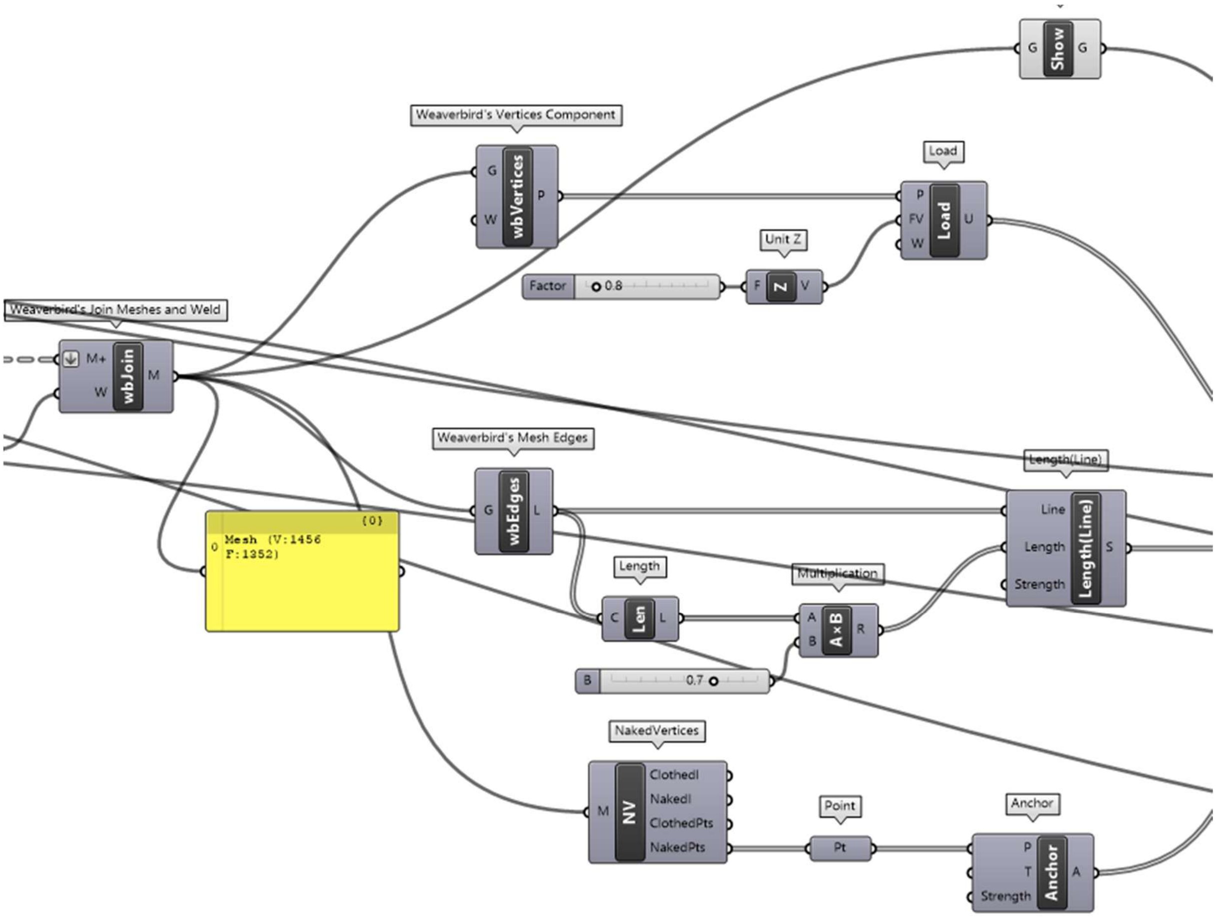

Figure A.3 - British Museum Grasshopper file Part 3

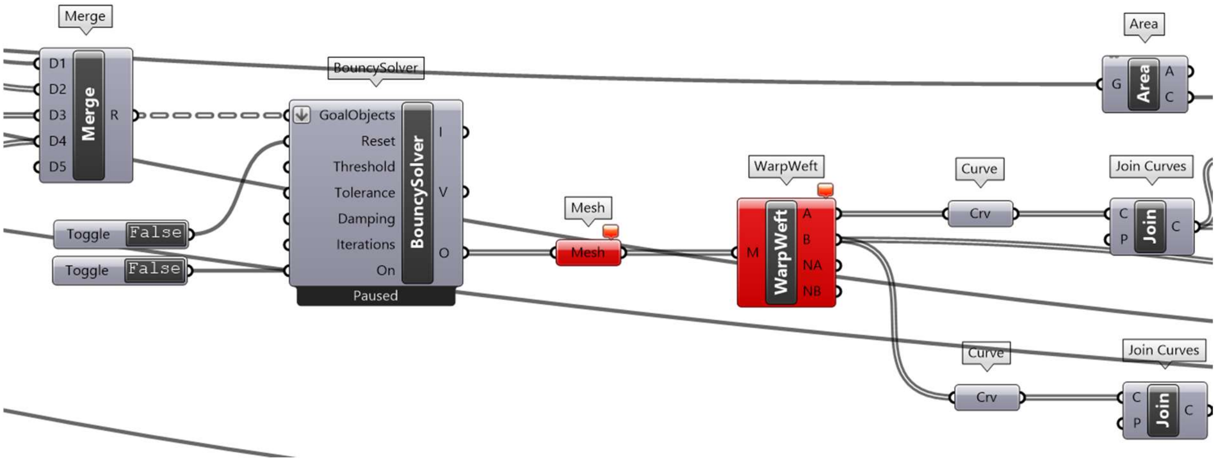

Figure A.4 - British Museum Grasshopper file Part 4

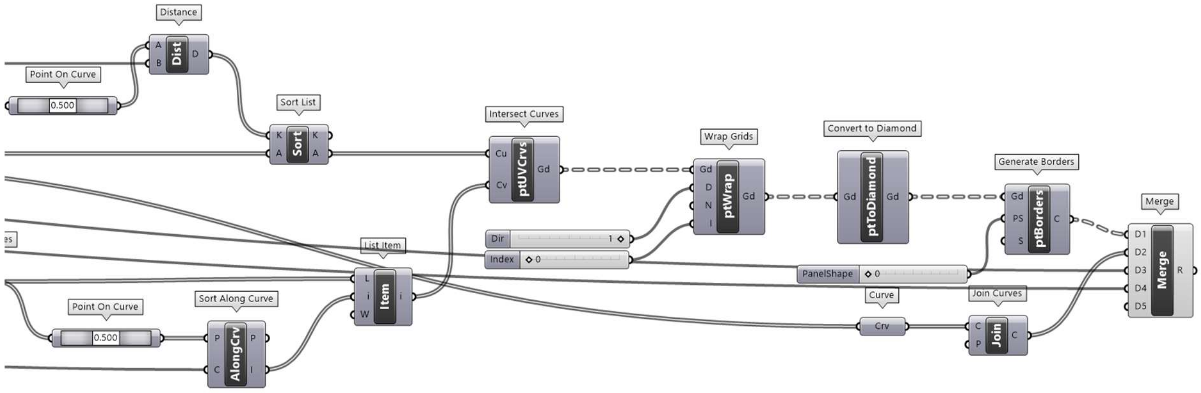

Figure A.5 - British Museum Grasshopper file Part 5

APPENDIX B

B.1 Ameba topology optimization seventh attempt

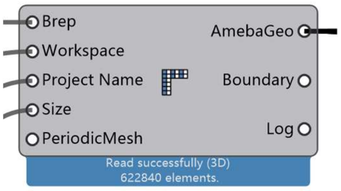

Figure B.1 - "MeshParting" component

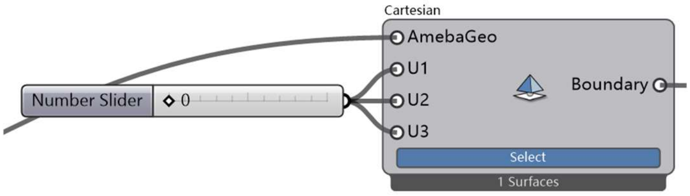

Figure B.2 - "Support3dSurface" component

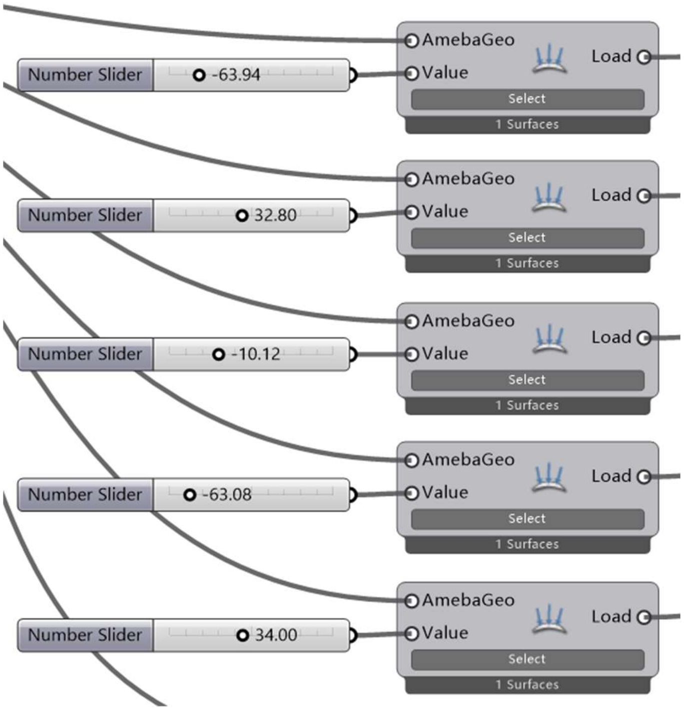

Figure B.3 - "Load3dSurfaceNormal" component

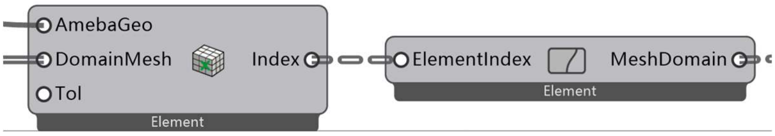

Figure B.4 - "DomainMesh" and "NonDomain" components

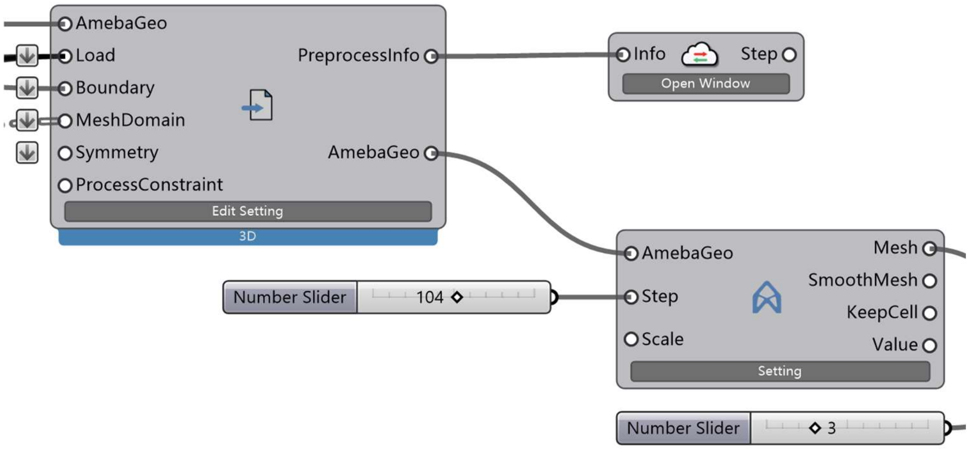

Figure B.5 - "PreProcessing", "Solver" and "Display" components

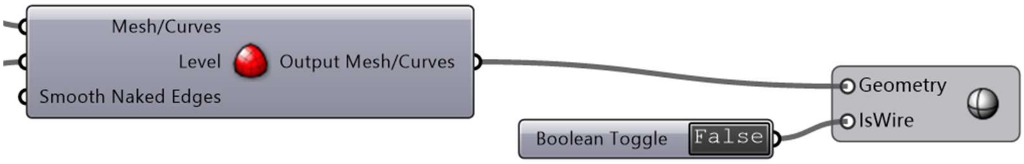

Figure B.6 - "Weaverbird's Catmull-Clark Subdivision" and "RenderDisplay" components

B.2 nTopology topology optimization seventh attempt

B.2.1 Node definition

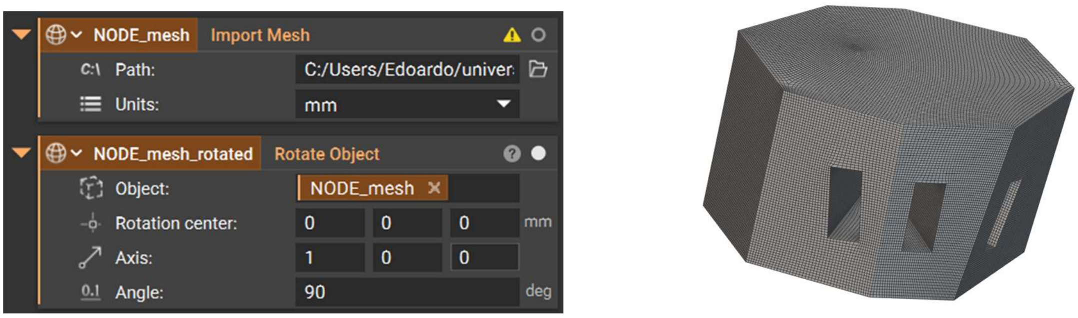

NODE_mesh Import Mesh
Path: C:/Users/Edoardo/univer
Units: mm

NODE_mesh_rotated Rotate Object
Object: NODE_mesh
Rotation center: 0 0 0 mm
Axis: 1 0 0
Angle: 90 deg

Figure B.7 - Imported Mesh

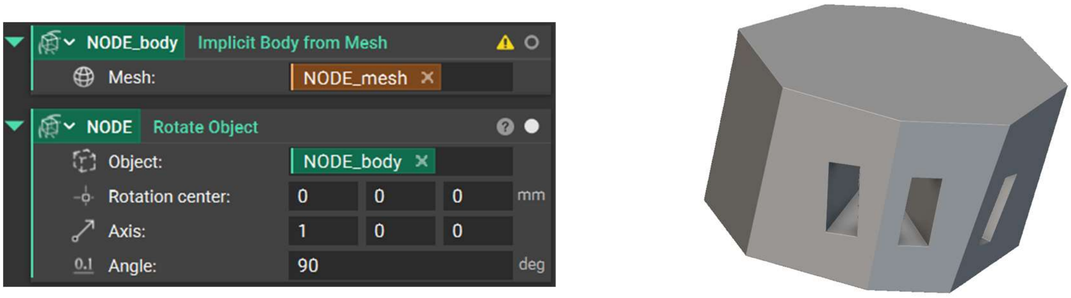
NODE_body Implicit Body from Mesh

Mesh: NODE_mesh

NODE Rotate Object

Object: NODE_body

Rotation center: 0 0 0 mm

Axis: 1 0 0

Angle: 90 deg

Figure B.8 - Initial implicit body

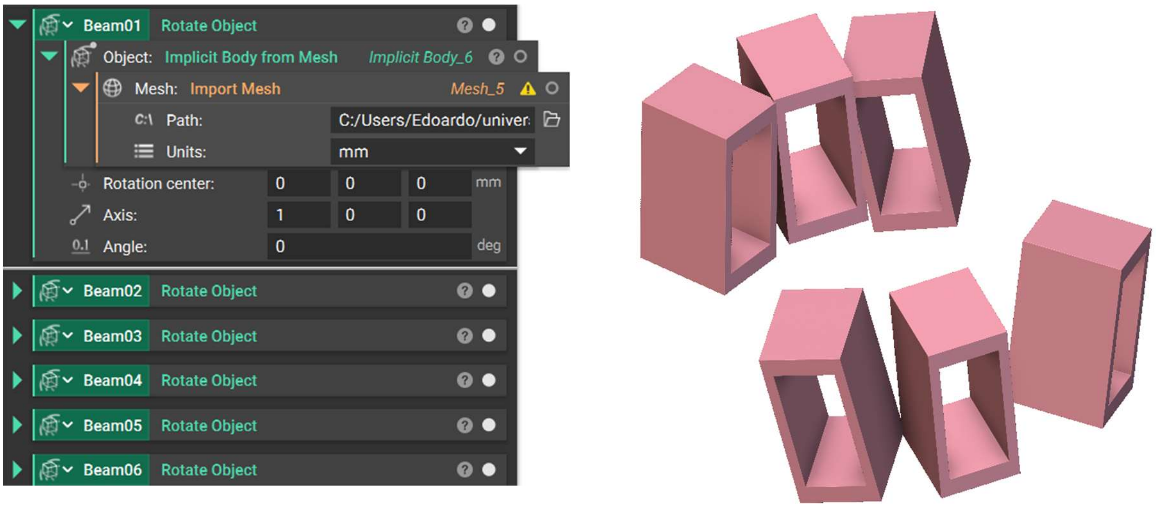
Beam01 Rotate Object

Object: Implicit Body from Mesh *Implicit Body_6*

Mesh: Import Mesh *Mesh_5*

Path: C:/Users/Edoardo/univer

Units: mm

Rotation center: 0 0 0 mm

Axis: 1 0 0

Angle: 0 deg

Beam02 Rotate Object

Beam03 Rotate Object

Beam04 Rotate Object

Beam05 Rotate Object

Beam06 Rotate Object

Figure B.9 - Implicit bodies of the non-domain regions

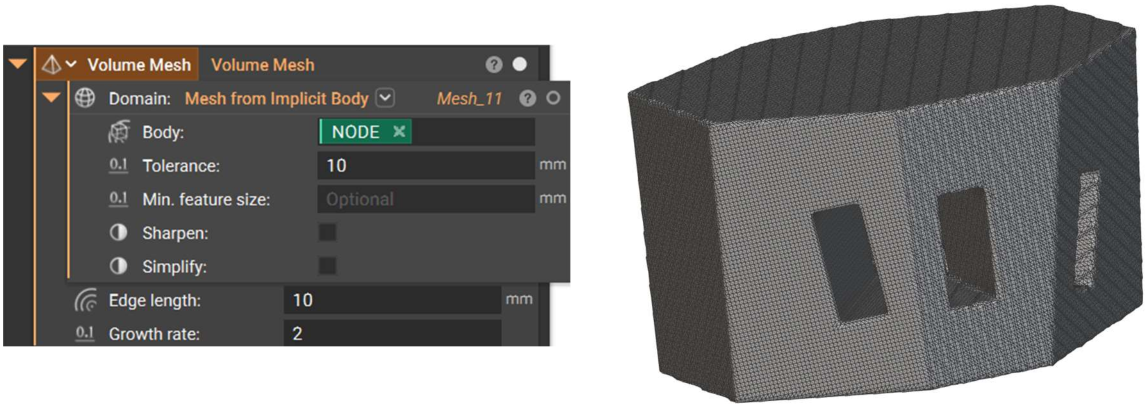
Volume Mesh Volume Mesh

Domain: Mesh from Implicit Body *Mesh_11*

Body: NODE

Tolerance: 10 mm

Min. feature size: Optional mm

Sharpen: ☐

Simplify: ☐

Edge length: 10 mm

Growth rate: 2

Figure B.10 - Volume mesh

B.2.2 FE model

FE Volume Mesh — FE Volume Mesh

Material — Isotropic Material
Properties: Isotropic Linear Ela... — Isotropic Linea...
0: Isotropic Linear Elastic Property — Isotropic Linear El...
Young's modulus: 2e+11 Pa
Poisson's ratio: 0.3
Density: 0.00785 mm^3 g

FE Model — FE Model
Components: FE Compone... — FE Component...
0: FE Component — FE Component_0
Mesh: FE Volume Mesh
Attributes: FE Attribute List (1) — FE Attribute List_0
0: FE Solid Attribute — FE Attribute_0
Material: Material
Frame: Optional
Region: Optional
Connectors: Optional

Figure B.11 - FE model

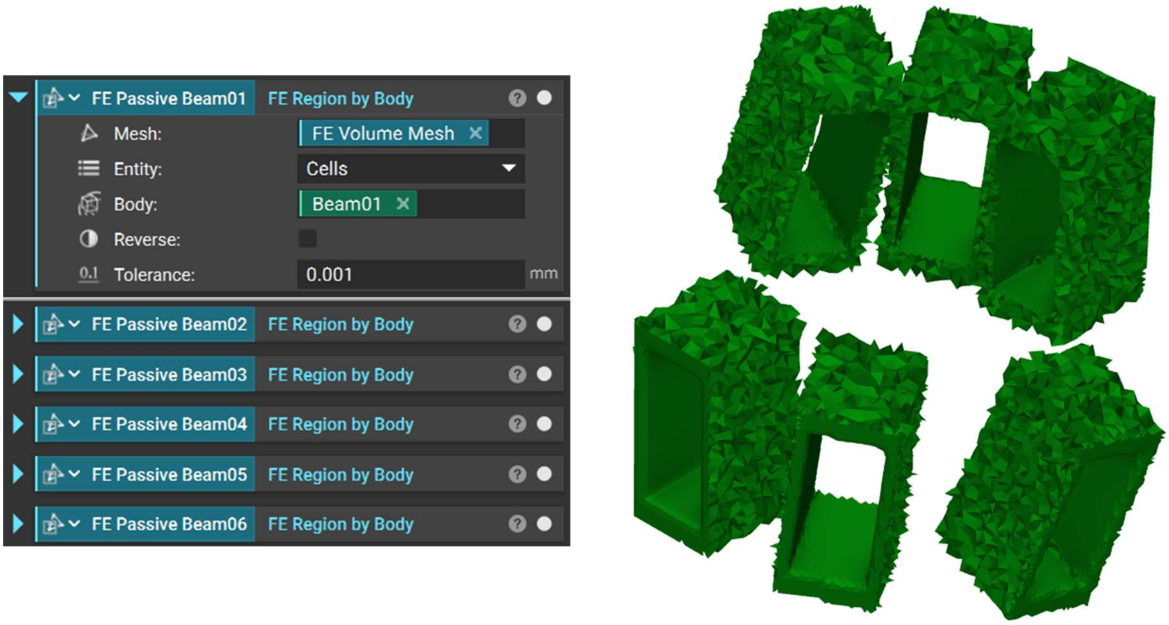

FE Passive Beam01 — FE Region by Body
Mesh: FE Volume Mesh
Entity: Cells
Body: Beam01
Reverse: ☐
Tolerance: 0.001 mm

FE Passive Beam02 — FE Region by Body
FE Passive Beam03 — FE Region by Body
FE Passive Beam04 — FE Region by Body
FE Passive Beam05 — FE Region by Body
FE Passive Beam06 — FE Region by Body

Figure B.12 - FE non-domain regions

B.2.3 Boundary conditions

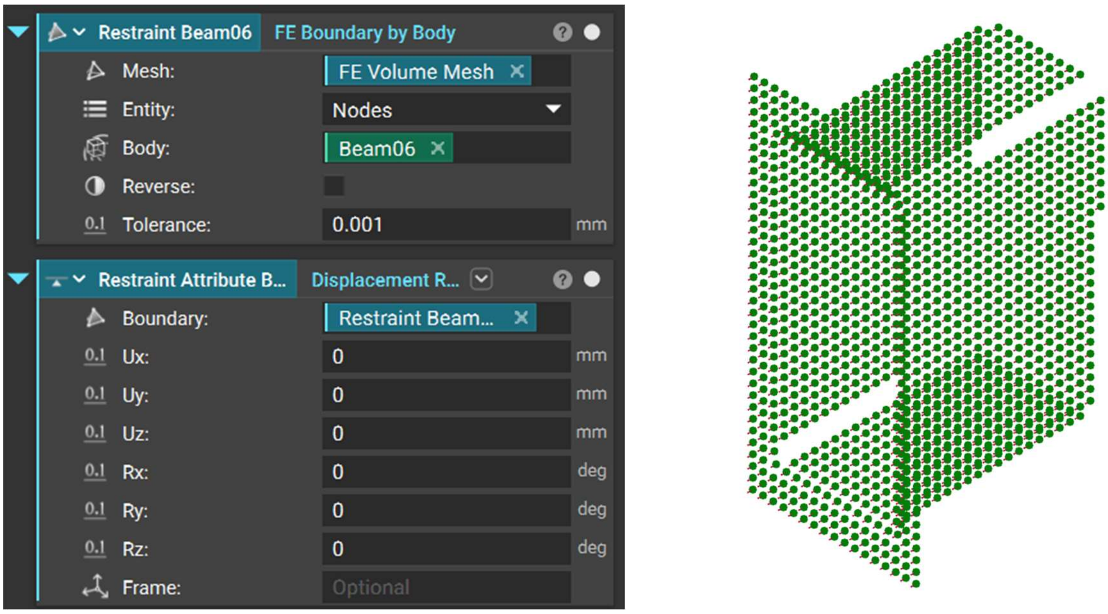

Restraint Beam06 — FE Boundary by Body
Mesh: FE Volume Mesh
Entity: Nodes
Body: Beam06
Reverse: ☐
Tolerance: 0.001 mm

Restraint Attribute B... — Displacement R...
Boundary: Restraint Beam...
Ux: 0 mm
Uy: 0 mm
Uz: 0 mm
Rx: 0 deg
Ry: 0 deg
Rz: 0 deg
Frame: Optional

Figure B.13 - Boundary conditions

B.2.4 Load conditions

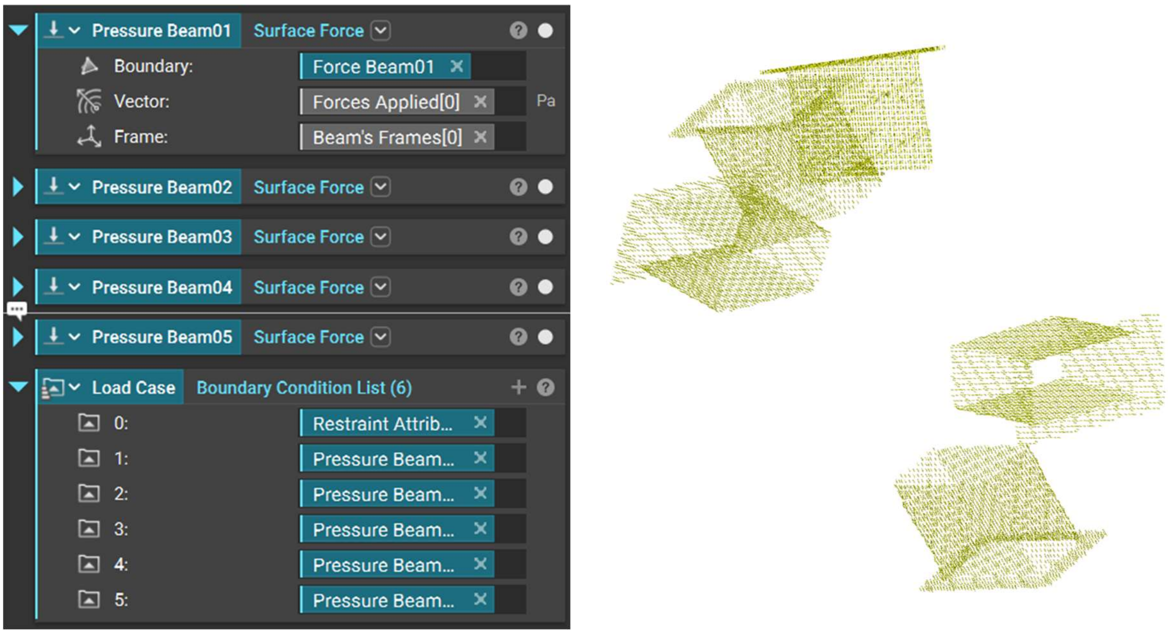

Pressure Beam01 — Surface Force
Boundary: Force Beam01
Vector: Forces Applied[0] Pa
Frame: Beam's Frames[0]

Pressure Beam02 — Surface Force
Pressure Beam03 — Surface Force
Pressure Beam04 — Surface Force
Pressure Beam05 — Surface Force

Load Case — Boundary Condition List (6)
0: Restraint Attrib...
1: Pressure Beam...
2: Pressure Beam...
3: Pressure Beam...
4: Pressure Beam...
5: Pressure Beam...

Figure B.14 - Load conditions

B.2.5 Topology optimization

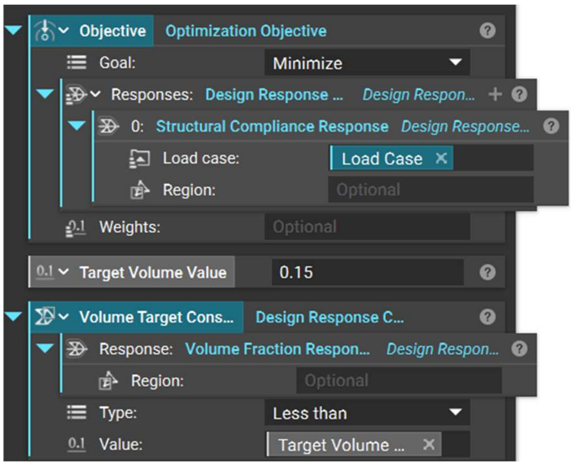

Objective: Optimization Objective
Goal: Minimize
Responses: Design Response ... Design Respon...
0: Structural Compliance Response Design Response...
Load case: Load Case
Region: Optional
Weights: Optional
Target Volume Value: 0.15
Volume Target Cons... Design Response C...
Response: Volume Fraction Respon... Design Respon...
Region: Optional
Type: Less than
Value: Target Volume ...

Figure B.15 - Objectives and constraints of the analysis

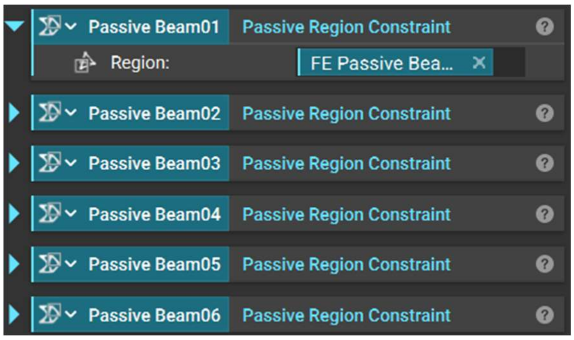

Passive Beam01: Passive Region Constraint
Region: FE Passive Bea...
Passive Beam02: Passive Region Constraint
Passive Beam03: Passive Region Constraint
Passive Beam04: Passive Region Constraint
Passive Beam05: Passive Region Constraint
Passive Beam06: Passive Region Constraint

Figure B.16 - Non-domain regions

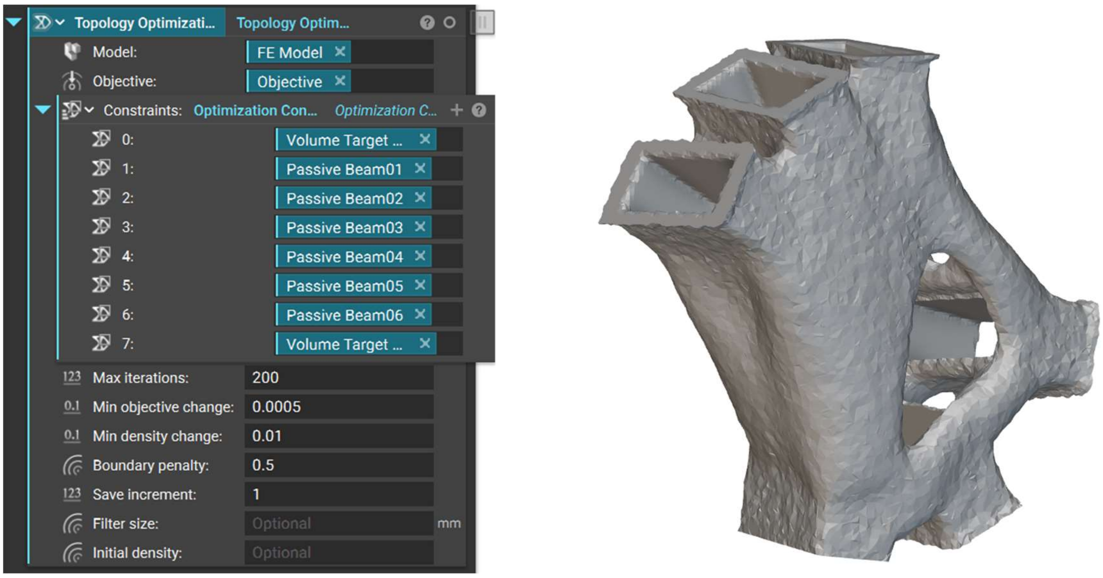

Topology Optimizati... Topology Optim...
Model: FE Model
Objective: Objective
Constraints: Optimization Con... Optimization C...
0: Volume Target ...
1: Passive Beam01
2: Passive Beam02
3: Passive Beam03
4: Passive Beam04
5: Passive Beam05
6: Passive Beam06
7: Volume Target ...
Max iterations: 200
Min objective change: 0.0005
Min density change: 0.01
Boundary penalty: 0.5
Save increment: 1
Filter size: Optional mm
Initial density: Optional

Figure B.17 - Topology optimization analysis

B.2.6 Post-processing

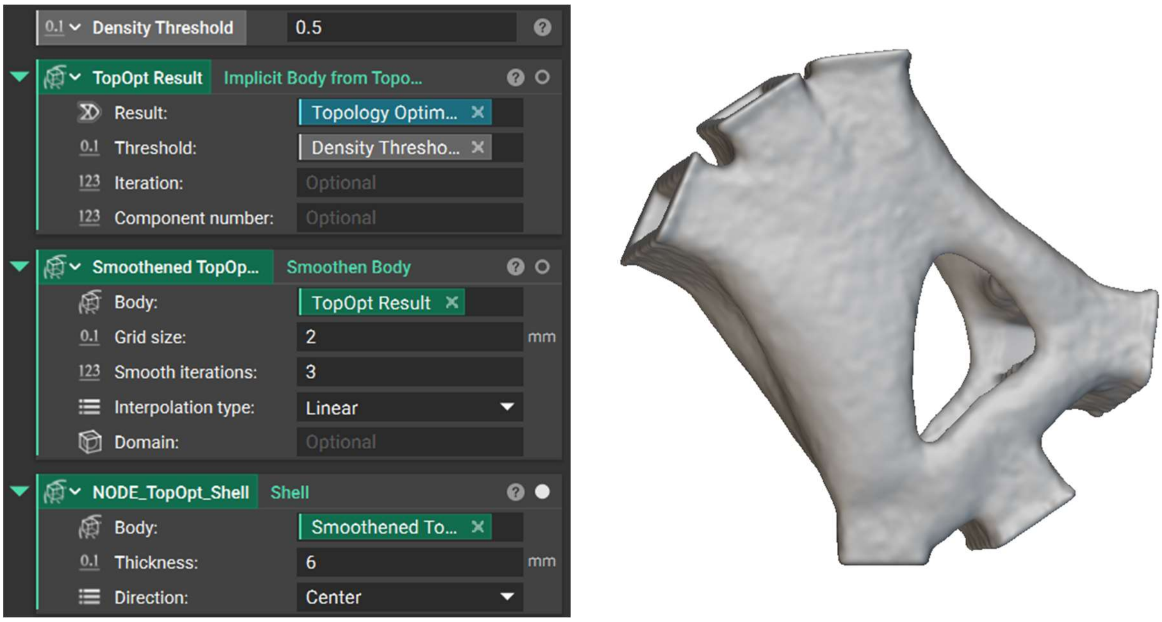

Density Threshold: 0.5

TopOpt Result — Implicit Body from Topo...
Result: Topology Optim...
Threshold: Density Thresho...
Iteration: Optional
Component number: Optional

Smoothened TopOp... — Smoothen Body
Body: TopOpt Result
Grid size: 2 mm
Smooth iterations: 3
Interpolation type: Linear
Domain: Optional

NODE_TopOpt_Shell — Shell
Body: Smoothened To...
Thickness: 6 mm
Direction: Center

Figure B.18 - Post-processing

APPENDIX C

C.1 Buckling analysis results

	Beam01	Beam02	Beam03	Beam04	Beam05	Beam06
			Buckling factors			
Mode 1	19.1431	20.6393	29.533	22.8698	28.1665	23.5258
Mode 2	22.1683	21.4959	34.9671	24.3694	31.3702	26.9124
Mode 3	23.4929	29.2497	38.014	33.9301	33.0674	27.686
Mode 4	27.1755	31.0123	38.1241	37.9618	33.9804	28.548
			Buckling loads (kN)			
Mode 1	19143.1	20639.3	29533	22869.8	28166.5	23525.8
Mode 2	22168.3	21495.9	34967.1	24369.4	31370.2	26912.4
Mode 3	23492.9	29249.7	38014	33930.1	33067.4	27686
Mode 4	27175.5	31012.3	38124.1	37961.8	33980.4	28548

Table C.1 - Buckling factors with 6 mm thickness

	Beam01	Beam02	Beam03	Beam04	Beam05	Beam06
			Buckling factors			
Mode 1	78.9186	75.3877	118.901	116.002	96.894	93.8826
Mode 2	86.6612	78.5858	133.247	128.138	105.973	96.3217
Mode 3	107.477	103.783	141.183	144.604	108.613	100.758
Mode 4	112.63	107.829	145.988	159.374	112.1	108.136
			Buckling loads (kN)			
Mode 1	78918.6	75387.7	118901	116002	96894	93882.6
Mode 2	86661.2	78585.8	133247	128138	105973	96321.7
Mode 3	107477	103783	141183	144604	108613	100758
Mode 4	112630	107829	145988	159374	112100	108136

Table C.2 - Buckling factors with 12 mm thickness

The deformed shapes for mode 1, the ones with the lowest eigenvalues, and thickness 6 mm are reported in Figure C.1:

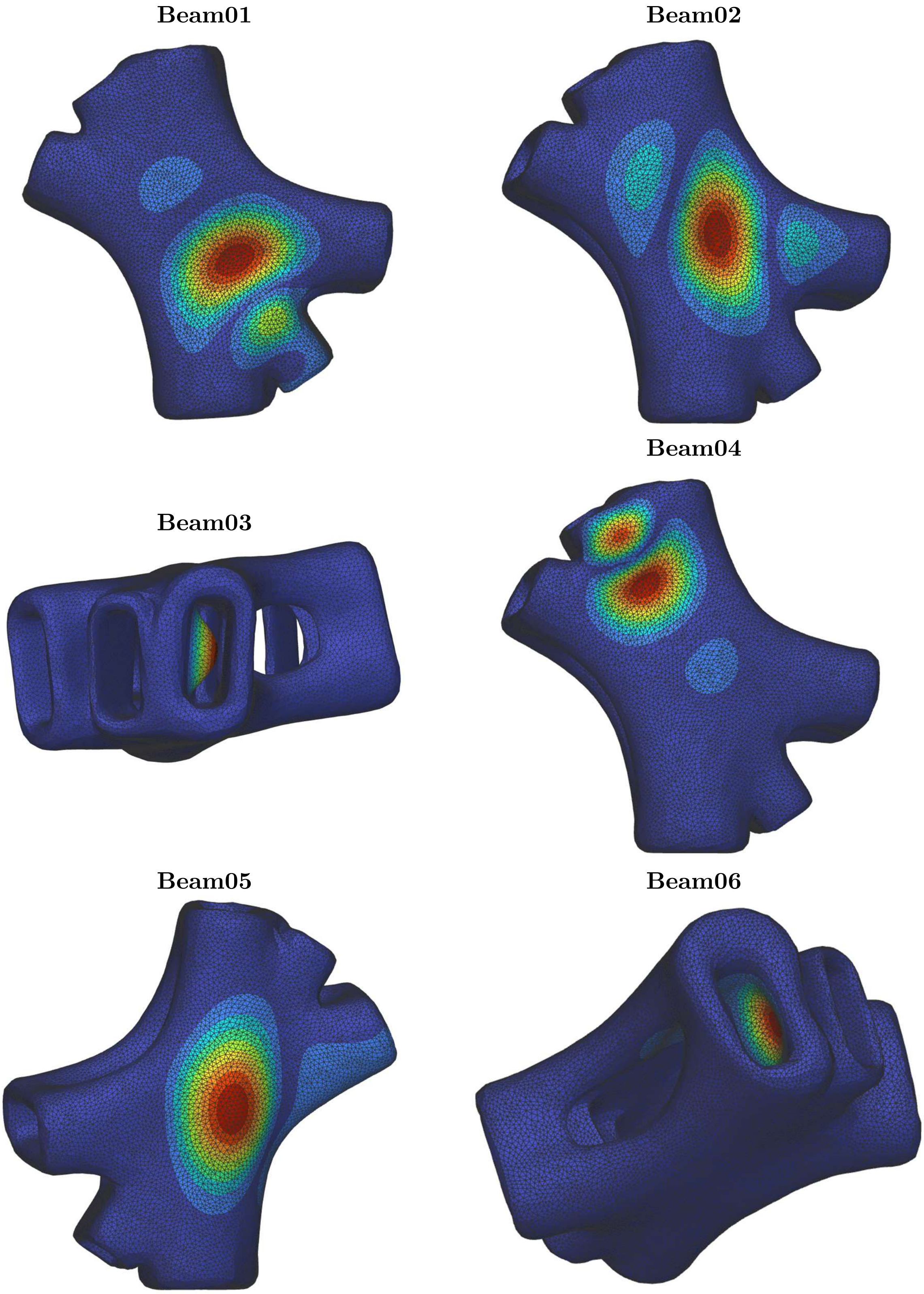

Figure C.1 - Deformed shapes for mode 1 considering the joint with a thickness of 6 mm

The deformed shapes for mode 2 and thickness 6 mm are reported in **Figure C.2**:

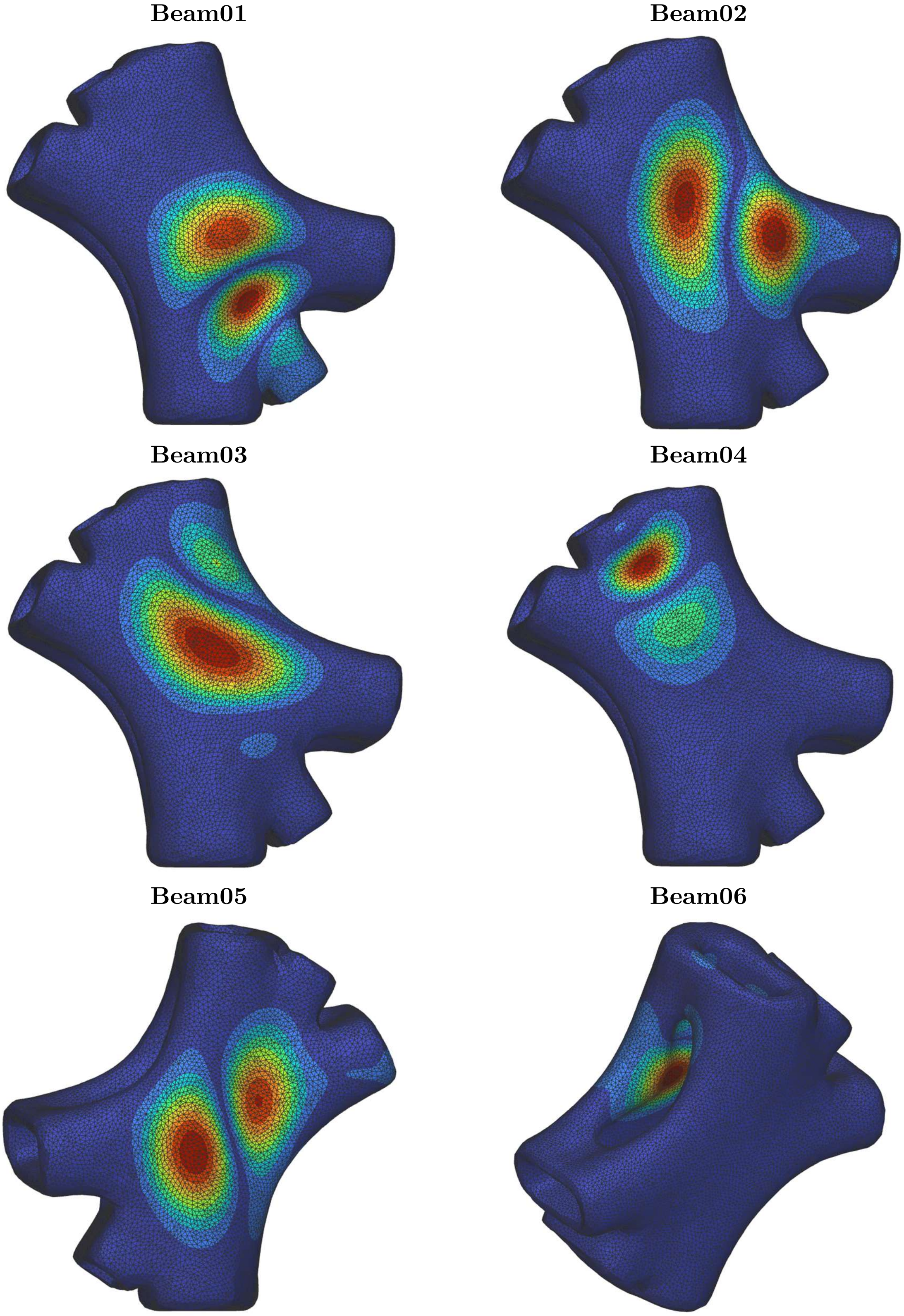

Beam01

Beam02

Beam03

Beam04

Beam05

Beam06

Figure C.2 - Deformed shapes for mode 2 considering the joint with a thickness of 6 mm

The deformed shapes for mode 3 and thickness 6 mm are reported in Figure C.3:

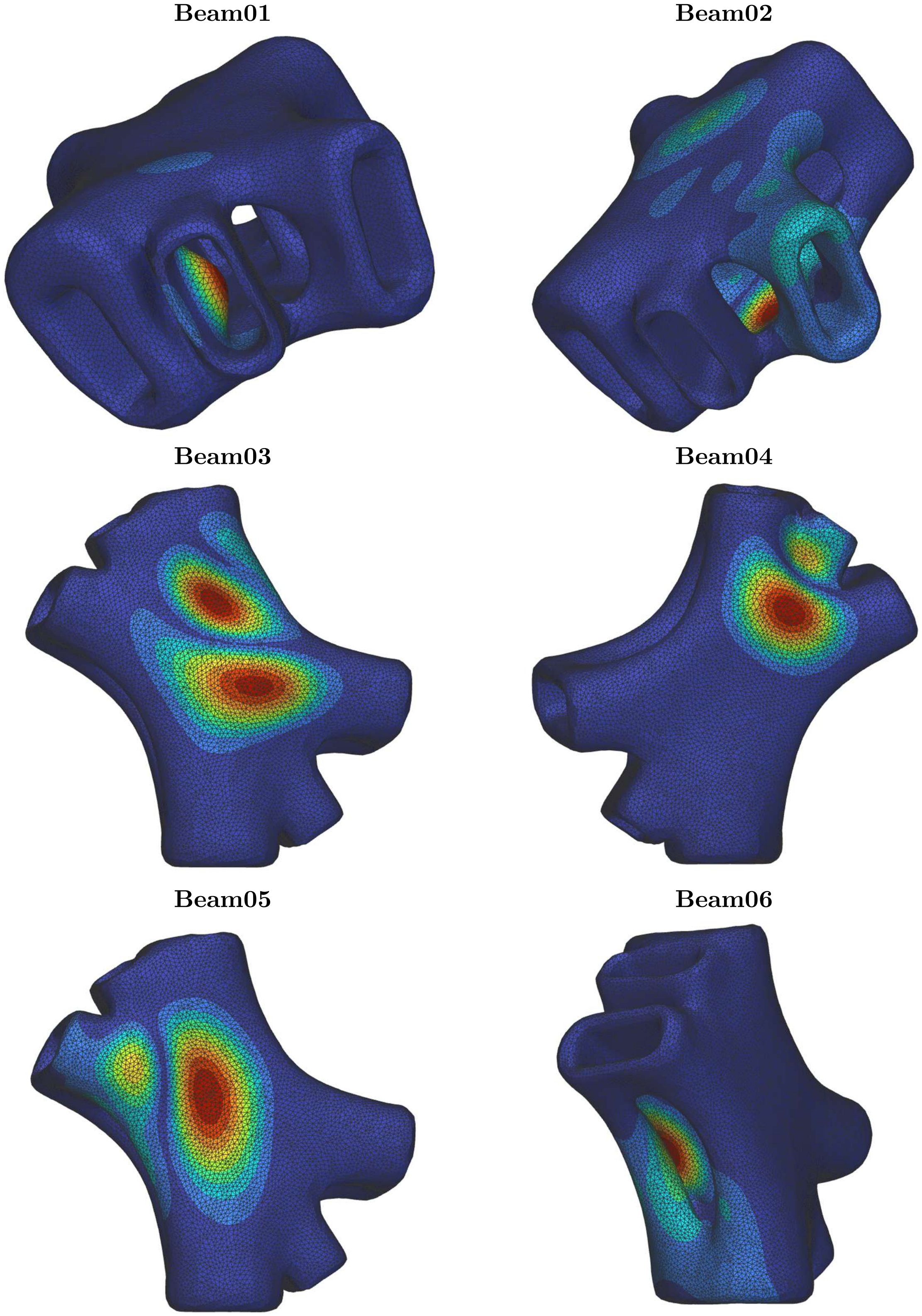

Figure C.3 - Deformed shapes for mode 3 considering the joint with a thickness of 6 mm

The deformed shapes for mode 4 and thickness 6 mm are reported in Figure C.4:

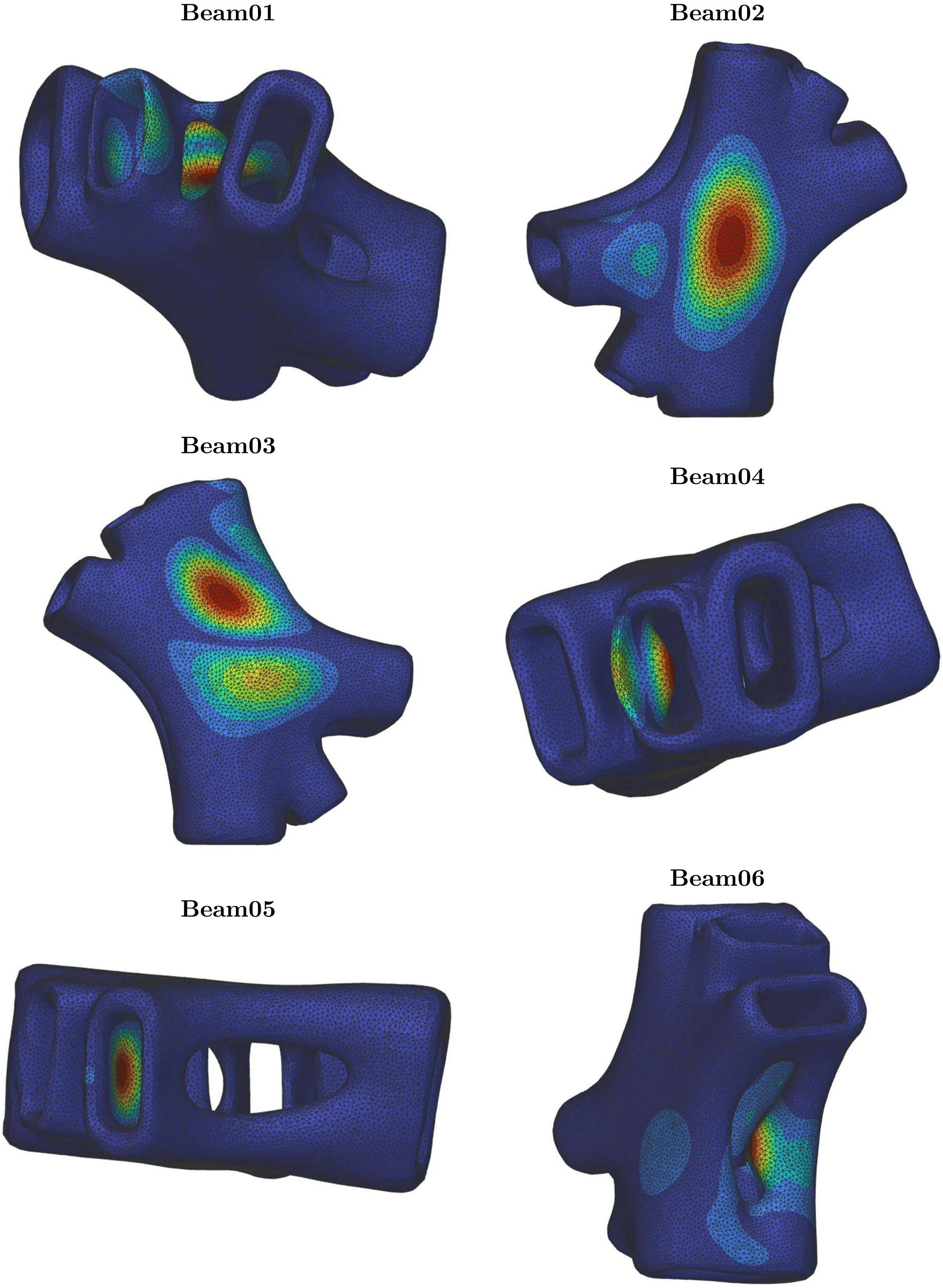
Beam01

Beam02

Beam03

Beam04

Beam05

Beam06

Figure C.4 - Deformed shapes for mode 4 considering the joint with a thickness of 6 mm

Instead, the deformed shapes for mode 1 and thickness 12 mm are reported in Figure C.5:

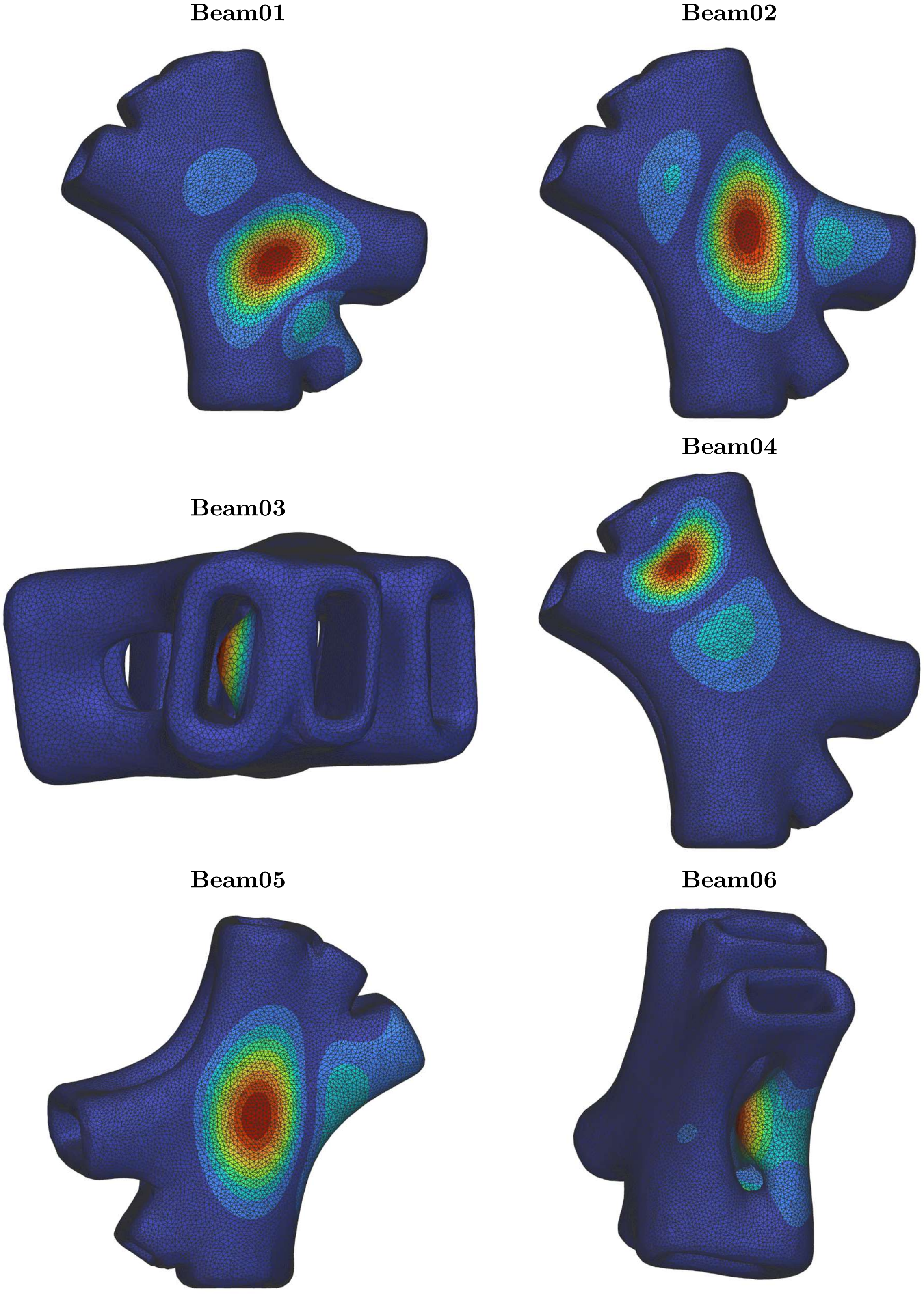
Beam01

Beam02

Beam03

Beam04

Beam05

Beam06

Figure C.5 - Deformed shapes for mode 1 considering the joint with a thickness of 12 mm

The deformed shapes for mode 2 and thickness 12 mm are reported in Figure C.6:

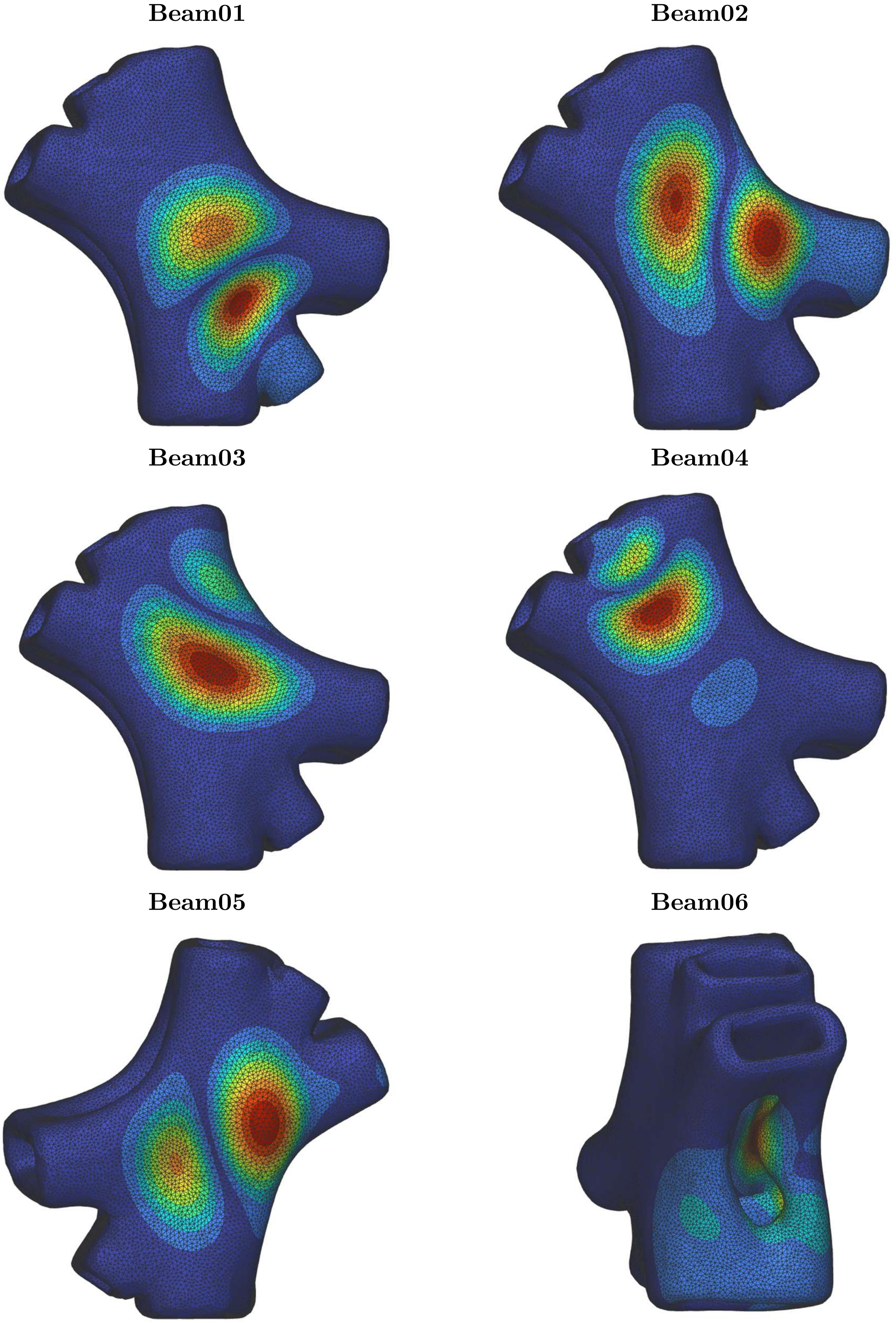

Beam01

Beam02

Beam03

Beam04

Beam05

Beam06

Figure C.6 - Deformed shapes for mode 2 considering the joint with a thickness of 12 mm

The deformed shapes for mode 3 and thickness 12 mm are reported in Figure C.7:

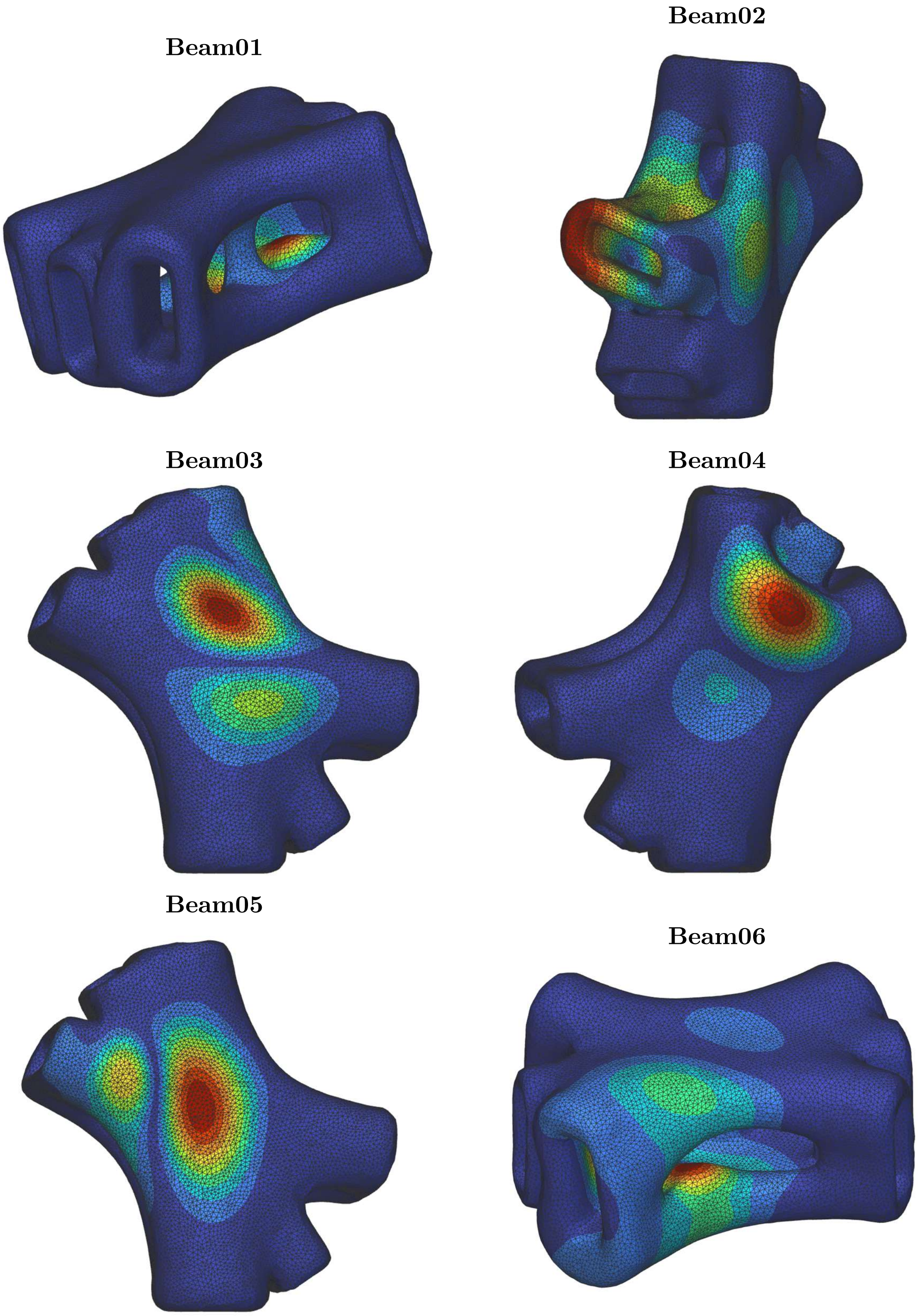

Beam01

Beam02

Beam03

Beam04

Beam05

Beam06

Figure C.7 - Deformed shapes for mode 3 considering the joint with a thickness of 12 mm

The deformed shapes for mode 4 and thickness 12 mm are reported in Figure C.8:

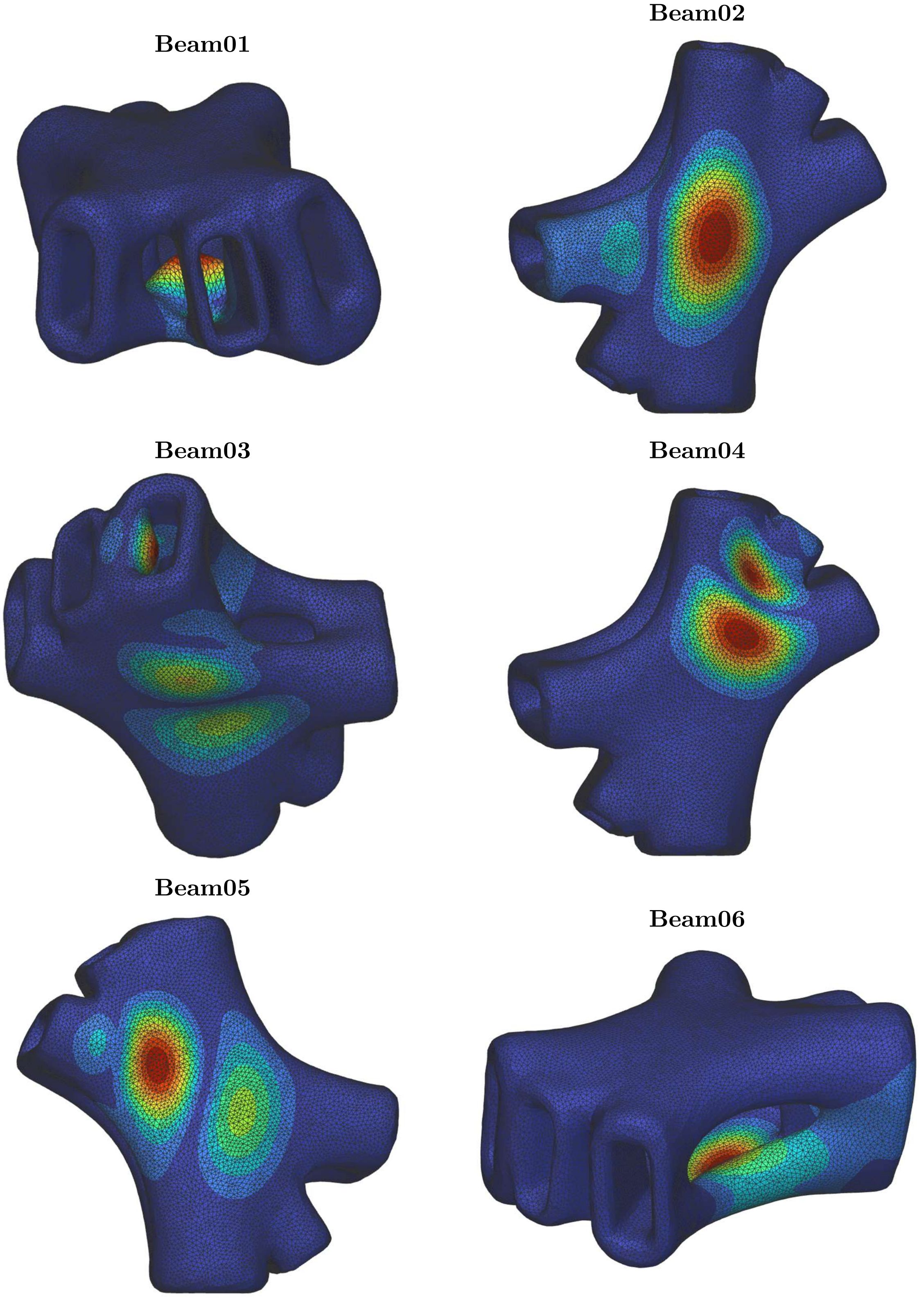

Figure C.8 - Deformed shapes for mode 4 considering the joint with a thickness of 12 m

TABLE OF FIGURES

INDEX OF TABLES
